ADVANCED MULTIMODAL METHODS IN BIOMEDICINE: RAMAN SPECTROSCOPY AND DIGITAL HOLOGRAPHIC MICROSCOPY

Naomi McReynolds

A Thesis Submitted for the Degree of PhD
at the
University of St Andrews

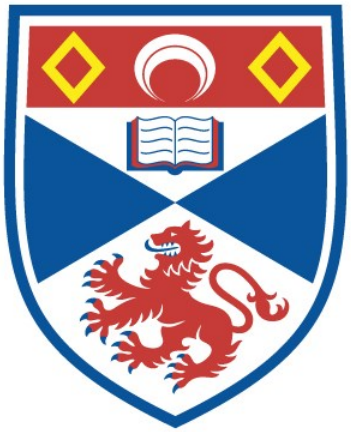

2017

Advanced Multimodal Methods in Biomedicine: Raman Spectroscopy and Digital Holographic Microscopy

Naomi McReynolds

This thesis is submitted in partial fulfilment for the degree of Doctor of Philosophy

Optical Manipulation Group
School of Physics and Astronomy
University of St. Andrews

August 14, 2017

Declaration of Authorship

I, Naomi MCREYNOLDS, hereby certify that this thesis, which is approximately 56150 words in length, has been written by me, and that it is the record of work carried out by me, or principally by myself in collaboration with others as acknowledged, and that it has not been submitted in any previous application for a higher degree. I was admitted as a research student in September 2013 and as a candidate for the degree of Doctor of Philosophy in September 2013; the higher study for which this is a record was carried out in the University of St Andrews between 2013 and 2017.

Date: _____ Signature of candidate: _____

I hereby certify that the candidate has fulfilled the conditions of the Resolution and Regulations appropriate for the degree of Doctor of Philosophy in the University of St Andrews and that the candidate is qualified to submit this thesis in application for that degree.

Date: _____ Signature of supervisor: _____

In submitting this thesis to the University of St Andrews I understand that I am giving permission for it to be made available for use in accordance with the regulations of the University Library for the time being in force, subject to any copyright vested in the work not being affected thereby. I also understand that the title and the abstract will be published, and that a copy of the work may be made and supplied to any bona fide library or research worker, that my thesis will be electronically accessible for personal or research use unless exempt by award of an embargo as requested below, and that the library has the right to migrate my thesis into new electronic forms as required to ensure continued access to the thesis. I have obtained any third-party copyright permissions that may be required in order to allow such access and migration, or have requested the appropriate embargo below.

The following is an agreed request by candidate and supervisor regarding the publication of this thesis: Embargo on all of printed copy and electronic copy for a period of 6 months on the following ground(s):

- Publication would be commercially damaging to the researcher, or to the supervisor, or the University

- Publication would be in breach of laws or ethics

Date: _____ Signature of candidate: _____

Signature of supervisor: _____

"If you want to find the secrets of the universe, think in terms of energy, frequency and vibration"

Nikola Tesla

Abstract

Moving towards label-free technologies is essential for many clinical and research applications. Raman spectroscopy is a powerful tool in the field of biomedicine for label-free cell characterisation and disease diagnosis, owing to its high chemical specificity. However, Raman scattering is a relatively weak process and can require long acquisition times, thus hampering its integration to clinical technologies. Multimodal analysis is currently pushing the boundaries in biomedicine, obtaining more information than would be possible using a single mode and overcoming any limitations specific to a single technique. Digital holographic microscopy (DHM) is a rapid and label-free quantitative phase imaging modality, providing complementary information to Raman spectroscopy, and is thus an ideal candidate for combination in a multimodal system.

Firstly, this thesis explores the use of wavelength modulated Raman spectroscopy (WMRS), for the classification of immune cell subsets. Following this a multimodal approach, combining Raman spectroscopy and DHM, is demonstrated, where each technique is considered individually and in combination. The complementary modalities provide a wealth of information (both chemical and morphological) for cell characterisation, which is a step towards achieving a label-free technology for the identification of human immune cells. The suitability of WMRS to discriminate between closely related neuronal cell types is also explored.

Furthermore optical spectroscopic techniques are useful for the analysis of food and beverages. The use of Raman and fluorescence spectroscopy to successfully discriminate between various whisky and extra-virgin olive oil brands is demonstrated, which may aid the detection of counterfeit or adulterated samples. The use of a compact Raman device is utilised, demonstrating the potential for in-field analysis.

Finally, monodisperse and highly spherical nanoparticles are synthesised. A short study demonstrates the potential for these nanoparticles to benefit the techniques of surface enhanced Raman spectroscopy and optical trapping, by way of minimising variability.

Acknowledgements

First and foremost, I would like to acknowledge my supervisor Prof. Kishan Dholakia for giving me an opportunity to work in his group. Working under his guidance for the past four years has helped me gain new skills and expertise. Special thanks must also go to Dr Simon Powis and Dr Gayle Doherty for their encouragement and support in many aspects of biology, and for discussions which helped boost my spirits. Next I would like to thank Prof. Frank Gunn-Moore for discussions at the Monday meetings and his tips on biology. I would also like to Dr Michael Mazilu for many insightful discussions, particularly with respect to data analysis.

I consider myself lucky to have had the opportunity to work alongside several outstanding researchers in the past four years, to whom I would like to express my gratitude. Mingzhou Chen has given me a lot of support throughout my PhD studies, particularly with respect to optics and Raman spectroscopy. He has also offered a lot of time to discuss various aspects of my studies. Yoshihiko Arita and Georgiy Tkachenko have been kind enough to share their insights and train me in optical trapping. I would also like to express my gratitude to Lisa Strother who spent valuable time training me in cell culture and biology techniques, and to Nicolas Marro and William Edwards who trained me in nanoparticle synthesis. Additional thanks should go to Derek Craig who helped me to get integrated into the group in the early days of my PhD, and Blair Kirkpatrick who spent valuable time training me on lithography techniques and use of the SEM. I would like to express my gratitude to Maciej Antkowiak for his scientific discussions and Klaus Metzger for his advice, support, and invaluable training in optical techniques. I would also like to express my sincere gratitude to all my colleagues during the course of my PhD for their friendship.

Special thanks must also go to all the administrative and technical staff whose help and support has been invaluable for the last few years. I would also like to express my gratitude to Jonathan Nylk and Frances Goff for proof reading and suggesting corrections to this thesis.

On a more personal note I would like to thank my family and friends for their

love and support throughout these years, with a special thanks to Geoffrey Raff for always keeping a smile on my face.

Contents

Publications

- M. Chen*, **N. McReynolds***, E. C. Campbell*, M. Mazilu, J. Barbosa, K. Dholakia, S. J. Powis, "The use of wavelength modulated Raman spectroscopy in label-free identification of T lymphocyte subsets, natural killer cells and dendritic cells", (2015) PLosOne 10(5): e0125158. *(* Authors have equal contribution)*
- **N. McReynolds**, J. M. A. Garcia, Z. Guengerich, T. K. Smith, K. Dholakia, "Optical Spectroscopic analysis for the discrimination of Extra-Virgin Olive Oil", (2016) Appl. Spectrosc., 70(11) 1872-1882
- **N. McReynolds**, F. G. M. Cooke, M. Chen, S. J. Powis, K. Dholakia, "Multimodal discrimination of immune cells using a combination of Raman spectroscopy and digital holographic microscopy", (2017) Sci. Rep., 7 (43631)

Conferences and courses attended

- 7th International graduate summer school- Biophotonics ’15, June 2015, poster "Label-free classification of human immune cells using wavelength modulated Raman spectroscopy"
- SPIE conference Optics and Photonics, Student chapter leadership workshop, August 2014
- Biophotonics north conference, November 2016, contributed talk
- SPIE conference BiOs: Multimodal Biomedical Imaging XII, January 2017, contributed talk "Multi-modal approach using Raman spectroscopy and digital holographic microscopy for the identification of immune cell subsets "
- SPIE conference OPTO: MOEMS and Miniaturized Systems XVI, February 2017, contributed talk "The use of Raman and fluorescence spectroscopy for the discrimination of extra-virgin olive oil"

List of Abbreviations

ADC	**A**nalog to **D**igital **C**onverter
BA	**B**ack **A**perture
BSA	**B**ovine **S**erum **A**lbumin
CARS	**C**oherent **A**nti-Stokes **R**aman **S**pectroscopy
CCD	**C**harge-**C**oupled **D**evice
CMOS	**C**omplimentary **M**etal-**O**xide-**S**emiconductor
COM	**C**entre **O**f **M**ass
CW	**C**ontinuous **W**ave
DHM	**D**igital **H**olographic **M**icroscopy
DC	**D**endritic **C**ell
DPSS	**D**iode-**P**umped **S**olid-**S**tate
EBV	**E**pstein-**B**arr **V**irus
EF	**E**nhancement **F**actor
EM	**E**lectro**M**agnetic
EVOO	**E**xtra **V**irgin **O**live **O**il
FACS	**F**luorescence **A**ctivated **C**ell **S**orting
FAME	**F**atty **A**cids and **M**ethyl **E**ster
FCS	**F**etal **C**alf **S**erum
FFA	**F**ree **F**atty **A**cids
FITC	**F**luoroscein **I**so**T**hio**C**yanate
FSC	**F**orward **SC**atter
FT	**F**ourier **T**ransform
FWHM	**F**ull-**W**idth **H**alf-**M**aximum
GC	**G**as **C**hromatography
GC-MS	**G**as **C**hromatography-**M**ass **S**pectrometry
GLCM	**G**rey **L**evel **C**o-occurrence **M**atrix
HSB	**H**orse **S**erum **B**lock
HPLC	**H**igh-**P**erformance **L**iquid **C**hromatography
HRP	**H**orse**R**adish **P**eroxidase

ICC	**I**mmuno**C**yto**C**hemistry
IOC	**I**nternational **O**live **C**ouncil
L-DOPA	**L**evo**DOPA**
LF	**L**ine **F**ilter
LOOCV	**L**eave **O**ne **O**ut **C**ross **V**alidation
LPS	**L**ipo**P**oly**S**accharide
LSPR	**L**ocalised **S**urface **P**lasmon **R**esonance
MBA	4-**M**ercapto**B**enzoic **A**cid
MHC	**M**ajor **H**istocompatibility **C**omplex
MO	**M**icroscope **O**bjective
NA	**N**umerical **A**perture
ND	**N**eutral **D**ensity
NF	**N**otch **F**ilter
NIR	**N**ear **I**nfra**R**ed
NK	**N**atural **K**iller
NP	**N**ano **P**article
OCT	**O**ptical **C**oherence **T**omography
OPD	**O**ptical **P**ath **D**ifference
OPL	**O**ptical **P**ath **L**ength
PBS	**P**hosphate **B**uffered **S**aline
PC	**P**rinciple **C**omponent
PCA	**P**rinciple **C**omponent **A**nalysis
PD	**P**arkinson's **D**isease
QPI	**Q**uantitative **P**hase **I**maging
RA	**R**etinoic **A**cid
RBC	**R**ed **B**lood **C**ell
REF	**R**azor **E**dge **F**ilter
ROI	**R**egion **O**f **I**nterest
RRS	**R**esonance **R**aman **S**pectroscopy
SSRS	**S**ubtracted **S**hifted **R**aman **S**pectroscopy
SEM	**S**canning **E**lectron **M**icroscope

SERDS	**S**hifted **E**xcitation **R**aman **D**ifference **S**pectroscopy
SERS	**S**urface **E**nhanced **R**aman **S**pectroscopy
SLM	**S**patial **L**ight **M**odulator
SNR	**S**ignal to **N**oise **R**atio
SORS	**S**patially **O**ffset **R**aman **S**pectroscopy
SRS	**S**timulated **R**aman **S**pectroscopy
SSC	**S**ide **SC**atter
SSRS	**S**ubtracted **S**hifted **R**aman **S**pectroscopy
TA	**T**exture **A**nalysis
TH	**T**yrosine **H**ydroxylase
TRRS	**T**ime-**R**esolved **R**aman **S**pectroscopy
US	**U**ltra **S**mooth
WBC	**W**hite **B**lood **C**ell
WD	**W**orking **D**istance
WMRS	**W**avelength **M**odulated **R**aman **S**pectroscopy

1 Introduction

Label-free technologies, based on directly probing physical processes such as molecular vibrations, are being developed to overcome some of the limitations associated with the use of labels. This is particularly important in biomedicine where labels can lead to misleading conclusions and introduce additional complexity. For example, attachment of a fluorescent protein to a protein of interest may impair protein function, or have an effect on subcellular localisation of proteins. Furthermore modification of antigen recognition sites may affect antibody-antigen mechanisms. Non-specific binding or autofluorescence from the sample could lead to false positives and misleading conclusions. The use of labels adds complexity to the experimental design through consideration of tag design, for example is it membrane permeable? what is its effect on protein function and localisation? how is the intensity affected during cell division? or how should one account for blinking?. Cytotoxicity effects must also be considered; aggregation of fluorescent proteins can lead to cellular toxicity and generation of free radicals during excitation are toxic to cells. It has also been shown that green fluorescent protein (GFP) can induce apoptosis in cells [1–3]. Further consideration should be given to the immune response towards fluorescent proteins as key immune cell subsets will be dealt with in this thesis. An immune response of the cytotoxic T cell (T_c) through recognition of the GFP antigen has previously been reported [4]. Quantification of the T_c cell response in mice after injecting wild-type pre-leukemia cells revealed a three-fold increase of the T_c cell response against GFP-expressing leukemia cells, when compared to non GFP-expressing leukemia cells [5].

Raman spectroscopy is a powerful optical spectroscopic technique that can provide specific molecular information regarding a samples chemical composition in a label-free manner. It has been frequently used to study cells and tissues in recent years [6–8]. Raman spectroscopy has many advantages which make it ideal for studying biological samples, such as being insensitive to water molecules, extracting specific molecular and structural information without requiring staining or

labelling, it may be combined with microscopy techniques and optical fibres making it useful to both in-vivo and ex-vivo analysis. The main limitation of Raman spectroscopy is its inherently weak cross-section (typically only 1 in 10^6 photons are Raman scattered), limiting the speed of the technique. Reducing acquisition times can compromise the signal to noise ratio (SNR) thus affecting reliability of results.

Chapter 2 introduces the basic theory and implementation of Raman spectroscopy. The role of Raman spectroscopy in the field of biomedicine and the food and drinks industry is discussed. This chapter then focusses on the issue of fluorescence suppression and describes the technique of wavelength modulated Raman spectroscopy (WMRS). A brief introduction to the principle of surface enhanced Raman spectroscopy (SERS) is then given. Following this, the construction of a free space Raman spectrometer is described and the key components required are outlined. Finally, the statistical methods used for analysis of Raman data are detailed.

Chapter 3 goes on to explore the ability of WMRS to discriminate between major immune cell subsets in a label-free manner. Current methods for detection cells of the immune system include cell fixation and staining to reveal cellular morphology. Morphologically similar cells however are classically identified using fluorescent labels, to target specific cell surface markers. Such labels have potential to alter cellular behaviour or even induce an immune cell response. This could introduce uncertainty for example in drug discovery and development. This chapter demonstrates the potential of using WMRS as a label-free haemograph, and its validity when samples are acquired from multiple donors.

The main limitation to integration of this technology to clinical and routine lab-use is the comparatively long acquisition times required when compared to traditional methods for cell counting or cell sorting, such as flow cytometry or fluorescence-activated cell sorting (FACS), which are able to record 10,000 events per second. Raman spectroscopy is not suggested to replace these techniques but rather be a valuable technology for applications where untouched cell populations are a priority.

One of the main challenges facing biomedicine, and in particular label-free technologies, is to extract large quantities of information from a sample (both in terms of quantity and variety of information) in a short period of time, either to enable

tracking of rapid dynamics or to ensure high throughput rates. Multimodal technologies can provide additional information than would be possible using any single modality alone, and in this way may overcome the limitations specific to a single technique. Complementary information can be obtained from two modalities that probe different physical interactions, such as chemical and morphological information, thus giving a more complete description of a sample.

Digital holographic microscopy (DHM) provides morphological information, arising from phase shifts introduced as light propagates through a cell. Morphological information would complement the chemical information available from Raman spectroscopy and may therefore be able to provide an improved discrimination ability between closely related immune cell subsets. Furthermore DHM is a rapid wide-field imaging technique, and thus has potential to act as an initial fast screening, where Raman spectroscopy can probe cells of interest for more chemically specific information. This approach may have potential to improve the throughput rate. Importantly DHM is also a label-free technique and is compatible with biological samples.

Chapter 4 provides an introduction to DHM, image analysis, and the design of the multimodal system. The system is designed so simultaneous and independent measurements can be acquired, so measurements can be considered rapid. Each modality is considered individually and in combination for the discrimination between key immune cell subsets.

Chapter 5 considers a different biomedical application, concerning dopaminergic neuronal cells. Current methods to identify dopaminergic neurons in primary cultures require cell fixation and staining. A label-free technology would be a significant advance for obtaining pure cultures of dopaminergic cells for further analysis and modelling of neurological disorders. The ability of WMRS to quantitatively detect dopamine and discriminate between closely related neuronal cells (SH-SY5Y cell line in various differentiation states) is assessed.

The work discussed in chapter 6 considers applications for Raman and fluorescence spectroscopy in the food and drinks industry. Rapid, easy to use and portable technologies for the detection of counterfeit food and food contamination would be invaluable to the food and drinks industry [9, 10]. Traditional methods for sensitive

analysis such as gas chromatography (GC), high-performance liquid chromatography (HPLC) and gas chromatography mass spectrometry (GC-MS) are powerful tools for determining composition and quantifying complex mixtures of chemicals, however they are time consuming, costly, destructive to the sample, and bulky, limiting their use for in-field analysis [11, 12]. Near infrared (NIR) spectroscopy is also a well established technique to rapidly monitor the composition and quality of food products, although it suffers from strong absorption of water limiting the spectral resolution in aqueous samples [13]. Fluorescence spectroscopy is able to provide information regarding molecules in food and drinks products, provided they possess the property of autofluorescence [14, 15].

The ability to discriminate between different brands of whisky and extra-virgin olive oil is assessed in chapter 6, using a Raman and fluorescence based approach. These two modalities provide information on both chemical composition and colour of a sample. This technology has the potential to identify different brands of whisky and extra-virgin olive oil which could aid the detection of counterfeit or adulterated samples. The label-free nature makes this technique ideal for integration to in-line procedures. Following this, a compact Raman device is utilised, demonstrating the compatibility with in-field analysis.

Chapter 7 considers a novel method to synthesis homogeneous and ultra-smooth gold nanoparticles and two potential applications: SERS and optical trapping. Size and shape have a direct relevance to plasmonic and trapping properties of gold nanoparticles. The ability for these nanoparticles to provide more reproducible measurements is explored.

The final chapter is a summary of the various applications detailed in previous studies, and a discussion on future directions that would enhance the applicability of Raman spectroscopy in clinical and research settings.

2 Raman spectroscopy: An overview

2.1 Introduction

Raman Spectroscopy is a molecular spectroscopic technique, based on the inelastic vibrational scattering of light. A Raman signature can provide a 'fingerprint' that is unique to a material, providing specific structural and chemical information, as well as characterising the effects of environment or stress on a sample. Raman spectroscopy has a variety of advantages over other vibrational spectroscopic methods such as requiring little or no sample preparation, an insensitivity to aqueous absorption bands enabling its use with solids, liquids and gases, as well as the ability to measure through transparent materials such as glass or quartz. All of this considered, Raman spectroscopy has found use in a wide variety of applications; to identify and study specimens in areas such as pharmaceuticals, analysis of material structures, the food and drinks industry, and bio-medical diagnostics [9, 16, 17].

This chapter will give a brief introduction to the theory of Raman spectroscopy and an overview of its use in bio-medicine and the food and drinks industry. An introduction to fluorescence suppression techniques will be provided, with particular attention paid to the method of wavelength modulated Raman spectroscopy (WMRS). This will be followed by a brief overview of a Raman signal enhancement technique 'surface-enhanced Raman spectroscopy' (SERS). The instrumentation required for Raman spectroscopy will be discussed, in the context of the free space system used for studies presented in this thesis. Finally the basic Raman processing techniques used throughout this thesis will be addressed.

2.1.1 Brief history

A. Smekal first provided the theoretical basis of inelastic light scattering in 1923 [18]. However it was Sir C. V. Raman who pioneered the first experimental observations, reported in 1928 [19, 20], for which he received the Nobel Prize in Physics in 1930 "*for his work on the scattering of light and for the discovery of the effect named after him*". In his original experiment sunlight was focussed by a telescope and a short-focus

lens to create a more powerful beam, this was focussed onto purified liquid samples. A second lens was used at 90° to collect the scattered light and a series of filters were used to show the presence of both elastic and inelastic light scattering. Incredibly Raman's eyes served as the detector. By purifying the liquid multiple times they were able to conclude the effect was not due to traces of fluorescence. When explaining the new phenomena he described that the frequency shift was characteristic of the molecule comprising the scattering medium, and that it did not depend on the incident wavelength; these are the main characteristics of Raman scattering.

2.2 Basic theory of Raman spectroscopy

Light may interact with matter either via absorption, scattering, or with no interaction at all. When the energy of the incident photon matches the energy gap between the ground and excited states of a molecule it may be absorbed; for scattering events however there is no such requirement for energy matching. Light may either scatter elastically, when there is no change in photon energy, or inelastically, when there is a change in the photon energy.

The classical wave interpretation of light is to consider light as electromagnetic radiation, containing an oscillating electric field. This field may interact with a molecule and polarise the electron cloud around the nuclei to form a short-lived 'virtual state'. Most commonly the electron cloud will relax without any nuclear movement, releasing a photon with the same energy as the incident radiation. This elastic form of scattering is known as Rayleigh scattering. Less frequently nuclei movement will be induced during the interaction. As the nuclei are much heavier than electrons this will cause an appreciable change in energy between the incident and scattered photons. This is inelastic scattering, and is known as Raman scattering. Only one in every 10^6-10^8 photons will be Raman scattered. During these events energy can either be transferred from the molecule to the photon (known as anti-Stokes scattering) or from the photon to the molecule (known as Stokes scattering), depending on whether the molecule is already in a vibrationally excited state or in its ground state respectively [21, 22]. These interactions are summarised in figure 2.1.

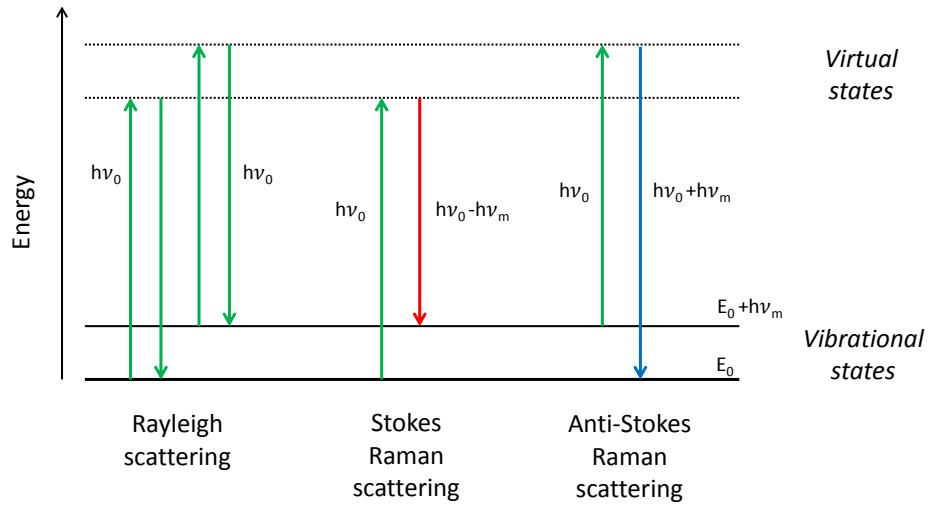

FIGURE 2.1: Jablonski diagram representing the three major types of scattering; Rayleigh elastic scattering, Stokes Raman scattering and anti-Stokes Raman scattering. Consider an incident photon of frequency ν_0 with energy hν_0, where h is Planck's constant, Stokes Raman scattering occurs with excitation from the ground vibrational state E_0 to a higher energy vibrational state, resulting in a scattered photon with a loss of one vibrational unit of energy ν_{m}. Anti-Stokes Raman scattering occurs when energy is transferred to the incident photon as the molecule goes from an excited vibrational state to the ground vibrational state.

At room temperature, most molecules will exist in their lowest vibrational level; consequently Stokes scattering is typically more intense than anti-Stokes scattering and therefore more commonly used. Anti-stokes scattering may however be useful in some applications, such as avoidance of fluorescence interference (which occurs at longer wavelengths than the incident radiation) or to measure temperature. The difference between the intensities of Stokes and anti-Stokes scattering is dependent on the population of molecules in the ground or excited states, which is governed by the Maxwell-Boltzmann equation as described in equation 2.1.

$$\frac{N_m}{N_0} = \frac{g_m}{g_0} e^{\left(\frac{-(E_m - E_0)}{kT}\right)} \tag{2.1}$$

Where N_m is the number of molecules in the excited vibrational energy level m, N_0 is the number of molecules in the ground vibrational energy level n (in figure 2.1 these energy levels are depicted as $E_0 + h\nu_m$ and E_0 respectively). $g_{0,m}$ is the degeneracy of the levels 0 and m, $E_m - E_0$ is the difference in energy between vibrational levels, k is the Boltzmann's constant, and T is the absolute temperature [21]. Nevertheless, due to the more intense Stoke's Raman signal (typically $N_m/N_0 \ll 1$)

it is Stokes Raman scattering that will be dealt with throughout this thesis.

Light scattering is sensitive to the polarisability of the electron cloud (the mobility of electrons in a bond) around a molecule. Equation 2.2 describes the linear dependence of the dipole moment on the electric field:

$$\mu_T = \mu + \alpha\epsilon(\nu') \tag{2.2}$$

where μ_T is the total electronic dipole moment vector, μ is the permanent dipole term in the absence of any field, and $\alpha\epsilon(\nu')$ is the electric field induced dipole moment, which is related to the polarisation of the electronic cloud of a molecule in the field. Specifically $\epsilon(\nu')$ is the oscillating electric field, and the induced polarisation is characterised by the polarisability term α [23]. Polarisability is a material property dependent on the molecular structure and nature of the bonds [24]. As Raman scattering relies on the transfer of energy to a vibrational mode it becomes clear that the more polarisable the molecule, the more intense will be the Raman scattering. Indeed this is the gross selection rule for Raman scattering; vibrations must cause a change in the polarisability of the electron cloud to be Raman active. In general, as symmetric vibrations tend to give the greatest displacement they typically give rise to the most intense Raman scattering [21]. On the other hand if a vibration does not greatly change the polarisability, then the intensity of the Raman band will be low. If, for example, a molecule is highly polar, such as the 0-H bond in water, the incident electric field cannot easily induce a change in the dipole moment, resulting in weak Raman scattering.

The vibrational frequency of a bond is dependent on the mass of the atoms connected to the bonds, the strength of the bond, and the geometry of the molecule. Any change in energy observed via Raman scattered photons is thus characteristic to a unique chemical bond and its type of vibration. For example, a bending vibrational mode requires less energy than stretching modes and so occur at lower frequencies for the same type of bond [21]. A Raman spectrum will contain peaks characteristic of any Raman active vibrational modes present in the sample being irradiated. In this manner it is often thought of as a chemical fingerprint.

An example of a Raman spectrum is shown in figure 2.2 of a polystyrene bead.

The y-axis gives the intensity of detected Raman scattered photons and the x-axis represents the Stokes Raman shift (the change in energy from the incident photons to the energy of the detected photons), displayed in wavenumbers with units cm^{-1} (equation 2.3), where $1\,\text{cm}^{-1}$ is equal to $30\,\text{GHz}$. Strictly the units should be written as Δ cm^{-1} but are often expressed as cm^{-1} for simplicity. The spectral resolution of the main Raman peak at $1001\,\text{cm}^{-1}$ is found to be $11\,\text{cm}^{-1}$, as determined by the full-width half-maximum (FWHM) of a Gaussian fit to the peak.

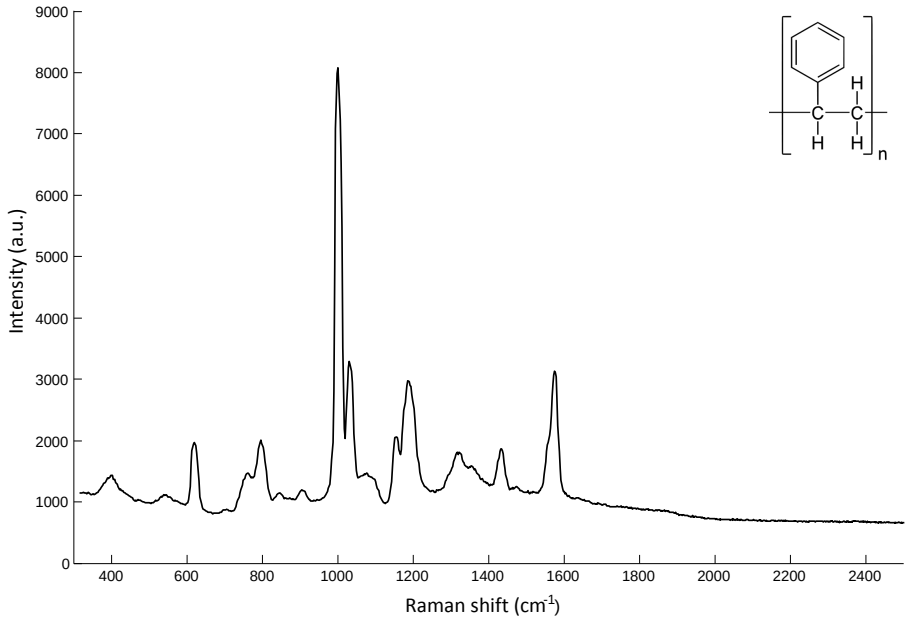

FIGURE 2.2: Raman spectrum for a $5\,\mu\text{m}$ polystyrene bead. A complex Raman spectrum is observed, with multiple bands corresponding to the various Raman active modes in polystyrene. (Inset illustrates the chemical structure of polystyrene.)

$$\text{Raman shift}\,(\text{cm}^{-1});\ \Delta\omega = \left(\frac{1}{\lambda_{\text{excitation}}} - \frac{1}{\lambda_{\text{Raman}}}\right) \text{x}\,10^{7} \tag{2.3}$$

Multiple Raman peaks can be observed such as those due to C-C vibrations (around $800\,\text{cm}^{-1}$), aromatic ring breathing mode ($1001\,\text{cm}^{-1}$), and C=C vibrations (around $1600\,\text{cm}^{-1}$). Interestingly, as the vibrational frequency of a molecule depends on the mass of the atoms involved and the strength of the bonds, the Raman signature corresponding to an aromatic group, such as a benzene ring, may vary depending on the attached aliphatic group. For example, the ring breathing mode observed at $1001\,\text{cm}^{-1}$ in polystyrene, would be observed at ($1004\,\text{cm}^{-1}$) in toluene

[25]. Similarly, the environment of the molecule can influence the observed Raman spectrum. An example of this is silicon dioxide, which exists in either a crystalline (quartz) or amorphous form (fused silica), where the disordered structure of fused silica leads to a broadening of the spectral lines when compared to those of quartz [26, 27]. Thus Raman spectroscopy can be a useful tool for structural analysis and polymorph characterisation of crystalline materials [28]. Often it is much more useful to consider the overall spectrum of a substance as a molecular fingerprint, as opposed to individual peaks, for comparison with known compounds.

The region between $400\,\mathrm{cm}^{-1}$ and $1500\,\mathrm{cm}^{-1}$ is typically known as the 'fingerprint' region and contains structural information related to the backbone of the molecule. Single bond groups such as carbon-carbon, carbon-hydrogen, phenyl and aromatic ring modes, as well as some oxygenated organics such as nitro- or sulpho- can be found in this region. The region between $1500\,\mathrm{cm}^{-1}$ and $1800\,\mathrm{cm}^{-1}$ typically contains double bonds such as C=O or C=C. Bands in the higher wavenumber region (<$2400\,\mathrm{cm}^{-1}$) often overlap and would require deconvolution algorithms for analysis. It is for this reason regions typically between $400\,\mathrm{cm}^{-1}$ and $1800\,\mathrm{cm}^{-1}$ are most commonly used for characterisation of a sample. Raman peaks in this region are spectrally narrow, just a few wavenumbers in width, making a Raman spectrum chemically very specific. This is in contrast to, for example, fluorescence spectroscopy which typically consists of very broad peaks.

The intensity of a Raman peak is directly proportional to the concentration of the scattering species and can therefore be used for quantitative analysis as well as qualitative. The intensity is also proportional to the power of the incident laser, irradiation times, and the Raman cross-section of the sample. The number of Raman photons scattered per second $\mathrm{N_R}(\mathrm{s}^{-1})$ is described by equation 2.4:

$$N_R = \sigma_R \Delta\Omega \frac{I_0}{h\nu} SNL \tag{2.4}$$

Where σ_R is the Raman cross section ($\mathrm{cm}^2\mathrm{molecule}^{-1}sr^{-1}$), $\Delta\Omega$ is the solid angle (sr^{-1}), I_0 and ν represent the incident laser irradiance and frequency respectively, S is the beam cross-section, N is the number density of the molecules in the sample volume, and L is the interaction length of the laser in the sample [29].

The Raman cross-section itself is inversely proportional to the wavelength of the incident light, λ, as described in equation 2.5.

$$\sigma_R \propto \frac{1}{\lambda^4} \tag{2.5}$$

Therefore the power of the scattered light,P_s can be described as

$$P_s \propto \frac{I_0}{\lambda^4} \tag{2.6}$$

The main drawback of Raman spectroscopy is that it is an inherently weak process, with only one in every 10^6 - 10^8 photons being Raman scattered. For samples which exhibit fluorescence, Raman scattering can often be challenging to detect, particularly in the Stokes Raman region. Techniques to overcome this obstacle and suppress fluorescence background will be discussed in section 2.5.

2.3 Raman spectroscopy for biomedical applications

Optical techniques are widely recognised for their ability to study biological systems evolving from the simple light microscope used by Charles Darwin, to the complex techniques for high resolution imaging, manipulation, and therapeutics used today.

Raman spectroscopy has proven to be a powerful optical technique in the study of biological systems as it can provide specific biochemical information in a label-free manner. Label-free techniques are becoming more and more important, owing to the fact they do not require the addition of exogenous agents which may interfere with biological processes. This can allow studies of live untouched cells in an environment which more closely reflects their natural surroundings.

Raman spectroscopy works on the principle of inelastic scattering of light. Incident light is modulated according to any vibrational modes present in the sample and the resulting spectrum is indicative of the molecular constituents of the sample; this can be thought of as a 'biochemical fingerprint'. The fact that Raman spectroscopy is a scattering technique allows a freedom of choice concerning the incident wavelength, independent of the absorption spectrum. For biological studies this means the wavelength can be chosen to be in the 'therapeutic region'

($\sim 750 - 1200\,\text{nm}$) thereby minimising absorption, and consequently photo-damage caused to cells or tissue during analysis. This optical window is located between the absorption of proteins in the visible and the increasing absorption of water towards the infrared [30, 31].

In addition to these properties Raman spectroscopy has several advantages which make it ideal for studying biological samples. For example, water is a weak Raman scatterer, minimising any interference to the Raman spectra due to the high water content normally found in biological samples. Furthermore, it permits the study of cells in their natural, aqueous environment. Raman spectroscopy is compatible with a standard microscope ideal for biological studies, as well as fiber optic probe based measurements which are particularly useful for *in-vivo* studies [6]. As a result Raman spectroscopy may be used in combination with other optical modalities such as optical trapping, optical coherence tomography (OCT), or quantitative phase imaging (QPI) techniques facilitating a wealth of possible applications. Multimodality will be explored further in chapter 4 where Raman spectroscopy is used in combination with DHM.

Perhaps the most important feature of Raman spectroscopy is that it offers high biochemical specificity and can provide information such as DNA, RNA, lipid, or protein content [7]. It is these features that characterise the cell or tissue under investigation; manifesting themselves as the absence or presence of certain peaks, or by small changes in peak intensity or peak shift. For example Raman spectroscopy has previously been used to classify cells as cancerous or normal based on changes to the nucleus-to-cytoplasm ratio, or the lipid and protein content [32, 33]. Indeed it is these molecular features that will distinguish the closely related immune cell types and neuronal cells analysed in this thesis (chapters 3-5). With all things considered one can understand the recent rise in the use of Raman spectroscopy for biological and biomedical studies [7, 17, 34–37].

2.4 Raman spectroscopy for the food and drinks industry

Raman spectroscopy has recently been gaining popularity as an analytical tool in the food and drinks industry. This may be due to advances in the technology but is also

likely due to the growing public interest in food quality, production, and safety.

Raman spectroscopy has certain advantages which make it well suited to studying food and drinks. It may be used to analyse substances in powder, solid, and liquid form, without any need for the addition of solvents or sample preparation. It is not sensitive to water content and is therefore ideal to analysing aqueous samples.

Traditionally techniques such as gas chromatography (GC), high-performance liquid chromatography (HPLC), and gas chromatography-mass spectroscopy (GC-MS) are used for food analysis. Although these methods are powerful for compositional determination they are time consuming, solvent wasting, and require sample preparations. Raman spectra however can take just several seconds to acquire, making Raman spectroscopy an ideal candidate for monitoring industry processes in real time. In addition to conventional Raman spectroscopy, techniques such as spatially offset Raman spectroscopy (SORS) [38] and enhancement techniques such as surface enhanced Raman spectroscopy (SERS) are being employed (see section 2.6). SORS is finding use in analysing samples through packaging [10], which is ideal for in-field testing, and SERS may be utilised to detect trace amounts of compounds [39].

Raman spectroscopy can be used to characterise nutritional parameters such as energetic value, and total carbohydrates, proteins and fat [40–42], to detect contamination on food surfaces [43–45], or for structural characterisation of crops [46, 47]. There have been a wealth of studies investigating free fatty acid (FFA) profiles in both plant and animal foods [48] including quantification of FFA content in vegetable oils [49] and olives [50], which may aid production of high quality olive oil [51]. With respect to beverages Raman spectroscopy has previously been employed to determine ethanol content in tequila [52] and whisky [53], as well as to quantify sucrose and aspartame content in soft drinks [54, 55]. Further applications can be found in reviews [9, 16, 56].

Raman spectroscopy can be employed in a wide range of applications and is becoming more commonly used for industry processes. In order to make Raman spectroscopy compatible with in-line processes compact Raman systems may be developed [57]. It is expected that Raman spectroscopy will play an important role in the in-line quality and safety control of food and beverage products in the future.

An additional concern for the food and drinks industry regards counterfeit and

adulterated samples, which not only affects the market but may also pose a food safety concern. Chapter 6 will deal with the use of Raman and fluorescence spectroscopy for the classification of whisky and extra-virgin olive oil samples; demonstrating a potential to aid the detection of counterfeiting or adulteration.

2.5 Wavelength modulated Raman spectroscopy

Raman signals are often hampered by broad fluorescence signals, which can overshadow weaker Raman signals. Biological studies suffer in particular as they often rely on detection from incredibly small areas, making any Raman scattered light intrinsically weak. Such studies would therefore greatly benefit from fluorescence suppression techniques to improve the signal to noise ratio (SNR).

Biomedical studies commonly use near-infrared (NIR) wavelengths for Raman spectroscopy which acts to naturally suppress the fluorescence emission. The lower energy excitation is often not sufficient to cause the excitation required for fluorescence. Even with filters in place to further reduce detection of fluorescence signals this is not sufficient to completely suppress fluorescence background, which continues to be a hindrance.

Background removal algorithms have been demonstrated, which make use of polynomial fits to subtract the background [58, 59]. This method is simple to integrate along-side Raman analysis, although any errors in the fit may introduce artefacts. The most ideal solution, to avoid such artefacts, would be to make use of the different physical principles between Raman and fluorescence spectroscopy.

Indeed a variety of such methods have been explored such as time-resolved Raman spectroscopy (TRRS), polarisation discrimination, and frequency modulation techniques [60].

TRRS makes use of the different lifetimes for Raman scattering and fluorescence emission [61–63]. Raman scattering is an instantaneous effect with typical time scales in the sub-picosecond to picosecond range [64], fluorescence however occurs in the 10 picosecond to 100 nanosecond range [65]. Time resolved methods therefore use pulsed laser excitation and limit the detection time to avoid collection of the fluorescence signal. This method can require the use of expensive components and is

limited where the lifetimes are similar or scattering is from thick samples [66].

Polarisation discrimination takes advantage of the different polarisation properties of Raman scattering and fluorescence emission. Raman scattering in symmetric vibrations is closely related to the excitation polarisation [67]. Using a polariser chopper and a lock-in amplifier the non-polarised fluorescence can be discriminated from the polarisation-dependent Raman signal [68, 69]. However it was reported that different degrees of polarisation altered the relative peak intensities of different Raman bands. Additionally this method would not be effective if the fluorescence signal is not completely depolarised.

A further property which may be exploited is that Raman peaks are directly related to the excitation wavelength, however the fluorescence peak is insensitive to the excitation wavelength for small variations in wavelength, following Kasha's rule [70]. The use of multiple excitation wavelengths can produce a varying Raman spectrum, which may be distinguished from the unchanging fluorescence signal. This idea for fluorescence suppression was first conceived in the 1970's [71, 72] and has since been investigated in various manners such as shifted excitation Raman difference spectroscopy (SERDS) [73], subtracted shifted Raman spectroscopy [74], and wavelength modulated Raman spectroscopy (WMRS) [75–77].

In contrast to SERDS which uses two slightly shifted excitation wavelengths WMRS uses an excitation source which is continuously modulated. Figure 2.3 illustrates these two different mechanisms. For WMRS measurements the spectra are defined by the continuous function $S(\nu)$. Individual Raman spectra are measured N times, each with an acquisition time of Δt, providing a total acquisition time $T = N\Delta t$. Each individual spectrum, indexed by j is measured over a discrete wavenumber set ν_i whilst the Raman excitation laser is shifted over a wavenumber region $\Delta\nu_j$. Measured spectra will contain contributions from both Raman peaks $S_R(\nu_i + \Delta\nu_j)$ and the fluorescence part $S_F(\nu_i + \Delta\nu_j)$, for small wavenumber shifts ($< 1\,\mathrm{nm}$) this can be approximated as $S_F(\nu_i)$. Individual Raman spectra can therefore be represented as

$$S_j(\nu_i) = S_F(\nu_i) + S_R(\nu_i + \Delta\nu_j) \tag{2.7}$$

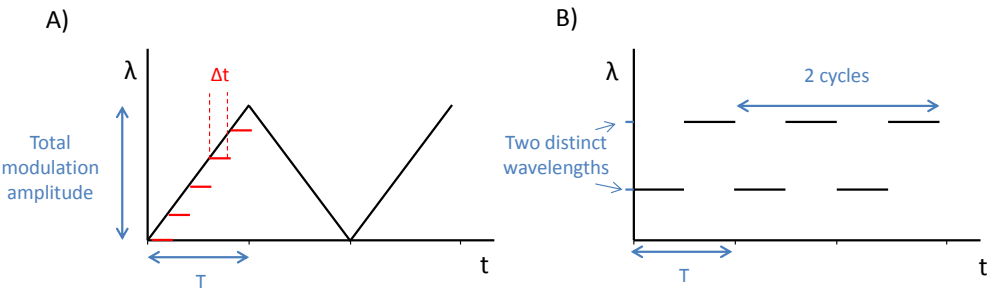

FIGURE 2.3: Illustration of A) continuous wavelength tuning used in WMRS and B) the use of two distinct wavelengths in SERDS. The various acquisition parameters for WMRS are depicted in A where the total modulation range is the amplitude over which the wavelength is tuned. The sampling rate N is the number of wavelength regions sampled during one cycle, in this case 5 individual Raman spectra are recorded, each with an acquisition time Δt, giving a total acquisition time T for one WMRS measurement.

For SERDS measurements two spectra are obtained $S_1(\nu_i)$ and $S_2(\nu_i)$. The difference spectrum is then calculated as $D(\nu_i) = S_1(\nu_i) - S_2(\nu_i)$. It has previously been demonstrated that the WMRS approach can provide a greater SNR [75, 76]. This can be understood from two key points: firstly, the noise level is additive when subtracting the two acquired spectra using the method of SERDS. Secondly, by increasing the modulation rate there is a resulting decrease in the $1/f$ noise in the method of WMRS. The disadvantage of continuously tuning the wavelength whilst acquiring Raman signal is that the resulting Raman bands will be broadened, resulting in a reduced spectral resolution.

Early methods of extracting the Raman signal required the use of a lock-in detector, synchronised with the excitation source. It has since been demonstrated that statistical methods may be used instead, eliminating the need for lock-in technology. A study conducted by Mazilu et al explored the use of several mathematical approaches to analyse modulated Raman spectra including standard deviation, Fourier filtering, or principal component analysis (PCA) algorithms [76]. It was reported that the optimal method, providing the greatest SNR and avoiding any distortion to the Raman signal, was PCA, which will be discussed in section 2.8.3. The first principal component extracts the maximum variation between the set of N spectra, which is directly associated with the differential Raman spectrum. Furthermore this method does not require any wavenumber calibration or synchronisation

making it applicable to real-time applications. The improved SNR enables reduced acquisition times; overall making WMRS easy to implement and a viable option for biological studies [32, 77]. However, to be effective WMRS does require that the Raman signal is greater than the background noise level, in contrast to TRRS. Practical limitations include the readout noise which can become comparable to Raman peak intensities when short acquisition times are used [75].

Figure 2.4 illustrates the principle of WMRS, where the Raman signal is continuously shifted, corresponding to the shift in excitation wavelength. Using PCA on the multiple shifted spectra produces a WMRS differential spectrum, where the zero crossing points correspond to Raman peaks. Any fluorescence information will be contained in higher order PCs which are discarded.

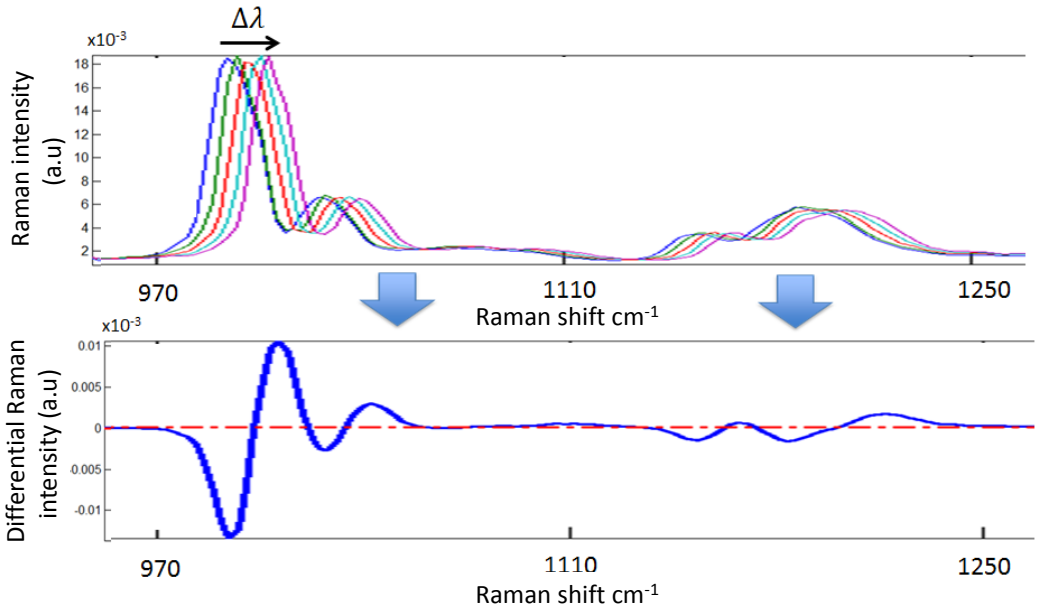

FIGURE 2.4: Illustration of the acquisition of a WMRS spectrum. Five standard Raman spectra (top) are recorded whilst continuously modulating the excitation wavelength, producing five spectra with shifted Raman peaks. PCA is used to analyse the spectra, producing a differential (WMRS) spectrum (bottom) where the zero crossing points correspond to Raman peaks.

Praveen et al have previously investigated how the various acquisition parameters for WMRS measurements may be optimised to achieve minimum acquisition times [78], which is important for improving throughput rates. It was reported that the wavelength modulation $\Delta\lambda$ must be greater than $0.32\,\mathrm{nm}$ to resolve Raman

bands of biological samples and that the SNR increases with both the single and total acquisition times. It was also noted that the sampling rate did not affect the SNR so long as three or more wavelength regions were sampled. Therefore to optimise the acquisition parameters would be to use the maximum $\Delta\lambda$, which is constrained by the mode-hop free region of the laser and the narrow transmission band of the Raman line-filter (typically $3\,\mathrm{nm}$). The sampling rate must be sufficient to minimise broadening of the Raman bands, where each individual acquisition time must be long enough that the SNR is not hampered by the readout noise.

2.6 Surface-enhanced Raman spectroscopy

Studies presented in chapter 7 include the use of surface-enhanced Raman spectroscopy (SERS); a brief overview of the underlying principles will therefore be provided here.

Raman scattering is typically considered a weak scattering process. For example, Raman cross-sections are typically on the order of $10^{-30}\,\mathrm{cm}^2$ [79], in comparison the absorption cross-section of fluorescent molecules are typically on the order of $10^{-16}\,\mathrm{cm}^2$ [80]. This is often a limiting factor for Raman spectroscopy with respect to detection of substances of low concentrations and impedes the potential for single molecule studies. This is particularly true in the presence of a strong fluorescence background. Thus a technique to provide a significant enhancement in Raman sensitivity would be of great value. Furthermore, enhancing Raman signal would permit shorter acquisition times and potentially enable greater throughput rates.

SERS is a technique that takes advantage of localised surface plasmon resonances (LSPR), in nano-scale systems based on metals such as gold and silver, to enhance Raman signals. Enhancements factors (EF), provided by SERS, range from $10^6 - 10^{16}$ [81–84], producing comparable signals to fluorescence spectroscopy and enabling single molecule studies [79, 85–87]. Although the SERS effect was first observed in 1974 by Fleischmann et al [88], it wasn't until the discovery of single molecule SERS, and the growing excitement around plasmonics, that SERS really experienced a drive in its development.

As the SERS effect was first observed experimentally many theories were proposed in the early stages. The exact mechanism is still a matter of debate, however it is now generally accepted that there are two parts to the theory: charge-transfer (chemical) enhancement and electromagnetic enhancement. The two mechanisms may act in concert although it is generally believed that the electromagnetic enhancement plays a larger role [89]. A brief explanation of the two theories is provided here.

2.6.1 Charge transfer enhancement

Charge transfer or chemical enhancement involves the formation of a bond between the analyte and the metal surface. Electrons from the metal surface can transfer to the molecule and back to the metal during excitation, hence providing a larger Raman polarisability of the molecule, that is to say $\alpha_{\mathrm{SERS}} > \alpha_R$. Consequently, the induced Raman dipole moment μ can be enhanced (equation 2.2) [21, 90]. For example the thiol-group, typically used in SERS, forms a bond to metal surfaces such as gold and silver; Saikin et al calculated the Raman cross-section of thiophenol when it binds to silver clusters and reported an overall increase in the Raman cross-section when compared to isolated thiophenol [91]. This is known as changing the 'static' Raman polarisability of the molecule. An additional mechanism that has been proposed is that of "charge-transfer" transitions wherein the intermediate state of the scattering process does not have to be the virtual state as described earlier (figure 2.1), but can also be an unoccupied electronic state of the metal [90, 92]. Another enhancement contribution may arise via a Raman band corresponding to the charge transfer of electrons from the metal to the lowest unoccupied molecular orbital, which may act as a resonant intermediate for Raman scattering. That is to say that enhancement may be caused by tuning into the charge transfer band of a 'surface-molecule' complex, yielding resonant Raman scattering at a particular wavelength [93].

2.6.2 Electromagnetic enhancement

Raman scattering is proportional to the induced dipole moment which is the product of Raman polarisability and the magnitude of the incident electromagnetic field

(see equation 2.2). The electromagnetic enhancement arises as a consequence of exciting the LSPR of a metal nanoscale surface, providing an enhancement to the local electromagnetic field [94–96]. The LSPR effect is illustrated in figure 2.5.

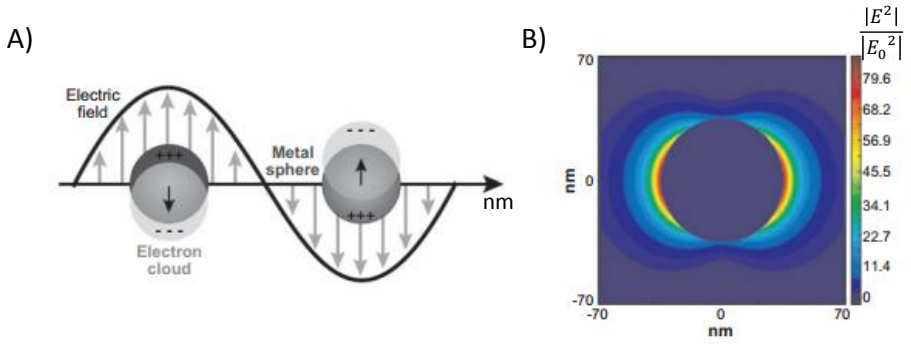

FIGURE 2.5: Taken from [96]. A) Illustration of the localised surface plasmon resonance effect. B) E^2 contours for a silver nanoparticle of 35 nm radius in vacuum. Local electric field maxima occur at two points along the axis going through the centre of the sphere, oriented in the direction of the external field, due to the superposition of the induced dipole and external field.

A simple description of electromagnetic SERS can be provided assuming a spherical nanoparticle of radius a irradiated by wavelength λ in the long wavelength limit ($a/\lambda < 0.1$), which leads to the assumption that the electric field around the nanoparticle is uniform [96]. The resulting electric field at the surface of a small metal sphere can be described by equation 2.8

$$E_r = E_0 \cos\theta + g\frac{a^3}{r^3} E_0 \cos\theta \tag{2.8}$$

where E_r is the total electric field at a distance r from the sphere surface, θ is the angle relative to the direction of the electric field and g is a constant related to the dielectric constants, as described in equation 2.9

$$g = \frac{\epsilon_1(\nu_L) - \epsilon_0}{\epsilon_1(\nu_L) + 2\epsilon_0} \tag{2.9}$$

where ϵ_0 and ϵ_1 are the dielectric constants of the environment surrounding the sphere and of the metal nanoparticle respectively, and ν_L represents the frequency of the incident laser [21].

The magnitude of the enhancement is wavelength dependent, owing to the wavelength dependence of the real part of ϵ_1. The maximum enhancement therefore occurs when the denominator of g approaches zero. At this frequency, the plasmon resonance frequency, the excitation of the surface plasmon greatly increases the local field experienced by a molecule in close proximity to the metal surface. It can be observed from equation 2.8 that the electromagnetic enhancement decays as $1/r^3$.

Equation 2.10 relates the metal polarisability, α to g demonstrating that the polarisability of the surface electrons is enhanced at the plasmon frequency [96]. The electrons in the analyte molecule can interact with this freely moving electron cloud essentially enhancing the polarisation around the molecule.

$$\alpha = ga^3 \tag{2.10}$$

A further consideration is that the scattered Raman intensity is linear with the incident field intensity $|E_0|^2$. Due to the plasmon resonance, the amplitude of the field close to the surface $|E_{Loc}|$ experiences an intensity enhancement factor $M_{Loc}(\nu_L)$ with respect to incident field, as described in equation 2.11

$$M_{Loc} = \frac{E_{Loc}^2}{E_0^2} \tag{2.11}$$

Similarly the Raman dipole emission at ν_R will be affected and modified by a radiation enhancement factor $M_{Rad}(\nu_R)$. Assuming the stokes shift is small the total electromagnetic SERS EF can be approximated as $|E|^4$ [97], according to equation 2.12

$$EF_{EM} = M_{Loc}(\nu_L)M_{Rad}(\nu_R) = \frac{|E_{Loc}|^2(\nu_L)\,|E_{Loc}|^2(\nu_R)}{|E_0|^4} \approx \frac{|E_{Loc}|^4}{|E_0|^4} \tag{2.12}$$

The enhancement factor is often measured experimentally, in which case it can be described by equation 2.13

$$EF = \frac{I_{SERS}/N_{\mathrm{Surf}}}{I_{NRS}/N_{\mathrm{vol}}} \tag{2.13}$$

Where I_{SERS} is the surface-enhanced Raman intensity, N_{Surf} is the number of

molecules bound to the enhancing metallic substrate, I_{NRS} is the normal Raman intensity, and N_{vol} is the number of molecules in the excitation volume [96].

Fluorescence also experiences a surface enhancement although the intensity scales as the square of the near-field enhancement [98]. This emphasizes that is the large field enhancement that is important (as opposed to a large field intensity) in order to separate Raman scattering from background fluorescence.

It is also important to consider how SERS spectra can differ from standard Raman spectra. There are three key points to consider: firstly as SERS is a localised effect only the signal from the part of the molecule close to the metal nanoparticle (or SERS substrate) will be enhanced. Secondly, if a molecule is adsorbed on the surface of the metal its symmetry may change, which may affect the Raman selection rules. Finally, the EF is wavelength dependent causing different Raman bands to be enhanced differently, thus distorting the relative peak intensities.

The nature of SERS enhancement is quite complex and varies according to the choice of metal, size, and shape of the nanoparticle [95, 99, 100], or roughness of the surface [101]. Additionally significant enhancements can be experienced at positions known as SERS hotspots [102], such as the gaps between metallic nanoparticle aggregates [81, 95, 100, 103] or tip enhancement [104, 105].

2.7 Raman instrumentation

There are a few key components when designing a free space Raman spectrometer. Two of the most important considerations are the excitation source and the detector. This section will give a detailed overview of factors influencing the choice of components. Finally, a description of the design and components used in the free space Raman spectrometer used for studies presented in this thesis will be given.

2.7.1 Choice of excitation source

When selecting an excitation wavelength for Raman measurements there are several considerations to made. It has been shown in equation 2.6 that scattering power is inversely proportional to the fourth power of the incident wavelength; it may seem natural then to choose the shortest possible wavelength and increase the Raman

scattering intensity. However higher energies are often accompanied by greater absorption and higher levels of fluorescence. As mentioned previously in section 2.3 there is an optical window between $750\,\mathrm{nm}$ and $1200\,\mathrm{nm}$ where absorption (due to proteins or water) is minimal. Studies presented in this thesis involve biological materials, olive oil, and whisky, which all have a high water content. Reduced photon absorption is key to minimising photo-damage and heating to the samples. A Raman excitation wavelength of $785\,\mathrm{nm}$ was therefore chosen. NIR wavelengths also have the advantage of providing a natural fluorescence suppression. Furthermore, working at a low absorption region means higher powers or longer acquisition times can be employed, which can compensate for the reduced scattering intensity.

An additional consideration which must be made is the wavelength-dependent sensitivity of the detector. Silicon-based detectors, for example, are most efficient at wavelengths between 800 and $1000\,\mathrm{nm}$. The efficiency is greatly diminished at longer wavelengths as the photon energy is less than the silicon band gap. Therefore, although working at longer wavelengths could further suppress the fluorescence, it would compromise detection sensitivity.

Overall the choice of excitation wavelength is a compromise between scattering power, fluorescence suppression, sample damage, and detector sensitivity. The optimum wavelength therefore varies depending on the specific application and the sample being analysed, and should always be considered on a case by case basis.

Raman bands are directly affected by the linewidth of the excitation source; the observed width of a Raman band is a convolution of the natural linewidth of the vibrational band with the laser linewidth [106]. Hence, in order to resolve closely spaced Raman peaks and achieve high Raman selectivity, a narrow excitation linewidth (tens of MHz) is desirable. This makes the laser an ideal source of excitation as the output is typically monochromatic (very narrow linewidth). For WMRS applications the ability to smoothly tune the wavelength is also required.

The Ti:Sapphire laser can meet these requirements. The Spectra-Physics Model 3900S is a continuous wave (CW), solid-state laser, which may be tuned over a broad range of NIR wavelengths (between 700 and $1000\,\mathrm{nm}$). It has a maximum output power of $1\,\mathrm{W}$ and a narrow linewidth ($0.5\,\mathrm{GHz}$). Tuning of the output wavelength is achieved with the use of a birefringent filter. A birefringent filter causes wavelength

dependent polarisation changes where only one wavelength will make a complete 180° change and return linearly polarised. All other wavelengths will have elliptical polarisation, causing them to suffer losses at any Brewster-angle surfaces within the cavity. This in turn prevents them from reaching lasing threshold. Rotation of the filter allows tuning for wavelength selection [107, 108]. The 3900S is used as the excitation source for the free space system used for studies presented in this thesis. The Ti:Sapphire laser is pumped by a Verdi V laser (Coherent), a diode-pumped solid-state (DPSS) laser, operating with a maximum output power of $5\,\mathrm{W}$ and an output wavelength of $532\,\mathrm{nm}$. This is an ideal pump laser as $532\,\mathrm{nm}$ corresponds to the maximum absorption of Ti:Sapphire.

It should also be noted that the choice of laser, and indeed excitation wavelength, depends on the type of Raman spectroscopy to be employed. Table 2.1 compares various different Raman spectroscopy techniques and their respective laser considerations. Non-linear Raman spectroscopy techniques such as anti-Stokes Raman spectroscopy (CARS) and stimulated Raman spectroscopy (SRS) can provide an enhanced signal, however the use of two ultrafast lasers makes these techniques more costly, limiting their use to research applications.

2.7.2 Choice of detector

The role of the spectrometer is to identify the various frequency components within the scattered light. There are two main types of spectrometers commonly used for Raman spectroscopy; the dispersive (Czerney-Turner) and the Fourier transform (FT) (Michelson interferometer) spectrometers. Each have their own advantages and disadvantages making each more suitable in certain applications.

Dispersive spectrometers use a grating to spatially separate photons of different wavelengths (see figure 2.6), while FT spectrometers measure the entire spectrum simultaneously in the form of an interferogram. The resolution of the spectrometer determines how well Raman bands can be resolved; for dispersive spectrometers this is a function of the slit width, the pixel size on the detector, and the groove spacing in the grating. Double or triple gratings may be used to enhance the resolution and improve rejection of Rayleigh scattering however greater losses will be

Raman technique	Overview	Commmon use	Laser requirements	Advantages and Disadvantages	Refs
nRS	Detection of spontaneous Raman scattering	Coupling with microscopes for mapping of molecular properties (via raster scanning) or acquisition of single-point spectra combined with multivariate analysis for sample characterisation	Narrow linewidth, high wavelength stability. Solid state lasers and external cavity diode lasers frequently used, can employ diode lasers for compact systems. Need sufficient power to detect weak Raman scattering.	Label-free, non-invasive, no sample preparation, compatible with miniaturised systems, weak signal may be overshadowed by background fluorescence	[6, 8, 9, 109]
RRS	Particular bands are enhanced by using an excitation wavelength close to that of an electronic transition of the target molecule	Characterising specific biomolecules such as caroteniods or cytochrome, and investigating chromophores	Analogous to nRS but with a frequency close to that of an electronic transition, ideally a tunable laser would be used.	$10^3 - 10^5$ fold increase in SNR, can be coupled with SERS (SERRS) for further enhancement, may induce greater fluorescence	[110–112]
SERS	Signal enhancement is achieved via resonant interaction with surface plasmons on a metallic surface (see section 2.6)	Detect specific antibodies through nanoparticle conjugation, or trace elements in food and drinks analysis	Analogous to nRS. Maximum enhancement when the laser frequency is slightly blue-shifted from plasmon resonance	up to 10^15 fold enhancement enabling single molecule studies, poor reproducibility of signal, nanoparticles may perturb a biological system.	[39, 87, 93, 101, 113–115]
CARS	Non-linear process requiring a pump (frequency ν_p) and stokes laser (frequency ν_s) to excite a molecular vibrational mode of interest ($\nu_v ib = \nu_p = \nu_s$) thus inducing coherent molecular vibrations in the sample. Two pump photons are absorbed generating photons corresponding to the anti-Stokes frequency.	Often used to image CH stretching vibrations in lipids and proteins with high spatial resolution.	Two or three different laser sources. Nonlinear process requires phase matching of beams and high power (two pulsed lasers). The stokes frequency should be tunable (achieved with solid state laser and OPO)	5x increase in SNR, fast molecular imaging, high spatial resolution due to multiphoton nature of light-matter interaction, blue shifted signal separable from fluorescence, reduced spectral information (only one Raman frequency probed), reduced spectral linewidth due to femtosecond excitation, increased complexity and cost	[116–119]
SRS	Similar to CARS but involving only one pump and one stokes photons. When the difference frequency matches the frequency of a molecular vibrational mode, stimulated excitation of vibrational transition occurs.	High speed images, determination of vibrational lifetimes	Analogous to CARS but using only two laser frequencies.	5x increase in SNR, label-free video-rate biomolecular imaging, high spatial resolution, reduced spectral information, increased complexity and cost.	[120–125]
SORS	Raman scattering is measured at a site offset from the point of excitation.	Deeper analysis in tissue, allowing detection of calcifications and cancer margins in breast tissue. Analysis through packaging with unknown spectrum for in-field analysis of liquids or concealed explosives	Analogous to nRS with at least two detection positions	Can analyse up to $10 - 20\,\mathrm{mm}$ depth but cannot provide information on spatial distribution	[38, 126, 127]
Fibre probe RS	The use of optical fibres for excitation and collection of Raman scattered light for use as a flexible probe.	In vivo analysis of tissue or hollow organs such as lungs, stomach and colon. May also be used with a needle for solid organs such as lymph nodes or breast tissue	Laser requirements analogous to nRS. Restriction on probe design; $< 2\,\mathrm{mm}$ diameter for biomedical applications, design of optical filters to reject probe background, low OH silica for NIR wavelengths.	Diagnostic guided surgery, may be combined with other medical imaging modalities such as MRI and with other Raman techniques such as SERS, RRS, CARS and SORS	[128–133]

TABLE 2.1: Summary of various Raman spectroscopy techniques. nRS- normal Raman spectroscopy, a-S- anti-Stokes, RS- Raman spectroscopy, RRS- Resonance Raman spectroscopy, SERS- surface enhanced Raman spectroscopy, CARS- coherent anti-Stokes Raman spectroscopy, SRS- stimulated Raman spectroscopy, SORS- spatially offset Raman spectroscopy, OPO- optical parametric oscillator).

incurred, which can make detection of the already weak Raman signal more difficult. For FT spectrometers the resolution is determined by the scanning distance of the moving mirror, typically a high resolution can be obtained over a wide spectral window. However FT spectrometers are most efficient at $1064\,\mathrm{nm}$ and require computer processing to analyse the spectra. Single grating dispersive spectrometers are often chosen for their simplicity and smaller size [106].

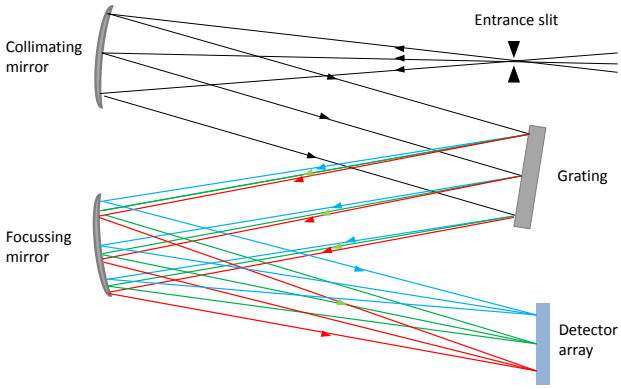

FIGURE 2.6: Schematic of the single grating dispersive (Czerney Turner) spectrograph. The incoming light is collimated by a mirror onto the grating where the various frequency components are spatially separated. The focussing mirror focuses the dispersed beam on to a detector, typically a CCD sensor.

For the free space system used for studies presented in this thesis a single grating spectrograph is used (Shamrock SR-303i, Andor Technology). An important consideration is the groove spacing (lines/mm) of the grating which presents a compromise between resolution and spectral width; narrower groove spacings give an enhanced resolution, R (see equation 2.14) but reduce the spectral window [134].

$$R = \frac{Nd(\sin\alpha + \sin\beta)}{\lambda} \tag{2.14}$$

Where N is the total number of grooves illuminated on the surface of the grating, d is the groove spacing, α and β are the incident and diffraction angle of irradiation respectively. To analyse Raman spectra in the range 600-1800 cm^{-1} with optimum resolution a 400 lines/mm grating was used.

Moreover the grating is blazed at $850\,\mathrm{nm}$; a blazed grating is specifically designed to maximise optical power to a specific diffraction order. By minimising the power

lost to the zeroth order the SNR can be improved. This is ideal for the inherently low light measurements in Raman spectroscopy.

This spectrometer was used with a deep depletion, thermoelectrically cooled, and back-illuminated charge-coupled device (CCD) camera (Newton 920, Andor). A CCD is a silicon based photosensitive array, where each pixel (or bin) may both generate and store a charge. The charge generated is directly linked to the number of photons hitting that particular pixel. The charge can continuously accumulate throughout the entire acquisition time, which is ideal for Raman measurements which often require long acquisition times due to the weak scattering intensity. An analog to digital converter (ADC) is then used to convert the charge to a digital read out.

It is important to consider the noise level associated with any detector. As thermal energy is sufficient to excite electrons and generate dark current in a CCD, it is beneficial to work at low temperatures. It is generally regarded that for every 6-7° cooling there is an associated 2 times reduction in dark current generated. In the studies presented here the CCD is cooled to -70° during operation. The read out noise is typically very low for CCD cameras, making the next most important consideration maximising the quantum efficiency (ability to convert photons to an electric signal). Back-illumination can improve the efficiency of a detector from about 40% (for front-illumination) to 80%. This is a consequence of the sensor surface necessarily being covered in electronics, such as transistors and wiring, limiting the number of photons which can reach the pixels. Microlenses can be used to minimise this problem however back-illuminated sensors are commonly employed as they inherently increase the photoactive area available. Back illuminated sensors however require an additional coating, some (such as the Newton CCD camera) are specially doped to enhance sensitivity towards the red end of the spectrum, this is known as deep depletion [106, 135].

2.7.3 Design of a free space Raman spectrometer

This section will discuss the other components required to build a free space Raman spectrometer, using the free space system used for studies in this thesis as an example.

Confocal microscopy

Raman spectrometers are easily integrated around a microscope stage. This has significant advantages, particularly for biological studies, as it provides the possibility to look at extremely small samples. The free space Raman spectrometer described here was designed around a confocal microscope. Confocal microscopy is commonly employed for biomedical studies. It works on the principal that an aperture at the conjugate plane to the sample provides the ability to reject any out-of-focus light (see figure 2.7 A). This can provide a more efficient collection of Raman scattered light from the point of interest in a sample and aid background rejection, for example fluorescence or out-of-plane contributions such as from microscope slides or the surrounding medium.

The confocal volume, or the in-focus volume, within a sample is typically described by a cylinder of radius, r_0 and depth, d, as described in equations 2.15 and 2.16. r_0 is given by the ratio of the physical radius of the confocal aperture, r and the magnification of the system, M. The confocal depth however is related to the numerical aperture, NA of the objective and the refractive index, n of the medium between the sample and objective [29].

$$r_0 = \frac{r}{M} \tag{2.15}$$

$$d = r_0 \, cot \, (sin^{-1}(\frac{NA}{n})) \tag{2.16}$$

Let us consider the free space system used throughout this thesis; a 50X magnification, oil immersion objective with NA of 0.9 (Nikon) is used to focus the laser light on to the sample. Raman scattered light is collected in reflection, through the same objective. The magnification of the system is calculated from the magnification of the objective, the focal length of the objective ($200\,\mathrm{mm}$), and the focusing lens to the confocal aperture ($160\,\mathrm{mm}$). A multimode fiber with $105\,\mu\mathrm{m}$ core (FG105LCA, Thorlabs) is used to collect the light, which acts as a confocal aperture. It follows then that the radius of the confocal cylinder is $1.31\,\mu\mathrm{m}$ with a depth of $1.37\,\mu\mathrm{m}$.

Without confocal microscopy the sampling volume is equal to the volume of

sample irradiated with high power density as illustrated in figure 2.7 B. The diameter and length can be approximated by equation 2.17 and 2.18.

$$D = \frac{4\lambda f}{\pi d} \tag{2.17}$$

$$L = \frac{16\lambda f^2}{\pi d^2} \tag{2.18}$$

Where D is the diameter of the cylinder, L is the length of the cylinder, λ is the laser wavelength, d is the diameter of the unfocussed laser beam, and f is the focal length of the focussing lens [21]. Therefore in the absence of confocal microscopy the sampling volume would be approximated to have a D of $33\,\mu\mathrm{m}$ and L of $4.4\,\mathrm{mm}$, which highlights the importance of confocal microscopy for rejecting background signal, particularly when working with small samples, such as single cells.

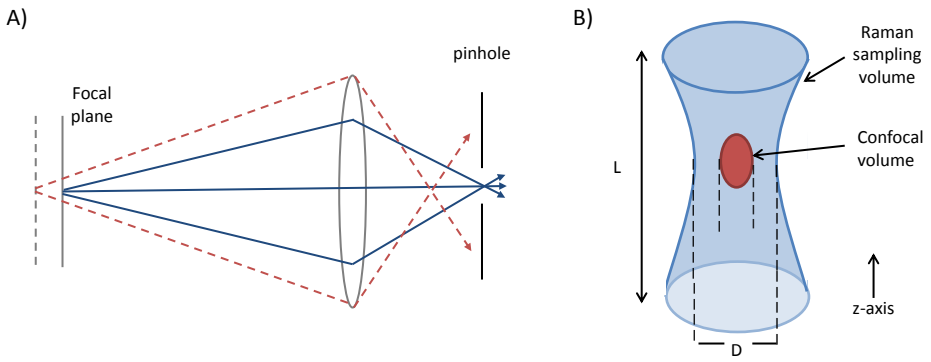

FIGURE 2.7: A) Schematic diagram illustrating the principle of confocal microscopy. By placing a confocal aperture at the conjugate plane of the sample out of focus rays (red) are rejected and light from the focal plane (blue) is allowed to pass. B) Illustration of the sampling volume (blue) which is modified in a confocal system (red volume). Collecting scattered photons from a smaller region can minimise the background signal.

Laser stability

A tunable Ti:Sapphire laser operating around $785\,\mathrm{nm}$ is employed for Raman excitation, utilising a Verdi pump laser at $532\,\mathrm{nm}$ (as described in section 2.7.1). As Raman measurements are based on detecting a change in wavelength laser stability is key, to achieve this the room temperature is controlled and maintained at a constant. The laser is operated at maximum output power for optimum performance, where any

power adjustments are made with the use of a half wave-plate and polarising beam splitter (PBS).

Power in the sample plane

A telescopic pair of lenses are used to expand the beam to overfill the back aperture (BA) of the objective. This is an important step as the NA stated for an objective assumes a planar wave entering the BA, however laser beams have a Gaussian profile making overfilling necessary in order to use the full NA. The output beam diameter from the laser is approximately $1\,\mathrm{mm}$ and the BA of the objective is $6\,\mathrm{mm}$. The telescopic lens arrangement uses two lenses of focal lengths $30\,\mathrm{mm}$ and $250\,\mathrm{mm}$, which gives an expansion of 8.3 times the original size, which is sufficient to overfill the BA.

Power is lost through the microscope objective (MO) due to its transmission efficiency as well as due to overfilling the BA. The loss due to overfilling can be calculated as the ratio of the total beam area, A_T and the area of the BA, A_{BA} as shown in equation 2.19. The transmission of the MO, T_{MO} is approximately 58%. Measuring the power in the sample plane directly can be challenging; therefore the power is measured before the MO and estimated in the sample plane using equation 2.20. For example, when $500\,\mathrm{mW}$ is measured after the PBS, the power in the sample plane can be estimated as $150\,\mathrm{mW}$.

$$\text{Loss due to overfilling BA} = \frac{A_{\mathrm{BA}}}{A_T} \propto \frac{r_{\mathrm{BA}}^2}{r_T^2} \tag{2.19}$$

$$P_{\mathrm{SP}} = P_{\mathrm{PBS}} \times T_{\mathrm{MO}} \times \frac{r_{\mathrm{BA}}^2}{r_T^2} = P_{\mathrm{PBS}} \times 0.58 \times 0.52 \tag{2.20}$$

Where P_{SP} and P_{PBS} are the power estimated in the sample plane and measured after the PBS respectively, and $r_{BA/T}$ are the radii of the BA and the incident beam before transmission through the MO.

Filters

Raman spectroscopy requires a pure excitation signal however the laser output can include spontaneous broadband fluorescence in addition to the laser line, not to

mention other optical components in the beam path which may provide fluorescence contributions. A line filter (LF) (LL01-785-12.5, Semrock) is employed to 'clean-up' the laser line after the beam expander. The LF has a FWHM of approximately $3\,\mathrm{nm}$, which is sufficient to transmit the full range of incident wavelengths during WMRS measurements ($\Delta\lambda = 1\,\mathrm{nm}$). The LF thus ensures a narrow excitation wavelength is incident on the BA of the MO and focussed on the sample. A 3-D translational stage is used for controlled movement of the sample. Light scattered by 180° is collected through the same objective (i.e. photons are collected in reflection mode).

A razor edge filter (REF) (LPD02-785RU-25, Semrock) is placed at 45° which effectively reflects the laser line, rejecting the more intense Rayleigh scattering (reflection is around 94% at $785\,\mathrm{nm}$), and transmitting the longer Raman-shifted wavelengths (transmission is > 93% in the range 795.2 to $1213\,\mathrm{nm}$). The use of filters, as opposed to two or three monochromators, allows more efficient collection of light, although it can impede recording of Raman scattering very close to the Raman line. The REF boasts a very steep transition from reflection to transmission, which permits detection of Raman scattered light at a minimum of $164\,\mathrm{cm}^{-1}$. This is sufficient for detecting low frequency vibrations and effectively measuring light in the fingerprint region. The use of filters does mean there is less freedom to change the excitation wavelength although this is not of particular concern for the studies presented in this thesis.

A focusing lens ($f = 160\,\mathrm{mm}$) is used to couple the light into a multimode low-OH optical fiber with $105\,\mu\mathrm{m}$ core (FG105LCA,Thorlabs), which guides the Raman scattered light to the spectrometer (Shamrock SR-303i, as described in section 2.7.2). A slit width of $150\,\mu\mathrm{m}$ is used which effectively collects all the light from the fiber. An additional notch filter (NF) (NF03-785E-25, Semrock) is used before the spectrometer to block out Rayleigh scattered light, which may saturate or damage the CCD due to its high intensity.

Köhler illumination is used to provide white-light sample illumination. A dichroic edge filter (Di02-R561, Semrock) is utilised in the collection path to direct this light to a CCD camera (DFK 42AUC03, Imaging Source) for imaging. The CCD is placed at the focal length of the $f = 160\,\mathrm{mm}$ lens to image the sample plane. The ability

to image is useful for checking the beam profile and to position samples at the focal point of the beam. In addition it provides the ability to monitor any damage or activation of cells in real time.

A schematic of the free space confocal Raman spectrometer is illustrated in figure 2.8. There are other systems that would compact this, making Raman spectroscopy more amenable to in-field testing or point-of-care analysis. One such system, the IDRaman mini, is detailed in section 6.2 and will be used for studies presented in chapter 6.

Wavelength tuning

Wavelength tuning is required for WMRS measurements and is obtained by rotation of the birefringent filter. This is modulated by an external micrometer, which is controlled digitally with the use of an actuator for smooth tuning. Start and end positions for the micrometer can be set and the speed of rotation fixed (SMC100 controller, Newport Corporation).

A wavemeter (High Finesse ws-7) was used to calibrate the micrometer position to the output wavelength. Figure 2.9 shows a tuning graph of the output wavelength over a range of micrometer positions. For example, to provide a change in wavelength of $1\,\mathrm{nm}$ about a centre wavelength $785\,\mathrm{nm}$, the actuator was shifted between positions $13.91\,\mathrm{mm}$ and $13.85\,\mathrm{mm}$.

For WMRS measurements the micrometer is tuned continuously in one direction for the entire acquisition period, once complete the micrometer returns to the starting position. It is important that each WMRS measurement starts at the same wavelength and is tuned over the same range, so as to not contribute to differences detected in PCA. To control this and mitigate any human error between initiating the wavelength tuning and starting the spectrum acquisition this process is fully automated using a cursor moving software (AutoIt).

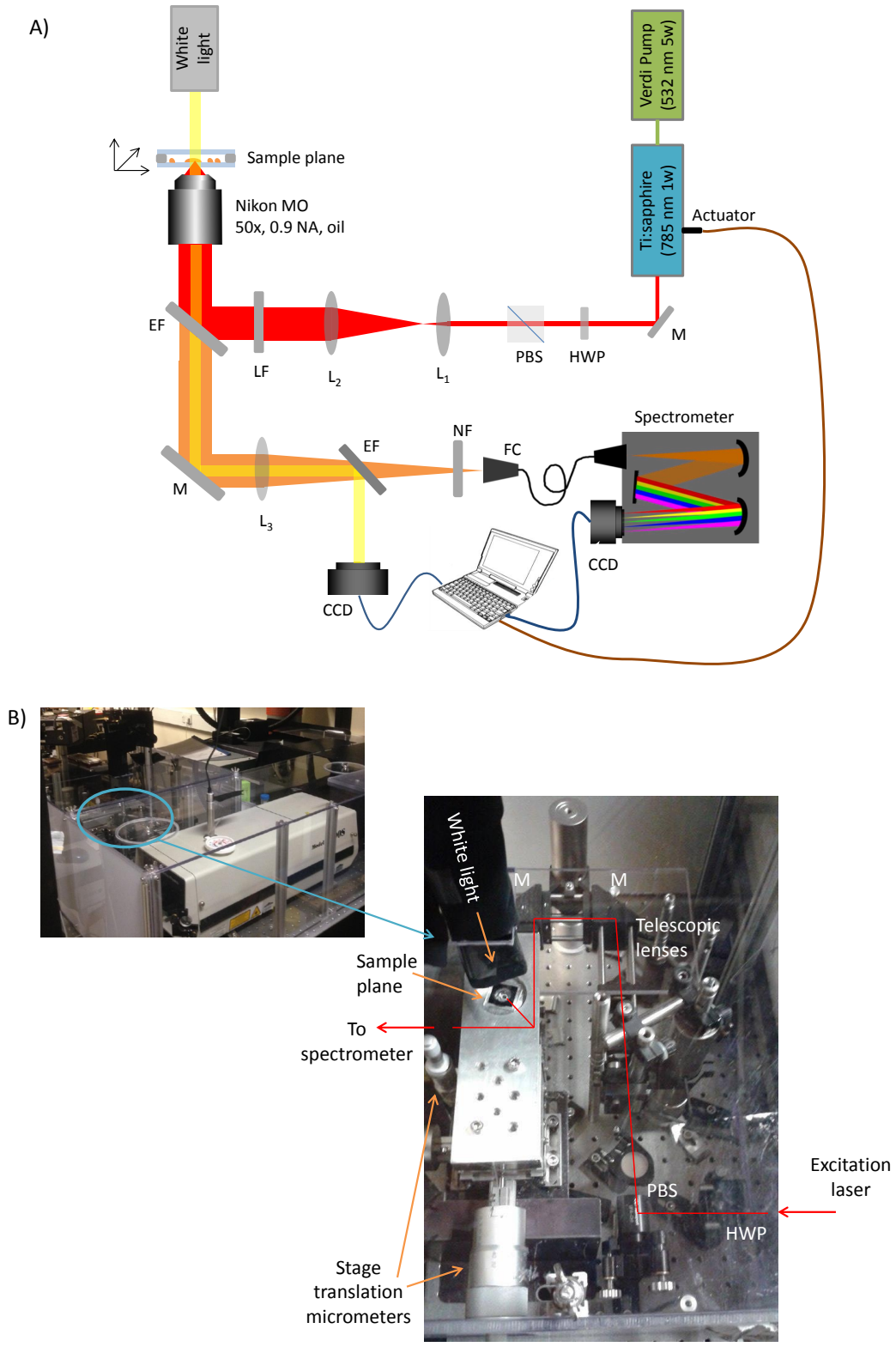

FIGURE 2.8: A) Schematic of free space confocal Raman spectrometer (not to scale). Abbreviations: M- mirror, L-lens (L_1: f=30 mm, L_2: f=250 mm, L_3: f=160 mm) LF - line filter, EF- edge filter, NF- notch filter, HWP - half wave-plate, PBS- polarising beam splitter, MO- objective, FC- fiber coupler. B) Photograph shows the free space system and 3900S laser, which occupy a whole optical bench. A birds eye view of the excitation path and sample plane is enlarged with the beam path illustrated in red.

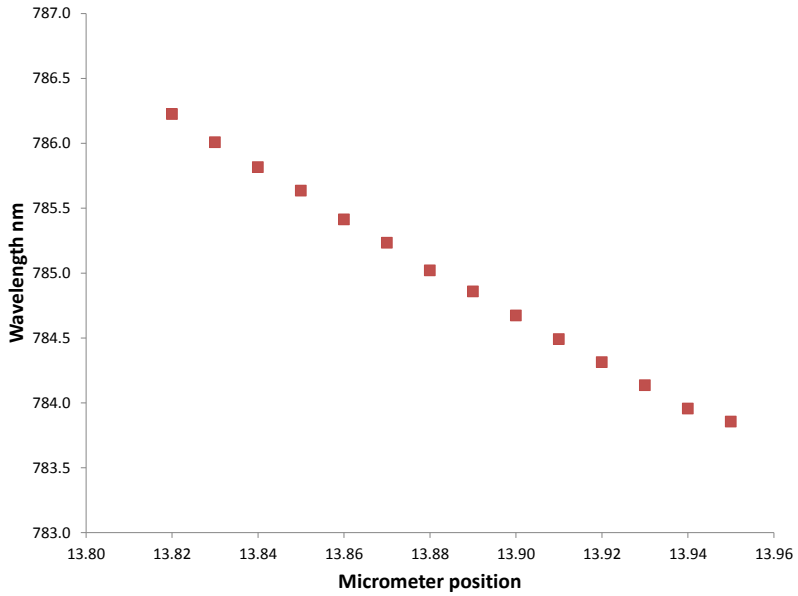

FIGURE 2.9: Rotation of the birefringent filter for wavelength tuning is achieved using an external micrometer. Micrometer positions are calibrated using a wavemeter allowing selection of tuning range for WMRS measurements.

2.8 Analysis of Raman spectra

2.8.1 Cosmic ray treatment

CCD detectors are used for acquiring the Raman spectra. They are common detectors in Raman spectroscopy due to their high sensitivity and low noise, however they are vulnerable to cosmic rays which produce random spikes in Raman spectra. Characteristically the spikes are very narrow in bandwidth and have a strong positive intensity. As they appear randomly and can distort Raman peaks it is important to apply a cosmic ray removal algorithm. This is particularly important when employing PCA as the spike due to a cosmic ray may be picked out as an important contribution to variation.

To treat spectra for cosmic rays the mean spectrum is found for a data set. Each spectrum is then compared to the mean, where any points differing from the mean by more than three standard deviations is considered a distortion due to cosmic rays. This point is then replaced by the mean value. This method is only applied where cosmic rays are not near a Raman peak or within the fingerprint region. In the case where cosmic rays overlap with a Raman band the spectrum is discarded. This method is applicable for studies presented here where large data sets are acquired

and the average spectrum is representative, however for other applications a more sophisticated analysis may be required [136].

2.8.2 Calibration and normalisation of spectra

The stability of the incident wavelength is crucial, as Raman measurements are based on detecting a change in wavelength. Although the environment is controlled there may still be some laser drift over the period of time needed to acquire a full data set. To account for this, and improve the robustness of our measurements to wavelength drift, calibration spectra are acquired frequently (approximately every 2 hours) from $5\,\mu\mathrm{m}$ polystyrene beads. Polymer beads have strong characteristic peaks and can be used to calibrate the wavenumber shift for subsequent spectra. Each spectrum is calibrated according to the polymer spectrum acquired nearest in time.

To compensate for any power fluctuations in the laser, the spectra are also normalised according to the total volume under the curve.

2.8.3 Principal component analysis

The dataset is then treated using a pattern recognition algorithm, principal component analysis (PCA). PCA is widely used in a variety of fields and is well established for its use in Raman spectroscopy [137]. It is a statistical tool to extract useful information from large data sets and can commonly be found in facial or vocal recognition technologies.

PCA is an orthogonal linear transformation of data to a new coordinate system in such a way as to reduce the dimensionality of the data set such that a small number of components (PCs) may effectively describe the variance across the data set. The first PC accounts for the greatest variance, the second PC accounts for the second greatest variance and so on. Suppose there are n samples, and for each m variables are measured. For the i^{th} sample measurements would be recorded in a vector $\vec{x}_i$ of length m. The mean of all m variables for n samples can be recorded as a single vector $\vec{\mu}$:

$$\vec{\mu} = \frac{1}{n}(\vec{x}_1 + ... + \vec{x}_n) \tag{2.21}$$

It is common to recentre the data such that the mean is zero, by subtracting $\vec{\mu}$ from each sample vector $\vec{x}_i$. Let there be three sample vectors each containing 4 measurements. A mean adjusted mxn matrix B can be recorded such that the i^{th} column is $\vec{x}_i - \vec{\mu}$, such that

$$B = \begin{bmatrix} a_1 - \mu_1 & b_1 - \mu_1 & c_1 - \mu_1 \\ a_2 - \mu_2 & b_2 - \mu_2 & c_2 - \mu_2 \\ a_3 - \mu_3 & b_3 - \mu_3 & c_3 - \mu_3 \\ a_4 - \mu_4 & b_4 - \mu_4 & c_4 - \mu_4 \end{bmatrix} \tag{2.22}$$

The covariance matrix S may then be calculated, which is essentially the variance calculated between each dimension [138]. The i, j entry of S would be

$$S_{i,j} = \frac{1}{n-1}((a_j - \mu_j)(a_i - \mu_i) + (b_j - \mu_j)(b_i - \mu_i) + (c_j - \mu_j)(c_i - \mu_i)) \tag{2.23}$$

For example the 2,1 entry of S would be calculated as

$$S_{2,1} = \frac{1}{3-1}((a_1 - \mu_1)(a_2 - \mu_2) + (b_1 - \mu_1)(b_2 - \mu_2) + (c_1 - \mu_1)(c_2 - \mu_2)) \tag{2.24}$$

From the covariance matrix the eigenvalues λ and respective eigenvectors $\vec{u}$ are found. The eigenvector with the largest eignevalue gives the first PC, the eigenvector with the second largest eigenvalue is the second PC, and so on [139]. The sum of all the eigenvalues is the total variance of all m variables. It is often the case that the largest few eigenvalues of S are much greater than all the others. For example, suppose m=15, the total variance is 100, and the largest eigenvalue $\lambda_1 = 90.1$, $\lambda_2 = 9.2$, and the remaining $\lambda_{3,...15}$ are all less than 0.1. The first and second PC therefore account for 99.3% of the total variation in the data. Although the data points form a 15 dimensional cloud, they cluster near a two-dimensional plane described by the eigenvectors $\vec{u}_1$ and $\vec{u}_2$. The problem can therefore effectively be reduced from fifteen dimensions to two [138].

PCA is used here for processing WMRS data, where the N individual Raman spectra, each corresponding to a different excitation wavelength, are considered a sample and each pixel (Raman shift value) is considered a measurement (see section

2.5). PCA is also used for feature selection when discriminating between sample types, in which case each data point (spectrum) is considered a sample. After finding the eigenvalues and eigenvectors a feature vector is formed by rearranging the eigenvectors in descending order of their respective eigenvalues. The eigenvectors represent the direction of the axes (or PCs) which characterise the data. The next step is to project the data points on the new PC axes. Data points that are statistically similar to each other will occupy a similar space in PC scatter plots. The first few PCs are selected, which contain the most useful information to describe the data set; these make up the new coordinate system. Higher order PCs can be discarded resulting in a reduced dimensionality of the dataset. The reduced dataset can be used for classification using algorithms such as leave-one-out cross-validation and nearest neighbour analysis.

2.8.4 Leave-one-out cross-validation

When discriminating between samples, the discrimination efficiency is calculated according to the methods of leave-one-out cross-validation (LOOCV) [140, 141] and the nearest neighbour algorithm [142]. The PCs are calculated from the training data set, with one data point left out; in this case a spectrum corresponding to one measurement. The left-out spectrum is then projected into the new space, which is defined by the PCs, and characterised according to the nearest neighbour method. This is repeated for all data points. Correct and incorrect cell classifications are then summarised in a confusion matrix, a table where each column represents the predicted class and each row represents the actual class.

Sensitivity and specificity are used as a quantitative measure of the discrimination ability. Sensitivity is defined as the ability to correctly identify positive samples (true positive rate) and specificity is the ability to correctly identify negative samples (true negative rate) as described in equation 2.25 and 2.26.

$$\text{Sensitivity} = \frac{\text{True positives}}{\text{True positives} + \text{False negatives}} \tag{2.25}$$

$$\text{Specificity} = \frac{\text{True negatives}}{\text{True negatives} + \text{False positives}} \tag{2.26}$$

2.8.5 Parametric student's t-test

In addition to this analysis Raman spectra may be compared in a pairwise manner with the use of a student's t-test. This is a statistical method to determine if there is a significant difference between two independent sample groups. The test statistic, t_s is calculated from the sample mean, $\bar{X}_i$, variance, s_i^2, and size n_i from the i^{th} sample population ($i = 1, 2$), as shown in equation 2.27. The probability (p-value) of the observed t_s value being under the null hypothesis is calculated by comparison with the t-distribution, whose degree of freedom, DoF is defined by equation 2.28. The p-value determines the likelihood of the null hypothesis being true, and thus determines the significance of the difference between the two sample populations, i.e. a small p-value indicates strong evidence against the null hypothesis and one may conclude that there a significant difference between sample populations does exist [143, 144].

$$t_s = \frac{(\bar{X}_1 - \bar{X}_2)}{\sqrt{\frac{s_1^2}{n_1} + \frac{s_2^2}{n_2}}} \tag{2.27}$$

$$DoF = \frac{(\frac{s_1^2}{n_1} + \frac{s_2^2}{n_2})^2}{(\frac{s_1^2}{n_1})^2/(n_1 - 1) + (\frac{s_2^2}{n_2})^2/(n_2 - 1)} \tag{2.28}$$

In this thesis the student's t-test is applied between the average spectra of two types of sample (for example two cell types), in a pairwise manner, to highlight any regions of significant difference. The significance level is set to show the most important Raman bands that characterise the differences between the respective samples. The student's t-test is not used for classification or discrimination purposes, rather just as an indicator of significant molecular differences between two samples.

2.9 Conclusions

This chapter laid the foundations for this thesis by providing an introduction to the classical theory of Raman spectroscopy. The origins of Stokes and anti-Stokes Raman scattering are discussed as well as the characteristics of a typical Raman spectrum.

The use of Raman spectroscopy in the field of biomedicine and the food and drinks industry is explored, including a discussion on how Raman spectroscopy can

be used in combination with other optical modalities for a more complete analysis. Furthermore a description of the physical origins which lead to the ability to discriminate between single cells is provided.

Fluorescence background can be a challenge for Raman studies, particularly for biomedical applications. A brief review of commonly employed fluorescence suppression techniques is provided, with particular focus given to the method of WMRS. A discussion is provided on the use of PCA to analyse modulated Raman spectra, the optimisation of WMRS acquisition parameters, and potential issues with the technique.

The next section provided an introduction to the principle of SERS, summarising the two main mechanisms for signal enhancement; charge transfer and electromagnetic enhancement. Differences which may be expected between a SERS spectrum and a standard Raman spectrum are discussed.

Further, this chapter explains the components required for a Raman spectrometer, including a discussion on the choice of excitation source, spectrometers, detectors (with their potential noise sources), and use of filters. Details are provided on the design of the free space system used for studies presented in this thesis, including a discussion on wavelength tuning for WMRS measurements. This chapter is intended to give a general overview, with specific details of instrumentation used in each study provided in the respective chapters.

Post-processing is an important step for analysis of Raman data. The basic steps used for qualitative and quantitative analysis are discussed in this chapter. The information provided is intended to give a general overview of the methods used, where specific parameters for each study will be detailed in the respective chapters.

3 Label-free identification of immune cell populations using wavelength modulated Raman spectroscopy

3.1 Introduction

Blood is an important bodily fluid, carrying out essential functions such as delivering oxygen and nutrients to cells and transporting waste away from those cells. The cellular component of blood can be thought of in terms of three main categories; red blood cells (erythrocytes), white blood cells (leukocytes), and platelets (thrombocytes). White blood cells (WBCs) are the cells of the immune system which interact to provide protection from infections; by responding to bacteria, viruses, fungi, and parasites that invade the body.

There are five major types of WBCs; neutrophils, eosinophils, basophils, monocytes, and lymphocytes; all derived from hematopoietic stem cells found in the bone marrow. These cell types may be classified further in to sub-populations, for example lymphocytes exist as T cells, B cells, or Natural Killer (NK) cells, and T cells are further classified into T helper cells (CD4+ T cells) or cytotoxic T cells (CD8+ T cells). The major cell populations and their development are illustrated in figures 3.1 and 3.2.

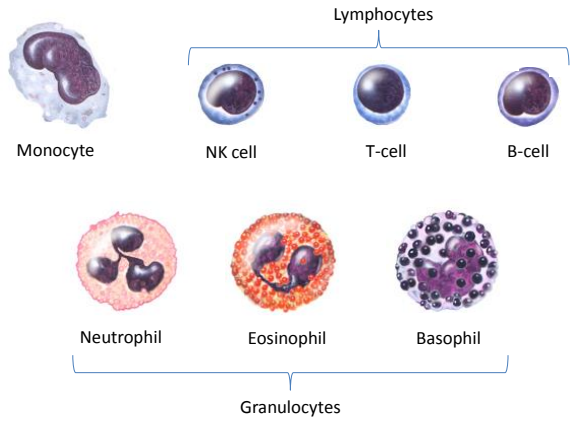

FIGURE 3.1: An artist's rendering of the major white blood cell subsets [145].

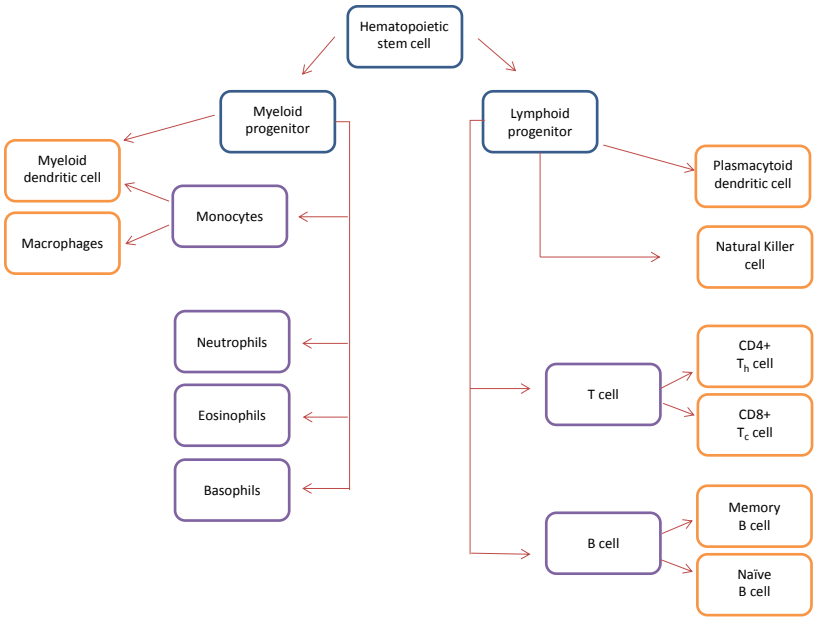

FIGURE 3.2: A hierarchical depiction of the major cell types found in the mammalian immune system.

Monitoring the numbers of WBC populations in the blood can indicate the presence of infection or inflammation, detect medical conditions such as autoimmune disease or bone marrow disorders, and monitor the body's response to drugs or radiation therapy.

3.1.1 Current methods of detection

Current methods for detecting cells of the immune system include cell fixation and chemical staining to reveal morphology. This method destroys the cells and is limited in sensitivity as closely related cells, such as B- and T-cells, are morphologically very similar. Alternatively, magnetic bead isolation or flow cytometry using fluorescently-labelled antibodies may be used. The use of exogenous tagging agents provides a more specific analysis, as they target specific cell surface markers, however they can damage or alter the behaviour of the cells. The development of a label-free method for the detection and isolation of untouched, live cells would therefore be beneficial in both research and clinical settings.

3.1.2 Why Raman spectroscopy?

The potential for Raman spectroscopy to provide a biochemical fingerprint has been previously discussed in section 2.3. Perhaps the most attractive property of Raman spectroscopy is its ability to provide specific molecular information in a label-free manner, moreover Raman spectroscopy does not require any sample preparation. Raman spectroscopy therefore offers a viable method to analyse live cells with minimal disturbance to the integrity and function of the cells.

Raman spectroscopy has previously been successful in the discrimination of cells and tissues [146, 147] and for the study of immune cells [**Smith:2010**, 148]. Ramoji et al have used Raman spectroscopy to discriminate between cells of the innate and adaptive immune system in the form of neutrophils and lymphocytes respectively [149]. Although this is a highly promising study and demonstrates the potential for Raman spectroscopy to discriminate between cells of the immune system, it should be noted that neutrophils and lymphocytes are derived from different progenitor lineages; myeloid and lymphoid respectively, and as such differ significantly in their morphology and chemical composition (see figures 3.1 and 3.2). It would be a greater challenge and of significant interest to investigate the discrimination ability between more closely related immune cell subsets. Ashok et al have demonstrated the use of WMRS to discriminate between CD4+ T cells, CD8+ T cells, and NK cells, as well as clear discrimination between dendritic cell subsets pDC and mDC from a single donor [150]. Key issues remain with regard to the validity of this study when samples are acquired from multiple donors and implementing accurate multivariate analysis in such a scenario. In working towards a label-free haemograph, it is essential that it be robust with respect to different donors to be truly applicable to clinical or research applications.

3.1.3 The role of immune cells in the body

Each cell type carries out specific functions and plays a distinct role in the immune system. A brief outline of the cells used within our study will be discussed. Firstly, the lymphocyte populations; T cells, B cells, and NK cells. After release from the

bone marrow, T cells do not enter the main circulation, but undergo further differentiation in the thymus, and can be distinguished from other cell types by the presence of T cell receptors on the cell surface. They are divided into two main groups based on their expression of CD4 and CD8 cell surface proteins [151]. CD4+ T cells (T helper or T_h cells) typically secrete small proteins, known as cytokines, which essentially act as a chemical instruction to the rest of the immune system, coordinating the immune response. These cells can further differentiate into one of several lineages; Th1, Th2, Th3, Th9, and TH17, each usually secrete specific cytokines in response to a variety of pathogens or stimuli [152]. CD8+ T cells (cytotoxic T cells or T_c cells) directly kill virally infected cells and tumour cells by induction of apoptotic pathways and the release of toxic granules [153].

B cells originate in the bone marrow, undergo full differentiation and are released into the blood. They function by, upon activation, producing antibodies (immunoglobulins) to bind and neutralise pathogens. They can be distinguished from other lymphocytes by their expression of B cell receptors on their cell membrane, which enables the B cell to bind a specific antigen, which will alert the body to their presence and initiate an immune response [154]. Activated B cells have a lifespan of several weeks when actively secreting large amounts of antibodies, but a subpopulation may become memory B cells which reside in lymph nodes for extended periods of time; these cells can initiate a stronger and faster response to the specific antigen which activated their parent cell [155]. The process of immunisation/vaccination is indeed focussed on generating such memory B cells that can rapidly expand and generate a protective immune response if the pathogen is encountered. When a B cell is activated (with the help of a T cell), it proliferates and differentiates into an antibody-secreting 'effector cell' [156].

The third lymphocyte sub-population, NK cells, are somewhat similar to CD8+ T cells in that they are anti-viral (cytotoxic) in nature [157], though often classed as large granular lymphocytes due to their slightly larger size in comparison to T cells. NK cells are uniquely able to recognise infected/stressed cells in the absence of antibodies and therefore provide a fast immune response. Importantly, this also enables them to detect harmful cells missing markers of the major histocompatibility complex (MHC), which would not be detected by other immune cells. Similarly,

cancer cells often down regulate MHC class I molecules, and NK cells provide a first line of defence that can eliminate potential cancer cells early in the neogenesis process. NK cells may be distinguished from other lymphocytes by the expression of CD56 (in human blood) and are generally larger than B- or T- cells.

Dendritic cells (DCs) develop in the bone marrow and can be separated by cell surface markers and function into either myeloid (mDC) or lymphoid/ plasmatcytoid (pDC) populations [158]. They are distributed around the body, especially at mucosal surfaces, or tissues in contact with the external environment, and once activated (upon detection of pathogens) will migrate to local lymph nodes. They are antigen-presenting and in this manner act as messengers between the innate and adaptive immune systems, initiating and controlling many immune responses [159–162]. DCs are quite rare in the normal blood stream and pose a particular challenge in research as they are also difficult to isolate. As a result little is understood about their development and function making them an area of interest for immunologists.

The last cell subset that will be dealt with in this chapter are monocytes. Monocytes develop in the bone marrow and circulate in the blood for only about a day before entering the tissue to mature into macrophages. Once they have entered the tissue, they remain as long-lived resident cells and keep the tissues clear of antigens and dead cell debris via phagocytosis. Monocyte production and release from the bone marrow is increased during an immune response. Monocytes have several roles, one example is migration in response to inflammation signals. Excess monocytes in the blood may therefore be indicative of conditions such as chronic inflammation or sarcoidosis [163].

This chapter will deal with investigating the ability of WMRS to discriminate between these immune cells sub-populations; section 3.3 will deal with discrimination between NK cells and T cell populations CD4+ and CD8+, notably using cells derived from multiple donors to verify the robustness of this method. Section 3.4 will deal with the discrimination between pDC and mDC populations, section 3.5 will investigate the discrimination ability between further cell populations B cells, monocytes, and CD4+ and CD8+ T lymphocytes, and finally section 3.6 will investigate the potential for Raman spectroscopy to identify B cells in either the activated or inactivated state.

3.2 Methods

3.2.1 Cell preparation for Raman spectroscopy

This study was approved by the School of Medicine Ethics Committee, University of St Andrews (Ethics statement is provided in appendix A). Samples were obtained from healthy donors after obtaining informed and written consent. Participation information sheets and consent forms were also approved by the School Ethics Committee.

CD4+ T cells, CD8+ T cells, NK cells, pDCs, mDCs, B cells and monocytes were isolated and purified. Negative depletion isolation kits were used to separate cells in an untouched manner. This method was chosen to avoid the use of labels which may alter the activation state of cells and change their behaviour. Full details of this method are provided in appendix B. This section also shows the results of analysis by flow cytometry and functional assay characterisation to analyse the purity of samples.

Cells were prepared on quartz slides for analysis by Raman spectroscopy. A thick quartz slide ($25.4\,\mathrm{mm}$ x $25.4\,\mathrm{mm}$, $1\,\mathrm{mm}$ thickness, SPi Supplies, UK) was used, forming a chamber by placing a vinyl spacer of $80\,\mu\mathrm{m}$ thickness on top. Live cells were suspended in phosphate buffered saline (PBS) and $20\,\mu\mathrm{l}$ was placed in the well. A second thin quartz slide ($25.4\,\mathrm{mm}$ x $25.4\,\mathrm{mm}$, 0.15 to $0.18\,\mathrm{mm}$ thick) was placed on top to form a seal. The chamber was inverted, allowing the cells to settle on the thin slide for 30 minutes, which would prevent any movement caused by optical forces during measurements. The sample was placed on the confocal microscope with the thinner slide towards the objective.

It is considered an important aspect of biological studies that there is a large sample size. Biological material have an inherent variability; a larger sample size can provide an averaging effect and produce a more accurate representation. The number of cells analysed here is therefore only constrained by practical considerations. For example, cells remain healthy in the quartz chamber (outside of an incubator) for approximately 2 hours, during which time approximately 60 cells can be analysed by WMRS. This in turn depends on the concentration of cells; dendritic cells are quite rare in the blood and can be more difficult to find, therefore fewer data are recorded

for these cells. Additionally there is a limited lifetime for cells extracted from fresh blood, meaning all data must be acquired within three days after isolation. It is a combination of these factors that limit the number of cells which may practically be analysed. Blood samples were taken from three healthy donors to make the study more clinically relevant and to ensure the method is robust against different donors.

3.2.2 Performing Raman spectroscopy

Details of the instrumentation used for the Raman spectrometer are provided in section 2.7.3. $150\,\mathrm{mW}$ power was provided to the sample plane. For WMRS measurements the wavelength was tuned over a total range of $\Delta\lambda = 1\,\mathrm{nm}$. Five spectra were acquired at five equidistant wavelengths within this range where each single spectrum was acquired for $5\,\mathrm{s}$; in total an acquisition time of $25\,\mathrm{s}$ was required for a WMRS point spectrum of a single cell. The method of processing WMRS data to obtain a single differential spectrum is detailed in section 2.5. All Raman spectra were normalised according to the area under the curve, to account for any fluctuations in power before processing the WMRS data.

Cells were irradiated continuously for 5 minutes and no change was observed in the Raman spectrum; this indicates there was no photodamage at this laser dosage on the time scales used. Raman spectra were also collected on different days to confirm the stability of the system.

Hoboro et al [164] have compared the use of either single point Raman spectra or Raman imaging for the analysis of immune cells; it was reported that whilst single point spectra do not acquire information from the whole cell, they are still largely representative of the cell as a whole. There are some spectrum to spectrum differences due to variations in position in the cell, which highlights the importance of basing these studies on a large number of cells. Furthermore, when acquiring a Raman image of a whole cell the acquisition time required increases dramatically (several minutes per cell), limiting throughput of cells analysed. Reducing the spectral quality can improve the throughput rate of Raman images but decreases the signal-to-noise ratio achieved and subsequently the discrimination efficiency. This comparison validates that the approach of acquiring single point Raman spectra is a robust and appropriate method.

3.2.3 Statistical analysis on Raman spectra

A detailed description of statistical analysis methods used is given in section 2.8. Specific details pertaining to this study will be outlined in this section. Raman spectra were analysed in the region of $600\,\mathrm{cm}^{-1} - 1800\,\mathrm{cm}^{-1}$. A parametric student's t-test was used to highlight regions of significant difference between the mean spectra of any two cell subsets. This indicates the Raman peaks which vary most, and hence any biochemical differences between two different cell populations. A significance level of $p< 10^{-7}$ was used. PCA was applied to the data set to reduce the dimensionality and the first 7 PCs were selected, which accounted for the major variance across the data set. Cluster plots were produced using the first 3 PCs to visualise trends in the data. The discrimination efficiency of this training data set was assessed by means of LOOCV. The left-out spectrum was defined according to the nearest neighbour algorithm. This was repeated for each spectrum and correct and incorrect cell classifications were summarised in a confusion matrix. Sensitivities and specificities were then calculated in a pairwise manner for each two cell subsets.

3.2.4 Daily procedure

Before acquiring Raman spectra the performance of the Raman system was assessed and optimised. As a first step the output power of the laser was measured. If the power had fallen from the expected power output, small adjustments to the output mirror and cavity high reflector was normally sufficient to regain the optimum power output. Secondly, the beam shape was assessed by viewing the reflection pattern from a glass surface in the sample plane. Tuning above and below the focal point should reveal a series of circular confocal rings expanding around a constant centre. If the optical axis were misaligned or the beam shape had lost its circular symmetry, realignment was achieved by 'beam walking'. As a next step Raman spectra were acquired from $5\,\mu\mathrm{m}$ polymer beads; the acquired spectrum will be most intense when the bead occupies the confocal volume (figure 2.7), at this point the bead should appear in focus on the CCD camera. By comparison to a reference spectrum one can ensure optimal performance; any significant drop in the maximum signal

intensity may be due to the collection efficiency, which can be optimised by adjusting the position of the confocal pinhole. The region of the spectrometer CCD camera on which Raman scattered light is detected can be observed. The acquisition region was cropped to the appropriate pixels to minimise any dark noise contributions. Once the system was optimised, cells were prepared on quartz slides as previously described, and data collection could begin. To account for any drift in laser wavelength throughout the day calibration spectra were acquired from polymer beads every 2 hours, that is before and after each batch of cells (see section 2.8.2).

3.2.5 Potential problems

There are a range of potential issues that may arise and this section aims to address how they are managed. The laser cavity is sensitive to any temperature fluctuations in the lab which may cause thermal expansion and consequently misalignment of mirrors. Typically this can affect the output power, beam quality, and laser noise, and in extreme cases loss of lasing. The laboratory temperature is controlled to minimise these effects and regular laser maintenance can avoid the total loss of lasing. The system also experiences a drift in wavelength over time and although spectra are calibrated (section 2.8.2), caution must be taken to ensure the data are robust. Data were therefore acquired from each cell type on different days and PCA was employed to validate that no significant variations were introduced due to the Raman system. Considering WMRS measurements, each wavelength shift produces a spectrum with a different output intensity. This is due to the wavelength dependent parameters of the laser cavity and filters used in the Raman system. Each spectrum is normalised according to the area under the curve before further processing however if the variation is large it can affect the cosmic ray treatment and analysis by PCA (see section 2.8). It is vital that the centre wavelength corresponds to the centre of the transmission linewidth of the line filter, otherwise the first or last spectrum may have a significant drop in intensity.

3.3 Classification of T-cell populations CD4+ and CD8+, and natural killer cells

3.3.1 Identification of T-cell subsets and NK cells using WMRS

Flow cytometry and functional characterisation revealed that CD4+ T lymphocytes were obtained at a purity level typically up to 96%, CD8+ T lymphocytes were obtained at a purity level typically up to 76%, CD56+ NK cells were obtained at a purity level typically up to 88.7% (details of this can be found in appendix B).

WMRS spectra were recorded for 60-80 cells derived from each of three different healthy donors. In total, spectra were collected for 180-240 cells from each of the three lymphocyte cell subsets CD4+ T cells, CD8+ T cells and NK cells. Figure 3.3 A illustrates the average standard Raman spectrum for each cell subset and Figure 3.3 B-D illustrate a pairwise comparison of the average WMRS spectra acquired. Raman bands showing significant difference across two cell subsets are highlighted by grey vertical bars, as calculated by the student's t-test at a significance level of $p< 10^{-7}$.

Based on the zero-crossing points of the WMRS spectra and on published observations [164–167] it is possible to suggest some key areas of difference between the cell types. Major differences between Raman spectra of CD4+ and CD8+ T lymphocytes are found mainly from C-C twist in tyrosine (around $645\,\mathrm{cm}^{-1}$), the O-P-O symmetric stretching (around $800\,\mathrm{cm}^{-1}$ and $1097\,\mathrm{cm}^{-1}$), symmetric ring breathing mode of phenylalanine (around $1007\,\mathrm{cm}^{-1}$), amide III (around $1259\,\mathrm{cm}^{-1}$), polynucleotide chain (around $1345\,\mathrm{cm}^{-1}$), thymine/adenine/guanine (around $1378\,\mathrm{cm}^{-1}$), CH2 deformation in lipids (around $1445\,\mathrm{cm}^{-1}$), adenine/guanine (around $1585\,\mathrm{cm}^{-1}$), and amide I (around $1665\,\mathrm{cm}^{-1}$). Even more differences were found in the Raman spectra of T cells and NK cells, such as C-C twist in phenylalanine (around $621\,\mathrm{cm}^{-1}$), C-S stretching in cysteine (around $671\,\mathrm{cm}^{-1}$), adenine ring breathing (around $725\,\mathrm{cm}^{-1}$), skeletal C-C stretch in lipids (around $1129\,\mathrm{cm}^{-1}$), phenylalanine/tyrosine/C-N stretching (around $1209\,\mathrm{cm}^{-1}$), and adenine/amide III (around $1304\,\mathrm{cm}^{-1}$). We can expect more regions of difference between T lymphocytes and NK cells, compared to the two T lymphocyte subsets CD4+ and CD8+; as the T lymphocyte subsets share a common lineage they are expected to be most

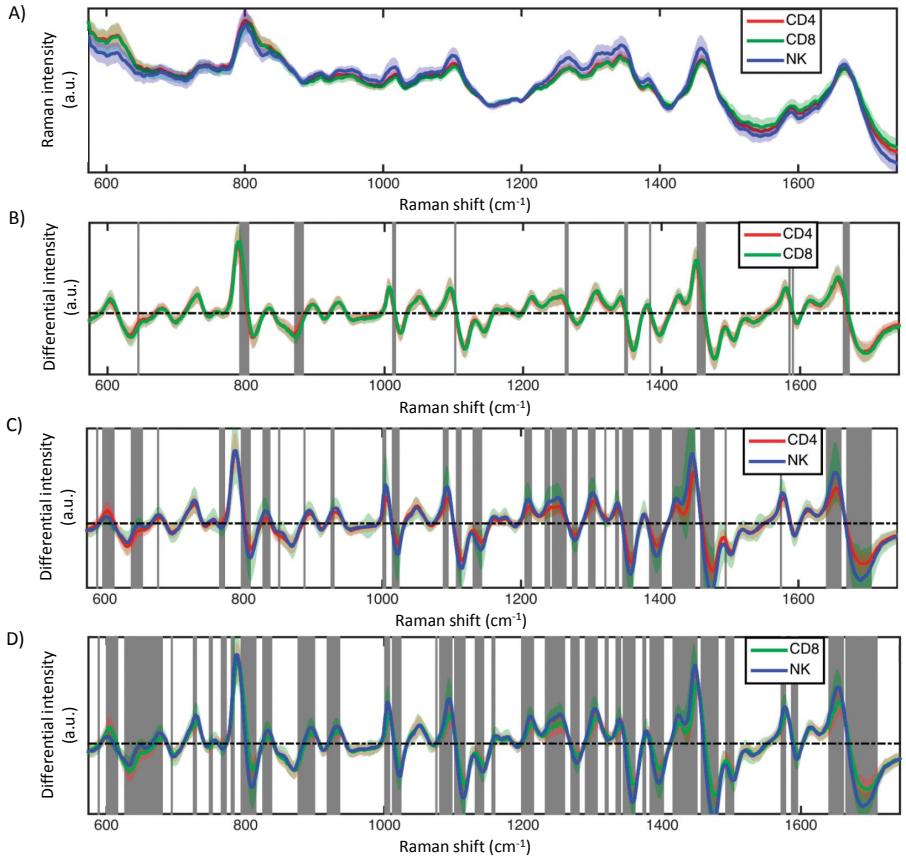

FIGURE 3.3: WMRS spectra of purified immune cell subsets CD4+ T cells, CD8+ T cells and NK cells. A) Mean standard Raman spectra of CD4+, CD8+ and NK cells. Pairwise comparison of the mean WMRS spectra of B) CD4+ and CD8+ T cells, C) CD4+ T cells and NK cells, and D) CD8+ T cells and NK cells. Solid lines show the average spectrum of each cell population and shaded regions show the standard deviation. Grey vertical bars indicate regions of significant difference between two cell subsets, as estimated by student's t-test at a significance level of $p < 10^{-7}$.

closely related and biochemically most similar. These Raman bands are summarised in Appendix C.

PCA was applied to the training data set of all three cell subsets, to achieve feature reduction. The first three PCs were used to produce cluster plots as shown in figure 3.4. Each spectrum, correlating to a single cell, was projected onto the PC space as a single data point, and distinct clusters were formed for each of the cell subsets. This indicates WMRS is successful at determining a distinct biochemical fingerprint for each of the CD4+, CD8+, and NK populations. It can be observed in figure 3.4 B that there is slightly more overlap between the CD4+ and CD8+ T cell populations compared to T cell and NK populations, again this can be expected as

they are more closely related and would be most biochemically similar. This is in agreement with fewer Raman bands being highlighted by the student's t-test.

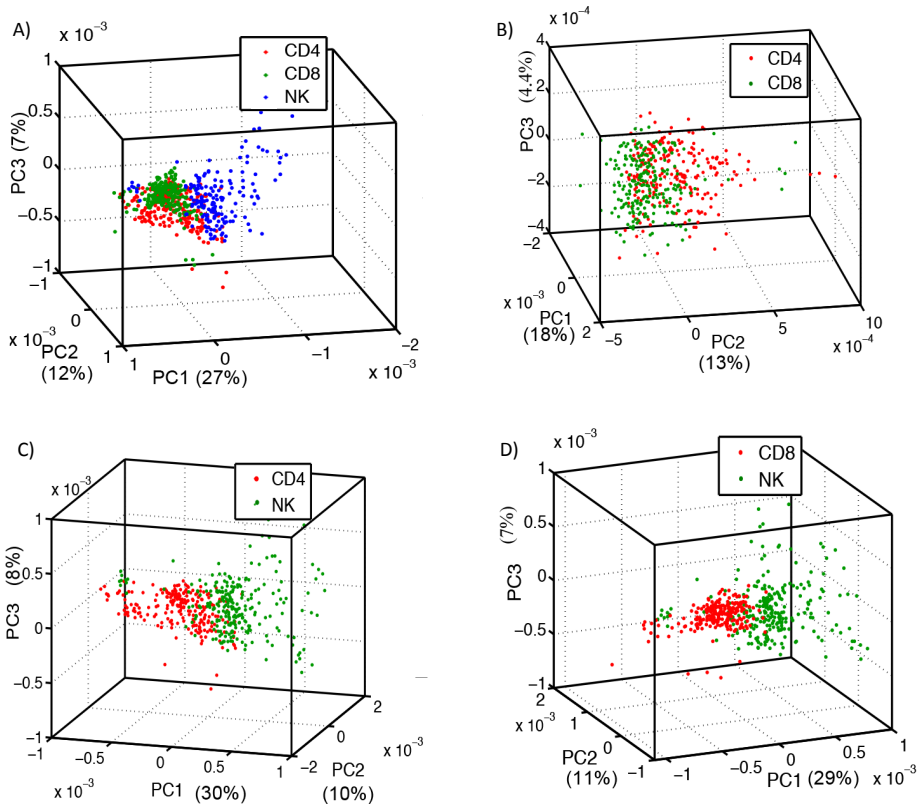

FIGURE 3.4: Cluster plots showing the first three principal components for each cell subset CD4+, CD8+ and NK cells. Cluster plot for A) all three lymphocyte populations CD4+, CD8+ and NK cells, B) T lymphocyte subsets CD4+ and CD8+, C) CD4+ and NK cells, and D) CD8+ and NK cells. The axes indicate the first three PCs and the amount of variation each accounted for respectively.

To quantify the ability of WMRS to discriminate between the three cell subsets and achieve a measure of the efficiency of the technique, LOOCV was applied to the training data set using the first 7 PCs, and each spectrum was classified according to the nearest neighbour algorithm. The discrimination of T lymphocytes CD4+ and CD8+ from NK cells yielded a specificity of 93% and 96% respectively and a sensitivity of 92% and 97% respectively. Between CD4+ and CD8+ T cells the discrimination was lower at 68% specificity and 69% sensitivity, this again indicates that the T cell subsets are most closely related and the most difficult to discriminate between. The entire data set of 638 cells was used to generate a confusion matrix (table 3.1), where correct classifications are indicated by values on the diagonal and incorrect classifications are indicated by off-diagonal values.

	Predicted CD4+	Predicted CD8+	Predicted NK
Actual CD4+	135	84	12
Actual CD8+	81	149	1
Actual NK	24	4	148

TABLE 3.1: Confusion matrix illustrating the efficiency of WMRS to discriminate between three lymphocyte populations CD4+ T cells, CD8+ T cells, and NK cells. Values on the diagonal represent those correctly identified, off-diagonal values represent those incorrectly identified. The majority of numbers lie on the diagonal indicating a good discrimination ability.

3.3.2 Identification using standard Raman spectroscopy

It is instructive to compare the discrimination ability of WMRS with standard Raman spectroscopy. It was observed that although standard Raman spectroscopy still achieves a high discrimination ability, for example CD4+ T cells and NK cells yielded a specificity and sensitivity of 91% and 90% respectively, it was not as clear as WMRS. This reinforces the benefits of recording spectra with background suppression to improve the discrimination efficiency achieved when identifying immune cell subsets.

3.3.3 Inter-donor variability

Variability in the WMRS spectra between a single cell type derived from different donors would severely limit the applicability of this technique in research or in clinical settings. Inter-donor variability between the cell subsets was investigated by analysing all WMRS spectra obtained from three different donors. Initially a student's t-test was performed at significance level of $p < 10^{-7}$ to compare WMRS spectra obtained from different donors for the same cell subset and no regions of significant difference were highlighted. PCA was then conducted on the training data set and cluster plots were produced using the first three PCs (figure 3.5). No distinct clusters were formed and the plots display significant overlap for each of the three donors for each isolated cell type. This indicates that there are no significant differences between cells derived from different donors as the Raman signature for each cell subset is consistent. This is reassuring, and is consistent with a previous study

on neutrophils using standard Raman spectroscopy, in which no variation between donors was noted [149].

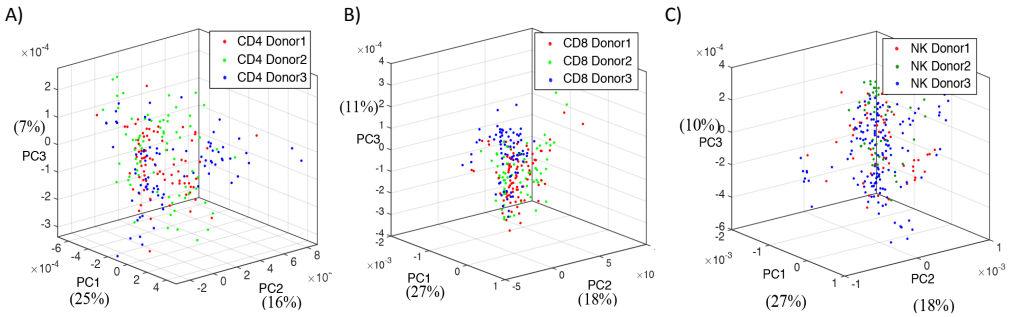

FIGURE 3.5: Cluster Plots showing the first three principal components for each cell subset CD4+, CD8+ and NK cells from three different donors. Cluster plot for A) CD4+ T cells, B) CD8+ T cells, and C) NK cells. The axes indicate the first three PCs and the amount of variation each accounted for respectively. Significant overlap between different donors indicate there is no significant difference in the spectra of a single cell type when derived from a different donor.

A comparison of the discrimination ability achieved when cells are derived from a single donor showed that marginally higher sensitivities and specificities were achieved for a single donor, where discrimination between T lymphocytes CD4+ and CD8+ from NK cells yielded a specificity of 97.5% and 96% respectively, and a sensitivity of 92% and 97.5% respectively, and between CD4+ and CD8+ T cells 71% specificity and 69% sensitivity was achieved.

3.4 Classification of dendritic cell populations

The scarcity of dendritic cells in the blood and the lack of specific markers have made DCs a particular challenge and an area of great interest in immunological research. For example the pathway for differentiation of the various types of DC is still not fully understood, with a recent report identifying a novel progenitor for pDC [168]. Methods are being developed to generate DCs and proliferate DC progenitors in the blood in order to overcome these obstacles [159], however a label-free method of identification would be a significant advantage.

Flow cytometry and functional characterisation revealed that plasmacytoid DCs were obtained at purity levels up to 92.1% and myeloid DCs were obtained at purity

levels up to 77.8% (full details in appendix B).

Fewer cells were recorded for dendritic cell populations pDC and mDC, as these are present in much lower concentrations. In total, WMRS was performed on 53 isolated pDC cells from two donors, and 123 mDC cells from three donors, in the same manner as described for lymphocytes in section 3.3. Using all the acquired spectra as a training data set for PCA, a cluster plot was generated using the first three PCs (figure 3.6). The formation of distinct clusters indicates that WMRS is successful at producing distinct signatures for the two DC subsets. Sensitivities and specificities were calculated as 71.1% and 87.7% respectively.

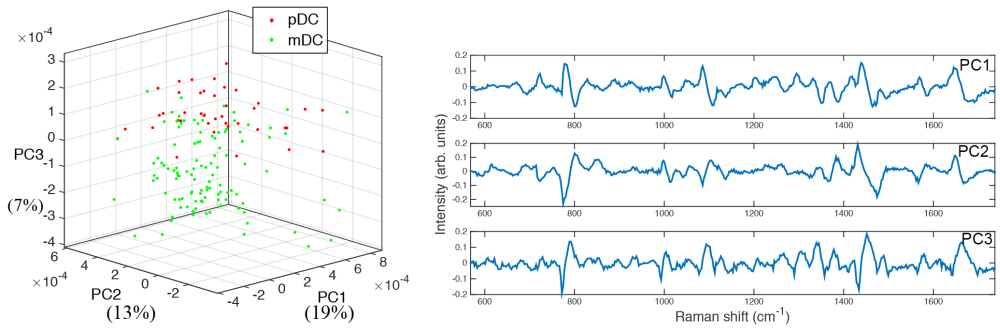

FIGURE 3.6: Classification of dendritic cell subsets pDC and mDC. Left hand side shows cluster plot achieved using first three PCs. Axes indicate amount of variance accounted for in each PC. The formation of distinct clusters illustrates the ability of WMRS to identify pDC and mDC populations. Right hand side panels illustrate PC loadings for the first three PCs. Peaks present in the PC loadings are the most significant bands in the WMRS spectra contributing to discrimination.

WMRS is thus an effective technique to identify the rare dendritic cell populations and may be useful for challenges such as further distinguishing DC lineages.

3.5 Classification of B cells, monocytes and T cell populations CD4+ and CD8+

The previous sections illustrate that WMRS is effective at discriminating between lymphocyte populations CD4+ T cells, CD8+ T cells, and NK cells, as well as the rarer dendritic cell populations mDC and pDC. For this method to be truly applicable in a research setting or clinical setting it is instructive to explore the ability of WMRS to characterise a full library of cell populations. This section will investigate

the ability of WMRS to identify T cell populations CD4+ and CD8+ from further cell subsets B cells and monocytes.

Fluorescent- activated cell sorting (FACS) assays of the isolated cell populations, from two donors, revealed purity levels of 89% and 91% for CD4+ T cells, 80% and 91% for CD8+ T cells, 100% and 100% for B cells, and 96% and 99% for monocytes. Further details of this can be found in appendix B.

WMRS spectra were recorded for 57 CD4+ T cells, 175 CD8+ T cells, 52 B cells, and 127 monocytes. These were derived from a single donor as the previous studies have shown no inter-donor variability. Data were collected over three days to ensure the stability of the system; reassuringly no variation was observed from data collected on different days. Figure 3.7 A illustrates the average standard Raman spectra recorded for each cell type, panels B-D show a pairwise comparison of WMRS spectra acquired for B cells and the other three cell types CD4+, CD8+, and monocytes respectively. Similar plots comparing CD4+ T cells and CD8+ T cells against the other cell populations can be found in Appendix D. The grey vertical bars indicate Raman bands of significant difference between the two cell subsets, as calculated by student's t-test at a significance level of $p < 10^{-15}$.

Using the zero crossing points of the WMRS spectra and literature observations [164–167] it is possible to suggest biochemical differences between the cell subsets; Raman bands highlighted by the student's t-test between B cells and CD4+ T cells, CD8+ T cells and monocytes may be assigned as follows: C-C twist in tyrosine ($645\,\mathrm{cm}^{-1}$) , C-S stretching in cysteine ($671\,\mathrm{cm}^{-1}$), adenine ring breathing mode ($725\,\mathrm{cm}^{-1}$), O-P-O symmetric stretching ($800\,\mathrm{cm}^{-1}$ and $1097\,\mathrm{cm}^{-1}$), symmetric breathing mode of phenylalanine ($1007\,\mathrm{cm}^{-1}$), skeletal C-C stretch in lipids ($1129\,\mathrm{cm}^{-1}$), phenylalanine/ tyrosine/ C-N stretching ($1209\,\mathrm{cm}^{-1}$) , amide III ($1259\,\mathrm{cm}^{-1}$), adenine/ amide III ($1304\,\mathrm{cm}^{-1}$), polynucleotide chain ($1345\,\mathrm{cm}^{-1}$), thymine/adenine/guanine ($1378\,\mathrm{cm}^{-1}$), CH_2 deformation in lipids ($1455\,\mathrm{cm}^{-1}$), adenine/guanine ($1585\,\mathrm{cm}^{-1}$), and amide I ($1665\,\mathrm{cm}^{-1}$). A full table of the Raman bands of interest can be found in appendix C.

The first PC for each pairwise comparison can provide an indication of the most important bands for characterisation. For CD8+ T cells versus B cells, the most significant bands correlate to O-P-O symmetric stretching, polynucleotide chain,

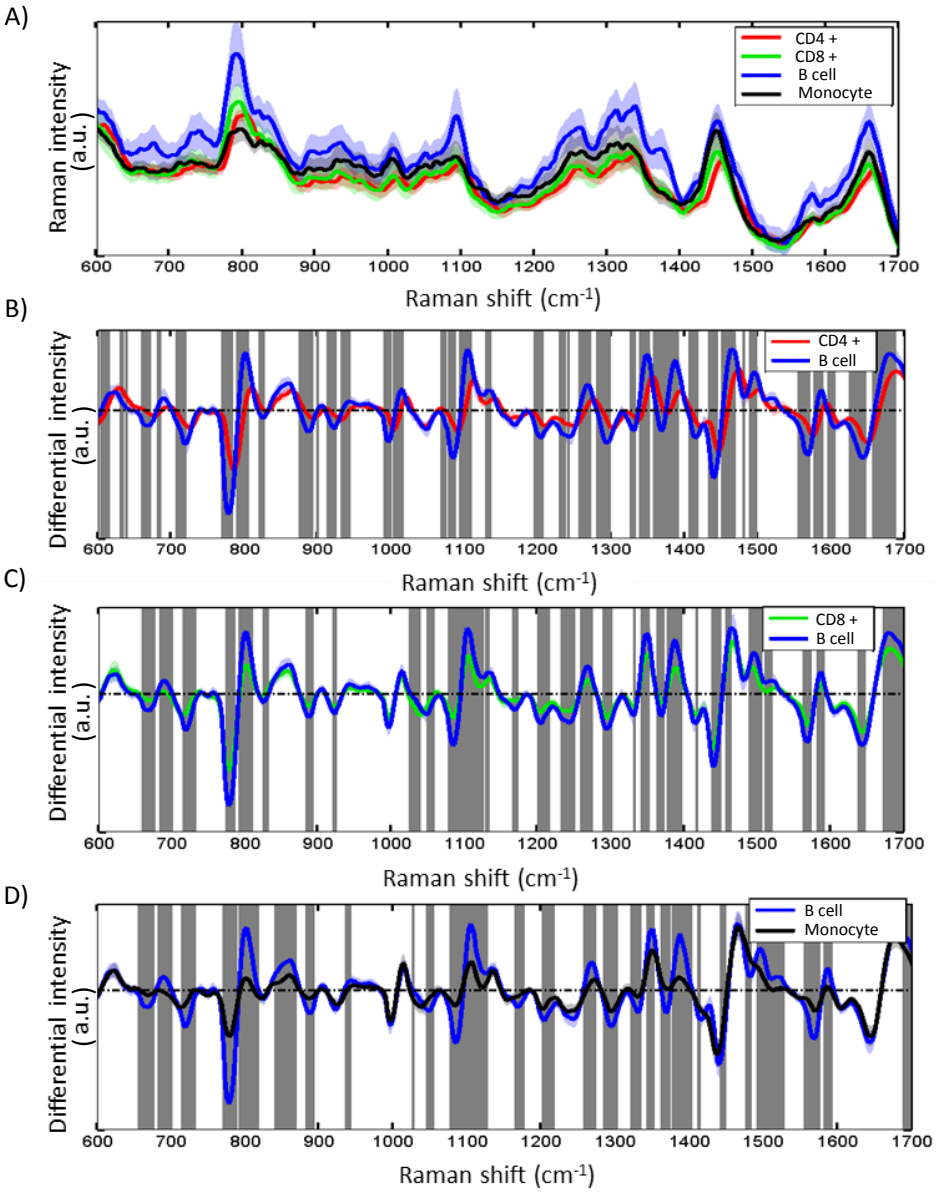

FIGURE 3.7: WMRS spectra of purified immune cell subsets CD4+ T cells, CD8+ T cells, B cells and monocytes. Pairwise comparison of A) CD4+, CD8+, B cells and monocytes. Pairwise comparison between mean standard Raman spectra of B) CD4+ T cells and B cells, C) CD8+ T cells and B cells, and D) B cells and monocytes. Solid lines show the average spectrum of each cell population and shaded regions show the standard deviation. Grey vertical bars indicate regions of significant difference between two cell subsets, as estimated by student's t-test at a significance level of $p < 10^{-15}$.

thymine, adenine, guanine, and amide III content. For CD4+ versus B cells there are additional bands which correlate to the symmetric breathing mode of phenylalanine and amide I. The Raman bands appearing in the first PC for monocytes versus B cells correspond to the O-P-O symmetric stretching, thymine, adenine, guanine, adenine ring breathing mode, and CH_2 deformation in lipids.

By conducting PCA on the whole data set cluster plots were produced using the first three PCs (figure 3.8). Distinct clusters can be observed for each cell subset indicating there is a distinct WMRS signature for each cell type.

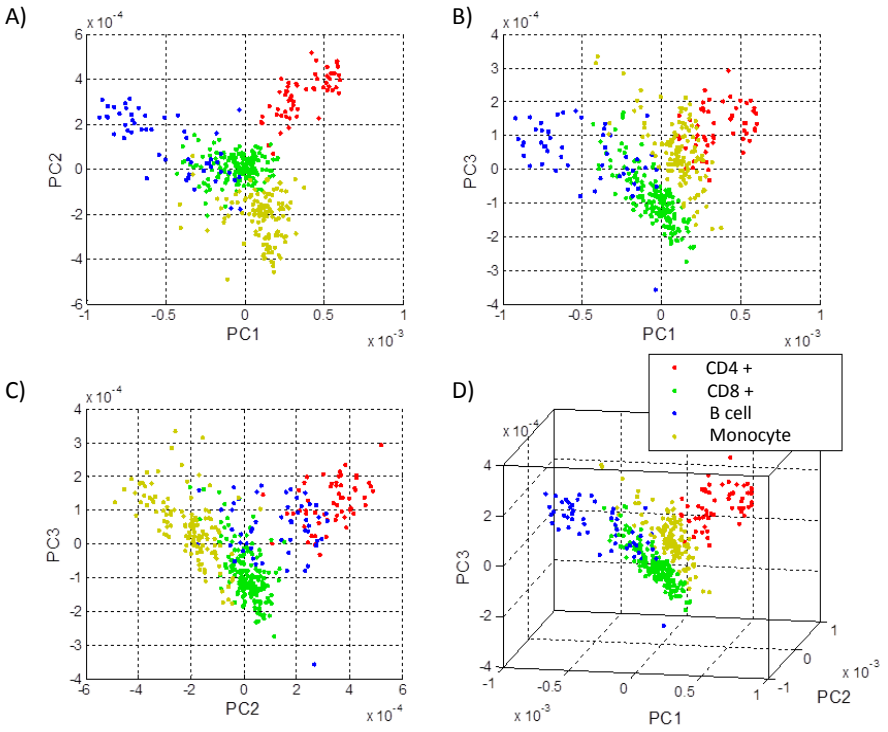

FIGURE 3.8: Cluster Plots showing the first three principal components for each cell subset CD4+ T cells, CD8+ T cells, B cells and monocytes. The formation of distinct clusters indicates that WMRS is able to successfully identify each cell subset.

To estimate the discrimination efficiency the first seven PCs were selected, and LOOCV was used to characterise the cells. Cell classifications are summarised in a confusion matrix (table 3.2) where values on the diagonal represent those which were correctly identified and off-diagonal values represent those which were incorrectly identified. Sensitivities and specificities were then calculated in a pairwise manner and are summarised in table 3.3. Comparing CD4+ T cells to CD8+ T cells, B cells, and monocytes, sensitivity and specificity values of 100% were achieved. CD8+ T cells showed some overlap with B cells in the PC cluster plots and had a slightly lower discrimination ability, with sensitivity and specificity values of 94.4% and 84.8% respectively. CD8+ T cells and B cells compared to monocytes achieved sensitivity and specificity values of 98.8% and 100% respectively, and 97.6% and

92.9% respectively.

	Predicted CD4+	Predicted CD8+	Predicted B cell	Predicted Monocyte
Actual CD4+	57	0	0	0
Actual CD8+	0	168	7	0
Actual B cell	0	0	39	3
Actual Monocyte	0	2	3	122

TABLE 3.2: Confusion matrix illustrating the efficiency of WMRS to discriminate between populations CD4+ T cells, CD8+ T cells, B cells, and monocytes. Values on the diagonal represent those correctly identified, off-diagonal values represent those incorrectly identified. The majority of number lie on the diagonal indicating a good discrimination ability.

	Sensitivity %	Specificity %
CD4+ vs CD8+	100	100
CD4+ vs B cell	100	100
CD4+ vs monocyte	100	100
CD8+ vs B cell	94.4	84.8
CD8+ vs monocyte	98.8	100
B cell vs monocyte	97.6	92.9

TABLE 3.3: Summary of sensitivities and specificities achieved used LOOCV statistics to estimate the discrimination ability of WMRS to identify CD4+ T cells, CD8+ T cells, B cells and monocytes.

It is noteworthy that in figure 3.8 B cells appear to form two distinct clusters. It is thus interesting to investigate if this difference is due to the presence of two B cell sub-populations, such as activated or naïve B cells. This will be discussed in more detail in the next section. It is also interesting to note that CD8+ T cells and B cells share some overlap. Further investigations into the biochemical similarities between these cell types would be interesting, although beyond the scope of this chapter. It has been reported that CD8+ memory T cells are generated by the same mechanism as memory B cells, that is to say the triggering of CD40 surface proteins [169, 170]. It may therefore be interesting in future studies to investigate if this overlap occurs only with memory B cells and memory CD8+ T cells.

3.6 Classification of naïve and activated B cell populations

The formation of two distinct clusters within the B cell cluster observed in figure 3.8 indicated a potential that WMRS may be able to detect B cell sub-populations. To investigate this further this section will deal with the intentional activation of an isolated population of B cells for comparison to non-activated B cells. The ability to distinctly identify these two populations in the blood would be of particular importance as it could be developed further as a tool for drug screening to sense B cell activation.

Lipopolysaccharide (LPS) was used to activate the B cells through the TLR4 receptor [171, 172]. LPS is the main structural component of the cell wall of gram-negative bacteria, which are the pathogens targeted by B cells. Toll-like receptors (TLRs) are a family of transmembrane proteins responsible for pathogen recognition and initiating responses. TLR4 has been shown to be the signal-transducing receptor for LPS [173–175].

WMRS data were recorded for a total of 100 activated and 109 non-activated B cells. Upon activation B cells may differentiate into effector cells, producing and secreting antibodies; as a result they may undergo a dramatic morphological change. Naïve B cells are small (about $7\,\mu\mathrm{m}$) and are mostly nuclear. Effector B cells are larger and have a distinct clear perinuclear region of cytoplasm. Figure 3.9 A-B illustrate typical white light microscopy images of activated and non-activated B cells respectively. Single point Raman spectra were always recorded in the nuclear region of each cell.

Figure 3.9 C illustrates the mean WMRS spectra for activated and non activated B cells, with regions of significant difference highlighted by grey vertical bars, as calculated by the student's t-test at a significance level of $p< 10^{-15}$. D-E illustrate cluster plots using the first 3 PCs. The formation of distinct clusters indicates a good discrimination ability for WMRS to identify these B cell subsets. LOOCV was used to calculate the discrimination ability, which yielded sensitivity and specificity values of 94.9% and 94.5% respectively. The most important bands for discriminating between the two cell types, as indicated by the first PC loading, are found at $800\,\mathrm{cm}^{-1}$, $1097\,\mathrm{cm}^{-1}$, $1345\,\mathrm{cm}^{-1}$, $1378\,\mathrm{cm}^{-1}$, $1455\,\mathrm{cm}^{-1}$, and $1585\,\mathrm{cm}^{-1}$. These band

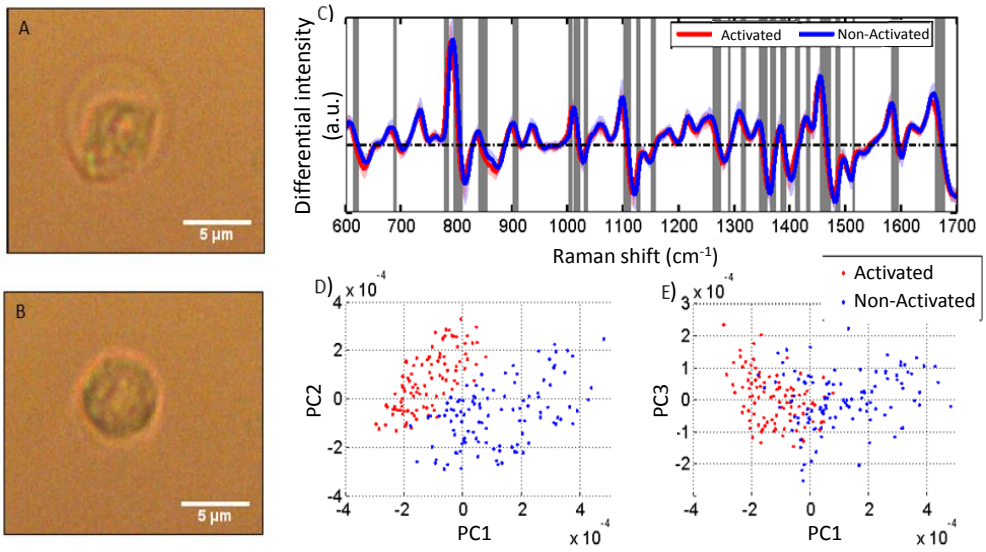

FIGURE 3.9: A comparison of activated and non-activated B cells. Typical white light microscopy images are shown of A) an activated B cell and B) a non-activated B cell. C) Mean WMRS spectra of activated and non activated B cells where solid lines show the average spectrum of each cell population and shaded regions show the standard deviation. Grey vertical bars indicate regions of significant difference between two cell subsets, as estimated by student's t-test at a significance level of $p < 10^{-15}$. D-E illustrate cluster plots using the first 3 PCs; distinct clusters for each cell subset indicates there are distinct WMRS signatures for activated and non-activated B cells.

assignments are discussed in previous sections (3.3 and 3.5) and are summarised in appendix C.

It must be noted that this study is limited in its applicability as it has recently been reported that there may be a divergence in TLR4 levels on B cells from mice or humans [176]. It is suggested that only mice have good TLR4 levels on B cells, and not human B cells. The change in morphology of the B cells, as observed under white light imaging, would suggest activation has occurred although to be a more robust study these measurements should be repeated using an alternative method for B cell activation.

It would be interesting to expand this study further and include data for other cell subsets and specific immune cell subset activation in mixed cell cultures.

3.7 Conclusions

The ability to detect distinct immune cell subsets non-disruptively and in a completely label-free manner would be of significance for both *in vitro* and *in vivo* studies of the immune system. With the increased focus on abilities to study cellular behaviour and contents at a single cell level, the necessity of isolating and characterising cells that have not been altered becomes increasingly important. Commonly used techniques such as flow cytometry relies on optical scattering, which is limited in sensitivity for morphologically similar cells, or specific antibody labelling with fluorescence or magnetic beads which may cause partial modification or activate the cells.

This chapter has illustrated that WMRS can successfully identify of a number of important immune cell subsets, including those found in abundance in the human blood stream, such as CD4+ and CD8+ T cells, NK cells, B cells, monocytes, and the much rarer subsets mDC and pDC. It was noted that the most difficult cell populations to distinguish between were CD4+ and CD8+ T cells, which may reflect their closely related differentiation lineage in the thymus [177]. On the other hand T cell subsets were distinctly different from NK cells, which normally contain lytic granules [178].

A recent study [164] has also shown successful discrimination between T and B lymphocytes, and between individual T- and B- cell lines. As cell lines are transformed cells, often derived from tumours, not all cell lines within a general class were alike and provided some unique Raman markers. In the study presented in this chapter, freshly donated cells from healthy donors were used, which are of more direct biomedical relevance. Furthermore no variation was demonstrated between cells derived from three different donors.

This technology could find use in both a clinical and research setting, for example a label-free haemograph for detection of infection, inflammation or disease conditions, or for monitoring the immune response to drugs or radiation treatment. Of particular interest is the ability to identify DC subsets which may help further distinguish DC lineages, or to discriminate between naïve and activation states of B cells which would be of significant interest in drug testing and vaccine development.

In future studies it would be interesting to include other cell populations in both activated and naïve states to enable analysis of cell-cell interactions *in vivo*. Comparing positively isolated cells to untouched populations would also help define a full library of cells. Furthermore investigating the ability to distinguish further cell subsets would be of interest. For example, CD4+ T cells can further differentiate into TH1, TH2, and TH17 cells. Identifying the ratio in which these are present, in a label-free manner, would have significant potential. TH17 cells, for example, are associated with a number of disease conditions [179–182].

The disadvantage of Raman spectroscopy is that it takes a relatively long time to acquire spectra from a single cell which severely limits the throughput rate. Current acquisition times are 25 seconds per cell, where as flow cytometry may analyse up to 100,000 events per second. Techniques such as stimulated Raman spectroscopy (SRS) have been used to achieve throughput rates of 11,000 particles per second [121–124]. This is a significant enhancement and demonstrates the potential of this technique to achieve the required throughput rates. Combining Raman spectroscopy with other optical modalities may also be of interest, for example using optical tweezers with Raman spectroscopy, to isolate cells of interest from complex cultures for further analysis, such as cytokine-specific rtPCR or full transcriptome analysis by RNA-Seq [183, 184]. Combining Raman spectroscopy with a phase imaging modality may also prove interesting for studies characterising both chemical and morphological cellular profiles.

Relevant Publications

- M. Chen*, **N. McReynolds***, E. C. Campbell*, M. Mazilu, J. Barbosa, K. Dholakia, S. J. Powis, "The use of wavelength modulated Raman spectroscopy in label-free identification of T lymphocyte subsets, natural killer cells and dendritic cells", (2015) PLosOne 10(5): e0125158.

  ** Authors have equal contribution*

Contributions

I was involved in the acquisition of Raman spectra, data analysis, and Raman band assignments, as well as assisting M.C. with system optimisation and calibration of

laser wavelength modulation. M.C was involved in designing and maintaining the WMRS system, as well as data collection and analysis for data presented in sections 3.3 and 3.4. M.C. and M.M. wrote the code for PCA, which I modified for specific studies. E.C.C, F.G.M.C. and S.J.P. isolated the cell subsets and performed flow cytometric characterisation.

4 Multimodal analysis of immune cell subsets: Raman spectroscopy and digital holographic microscopy

4.1 Introduction

The high spectral resolution and chemical specificity of Raman spectroscopy makes it a very powerful optical method for sample analysis. However its inherent weak scattering cross-section has made it a prime candidate for use along-side complimentary optical techniques. To enhance signals the use of Raman tags [185] or nanoparticles [186] may be used, however these techniques require the use of exogenous labels. As previously discussed, there is a real drive in both research and clinical settings for label-free technologies, particularly for the study of live cells where labels may interfere with biological processes.

In the absence of exogenous contrast agents the measured signal must originate from a direct interaction between the light and the sample. Such interactions can occur via a variety of physical processes. The essence of multimodal analysis is to retrieve information from additional modes, hence obtaining more information than would be possible using any single mode alone and providing an opportunity to overcome any limitations specific to a single technique. The development of multimodal systems is thus pushing the boundaries for diagnostic techniques and is one of the main challenges facing biophotonics today. It is typically used to enhance the amount of information recorded, either by obtaining more optical signal or observing different types of interactions, i.e. when the modes arise from different physical light-sample interactions [187].

The main challenge facing the implementation of a label-free spectroscopic haemograph, as discussed in chapter 3, is the long acquisition time ($25\,\mathrm{s}$) required for Raman measurements. Ideally high throughput rates (10,000 cells per second) are required to ensure a viable technology. A multimodal approach in which Raman

spectroscopy is used along-side a faster modality could permit a fast initial screening, allowing a more specific analysis on cells of interest to be carried out by the slow, yet chemically specific, Raman spectroscopy. Digital holographic microscopy (DHM) is an ideal candidate as it is a fast imaging modality, limited only by camera acquisition rates [188, 189].

An additional limitation of Raman spectroscopy is that it cannot provide any morphological information. There would therefore be significant advantage in combining Raman spectroscopy with a morphological imaging modality to obtain a more complete description of the sample. Raman spectroscopy has been used alongside OCT for the characterisation of tissue [190] and cancers [191, 192]. Shape and optical thickness are useful morphological parameters for the discrimination between cells, and may be recorded with the use of quantitative phase imaging (QPI). DHM is an interferometric imaging modality which provides quantitative information on the phase shifts induced by a sample [193, 194].

DHM has been used previously for studying blood cells, such as the discrimination between the maturity levels of red blood cells (RBC) [195], label-free cell counting [196], and determining morphological information of cells for identification and disease diagnosis [197, 198]. Raman spectroscopy and DHM have recently been implemented simultaneously by Pavillon et al for the determination of local molecular content by Raman spectroscopy whilst simultaneously observing dynamic sample morphology at video rates [199]. A further use was to determine the relationship between Raman information and the quantitative phase information extracted from a cell [187, 200]. Kang et al have also employed a combined Raman spectroscopy and QPI system; in this case DHM is utilised as a screening tool for malaria infected RBCs. Phase information can locate suspicious cells from a wide field of view, due to their abnormal shape and refractive index, and Raman spectroscopy can be used as a means of validation, confirming the presence of hemozoin [201]. In this system a single excitation source is used eliminating the need for two laser sources but preventing the simultaneous acquisition of phase and Raman information. RBCs are often used in DHM studies for their simple internal structure; immune cells on the other hand have a more complex internal structure and pose an interesting challenge for DHM. The potential for DHM to be used as a screening tool makes it an

exciting candidate for overcoming the low throughput rates currently achieved by Raman spectroscopy alone. DHM boasts rapid acquisition times and has proven capable of quantitatively studying cellular dynamics in real time [202]. This chapter will present the first time this technology has been applied to the study of immune cell populations with statistical analysis for discrimination purposes.

An overview of various multi-modal Raman spectroscopy techniques for biomedical applications can be found in table 4.1. Further information can be found in reviews [203] and [187], where the latter focuses on label-free multimodal microscopy methods.

In summary, DHM and Raman spectroscopy rely on complementary physical interactions; Raman spectroscopy relies on the inelastic vibrational scattering from the sample, whereas DHM relies on the linear elastic scattering of a wave front passing through a sample. The combination of these two modalities therefore provides complimentary information and builds a more complete description of the sample. The advantages of a label-free technology are not compromised as neither Raman spectroscopy nor DHM require the addition of any external tags, or sample preprocessing before measurements. Finally, the practicalities of assembling a multimodal system are relatively simple; DHM utilises a narrow linewidth illumination source, implemented here with $532\,\mathrm{nm}$, in contrast to Raman spectroscopy which uses an excitation wavelength of $785\,\mathrm{nm}$ and has a broad emission range at longer wavelengths. This makes it possible to isolate the two signals from each other, with the use of appropriate filters, ensuring simultaneous measurements are possible. Importantly, in contrast to Raman spectroscopy which is often hindered by its long acquisition times, DHM is a fast imaging modality limited only by camera acquisition rates (up to 20 fps in live mode). Therefore what makes this pairing of optical modalities truly exciting for the application of immune cell identification, is the prospect of high throughput measurements, paving the way for clinical use. The goal of this technology would be to use DHM for a fast initial screening where Raman spectroscopy can provide more specific chemical information on cells of interest.

This chapter will provide an introduction to DHM and discuss the design of the multimodal system. Raman spectra and DHM images are obtained simultaneously and processed separately. The method of processing DHM images will be discussed

Multimodal technique	Information provided	Applications
RS and OCT	OCT is a non-invasive imaging technique whose signal primarily comes from reflections due to refractive index boundaries. Structural information can be obtained from within tissues, with penetration depths up to several millimetres.	OCT can be used to guide acquisition of RS for cancer margin detection. This has been demonstrated with ex-vivo breast tissue, where OCT screened for highly scattering abnormal regions and normal fatty tissue, and Raman spectra probed the biochemical information revealing a high lipid content of normal tissue compared to a greater DNA and protein content in malignant sites [190]. Successful discrimination of colon adenocarcinoma from normal tissue has also been reported using multivariate analysis of texture analysis parameters from OCT images and Raman spectra [192]. In-vivo tissue applications have also been demonstrated by characterising a healing wound, where a scab was hyper-reflective in OCT and contained an increase in collagen as detected by RS [190]. A hand-held Raman-OCT probe has also been reported to characterize skin lesions where OCT can visualise microstructural irregularities and guide RS acquisition for biochemically specific spectra [191]. Raman and OCT information are generated from different layers of the tissue unless implemented with confocal RS. An example of this was demonstrated through concentration measurements of Tenofovir, a drug used to prevent transmission of HIV, in ex-vivo tissue samples. This combined technique could be used to understand drug diffusion through tissue layers [204].
RS and QPI	Phase imaging is a label-free method to visualise thin, optically transparent specimens such as cells. Diffraction and scattering as light propagates through the sample retards the phase thus providing information on the objects structure. By combination with RS for characterisation of the chemical profile both structural and chemical information can be related and dynamic cell processes can be monitored.	Integrated phase contrast microscopy and RS have been employed to characterise bacterial spores; dormant spores typically have a lower refractive index when compared to germinated spores and RS was able to characterise and quantify the diplicolinic acid and calcium ions in a single spore. This multimodal system can provide information on germination dynamics of *B. Subtilis* and *C.difficile*, and the impacts of heat shock in germination [205, 206]. DHM and Raman imaging have been employed simultaneously where dynamic measurements by DHM were able to monitor changes in cell morphology during Raman image acquisition, thereby identifying any movements that occurred during the measurement [199]. Wide-field DHM measurements were able to identify regions of interest for acquisition of Raman spectra from macrophage-like cell lines in oreder to maximise throughput for discrimination of cell types. A random scanning pattern was employed for rapid Raman acquisition, providing more statistically consistent spectra than single point RS and a greater SNR than Raman imaging [207]. The combined approach may be used to provide insight into the molecular source of phase contrast. This was demonstrated on HeLa cells where molecular species such as lipids and proteins were related to the source of phase contrast in a cell, indicating phase signal originating from cells is primarily due to proteins distributed throughout the cytoplasm and by dense regions of DNA [200]. Similarly malaria infected RBCs were analysed where wide-field QPI was able to locate suspicious RBCs due to their abnormal shape and refractive index. Raman spectra of the suspicious cells were then able to confirm hemozoin was localised in the region of greater refractive index [201]. It can thus be envisaged that this system could be useful in monitoring cell-drug interactions.
RS and fluorescence	Autofluorescence is a label-free method that can be used for tissue analysis; the strong signals provide a rapid analysis but have poor specificity for cancer. RS however has a high sensitivity and specificity for cancer versus normal tissue. The use of fluorescence labels have high molecular specificity but may perturb cell function.	Tissue autofluorescence may be used to rapidly isolate a region of interest for Raman spectroscopy to ensure margins of excised tissue are free from tumours [208–211]. The molecular specificity of fluorescence labels may also be used for validation of Raman imaging results [212]. Fluorescent molecules conjugated to AuNPs via a pH dependent linkage have enabled successful tracking of drug distribution and measurements of local pH [213].
RS and elastic scattering	Elastic scattering is due to differences in refractive index thus provides morphological information. It can be used to determine the size of cells in suspensions, but provides no chemical information.	Simultaneous Raman and elastic scattering measurements have enabled characterisation of composition, size and refractive index of a droplet, enabling monitoring of polymerisation reactions [214, 215]. An integrated microscope has been constructed to characterise both morphological and chemical information of bead mixtures and human immune cells (granulocytes and lymphocytes) [216, 217], as well as determining yeast cell wall thickness [218]. Long-term measurements were able to monitor PDT (photodynamic therapy) treated cells over several hours, revealing an initial decrease in scatterer size and protein concentration, followed by a decrease in lipid concentration after about 3-6 hours [219].
RS and Mass spectrometry (MS)	MS is able to discriminate between similar proteins but cannot separate positional isomers that RS can identify. MS is a destructive method and each modality is based on very different properties; combination is therefore non-trivial.	RS and MS have been combined using a tissue paper substrate, allowing SERS detection of positional isomers, followed by generation of elctrospray for sample analysis by MS. This enabled chemical reaction species in fast chemical reactions to be monitored online in real time [220]. MS mapping has been combined with Raman maps for visualisation of chemical structures in tissue, this combination was demonstrated with a cryosection of a mouse brain, where information on proteins, lipids and nucleic acids were provided by RS and complemented with specific lipid information from MS [221].

TABLE 4.1: Overview of multimodal Raman spectroscopy techniques for biomedical applications.

in detail. Three immune cell subsets, CD4+ T cells, B cells, and monocytes are then classified according to Raman spectroscopy alone, DHM alone, and by a combination of the two modalities. The discrimination ability of each modality, individually and in combination, is then determined.

4.2 Basic theory of digital holographic microscopy

4.2.1 Brief history

Dennis Gabor first discovered holography in 1947 [222], for which he was later awarded the Nobel prize in Physics in 1971 *"for his invention and development of the holographic method"*. He discovered a method based on interference and coherence to capture both phase and intensity information. This allows recording and reconstruction of the whole 3 dimensional information, in contrast to photography which can only record intensity. Gabor coined the term 'holography' from the Greek words *Holos*, meaning whole or entire, and *gramma*, meaning anything written or drawn. Practical uses of the technique only experienced significant advancements after the development of the laser in 1960, providing a much needed source of coherent light.

4.2.2 Basic principles of holography

Imaging an object requires both illumination of the object and detection of the scattered light. The scattered light is known as an object wave '**o**' and carries information regarding the object. This wave can be characterised by two parameters: amplitude (brightness) and phase (shape). The object wave is considered a complex light field and is a superposition of all the waves emerging from individual points in the object. In photography, when this is observed, either by camera or photographic film, only intensity information is recorded and the phase information is lost. The resulting image is 2 dimensional.

Holography makes use of the principles of interference and coherence in order to capture both intensity and phase information. To record phase information therefore a reference wave '**r**' is required. When light is transmitted through an object, or reflected off its surface, the wave-front is modified according to its shape and optical path differences. Consequently **o** will have a phase shift with respect to **r**. **o**

and **r** are combined before detection and cause interference. The generated interference fringes are then recorded. The complete object information is contained in the brightness and distance between the fringes [223]. An example interferogram of $5\,\mu\mathrm{m}$ polymer beads is shown in figure 4.1 where displacements of the interference fringes indicate a phase shift between **o** and **r**.

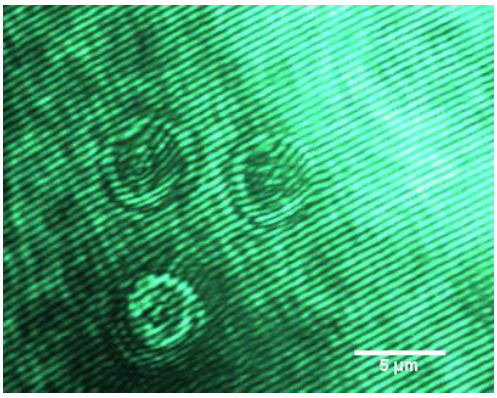

FIGURE 4.1: Recorded interference pattern of polymer beads. Displacement of the interference fringes indicates a phase shift between **o** and **r**. Scale bar shows $5\,\mu\mathrm{m}$.

The first step in holography is the recording of the interference pattern and the second step is the reconstruction. The recorded hologram contains both pure intensity terms (zero order diffraction) and the coherent orders (+1/-1 diffraction orders) as defined in equation 4.1.

$$I = |\mathbf{o} + \mathbf{r}|^2 = |\mathbf{o}|^2 + |\mathbf{r}|^2 + \mathbf{o}^*\mathbf{r} + \mathbf{o}\mathbf{r}^* \tag{4.1}$$

where * represents the complex conjugate. The first two terms are referred to as the zero-order terms and represent the intensity patterns of the object and reference fields. The last two terms represent the first order diffraction terms. It is the last term, containing the object wave '**o**' that is particularly important in holography as it corresponds to the coherent term and allows retrieval of the measured complex field.

o and **r** can be defined generally as $\mathbf{o} = oe^{i\Phi}$ and $\mathbf{r} = re^{i\Psi}$, where *o* and *r* represent the field amplitudes, and Φ and Ψ represent the phase terms, respectively at the

point of superposition. Substituting into equation 4.1 gives an intensity distribution

$$I = o^2 + r^2 + 2 \cdot r \cdot o \cdot cos(\Phi - \Psi) \tag{4.2}$$

A system of interference fringes form in space, between maxima and minima values of $I_{max} = r^2 + o^2 + 2ro$ and $I_{min} = r^2 + o^2 - 2ro$ [223].

When a holographic film is exposed to the interference pattern, the resulting pattern can be thought of as a grating. The reconstruction relies on the principle that, after development of the hologram, illumination of the grating by the reference wave '**r**' will cause diffraction in such a way as to generate the object wave. The reconstruction yields the light amplitude '**u**' according to equation 4.3. Let

$$\mathbf{u} \sim r \cdot I = \mathbf{r}(|\mathbf{o}|^2 + |\mathbf{r}|^2) + \mathbf{rro}^* + |\mathbf{r}|^2\mathbf{o} = \mathbf{u}_0 + \mathbf{u}_{-1} + \mathbf{u}_{+1} \tag{4.3}$$

The first term $\mathbf{u}_0$ describes the zeroth diffraction order, governing the reference wave. The second term $\mathbf{u}_{-1}$ describes the conjugate complex object wave $\mathbf{o}^*$ corresponding to the -1^{st} diffraction order. The last term $\mathbf{u}_{+1}$ is the component of most interest; the $+1^{st}$ diffraction order, which is the object wave itself reconstructed with the amplitude of the reference wave $\mathbf{r}^2$. The object wave can thus be completely reconstructed, containing the complete information regarding the object. The resulting image is 3 dimensional [223]. An example of reconstructed DHM images of red blood cells can be found in figure 4.2.

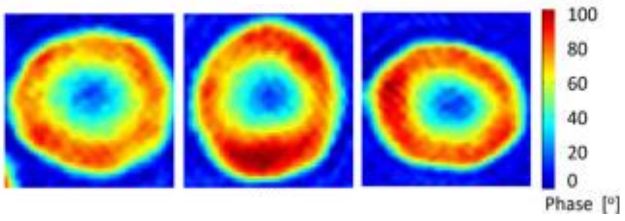

FIGURE 4.2: Taken from [224]. Reconstructed red blood cell (RBC) DHM images, providing 3-D information.

For digital holographic microscopy a camera may be used in place of holographic film. Attractive features of digital acquisition lies in the fast recording rates (up to video frequency) and the ability to reconstruct amplitude and phase contrast images

simultaneously. For studies presented in this thesis interferograms are recorded using a CMOS camera and phase information is retrieved using Fourier filtering as outlined in section 4.4.4.

Mach-Zender interferometer configurations are commonly used [202, 225–229] although common-path configurations [230–233] are sometimes preferred. One advantage of common-path interferometers is that they are less sensitive to vibrations, or instabilities of the system (mechanical or thermal) as both paths experience the same perturbations. However the spatial filtering required can involve non-trivial optical alignment, such as pinhole filtering [232], or expensive components such as spatial light modulators (SLM) [233]. A Mach-Zender configuration is used for studies in this chapter for ease of alignment and the freedom to independently tune the object and reference waves to optimise image quality. Additionally, exposure times are short ($10\,\mathrm{ms}$) preventing vibrations below KHz from influencing the measurement.

4.2.3 Off-axis holography

Leith and Upatneiks demonstrated off-axis holography in 1962 [234–236], which paved the way for practical applications of holography. The core principle behind off-axis is holography is that by tilting the reference wave the three diffraction orders are spatially separated [225], as illustrated in figure 4.3 A. The advantage over in-line (Gabor) holography is that the image and conjugate image are separated and therefore do not interfere during reconstruction. Off-axis methods typically allow faster acquisition as the phase information can be extracted from a single interferogram.

The distance, d between intensity maxima is given by equation 4.4, where λ is the laser-line wavelength:

$$d = \frac{\lambda}{sin(\alpha)} \tag{4.4}$$

as illustrated in the inset of figure 4.3. As a result, a greater angle between **o** and **r** means that the interference fringes will be much finer. By increasing the carrier frequency the first and zero order diffraction terms will experience a greater spatial separation on a Fourier transform. Ensuring there is no overlap between the terms

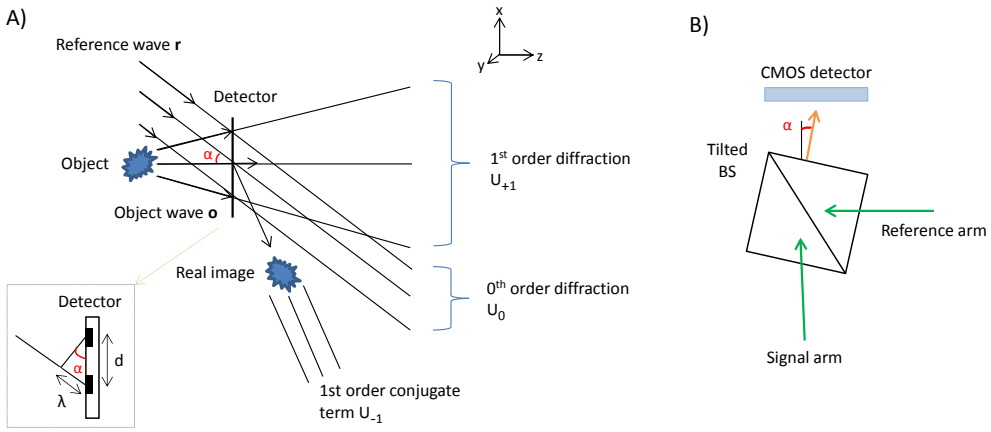

FIGURE 4.3: A) Schematic of off-axis holography. The reference wave and object wave interfere forming a grating pattern on the detector surface. Upon illumination with **r** during reconstruction the zero and first order diffraction terms will be spatially separated due to the tilt angle α. (Modified from [223] with permission). Inset illustrates the spatial separation between the intensity maxima. B) Schematic illustrating the tilt angle achieved by tilting the beam splitter where the reference and signal arms of a Mach-zender interferometer recombine.

improves the effectiveness of Fourier filtering to separate the intensity and phase information. This will be discussed further in section 4.4.4.

In combination with microscopy DHM is a valuable tool for the study of biological samples [237]. Biological material, particularly cells, are often transparent under white light imaging and differ only slightly from their surroundings in absorbance. The ability to record phase information is therefore crucial to obtaining morphological information. DHM offers the advantage of obtaining three dimensional information without any sectioning, such as in confocal scanning microscopy or OCT, which necessitate longer acquisition times and limit the throughput rate. Importantly DHM is a label-free method and does not require any sample preparation.

4.3 Design of the multimodal system

A digital holographic microscope is fairly simple to integrate around a Raman microscope. The design of a free space Raman system is described in detail in section 2.7.3 although specifications relevant to the multimodal system will be detailed here. The components used to build a digital holographic microscope around the Raman

microscope will also be described. A schematic of the multimodal system can be found in figure 4.4.

4.3.1 Raman spectrometer

The multimodal system was equipped with a CW Ti-sapphire laser (Solstis), provided by Msquared Lasers Ltd, UK. The Solstis laser has an extremely narrow linewidth ($< 50\,\mathrm{kHz}$) around $785\,\mathrm{nm}$, which is desirable for Raman measurements as it improves the spectral resolution (separation between individual Raman bands), as previously described in section 2.7.1. Unfortunately for the studies presented here there were some problems encountered with regards to the wavelength tuning of the solstis; the excitation wavelength would sometimes jump in steps of up to $0.2\,\mathrm{nm}$, which in turn affected the processing of WMRS data. As a result standard Raman spectroscopy is used (no wavelength tuning).

The beam was focussed through a 60X objective (Nikon, 0.80 NA) and focussed onto the sample plane, providing $150\,\mathrm{mW}$ power to the sample. The light was collected in reflection, through the same objective, and passed through a notch filter (NF) (Semrock, NFD01-785-25X36) to reject Rayleigh scattering. A lens (f=$200\,\mathrm{mm}$) focused the Raman scattered light into a low OH fiber (M25L01, Thorlabs) with a $200\,\mu\mathrm{m}$ core. The fiber acts as a confocal aperture producing a confocal volume with a base radius of $1.66\,\mu\mathrm{m}$ and depth of $2.2\,\mu\mathrm{m}$ in the sample plane (as calculated by equations 2.15 and 2.16). Before entering the fiber the light was transmitted through a second NF (Semrock, NF03-785E) which acts to further block the laser line.

The light was then coupled into a spectrograph (described in section 2.7.2). The spectrometer has an acceptance pyramid, often described by an F-number (f/#). For Raman spectroscopy, where the signal is often very weak, it is important to couple as much as light as possible into the spectrometer. For this reason f/# matching optics are used to optimally couple the light into the spectrometer. The f/# of the spectrometer is 4 and the f/# of the fiber may be calculated according to equation 4.5. The fiber has an NA of 0.22 which gives an f/# of 2.27.

$$f/\# = \frac{1}{2NA} \tag{4.5}$$

The ratio required to match these two f/# values is 1.76. A pair of convex lenses with focal lengths $30\,\mathrm{mm}$ and $50\,\mathrm{mm}$ were used to provide a magnification of 1.67. This is sufficient to provide f/# matching, however the beam from a $200\,\mu\mathrm{m}$ fiber would be expanded to $334\,\mu\mathrm{m}$. This means a substantial amount of the light would be rejected as the slit width used at the entrance to the spectrometer is $150\,\mu\mathrm{m}$. To overcome this an additional telescope is used between the first pair of lenses, containing two cylindrical lenses to modify the aspect ratio of the beam. The lenses have focal lengths of $8\,\mathrm{mm}$ and $50\,\mathrm{mm}$ modifying a circular beam to have an aspect ratio of $1:6.25$, effectively reducing the beam width to $53\,\mu\mathrm{m}$. This arrangement effectively couples the Raman scattered light to the spectrometer from the fiber.

Köhler illumination was used to provide white light illumination, allowing the sample plane to be viewed. A dichroic edge filter (Semrock, Di02-R561) was placed in the collection path such that the light was focussed on a complimentary metal-oxide-semiconductor (CMOS) detector (Imaging Source, DFK 42AUC03) for real-time imaging.

4.3.2 DHM instrumentation

A CW DPSS laser (Millennia Vs, Spectra Physics) with wavelength $532\,\mathrm{nm}$ was used for DHM illumination. The emitted laser light was coupled into a single mode fiber (P1-460B-FC-1, Thorlabs) with 40% efficiency. Misalignment of the coupling objective provided low power illumination at the sample plane ($30\,\mu\mathrm{W}$). Light was then coupled to a single mode optical fiber beam splitter (FC532-0B-FC, Thorlabs) with a coupling ratio of approximately 50:50 split of power between two output ports. Fiber collimators were used at the end of each port (F220FC-A, Thorlabs), which are designed to collimate light of $543\,\mathrm{nm}$ from a single mode fiber to give a beam diameter of $2\,\mathrm{mm}$. One arm was used to illuminate the sample and the other was used as a reference beam.

The illumination arm follows the same path as the white light illumination, from above the sample. A lens of focal length $f = 100\,\mathrm{mm}$ is placed $100\,\mathrm{mm}$ from the back aperture of a long working distance objective (M Plan APO, 10X, 0.23NA, Mitutoyo, UK), with $f = 200\,\mathrm{mm}$ and working distance, $WD = 0.35\,\mathrm{mm}$, to provide collimated light to the sample chamber. Light then passes through the sample and is collected

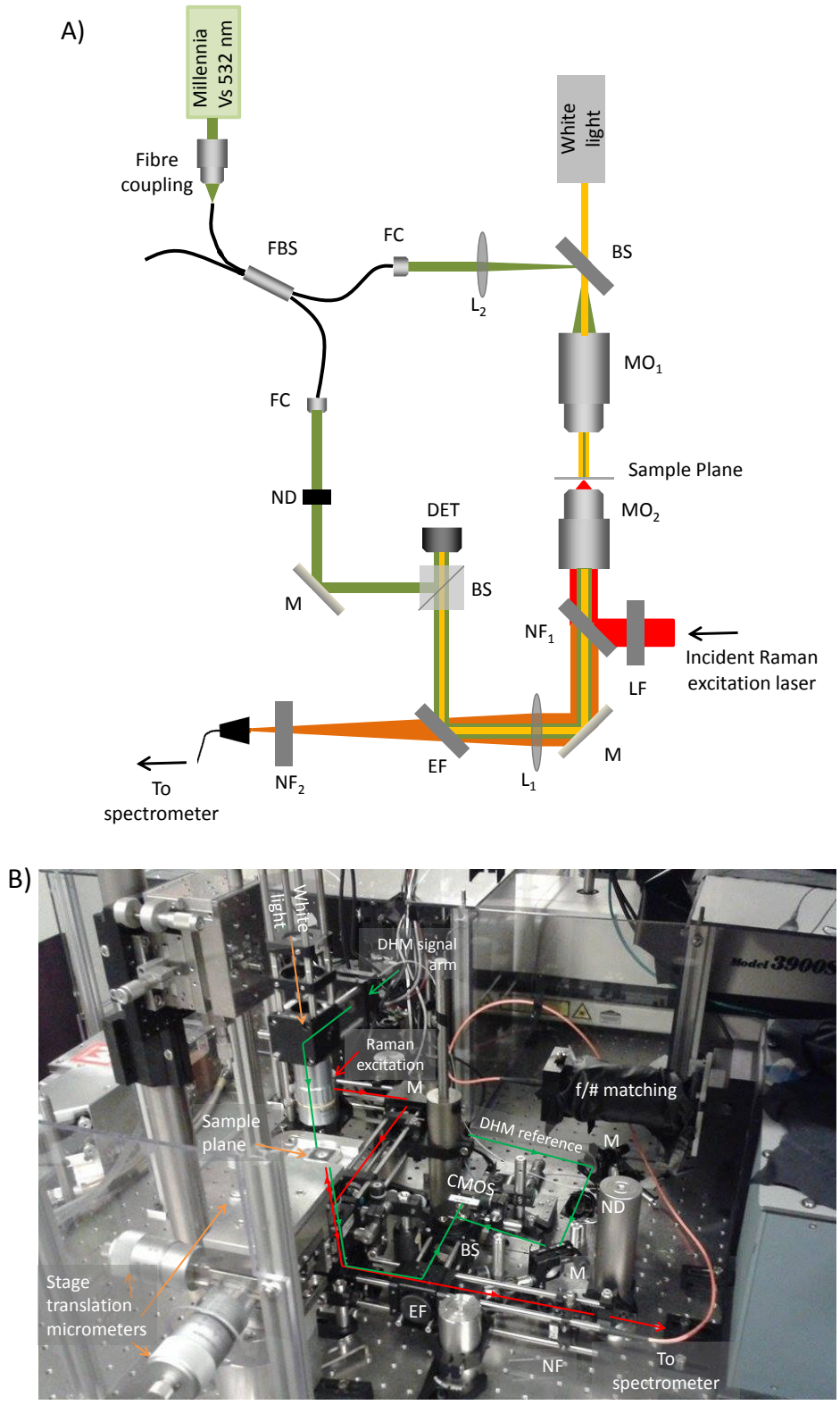

FIGURE 4.4: A) Schematic diagram of the multimodal system combining Raman spectroscopy and digital holographic microscopy (not to scale). M- mirror, L-lens (L_1: f=200 mm, L_2: f=100 mm) LF - line filter, EF- edge filter, NF- notch filter, MO_1- Mitutuyo M plane Apo objective (10X, NA=0.23), MO_2- Nikon objective (60X, NA=0.80), ND- neutral density filter, FC- fiber collimator, FBS- fiber beam splitter, BS- cube beam splitter, DET_1- CMOS camera. Millenia Vs provides 532 nm DHM illumination and a Ti:Sapphire laser provides 785 nm Raman excitation. See figure 2.8 for schematic of Raman excitation path and spectrometer. B) photograph illustrating the Raman path (red) and the DHM signal and reference arms (green).

by the 60X objective, sharing the same optical path as the Raman scattered light. The edge filter directing light to the CMOS camera, has high reflection ($> 99\%$) at $532\,\mathrm{nm}$ and high transmission ($> 93\%$) in the region $579 - 1200\,\mathrm{nm}$. This acts to separate the Raman photons from the DHM signal. The DHM signal is reflected towards the CMOS detector, whilst the Raman scattered light is transmitted towards the spectrograph.

The signal and reference arms are combined in a cube beam splitter (BS) at an angle (off-axis holography) (see figure 4.3 B) and the interference pattern was recorded on the CMOS detector. The tilt angle, α for the BS was determined by monitoring the Fourier transform of the interference pattern and maximising the spatial separation of the first and zero order components. The CMOS detector is made of 1024x960 8bit pixels, with an acquisition rate of 25 frames per seconds (fps). Importantly, the reference arm must have approximately the same optical path length as the signal arm. A neutral density (ND) filter was employed in the reference arm to compensate for differences in intensity between the reference and signal beams, as significant losses are experienced in the signal arm.

Considerations must be made for a double path interferometer, as it will be sensitive to environmental differences between the signal and reference arms, such as vibrations, air-flow, and temperature fluctuations. To minimise these effects the system was built on a floating table in a room with controlled temperature. A perspex box was designed to cover the system protecting it from dust and air currents.

4.4 Methods

4.4.1 Cell preparation

CD4+ T cells, B cells, and monocytes were isolated and purified using negative depletion isolation kits, to obtain freshly isolated cells in an untouched manner. Full details of this method are provided in appendix B. The purity of samples was analysed by FACS assay which is also detailed in Appendix B. The following purity levels were achieved from two donors; 89% and 91% for CD4+ T cells, 100% and 100% for B cells, and 96% and 99% for monocytes.

A sample chamber was formed using a thick quartz slide ($25.4\,\mathrm{mm}$ x $25.4\,\mathrm{mm}$ x $1\,\mathrm{mm}$ thickness), an $80\,\mu\mathrm{m}$ vinyl spacer, and a second thin quartz slide ($25.4\,\mathrm{mm}$ x $25.4\,\mathrm{mm}$ x $0.15\,\mathrm{mm}$ to $0.18\,\mathrm{mm}$ thick) on top. The cells were suspended in PBS and $18\,\mu\mathrm{l}$ was placed in the well. The sample chamber was inverted, allowing the cells to settle on thin quartz slide for around 30 mins, to prevent movement due to optical forces during measurements. The sample chamber was placed on the sample stage with the thin side towards the objective.

A total of 60 CD4+ T cells, 86 B cells, and 67 monocytes from a single donor were analysed by standard Raman spectroscopy and DHM. Sample numbers were limited according to the number of cells which could practically be isolated and analysed in a three day period. Previous studies (as detailed in chapter 3) indicate that there is no inter-donor variability amongst T cell populations CD4+ and CD8+, NK cells, and dendritic cell populations mDC and pDC. Data were collected on separate days, PCA was employed to ensure this did not introduce any variance contributions, thus confirming the robustness of the system. Cells were exposed to $785\,\mathrm{nm}$ irradiation at $150\,\mathrm{mW}$ power in the sample plane for 10 minutes and no changes were observed in the Raman spectra, indicating there was no photo-damage caused to the cells. The incident laser light at $532\,\mathrm{nm}$ has a power of approximately $30\,\mu\mathrm{W}$ in the sample plane. Additionally, the light is collimated before the sample plane ensuring a very low optical intensity is incident on the sample. No obvious damage was observed to the cells under white light imaging, and no changes were observed to the Raman spectra.

4.4.2 Raman and DHM measurements

Details of the instrumentation used are provided in section 4.3. $785\,\mathrm{nm}$ excitation wavelength was used for Raman spectroscopy with $150\,\mathrm{mW}$ power in the sample plane. Single point standard Raman spectra were taken with an acquisition time of $5\,\mathrm{s}$ per cell.

DHM images were taken using incident light of $532\,\mathrm{nm}$ and approximately $30\,\mu\mathrm{W}$ in the sample plane. Images were taken with an exposure time of $10\,\mathrm{ms}$. As the signal is sensitive to environmental conditions, the interference pattern intensity can fluctuate. To compensate for this several images were taken successively and the

image with the greatest contrast was used. There was no need to move the sample stage between Raman and DHM measurements enabling the two measurement modalities to occur simultaneously and independently.

4.4.3 Analysis of Raman spectra

A detailed description of the statistical analysis methods used is given in section 2.8. Specific details of this study will be outlined in this section. The Raman spectra were analysed in the region $900\,\mathrm{cm}^{-1}$ to $1700\,\mathrm{cm}^{-1}$ and normalised according to the total spectral intensity. A student's t-test was applied to highlight Raman bands of significant difference between pairwise mean spectra. The significance level was optimised for each set of data so as to best highlight the regions of difference. Cell lines that are most similar to each other required a larger significance level; the students t-test was calculated at a significance level of $p< 10^{-8}$ for CD4+ T cells and B cells (which are most closely related), $p< 10^{-13}$ for CD4+ T cells and monocytes, and $p< 10^{-18}$ for B cells and monocytes (which are chemically most different from each other).

The total data set from all the acquired Raman spectra was used to form a training data set on which PCA was conducted. Scatter plots were produced using the first 3 PCs to visualise any trends across the data set. The first 10 PCs were selected for quantitative analysis, where the discrimination ability was assessed by means of LOOCV. All correct and incorrect cell classification were summarised in a confusion matrix. Sensitivity and specificity values were calculated for pairwise comparisons of cell subsets.

As standard Raman data were collected (in contrast to WMRS) consideration must be given to fluorescence suppression. The data were analysed in the region of $900\,\mathrm{cm}^{-1}$ to $1700\,\mathrm{cm}^{-1}$ which naturally has a relatively flat baseline in the raw spectra, as illustrated in figure 4.5. Furthermore analysis in this spectral region would minimise Raman contributions due to quartz. According to database values most Raman bands associated with quartz occur in the region less than $600\,\mathrm{cm}^{-1}$, although a relatively weak peak is present at $804\,\mathrm{cm}^{-1}$. Not to forget that confocal Raman spectroscopy is employed, which offers the ability to effectively reject light

scattered from outside the sample plane. As the same quartz slides are used for every measurement any contribution from quartz is not expected to show in the lower order PCs used for discrimination. Nevertheless, to validate the data and analysis are robust to any background contributions, a third party background subtraction algorithm was applied [58]. The algorithm uses an asymmetric truncated quadratic cost function of polynomial order 6, which was applied to each spectrum after normalisation. Figure 4.5 demonstrates an example spectrum of each cell subset before and after background subtraction. The algorithm gave a good fit and resulted in a flat baseline for the processed spectra. The background subtracted data was then processed and resulted in comparable sensitivity and specificity values to data which did not undergo any background subtraction. As background subtraction algorithms can introduce artefacts the data presented in this chapter were analysed without any background subtraction or smoothing algorithms. The comparable discrimination abilities achieved from the two approaches infers that the raw data and method of analysis, without background subtraction, is robust.

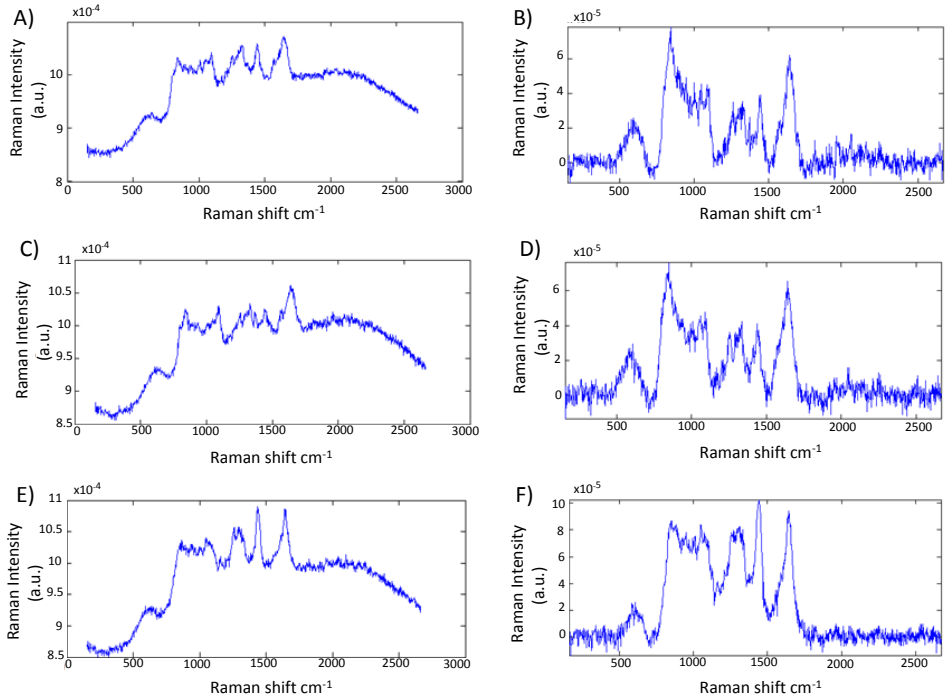

FIGURE 4.5: A comparison of the raw spectra (left hand side) and processed spectra after the background subtraction algorithm was applied (right hand side). Example spectra are shown for CD4+ T cells (A and B), B cells (C and D) and monocytes (E and F). The flat baseline in the processed spectra indicates that the algorithm provides a good fit. In the region $900\,\mathrm{cm}^{-1}$ to $1700\,\mathrm{cm}^{-1}$ the raw data has a relatively flat baseline.

4.4.4 Analysis of DHM images

The interference pattern generated by the signal and reference arm, containing both phase and amplitude information, was recorded on a CMOS camera. An off-axis configuration was used for spatial separation of the coherent terms in the Fourier transform. The offset angle, α (as illustrated in figure 4.3) contributes towards the carrier frequency, f_c [238]. Following equation 4.4 f_c can be described as

$$f_c = \frac{\sin(\alpha)}{\lambda} \tag{4.6}$$

This produces high frequency interference fringes; an example interferogram of a monocyte cell can be seen in figure 4.6.

In the Fourier transform the zero order diffraction term can be found in the centre and the coherent terms are separated on the diagonal. The spatial separation is related to f_c which in turn is related to the tilt angle in the cube beam splitter. The

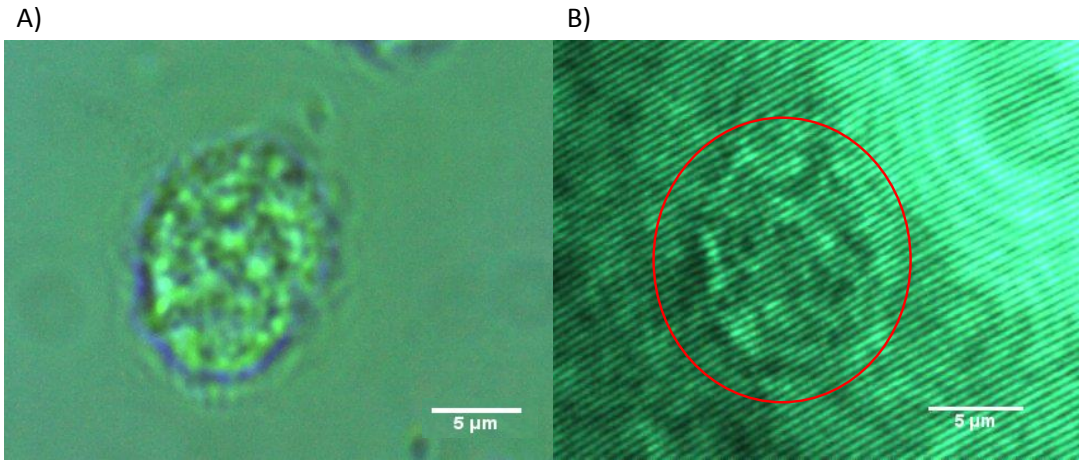

FIGURE 4.6: A) White light image and B) Interference pattern of a monocyte cell, as recorded by a CMOS camera. The cell introduces phase shifts and consequently perturbations to the fringe pattern can be observed (within red circle). Scale bar shows $5\,\mu\mathrm{m}$

first coherent term (+1 diffraction order) (as previously described in section 4.2.2) can be selected (figure 4.7 B), which is then centred on a blank matrix to remove the carrier frequency. The inverse Fourier transform retrieves the phase map with low frequency fringes (figure 4.7 D). Note that if any Raman light is picked up by the detector it would not interfere with the reference wave and would be filtered out at this stage. The zero order diffraction term contains intensity information and can also be separated. By taking the inverse Fourier transform an amplitude image can be produced (figure 4.7 C).

The phase map at this stage is wrapped, meaning the values are constrained to the $\pm\pi$ interval. Recovering the original phase values is a signal processing problem which has drawn attention since the 1970s [239] and continues to be important in many fields. There are a variety of techniques to perform phase unwrapping [240–242]. In the simplest case the algorithm searches for local inconsistencies which correspond to 2π discontinuities. These discontinuities can be removed either by adding 2π (when $\Delta\phi \leq -\pi$) or subtracting 2π (when $\Delta\phi > \pi$, where ϕ is the wrapped phase). The principle of phase unwrapping in 1 dimension is illustrated in figure 4.8, where the wrapped phase is processed to generate a smooth and continuous signal. For the process to accurately retrieve the absolute phase data, which may span many π, phase unwrapping algorithms rely on the assumption that the

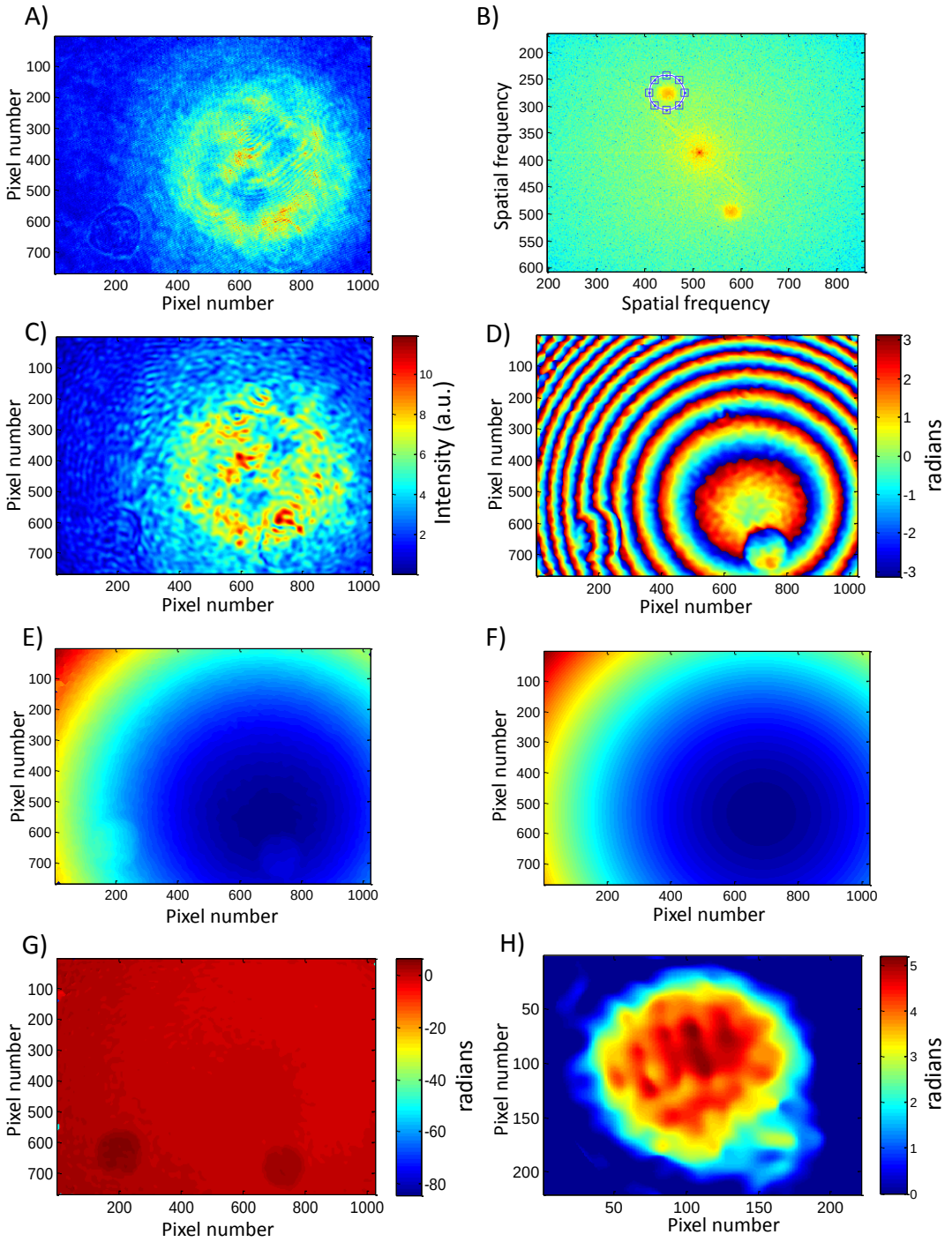

FIGURE 4.7: Illustration of steps to process a raw DHM image to produce a phase image. Axes represent pixels on the CMOS camera. A) shows the raw DHM image with interference fringes. B) is the Fourier transform with the zero diffraction order in the centre and ± 1 diffraction orders spatially separated on the horizontal. The +1 coherent term is selected as shown by ring of blue squares. C-D) represent the amplitude and phase components respectively after inverse Fourier transform of the zero and first order diffraction terms. E) is the unwrapped phase image and F) illustrates the quadratic fit, representing the differences in wavefront curvature between the object and reference waves. G) illustrates the resultant flat base-line unwrapped phase map after subtraction of the quadratic fit. Contrast is poor due to random errors around the edge. H) shows a cropped phase map of a monocyte cell where the colour bar represents phase in radians.

phase changes slowly enough that neighbouring points will be within one half cycle (π radians). For the case of immune cells, phase shifts are typically small enough that this assumption holds true. An unwrapping algorithm, as described by Ghiglia and Pritt [243] is applied to give a continuous phase map (in figure 4.7 E).

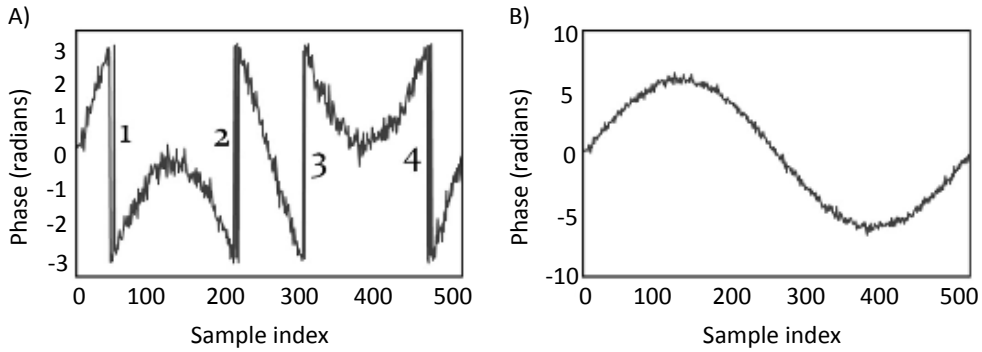

FIGURE 4.8: Taken from [244] with permission. A) illustrates four phase jumps (denoted 1-4) present in a wrapped 1-D signal. B) The unwrapped signal is a continuous sine wave.

The object and reference waves travel along different optical paths resulting in a difference in the curvature of the two wave-fronts. When they interfere the resulting phase map consequently has a quadratic background relative to the difference in wave-front curvatures. To remove this quadratic curvature a reference image, taken when no cell was present, may be subtracted. However, this technique is not always reliable as the two beams do not share a common path, therefore any vibrations or temperature fluctuations can cause variations. Alternatively, a quadratic fit may be calculated and subtracted. This can either be approximated by two 1 dimensional lines along x and y, or calculated in 2 dimensions. The calculation of two separate lines is much easier, however it is more sensitive to any object that may be on that line, which would introduce errors. A Matlab function 'polyfitn' was employed as it can generate a quadratic model in higher dimensions. A second order quadratic fit to the background can be seen in figure 4.7 F. Upon subtraction of the quadratic background a flat base-line phase image is produced (figure 4.7 G). The contrast is poor due to random values around the edge of the image. A 220x220 pixels region of interest (ROI) was cropped around the cell giving an unwrapped phase map of the cell.

One final consideration is to prevent the position of the cell from being a factor

for discrimination. For that reason the images were centred; a region around the cell was selected and the centroid of the image was calculated. The image was then shifted such that the centroid was in the centre of a 220 x 220 matrix. This selected region additionally acted as a mask where any values outside of this area were zeroed. This ensured that any neighbouring cells were removed from the image as well as reducing background noise. The result is a phase map of a single cell in the centre of a 220 x 220 matrix, as illustrated in figure 4.7 H for a monocyte cell. The Matlab code used to process the DHM images can be found in appendixE.

For discrimination analysis it was not possible to apply PCA directly to the phase map images as this would be computationally too intense. Two methods of characterising the images were thus employed for subsequent analysis.

1. The first method was to generate a histogram which records the number of pixels in specific intensity value regions. The phase value is directly proportional to the optical path difference (OPD) as described in equation 4.7. The histogram therefore contains information such as the maximum OPD, total OPD (phase volume), and size of the cell (number of non-zero pixels). By creating a histogram of each phase map each cell can be described by a new vector. PCA was conducted on this new data set and cells were classified according to LOOCV and the nearest neighbour algorithm.

$$\mathrm{OPD} = \frac{\Delta\psi \times \lambda}{2\pi} \tag{4.7}$$

   Where $\Delta\psi$ is the phase difference between the object and reference waves.

2. The second method is by texture analysis (TA). TA is a statistical method that quantifies parameters capable of describing properties of an image such as smoothness, contrast, or regularity. It is based on the relationship between neighbouring pixel intensities. TA is commonly used for analysis of OCT images of tissue samples [245, 246] but has not been widely explored for characterisation of DHM images. As a first step a grey level co-occurrence matrix (GLCM) is calculated; the image is first scaled to eight grey-levels and the frequency with which a pixel of grey scale intensity level *i* occurs adjacent to a

pixel of intensity j is recorded. This process is illustrated in figure 4.9. Several statistics can be derived from the GLCM which provide information about the texture of an image. The four texture parameters used are contrast, correlation, energy, and homogeneity. Contrast is a measure of the local variations in an image, correlation measures the frequency with which a pixel pair occurs across the image, energy is the sum of the squared elements in the GLCM, and homogeneity measures the amount of dominant grey-tone transitions in the image [247].

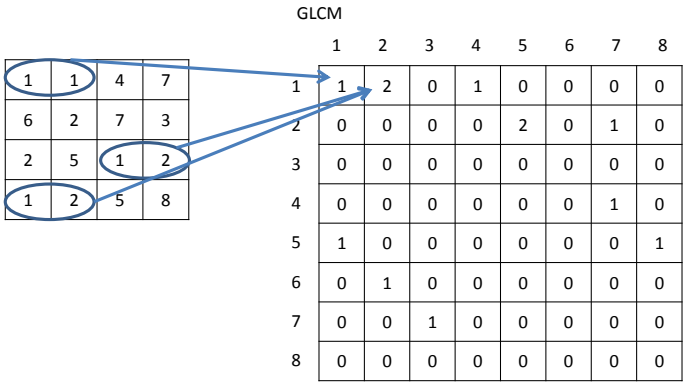

FIGURE 4.9: Representation of the process to produce a grey level co-occurrence matrix (GLCM). An intensity image is scaled to 8 grey level intensity values (left). Horizontal neighbouring pixel-pair values are recorded in an 8x8 GLCM (right).

By using TA each cell may be described by a new descriptor vector of 4 values. PCA was conducted on this new data set and cells were classified according to LOOCV and nearest neighbour algorithms.

The GLCM may be calculated along different directions. It was investigated if calculating the GLCM along four directions would provide more information and improve discrimination. 16 parameters were calculated from the four texture parameters along 4 directions: $0°$, $45°$, $90°$, $135°$. PCA and LOOCV were conducted on the new dataset, in which cells are described by a vector of 16 values.

3. Finally, the two vectors described above (histogram and TA parameters) were combined to form a new descriptor vector, containing both OPD and TA information. Discrimination ability was calculated according to PCA and LOOCV statistics.

The Matlab code used for post-processing of the phase map images is provided in appendixE.

4.5 Classification of CD4+ T cells, B cells, and Monocytes

4.5.1 Classification of cell subsets with the use standard Raman spectroscopy

Standard Raman spectra were recorded for CD4+ T cells, B cells, and monocytes on the multimodal system. The mean spectra from the three cell populations are shown in a pairwise manner in figure 4.10 A-C. The student's t-test was used to highlight regions of significant difference between two cell populations thus characterising the key molecular differences between them. The Raman bands identified as having significant variation are represented by grey vertical bars. The Raman bands between CD4+ T cells and B cells may be attributed to: CH_2 deformation in lipids ($1455\,\mathrm{cm}^{-1}$), adenine/guanine ($1585\,\mathrm{cm}^{-1}$), and amide I ($1665\,\mathrm{cm}^{-1}$); between CD4+ T cells and monocytes: protein α helix and protein C-C skeletal modes ($938\,\mathrm{cm}^{-1}$), skeletal C-C stretch in lipids ($1129\,\mathrm{cm}^{-1}$), and CH_2 stretching, adenine and guanine ($1421\,\mathrm{cm}^{-1}$). B cells and monocytes have the most differences with additional bands arising from amide III ($1259\,\mathrm{cm}^{-1}$), and adenine/amide III ($1304\,\mathrm{cm}^{-1}$) [165–167]. These band assignments are consistent with those found in WMRS analysis which are summarised in Appendix C, and with a recent study by Hoboro et al [164] which characterises a complete profile of Raman band assignments for T and B cell lines.

PCA analysis was conducted on the complete data set, the first three PCs are represented spectrally in figure 4.10 D, as an indication of what the discrimination is based on. Scatter plots were generated using the first 3 PCs (figure 4.10 E-F). Distinct clusters were formed for the three cell populations indicating there are distinct Raman signatures for the three populations and they may be successfully identified. Consider plot E where the PC space is defined by PC1 and PC2, the cluster corresponding to monocytes is most distinct whilst there is some overlap between B cells and T cells. This indicates that the molecular differences between monocytes and T- or B-cells contribute most to the total variance of the data set. It is only when PC3 is employed (plot F) that CD4+ T cell and B cell clusters become well separated.

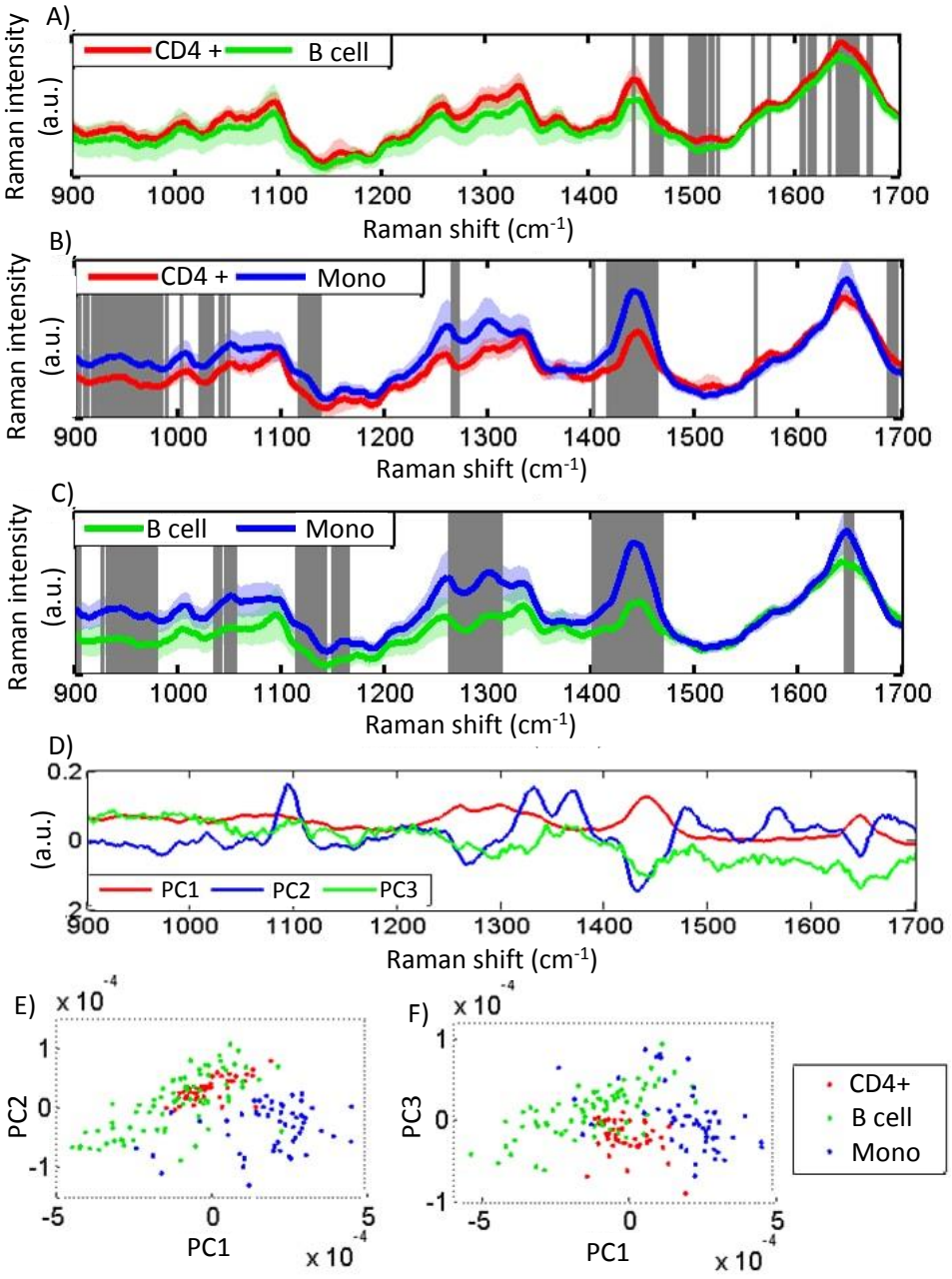

FIGURE 4.10: Standard Raman spectroscopy to classify CD4+ T cells, B cells, and monocytes using the multimodal system. A-C) illustrate pairwise comparisons between cell populations where solid lines represent the mean Raman spectrum for each cell subset and shadowed regions represent one standard deviation. Grey vertical bars highlight Raman bands of significant difference, as calculated by the student's t-test at a significance level of A) $p < 10^{-8}$, B) $p < 10^{-13}$, and C) $p < 10^{-18}$. D) illustrates the loadings for the first 3 PCs from the total data set of all three cell subsets. E-F) show scatter plots using the first 3 PCs. Distinct clusters for each cell type demonstrates the ability to successfully discriminate between populations.

The Raman bands that contribute to PC3 are around $1455\,\mathrm{cm}^{-1}$ and $1665\,\mathrm{cm}^{-1}$, as

observed in plot D. These bands correspond well with those highlighted by the student's t test between CD4+ T cells and B cells (plot A). Additionally, the cluster corresponding to B cells is noticeably broader which indicates there may by variation within the cell type. This correlates well with observations from section 3.5 and 3.6 and may be due to B cell subsets such as naïve or memory B cells.

The first 10 PCs were used for analysis with LOOCV, which accounts for 94.4% of the total variance. All correct and incorrect classifications are summarised in a confusion matrix (table 4.2) and pairwise sensitivities and specificities were calculated (summarised in table 4.4). Sensitivity and specificity values of 86.8% and 98.6% respectively were achieved for CD4+ T cells and B cells, 97.9% and 98.1% respectively for CD4+ T cells and monocytes, and finally 98.6% and 98.1% respectively for B cells and monocytes.

	Predicted CD4+	Predicted B cell	Predicted Monocyte
Actual CD4+	46	1	1
Actual B cell	7	69	1
Actual Monocyte	1	1	51

TABLE 4.2: Confusion matrix summarising the discrimination ability of Raman spectroscopy for the classification of cell subsets CD4+ T cells, B cells, and monocytes. Values on the diagonal represent those correctly identified and off-diagonal values represent those incorrectly identified. CD4+ T cells and B cells are most closely related and can be more difficult to discriminate, this is indicated by the increased number of incorrect classifications.

It was observed that the B cell and T cell populations are more closely related to each other than to monocytes. This is implied in the fewer regions of significant difference highlighted by the student's t-test, the observation of some confusion in the scatter plots, and in the lower sensitivity value achieved between B- and T-cell populations. The highest discrimination efficiency was achieved between monocytes and T- or B-cells, as monocytes generated the most distinct Raman signature (as indicated by the PC contributions). This is as expected as T cells and B cells originate from a common lymphoid progenitor lineage, whereas monocytes originate from a common myeloid progenitor lineage, as detailed in section 3.1.

4.5.2 Classification of cell subsets with the use of DHM

Phase maps were generated for each cell from the recorded interference pattern, following the procedure detailed in section 4.4.4. An example phase map for each cell type can be seen in figure 4.11 alongside its respective white light image. The white light images illustrate that monocytes are quite distinct and are much larger in size than T- or B-cells. T cells and B cells however pose a particular challenge as they are very similar in terms of morphology. This is often the limiting factor for identification by techniques such as flow cytometry, which relies on differences in size and shape to generate different scattering profiles.

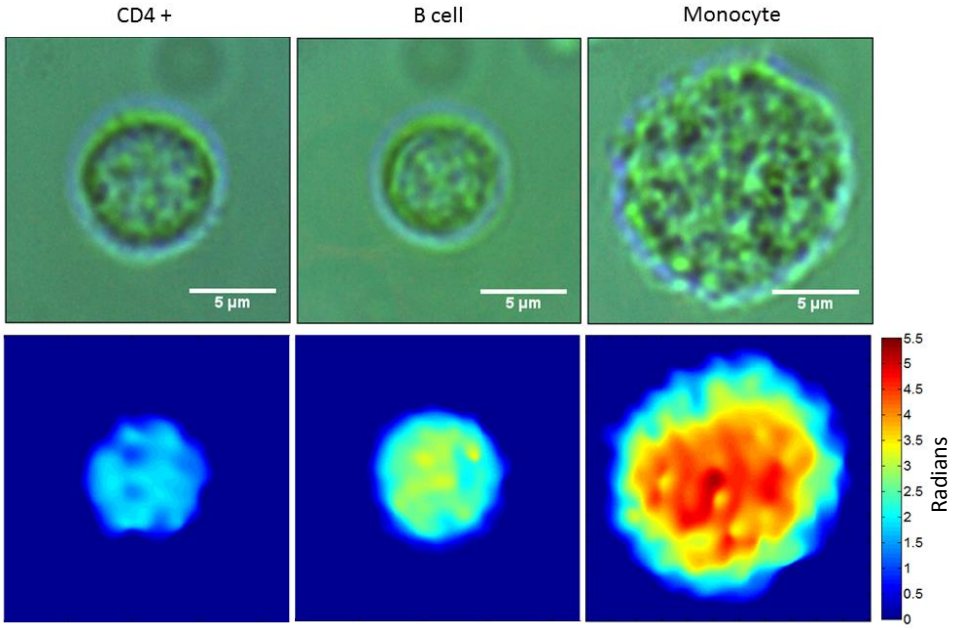

FIGURE 4.11: Top row represents a typical white light image for each of CD4+ T cell, B cell, and monocyte cell types. The scale bar denotes $5\,\mu\mathrm{m}$. The bottom row shows the respective phase map for each cell. The intensity shows the phase difference between the object and reference waves, which is directly proportional to optical path difference. Colour bar represents phase differences in units of radians.

The phase maps provide a measure of the OPD between the reference and object waves (equation 4.7) and can therefore be considered a map of the optical thickness across the cell. Optical thickness is related to both the absolute thickness of the cell and its intracellular structure. The intracellular structure inherently causes variations in the refractive index through the cell. Optical path length (OPL) can therefore be calculated as the integral of the absolute thickness, s and refractive index, n variations along a path, p, as shown in equation 4.8.

$$OPL = \int_p n(s)ds \tag{4.8}$$

To separate sample thickness from refractive index is non-trivial and would require a more sophisticated set-up, such as dual wavelength illumination [248, 249], scanning of the illumination angle [250, 251], or the introduction of phase shifts [252]. For the studies presented here measurement of the optical path length is sufficient and knowledge of the absolute cell thickness was not necessary.

For subsequent analysis the phase maps were described either in terms of a histogram of the pixel intensity values or by four texture parameters. First, a histogram was generated for each phase map, representing the number of pixels within specific intensity value ranges. A typical histogram for each of the three cell populations is shown in figure 4.12. Information may be extracted directly from these histograms regarding the cell size (the total number of non-zero pixels is equivalent to the 2 dimensional area), maximum OPD (largest pixel intensity value), and the phase volume (total of all pixel values). With each cell represented by a histogram vector a training data set was formed on which PCA was conducted. It should be noted that PCA may also be able to recognize patterns such as how evenly spread the values are, which is indicative of the uniformity across the phase map.

Scatter plots were produced using the first 3 PCs and can be seen in figure 4.13 A-C. PC1 shows an excellent ability to identify monocytes, which are morphologically quite different from T- and B-cells. Monocytes are typically larger in size and thicker, resulting in a larger total OPD and a higher maximum OPD value. This is consistent with the observations from both white light images (figure 4.11) and the histogram plots (figure 4.12). Higher order PCs are required to recognise more subtle morphological differences. It is PC3 that has the ability discriminate between the morphologically similar T cells and B cells, as observed in figure 4.13 B-C.

LOOCV statistics were applied to the full data set to quantify the discrimination ability of using histograms to represent the DHM images. Excellent sensitivity and specificity values were obtained and are summarised in table 4.4. Sensitivity and specificity values of 86.8% and 98.6% respectively were achieved for CD4+ T cells

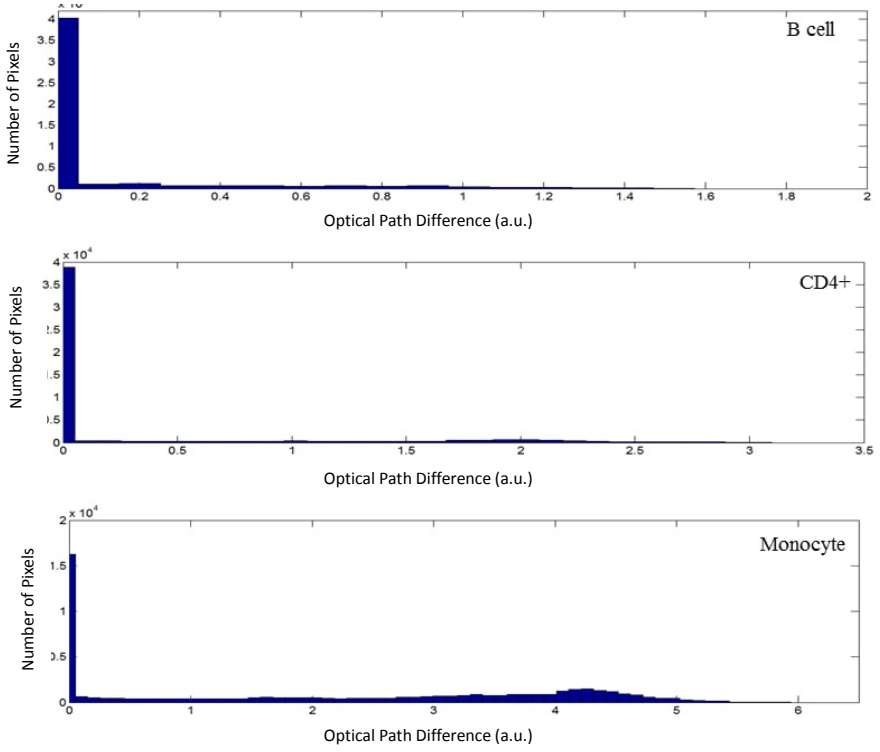

FIGURE 4.12: A typical histogram generated from the phase map of a B cell, CD4+ T cell, and monocyte (top to bottom). The range of pixel intensity values are recorded, which are related to the optical path lengths across a cell.

and B cells, 98.7% and 100% respectively for CD4+ T cells and monocytes, and finally 100% and 100% respectively for B cells and monocytes. The morphological similarity of T- and B-cells is reflected in the lower sensitivity and specificity values obtained in contrast to comparisons with the morphologically distinct monocytes, where sensitivity and specificity values of up to 100% are achieved.

The observed phase difference between B- and T-cells may be related to differences in their intracellular composition. Previous studies have investigated morphological differences between B and T lymphocytes finding variations in the amount of cytoplasm, stippled chromatin, and nuclear morphology; such as nuclear size, homogeneity, nuclear folds, thickness of nuclear membrane, and presence or uniformity of nucleoli [253, 254]. The most distinctive features reported by Parker et al were in the nuclear morphology, where B cells frequently have a characteristically round and regular nucleus with thick nuclear membrane, in contrast to T cells which typically have a nucleus with deep folds and an irregular configuration, stippled chromatin, and small or absent nucleoli. Additionally B cells often have an

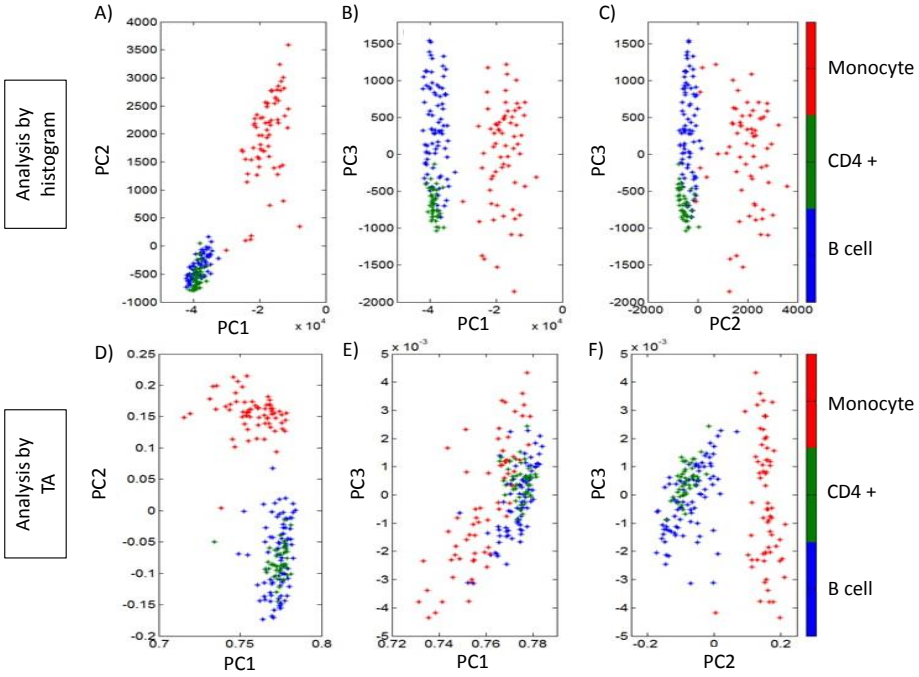

FIGURE 4.13: Scatter plots using the first three PCs for discrimination between CD4+ T cells, B cells, and monocytes. The top row (A-C) illustrates the discrimination ability when analysing DHM phase maps by means of a histogram descriptor vector. The bottom row (D-F) illustrates the discrimination ability when analysing DHM phase maps by means of four texture parameters. When employing the histogram vector method compared to TA, clusters appear to be more distinct and show less overlap between T- and B-cell populations.

abundant cytoplasm in comparison to T cells [253].

A second method of analysis was investigated, employing TA to characterise the phase maps. The four texture parameters calculated were contrast, correlation, energy, and homogeneity. The average values, and respective standard deviations, for each of these parameters for each cell type are recorded in table 4.3. Contrast and energy appear to be the most useful parameters, showing the most variation, particularly between monocytes and B cells or CD4+ T cells.

A vector made up of these 4 parameter values was generated for each phase map and PCA was conducted on the new training data set. Scatter plots were generated using the first 3 PCs (figure 4.13 D-F). Observing the PC loadings revealed that contrast was the most significant parameter and contributed most to PC1, and that energy contributed most to PC2. It can be observed in figure 4.13 D and F that PC2 (relating to energy) plays an important role in discriminating monocytes from B cells or T cells. The clusters correlating to B- or T-cells however show significant

		Contrast	Correlation	Energy	Homogeneity
CD4+	average	0.0388	0.9971	0.6718	0.9853
	std. dev.	0.0091	0.0006	0.0294	0.0012
B cell	average	0.0382	0.9961	0.6619	0.9828
	std. dev.	0.0082	0.0015	0.0637	0.0032
Monocyte	average	0.0803	0.9963	0.4121	0.9692
	std. dev.	0.0161	0.0008	0.0347	0.0043

TABLE 4.3: Average texture parameters for each cell subset. The most useful parameters for discrimination appear to be contrast and energy.

overlap and would be very difficult to successfully discriminate between.

PCA and LOOCV was applied to the whole data set and pairwise sensitivity and specificity values were calculated, which are summarised in table 4.4. Sensitivity and specificity values of 78% and 62.2% respectively were achieved for CD4+ T cells and B cells, 98.5% and 97% respectively for CD4+ T cells and monocytes, and finally 100% and 100% respectively for B cells and monocytes. The lower values achieved between CD4+ T cells and B cells is expected as they are morphologically quite similar to each other and their respective clusters in PC space were not well defined. In this sense analysis by TA does not show as strong a discrimination ability as when the phase maps were characterised by histograms.

	Raman Spectroscopy		**DHM Histogram**		**DHM Texture analysis**	
	sens %	**spec %**	**sens %**	**spec %**	**sens %**	**spec %**
CD4+ v B cell	86.8	98.6	93.8	85.4	78.0	62.2
CD4+ v Monocytes	97.9	98.1	98.7	100	98.5	97.0
B cell v Monocytes	98.6	98.1	100	100	100	100
Average	**94.4**	**98.3**	**97.5**	**95.1**	**92.2**	**86.4**

TABLE 4.4: Summary of sensitivity and specificity values achieved for each method of analysis. Raman spectroscopy and DHM are each capable of efficiently discriminating between cell subsets. Phase maps were either described in terms of a pixel intensity histogram or by four texture parameters; the use of histograms proved to be more efficient than using texture analysis.

TA was further investigated by calculating the four texture parameters along four directions ($0°$, $45°$, $90°$, $135°$), producing a vector of 16 values for each phase

map. However this did not show any improvement in the discrimination ability. TA along different directions is commonly employed for analysing tissue samples where directional features may be expected. However this is not an expected characteristic when analysing whole cells, particularly as they are at random orientations on the quartz slide.

Finally the two vectors (histogram and TA) were concatenated to generate a new descriptor that contained both OPD and TA information. PCA and LOOCV were applied to this data set and did not show any significant improvement in comparison to analysis by the histogram vector alone. It can be concluded that a histogram of the pixel intensity values is the most efficient method of characterising a phase map for discrimination between the three cell subsets.

4.5.3 Combining Raman spectroscopy and DHM for discrimination of cell subsets

DHM and Raman spectroscopy each provide information not available from the other modality. Combining the two signatures could provide a more complete description of the cell and may improve the discrimination efficiency. It is therefore of interest to combine the two data sets for analysis.

Multivariate analysis is commonly utilised with Raman spectra, however DHM images are typically used for visual analysis. In previous studies combining DHM and Raman spectroscopy the chemical information from Raman mapping is related to the phase information from DHM to aid interpretation of cellular composition and dynamics. Multivariate analysis however is only conducted on Raman spectra [200, 201]. In the study presented in this chapter DHM images are described using a histogram of their pixel values, which makes multivariate analysis based on DHM possible. To combine the Raman and DHM information a method was employed in which the two vectors were concatenated to provide a new multimodal descriptor vector for each cell. This provided a new training data set, where each cell was described by both its Raman signature and phase information. PCA was conducted on the new dataset and LOOCV was employed to determine the discrimination efficiency.

Although the multimodal analysis was successful at identifying each cell subset, it did not show any significant improvement when compared to treating the two modalities independently. Sensitivity and specificity values of 81.3% and 88.3% respectively were achieved for CD4+ T cells and B cells, 100% and 100% respectively for CD4+ T cells and monocytes, and finally 98.6% and 100% respectively for B cells and monocytes. Interestingly the discrimination ability between monocytes and B- or T-cells was slightly improved in comparison to Raman spectroscopy alone, but was less successful at discriminating between the more closely related B and T cells, when compared to Raman spectroscopy alone. Therefore combining the two data sets does not appear to offer any advantage as it does not always provide an improvement to the discrimination ability.

This result was surprising as it was expected that a more complete description of the sample should improve the discrimination ability. It would be worth further investigating the optimum way in which to combine the two data sets, for example Ashok et al have employed multivariate analysis on OCT images and Raman spectra by first calculating the first five PCs of each modality individually and then combining the PCs from the two datasets for multimodal classification [192]. This method may offer the advantage of ensuring the most valuable contributions from each modality are accounted for. It is possible that by combining the two datasets before PCA that the more subtle morphological differences between B- and T-cells, for example, contain less variation than noise in the Raman spectra, and would therefore be contained in higher order PCs and rejected as a component to contribute towards classification. This may explain why discrimination efficiency was improved between monocytes and B- or T-cells, as the morphological variations were significant between these cell subsets, and are therefore more likely to be contained in higher order PCs of the combined dataset.

4.6 Conclusions

The use of a multimodal system provided a means to independently and simultaneously acquire a Raman signature and quantitative phase information from key

immune cell subsets CD4+ T cells, B cells, and monocytes. Each method was successful at discriminating between all three cell types. Of particular interest is the discrimination between T- and B-cells which are morphologically very similar but perform distinct functions in the immune system.

T and B lymphocytes are generally considered morphologically indistinguishable due to their similar shape and size. They would normally be discriminated by flow cytometry where forward scatter (FSC) and side scatter (SSC) is not generally sufficient for discrimination. Typically cell surface markers such as CD3 and CD4 are used to identify T cells, and CD19 and CD20 are used to identify B cells. This problem is represented in figure 4.14, where human blood has been analysed by flow cytometry [255]. The first panel shows FSC v SSC which produces one population containing both B- and T-cells. They are seen separately only after CD3 and CD19 staining, as illustrated in the second panel. The additional information provided by holographic phase microscopy, such as information relating to the intracellular structure as well as morphological shape, was sufficient to discriminate between B and T cell subsets in a label-free manner and represents a significant advance in this respect.

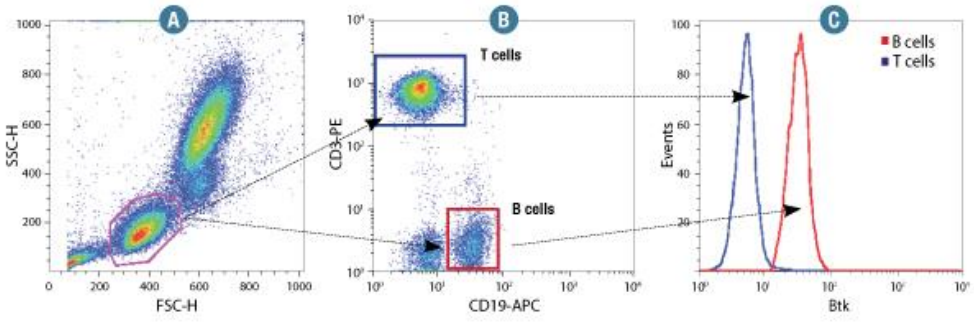

FIGURE 4.14: A) Flow cytometry based on FSC and SSC produces a single population (in purple circle) containing both B cells and T cells, which are morphologically very similar. B) They can only by separated after staining for cell surface markers CD3 and CD19 for T and B cells respectively. Image taken from [255].

Phase maps were generated from the DHM interference pattern and were analysed via two methods, that is to say either by generating a pixel intensity histogram or by texture analysis. The most effective method for discrimination was found to be via the generation of a histogram, in which discrimination was achieved based on variations in cell size and phase volume, which in turn is related to the cell thickness

and intracellular structure. Although TA was successful at discriminating monocytes from CD4+ T cells and B cells, it was not very effective at discriminating between the two lymphocyte cell subsets T and B cells.

The laser selected for DHM irradiance has a long coherence length. This has the benefit of simple alignment and analysis but gives relatively low spatial coherence as it is more susceptible to parasitic interference [256]. For the discrimination purposes presented here this simple set-up was sufficient, however it is worth noting that white light illumination [233, 257] or diode lasers [258] have a shorter coherence length and can provide higher spatial resolution, which may be of interest for further applications.

Standard Raman spectroscopy was able to successfully discriminate between the three cell subsets based on their molecular composition. The main Raman bands contributing to discrimination were related to the DNA profile, lipid, and protein content of the cell. One of the main challenges facing the implementation of Raman spectroscopy in a clinical or research setting is the long acquisition times required ($5\,\mathrm{s}$ per cell), which was the main motivation for combining Raman spectroscopy with a faster modality (DHM interference images were acquired in $10\,\mathrm{ms}$).

The combination of Raman spectroscopy and DHM did not provide an improved discrimination efficiency in terms of sensitivity and specificity but has four main benefits which are summarised below:

1. The two modalities validate one other, yielding a more robust analysis
2. Potential to simultaneously acquire both chemical and morphological information regarding a sample
3. Analysis is completely label-free
4. DHM boasts a fast acquisition time and may be able to provide a fast initial screening, allowing Raman spectroscopy to focus on cells of interest for a more specific molecular analysis.

The final point is of significant interest for future applications with the potential to provide high throughput rates. This would be a significant advance towards a label-free technology for the identification of immune cell subsets.

Relevant Publications

- **N. McReynolds**, F. G. M. Cooke, M. Chen, S. J. Powis, K. Dholakia, "Multimodal discrimination of immune cells using a combination of Raman spectroscopy and digital holographic microscopy", (2017) Sci. Rep. 7(11) p.43631

Contributions

I integrated a DHM around a Raman system and optimised for multimodal measurements, with advice from M.C. I wrote the Matlab code to analyse the DHM images. M.C. and M.M. wrote the PCA code which I modified specific to this study. I collected and analysed the data. F.G.M.C. and S.J.P. isolated the cell subsets and performed flow cytometric characterisation.

5 Monitoring dopamine levels in SH-SY5Y cells in a label-free manner

5.1 Introduction

In previous chapters Raman spectroscopy and DHM were used for label-free classification of immune cell subsets. To demonstrate a broader applicability of label-free methods, and as part of my PhD training, it was decided to expand into the neuroscience area. This section will introduce a key challenge with respect to modelling Parkinson's disease (PD), which may benefit from a label-free method to identify dopaminergic neurons.

PD is the second most prevalent neurodegenerative disease in the world after Alzheimer's, with a predicted prevalence of 9 million people by 2030 [259, 260]. The most recognisable symptoms of PD are movement related, such as resting tremor, slow movement, and rigidity.

The basal ganglia are a group of structures found in the brain whose function is most commonly associated with movement. The substantia nigra par compacta is a nucleus (collection of neurons) rich in dopaminergic neurons which supplies other compartments of the basal ganglia with dopamine, and which is critical for smooth movements. Patients with PD characteristically have low levels of dopamine in the basal ganglia, caused by death of dopaminergic neurons, including those from the substantia nigra par compacta. Consequently this leads to motor control problems [261–263].

PD is most commonly seen in adults over the age of 50. With an ageing population there is a real impact on the economy, society, and the friends and carers of the elderly. Understanding and managing PD is therefore an increasingly important and challenging aspect of medical practice. The exact pathogenetic mechanisms underlying the selective dopaminergic cell loss in PD are still not fully understood [259], however the interest of the scientific community in PD has grown substantially.

5.1.1 Raman spectroscopy for the detection of dopaminergic neurons

Dopaminergic neurons are commonly used to model PD *in vitro*. One of the main challenges surrounding the research is the difficulty of obtaining pure primary cultures of dopaminergic neurons, that is to say those directly from the brain of a model organism such as a PD model mouse. Currently to identify dopaminergic neurons in primary culture it is necessary to fix and stain the cultures with antibodies to dopaminergic biomarkers, which kills the cells [264]. A label-free technology to identify dopaminergic cells would be a significant advance. Furthermore, working with a mixed population leads to ambiguity over any extracted proteins, DNA, or RNA, where it is unclear if they are from dopaminergic cells or other cells present in the culture. The label-free nature of Raman spectroscopy, compatibility with biological samples, and its high chemical specificity makes it an ideal candidate. The first goal of this study is to assess the ability of Raman spectroscopy to provide a means to establish pure cultures of dopaminergic cells in a label-free manner.

5.1.2 Quantitative analysis

Current methods to measure cellular production of dopamine involve taking a sample of the culture media for analysis of dopamine levels. For example Chiu et al, in delineating the calcium ion (Ca^{2+}) dependency of dopamine release, recorded the extracellular concentration of dopamine via cyclic voltammetry [265]. Korecka et al, in characterising retinoic acid (RA) differentiated SH-SY5Y cells, determined the dopamine uptake of cells by liquid scintillation counting, after first lysing the cells in NaOH [266]. For drug analysis dopamine release may also be measured by oxidising dopamine to produce hydrogen peroxide (H_2O_2). H_2O_2 levels may then be measured in the culture media by chemiluminescence [267] or by use of an oxygen electrode [268]. Not only are these techniques invasive but it is always the extracellular dopamine concentration that is measured. This does not provide information on what is happening within the cells themselves. The ideal method would involve a label-free analysis of intracellular dopamine levels in living cells.

Raman spectroscopy can provide a quantitative analysis as peak intensities are directly related to the concentration of the scattering medium. The second goal of

this study is therefore to assess the ability of Raman spectroscopy to provide a quantitative method of intracellular dopamine detection. There are currently no technologies to do this and this would therefore be a significant advance.

There are two main applications for quantitative analysis of dopamine levels within cells; to monitor dopamine production in cells that make it and to measure the ability of cells to uptake dopamine. In order to reduce symptoms of PD a method to either increase dopamine synthesis or increase the uptake of the available dopamine in the striatum is required. To achieve this requires a method of analysing dopamine levels in living striatal neurons.

The most common treatment for PD is to enhance the production of dopamine in the basal ganglia. Dopamine itself cannot pass through the protective blood-brain barrier however Levodopa (L-DOPA), which is a precursor to dopamine neurotransmitters, can. L-DOPA is administered to promote synthesis of dopamine in the basal ganglia which can improve motor control and alleviate symptoms. There is some contention surrounding the effectiveness of L-DOPA, where the neuroprotection versus neurotoxicity of the treatment remains unclear. An improved cell model for dopamine regulation and drug screening *in vitro*, or dopaminergic cell implantation therapy *in vivo* is crucial to resolving the many unanswered questions regarding the diagnosis and management of PD [261, 269, 270].

5.1.3 SH-SY5Y cells

SH-SY5Y cells are human neuroblastoma cells which are commonly used for *in-vitro* models of neurodegenerative diseases [271, 272]. SH-SY5Y cells express dopaminergic markers such as tyrosine hydroxylase (TH) and dopamine-β-hydroxylase [273, 274] and consequently are commonly used for the study of PD [273, 275].

Various methods to differentiate human neuroblastomas have been reported [276, 277] including protocols to successfully differentiate the SH-SY5Y cell line to viable human neuronal cultures for modelling human disease [278, 279]. Different methods can select for specific neuron subtypes such as dopaminergic neurons [266, 275, 280]. One such method is that retinoic acid (RA) induces the expression of TH, which indicates a dopaminergic neurotransmitter phenotype [281]. TH is the rate-limiting

enzyme of catecholamine synthesis, from which dopamine is one of the produced neurotransmitters [282].

In this chapter SH-SY5Y cells will be grown to three differentiation states: undifferentiated, RA differentiated, and fully differentiated (with cells remaining in the cell cycle eliminated). The relative dopamine production of each differentiation state will be assessed by immunocytochemistry of TH. As a first step, the detection limit for Raman spectroscopy to detect dopamine will be found, and compared to physiologically relevant concentrations. Further to this the ability to discriminate between the three differentiation states by Raman spectroscopy will be assessed.

5.2 Methods

5.2.1 Cell culture and differentiation

Passaging cells is a method used to transfer some cells from a previous culture to fresh growth medium. Cell cultures were maintained in tissue culture grade flasks and had the culture media (supplemented with 10% fetal calf serum (FCS)) changed twice per week. The protocol to passage cells is provided in appendix F. Cells were not used after passage 20.

Before plating, cells were trypsonised and a $10\,\mu\mathrm{l}$ aliquot was used to count the number of cells/ml in the suspension (full details provided in appendixF). This was then diluted to give approximately 1×10^5 cells per ml. $2\,\mathrm{ml}$ was plated into 6-well cell culture plates for subsequent growth and differentiation.

SH-SY5Y cells were grown to provide three differentiation populations for analysis; undifferentiated, RA differentiated, and fully differentiated. A detailed protocol for establishing these cultures is provided in appendix G. Undifferentiated cells were plated and grown in 10% FCS and were ready (at about 70% confluence) after 48 hours. RA differentiated cells were established after a further 5 days incubation in a 1% FCS medium with $10\,\mu\mathrm{M}$ RA. Cells were cultured for a further 7 days in a 1% FCS medium with $80\,\mu\mathrm{M}$ 5-fdu, a mitotic inhibitor (MI), to achieve a fully differentiated population. RA encourages dopaminergic neuronal growth and the MI acts to prevent the division of any cells that did not differentiate. The FCS concentration was reduced while cells were differentiating as they grow slower. By reducing the

serum concentration from 10% to 1% the SH-SY5Y cells began to develop longer projections (neurites) characteristic of a neuronal cell. A time-line of the differentiation procedure is illustrated in figure 5.1. When cells were grown for analysis by western blot or immunocytochemistry, phenol red was added to the medium as colour changes can be indicative of any infections (cloudy) or low nutrition (orange). However when cells were grown for analysis by Raman spectroscopy phenol red was not used in order to minimise the fluorescence background.

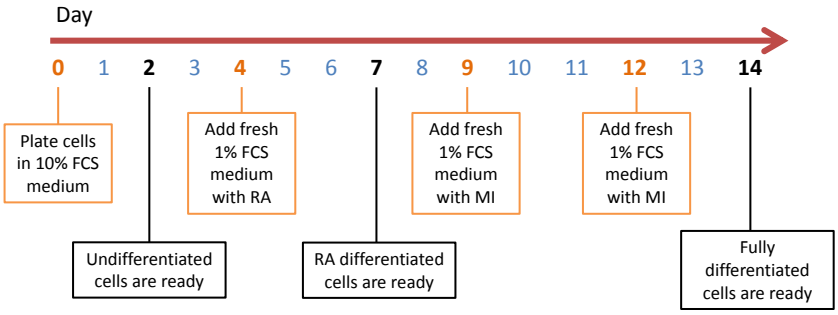

FIGURE 5.1: Time-line of the differentiation procedure. Cells were plated on day 0 in 10% FCS growth medium establishing a culture of undifferentiated cells after 48 hours. RA and serum deprivation is used to encourage differentiation of neuronal SH-SY5Y cells over 5 days. In the final week a mitotic inhibitor is used to establish a culture of fully differentiated SH-SY5Y cells. (FCS- fetal calf serum, RA- retinoic acid, MI- mitotic inhibitor.)

Figure 5.2 illustrates the typical morphological appearance of undifferentiated and fully differentiated SH-SY5Y cells. White light images were taken using a 50X magnification MO. The undifferentiated cells are characteristically rounder with few projections, while differentiated cells have many elongated neuritic projections.

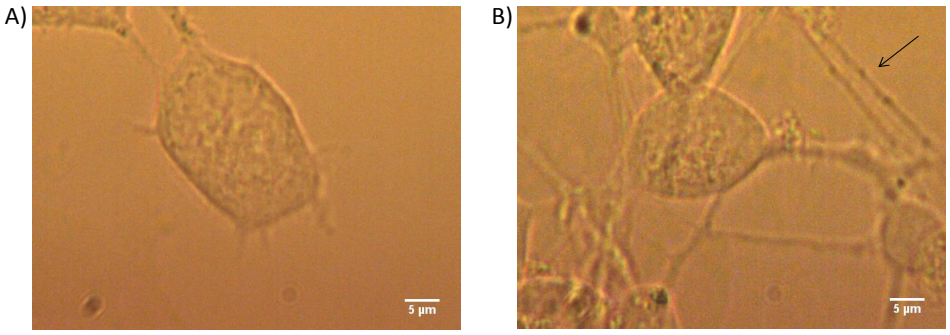

FIGURE 5.2: White light images of A) undifferentiated and B) differentiated SH-SY5Y neuronal cells illustrating typical morphological differences. Undifferentiated cells are typically more rounded with few projections and differentiated cells have extensive and long projections (highlight by arrow). Scale bars show $5\,\mu\mathrm{m}$

5.2.2 Immunocytochemistry

Immunocytochemistry (ICC) is a technique commonly used to assess the presence of a specific protein or antigen in cells. A specific antibody binds to an antigen enabling it to be visualised and examined under a microscope. In this study ICC was used to visualise the expression of TH, a dopamine precursor in cultures of SH-SY5Y cells at the three stages of differentiation: undifferentiated, RA differentiated, and fully differentiated.

Immunolabelling can be achieved either by direct or indirect methods. Direct methods would involve the use of an antibody that is directly conjugated to a fluorescent tag. An indirect method involves the use of a primary and secondary antibody; in this case the primary antibody is antigen-specific and the secondary antibody is conjugated to a tag and specifically binds to the primary antibody. It can be impractical to tag every antigen-specific antibody meaning indirect methods can offer more flexibility, and as a result are more commonly used. Furthermore the indirect method has shown to be more sensitive [283] and may provide better signal amplification, as more tags can attach per antigen [284].

As a first step, the optimum primary antibody concentration was determined and then ICC was used to assess the proportion of labelled cells in each of the three differentiation states from three different cell cultures. A detailed description of the ICC protocol is provided in appendix H, a brief description will also be provided here.

To determine the optimum primary antibody concentration 5 different concentrations were used on undifferentiated cells for a quick comparison. Cells were grown on 6 coverslips in a 24 well plate for 2 days to achieve the undifferentiated population (two slides from each of three different cultures). Cells were fixed in formalin and washed with PBS. Horse serum block (HSB) was added to block any non-specific binding, and consequently reduce the background. The primary antibody TH was added in horse serum block (HSB) in five different concentrations: 1:100, 1:250, 1:500, 1:1000, 1:2000, and a negative control with no primary antibody. This was left at 4° overnight. The secondary antibody (1:200 in HSB), conjugated with fluorescein isothiocyanate (FITC), was added the following day. DAPI, a fluorescent

stain which binds strongly to A-T regions of DNA, was also used to visualise the nuclei of cells. This acts as a control by indicating the presence of cells. The coverslips were then mounted on a microscope slide with antifade mountant. Images were acquired on a Zeiss microscope (Zeiss Imager, M2) with a 63X oil objective and CCD camera (AxioCam ICC 1). An acquisition time of $1200\,\mathrm{ms}$ was used for the green (FITC) channel and $1200\,\mathrm{ms}$ for the blue (DAPI) channel. Images were acquired and overlayed using ZenPro 2012 software.

Once the optimum primary antibody concentration was determined a full ICC analysis was performed, allowing each of the three cell cultures to grow to the three differentiation stages. Extra care must be given when transferring coverslips of differentiated cells, as they tend to form one layer which can easily slip off the coverslip if perturbed. Once the slides were prepared they were wrapped in tinfoil and stored in the freezer until all samples were ready for imaging.

5.2.3 Western Blot

Western blotting, first developed in 1979 [285], is now a routine technique used for protein analysis. In western blotting gel electrophoresis is used to separate proteins along a gel, which are then transferred (blotted) onto a second matrix, often a nitrocellulose membrane. Antibodies specific to a target protein are added in a similar fashion to ICC. Again, the indirect method involving a two step primary and secondary antibody is most commonly used [286, 287]. ICC and western blot are often used as complimentary techniques as ICC provides spatial information and the electrophoresis step of the western blot can resolve any cross-reactivity of antibodies.

Before a full western blot can be conducted there were two preparation steps: the optimal concentration for TH antibody was first determined by dot blotting, and the amount of protein from each sample was calculated by Bradford assay to aid equal loading.

Dot blotting is a simplified version of a western blot, as proteins are not first separated by electrophoresis. The whole mixture is instead applied directly to the membrane as a dot. A detailed procedure for western blot and dot blotting is provided in appendix I. Briefly, for the dot blot optimisation step, SH-SY5Y cells were grown to

an undifferentiated state. Proteins were extracted and denatured by placing in boiling water. Nitrocellulose membrane was cut into small squares (to fit in a 24 well plate) and $2.5\,\mu$l of the protein sample was placed in the centre of the paper. Milk was used to block non-specific binding and the primary TH antibody was added in five different concentrations: 1:500, 1:1000, 1:2000, 1:5000, and 1:10000 (diluted in the milk blocking solution). The secondary antibody, horseradish peroxidase (HRP), was added at a concentration of 1:10000 in TBS-T (a mixture of tris-buffered saline and Tween 20). The papers were transferred to a plastic sleeve and a chemiluminescent substrate reagent mix was used (Invitrogen) for chemiluminescence detection of HRP. ChemiDoc-It^2 was used as a dark environment for imaging with a cooled CCD camera. Images were acquired using 'Vision works' software.

For the western blot, SH-SY5Y cells were cultured in twelve wells; each of three SH-SY5Y cultures were grown to three differentiation stages with one spare well each. Protein lysates were collected from each sample, at each stage of differentiation, and stored in the freezer until all samples were ready for analysis. An aliquot of the extracted protein was used to conduct a Bradford assay. This was used to determine the protein concentration of each sample and hence calculate the appropriate loading volume, to ensure equal loadings ($30\,\mu$g) were used for the western blot.

The Bradford assay is based on the absorbance shift of the dye 'Brilliant Blue G' which turns from brown to blue in the presence of proteins. Standards of bovine serum albumin (BSA) were used with the following concentrations: 0.01, 0.1, 1, 10 and 100 μg/μl. A trendline was formed and the equation of which was used to determine the protein concentration of the samples from their respective absorbances. The full method is detailed in appendix I. Briefly, $10\,\mu$l of the extracted protein and $10\,\mu$l 1M sodium hydroxide (NaOH) were added to $500\,\mu$l Bradford reagent (Brilliant Blue G dye) in a 96 well plate. NaOH acts to solubilise membrane proteins. The protein-dye complex causes a shift in the absorption maximum of the dye from 465 to $595\,\mathrm{nm}$. The amount of absorption is proportional to the protein concentration. Absorbance was read with Biokit BP 800 at $590\,\mathrm{nm}$ and results were exported to Excel. Measurements were made for the five standards and for three differentiation states of the three separate cultures of SH-SY5Y cells.

Finally, Western blotting (full method detailed in appendix I) was conducted using the appropriate loading volumes (as calculated by Bradford's assay) and the optimised primary antibody concentration (as determined by the dot blot). A standard ladder was used for comparison against the 9 sample channels.

5.2.4 WMRS procedure

Dopamine hydrochloride (Sigma Aldrich) was dissolved in water to give a range of molarities for analysis by Raman spectroscopy to determine the lower limit of detection. A well was formed between two quartz slides (SPi Supplies) and a vinyl spacer of $80\,\mu\mathrm{m}$ thickness. $20\,\mu\mathrm{l}$ of the dopamine solution was placed in the well for analysis by Raman spectroscopy.

The Raman spectrometer is as described previously, in section 2.7, providing $150\,\mathrm{mW}$ power to the sample plane. WMRS measurements were taken with the wavelength tuned over a total range of $\Delta\lambda = 1\,\mathrm{nm}$. Five spectra were acquired at five equidistant wavelengths within this range with each single spectrum acquired for $5\,\mathrm{s}$, giving a total acquisition time of $25\,\mathrm{s}$ for a WMRS differential spectrum. The method of processing WMRS data is detailed in section 2.5 and 2.8.

5.3 TH expression in various stages of SH-SY5Y differentiation

5.3.1 Immunocytochemistry of SH-SY5Y differentiation states

To optimise the TH primary antibody concentration for ICC, five different concentrations were used with undifferentiated cells. Figure 5.3 shows the resulting fluorescence images. The optimum concentration was found to be 1 in 500. The strongest signal can be observed from a concentration of 1 in 200, however this would be a waste of valuable antibody.

ICC was then performed on the three differentiation stages of SH-SY5Y cells to determine the proportion of TH labelled cells in each, using a primary antibody concentration of 1 in 500. Figure 5.4 illustrates a typical image from each of the three differentiation states. It can be observed that FITC staining is strongest for fully

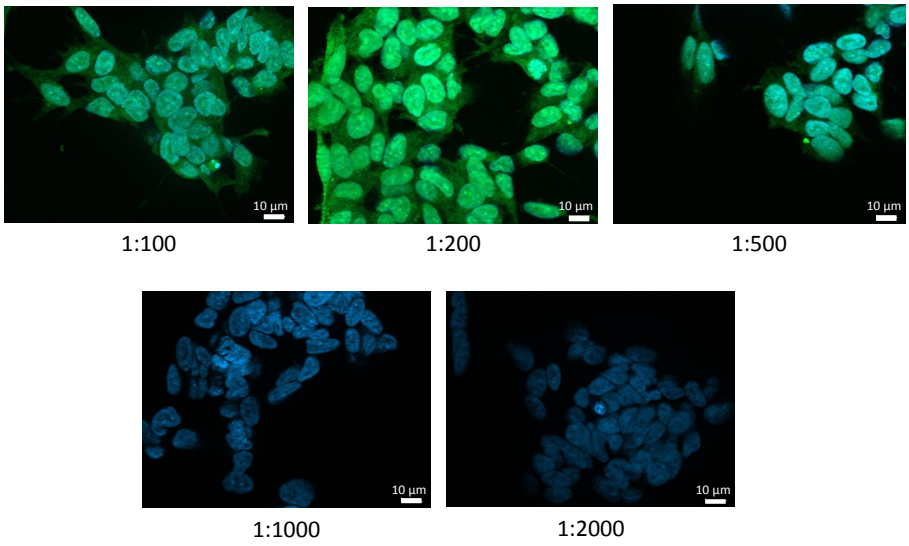

FIGURE 5.3: TH antibody optimisation on undifferentiated cells for ICC. Concentration of TH in HSB is given below their respective images. Green signal represents FITC stainingand blue signal is from nuclear staining with DAPI. The optimum concentration was found to be 1:500. Scale bar shows $10\,\mu$m.

differentiated cells and weakest for undifferentiated cells. This indicates that cells successfully differentiate into dopaminergic neuronal cells. TH staining is mostly observed in the membrane and along processes. These would therefore be ideal locations from which to collect Raman spectra for the detection of dopamine.

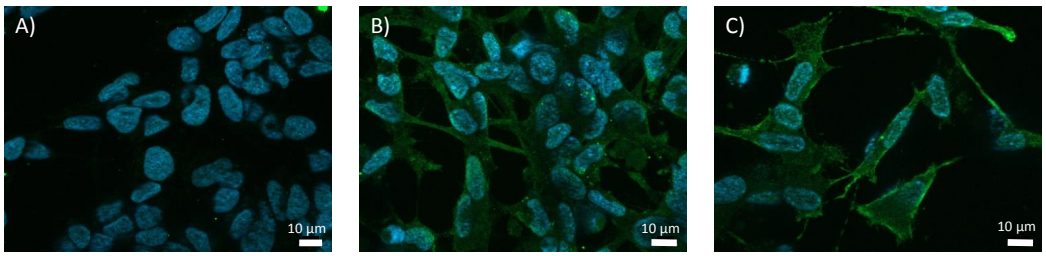

FIGURE 5.4: TH antibody staining of A) undifferentiated, B) RA differentiated, and C) fully differentiated SH-SY5Y cells. Green signal represents FITC stainingand blue signal is from nuclear staining with DAPI. Signal was brightest for fully differentiated population and weakest for undifferentiated cells. TH appears to be concentrated in the membrane and along processes. Scale bar shows $10\,\mu$m.

5.3.2 Western blot

A dot blot was used to determine the optimum primary antibody concentration. Figure 5.5 shows the resulting dot blot images. The brightest response was achieved

from a primary antibody concentration of 1 in 2000, which was then used for subsequent western blotting. It was observed that higher concentrations gave a very weak response which can sometimes happen if the antibody concentration is too high, causing it to use up all the substrate before being detected [288].

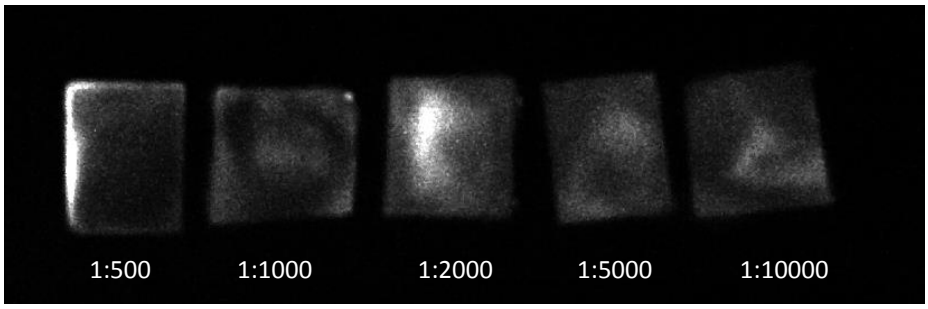

FIGURE 5.5: Dot blot for TH antibody concentration optimisation in preparation for western blotting. Five concentrations are applied to proteins extracted from undifferentiated SH-SY5Y cells. 1 in 2000 gave the optimum response.

The Bradford assay was used to determine the protein concentration in each sample. The BSA standards produced a trendline with R^2 value 0.969 and could therefore be used to calculate the protein concentration of each sample. Table 5.1 shows the volume required to ensure $30\,\mu$g protein and the total volume in 5X buffer. A buffer is required to ensure running of the proteins during gel electrophoresis and equal loadings are important so as not to bias the intensity readings. The total volume that can be loaded into the channels is $24\,\mu$l. The spare samples were grown to a fully differentiated population but appear to be of lower concentration, ie require greater volumes, therefore the spares were not used for the western blot.

Unfortunately the western blot was not successful, and did not provide a clear protein ladder for the 9 samples. Many problems can arise during a western blot that may result in no bands showing, which could be related to the antibody, antigen, sample degradation, washing steps, temperature fluctuations, or contamination of the buffer used [287].

5.4 Quantitative detection of dopamine concentration by WMRS

Dopamine hydrochloride was analysed by WMRS at various concentrations. Figure 5.6 illustrates the mean WMRS spectra acquired for a range of concentrations.

Sample	Volume for $30\,\mu$g protein μl	Total volume with 5X buffer /μl
Undifferentiated		
1	12.7	15.2
2	12.2	14.7
3	9.2	11.1
RA differentiated		
1	15.7	18.9
2	14.0	16.8
3	12.4	14.8
Fully differentiated		
1	16.7	20.1
2	20.3	24.3
3	17.1	20.6

TABLE 5.1: Protein concentrations from each sample as determined by a Bradford assay. The middle column represents the volume of each sample containing $30\,\mu$g of protein and the final column shows the total loading volume when mixed with 5X buffer.

The main peaks observed may be assigned as follows: C-H out of plane bending ($600\,\mathrm{cm}^{-1}$), asymmetric C-C-C bending ($718\,\mathrm{cm}^{-1}$), C-H(2,6) out of plane bending ($756\,\mathrm{cm}^{-1}$), C-H(2,5,6) out of plane bending ($793\,\mathrm{cm}^{-1}$), C-C-H bending ($953\,\mathrm{cm}^{-1}$), C-C skeletal stretch ($1030\,\mathrm{cm}^{-1}$), stretching of hydrogen bonding C-OH groups ($1160\,\mathrm{cm}^{-1}$), N-H deformation and C-C stretch ($1292\,\mathrm{cm}^{-1}$), C-O stretching, C-H deformation and N-H deformation ($1357\,\mathrm{cm}^{-1}$), and C=C stretching from aromatic rings (1448 and $1613\,\mathrm{cm}^{-1}$) [289, 290]. These peaks correspond with the chemical structure of dopamine (illustrated in the inset of figure 5.6).

The intensity of the main Raman band at $793\,\mathrm{cm}^{-1}$ was measured, as the peak to peak intensity, from 5 WMRS spectra for each concentration. The average intensity value was plotted against dopamine concentration, where error bars represent two standard deviations, as shown in figure 5.7. An R^2 value of 0.9934 confirms a linear relationship, indicating that WMRS may be used to quantitatively measure dopamine concentration.

Regarding the limit of detection, noise levels were measured as the peak to peak intensity from various spectral regions in the absence of a WMRS peak. The average noise value was used to calculate the SNR when compared to the $793\,\mathrm{cm}^{-1}$ peak intensity. The lowest concentration that was measured was $7\,\mathrm{mM}$ which had a SNR of 6:1. However, physical concentrations of dopamine in the body are extremely

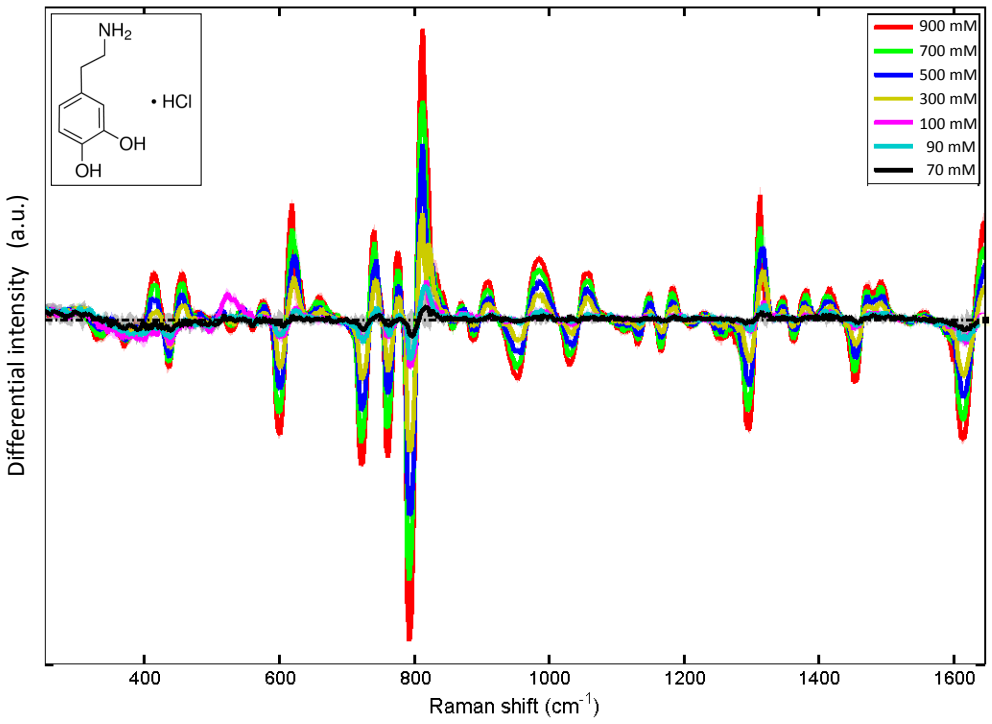

FIGURE 5.6: WMRS measurements for various concentrations of dopamine hydrochloride. Mean WMRS spectra are shown by solid bands and shadowed regions represent standard deviation. Zero crossing points correspond to Raman peaks. Inset shows chemical structure of dopamine hydrochloride.

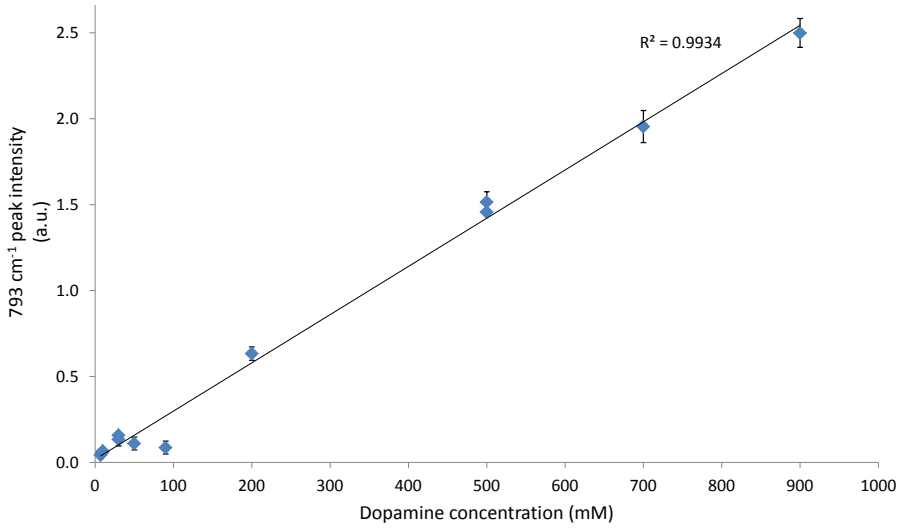

FIGURE 5.7: Relationship between WMRS intensity for the main Raman peak at $793\,\mathrm{cm}^{-1}$. Error bars indicate two standard deviations. An R^2 value of 0.9934 was achieved indicating a linear relationship between peak intensity and dopamine concentration. WMRS may therefore provide a quantitative analysis of dopamine concentration. Lowest measurements were made at a concentration of $7\,\mathrm{mM}$.

low; ranging between 0.01 - $1\,\mu\mathrm{M}$ in the extracellular fluid for a healthy person, and in the nanomolar range for patients with PD [291, 292].

A method to enhance the Raman signal, such as SERS (see section 2.6), could be employed to increase the signal from dopamine and improve the detection sensitivity. An et al have previously demonstrated the detection of dopamine by SERS spectroscopy, in which dopamine was immobilised on a self-assembled gold nanoparticle (AuNP) substrate. They also reported antigen-dopamine captured by an antibody-assembled gold surface for SERS detections, reporting a detection limit as low as $1\,\mathrm{nM}$ [293]. Furthermore, Huefner et al have employed AuNPs as intracellular probes in SH-SY5Y cells [294]. Cellular uptake of AuNPs was achieved by incubating the cells with citrate capped AuNPs at a concentration of 200,000 NPs per cell. The uptake rate was dependent on incubation time and NP size. As intracellular uptake occured via endocytosis the intracellular NPs were localised in endocytotic vesicles such as endosomes and lysosomes. The NPs were thus used as probes to visualise and track their movements. Functionalised NPs have previously been used to target intracellular molecules [295, 296], however a prerequisite to intracellular targeting is to ensure that the NPs can escape the endocytotic vesicles. Considerable efforts are being made to escape or bypass the endosomes; a review of various passive and active approaches can be found in [296]. An interesting future study would be to investigate the use dopamine-targeted AuNPs for intracellular SERS detection of dopamine levels.

5.5 Discrimination between SH-SY5Y differentiation states

A further important challenge is the identification of closely related cell types in a label-free manner. It is instructive to explore the ability of Raman spectroscopy to successfully discriminate between the three differentiation states; undifferentiated, RA differentiated and fully differentiated, based solely on a Raman signature, which is the aim of this section. This would find applications in assessing the purity of a culture, sorting cells in different differentiation states, or to separate neuronal from non-neuronal cells.

5.5.1 Substrate for cell growth and Raman spectroscopy

For ICC analysis SH-SY5Y cells were directly grown and differentiated on a microscope cover slip in a 24 well plate. However glass is typically not used for Raman measurements due to its high fluorescence background. The first challenge was to determine a suitable substrate to grow and differentiate SH-SY5Y cells that would not interfere with the Raman signal.

Cells were initially grown on quartz slides which have low fluorescence properties. However, it was observed that quartz is non-permissive, i.e. SH-SY5Y cells were not able to put out processes. Figure 5.8 A-D show example white light microscopy images of the cells, which have a rounded appearance and no projections.

Caponi et al investigated the Raman spectra of SH-SY5Y cells grown on silicon and metallic substrates, in comparison to cells adhering on organic polyaniline, particularly with respect to the adhesion of SH-SY5Y cells on various substrates, and their respective effects on the biochemical properties, or viability, of cells. It was reported that organic polyaniline not only allowed cell growth but also did not appear to affect the Raman spectra obtained [297]. Various other extracellular matrices have been reported for the growth and differentiation of neuronal cells; such as polylysine [298], polyornithine [299, 300], laminin [301–303], and cell attachment matrix [304]. Polylysine and polyornithine are commonly used to encourage cell adhesion. Cell attachment matrix or laminin permit a more rapid adhesion, which can provide a more even distribution of neurons over the whole area, as aggregation may occur when adhesion is slow [305]. These four coatings were applied to quartz slides to investigate their effect on cell growth and Raman spectra.

The following steps describe the procedure for the four quartz coatings:

1. **Polylysine**: Coat quartz with polylysine overnight, remove polylysine and add PBS immediately, ensuring it does not dry.

2. **Polyornithine**: Coat quartz with polyornithine for 4 hours (or overnight), remove polyornithine and wash three times in dH_2O. Leave it to dry

3. **Cell attachment matrix**: Complete step 2 as above followed by adding a coat of cell attachment matrix. Leave for 1 hour (up to overnight) then wash in PBS.

Finally leave in PBS and ensure it does not dry.

4. **Laminin**: Complete step 2 as above followed by adding a coat of laminin. Leave for 1 hour (up to overnight) then wash in PBS. Finally leave in PBS and ensure it does not dry.

The coated quartz slides were covered with PBS and Raman spectra were acquired from slightly above the quartz surface as an initial measure of the background fluorescence. Each generated a large fluorescence signal although the fourth coating (polyornithine with laminin) gave the smallest background signal and was therefore chosen to be used for subsequent SH-SY5Y cell growth. Practically it was very difficult to work with these slides, as water tension made it difficult to remove the thin quartz slide from the culture dish without disturbing the cells. This was particularly problematic for differentiated cell populations, as they tend to form a film, which can easily fall away when disturbed.

A final option was to use FluoroDishes (World Precision Instruments) which are cell culture dishes with a flat optical-quality glass bottom ($0.17\,\mathrm{mm}$ thick), ideal for a reduced fluorescence background. It was found that the cells grow and differentiate easily in these culture dishes, and although there is some fluorescence background from the glass, overall it was a much more practical solution. Figure 5.8 E-H illustrate SH-SY5Y cells grown in fluorodishes which show short processes and a flatter morphology.

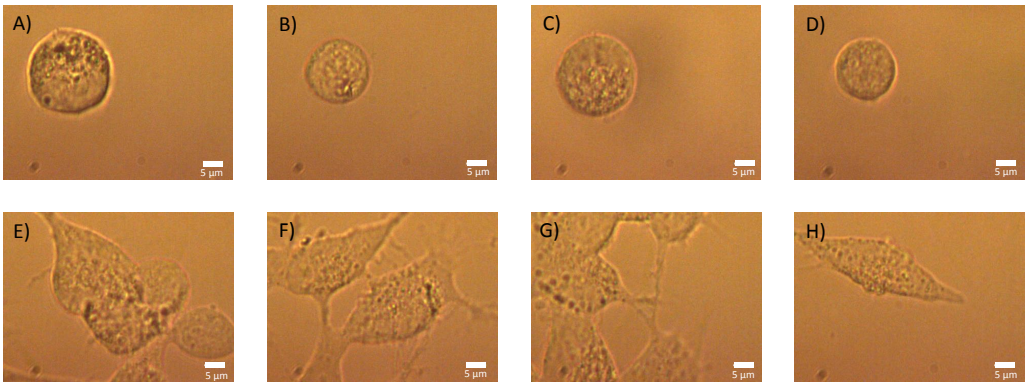

FIGURE 5.8: White light images of SH-SY5Y cells grown on A-D) quartz or E-H) FluoroDishes. Quartz is non permissive, preventing the cells from putting out processes. Cells grown in FluoroDishes have a flatter appearance and short processes, as expected for neuronal cells. Scale bar shows $5\,\mu\mathrm{m}$

5.5.2 WMRS measurements

Three different batches of SH-SY5Y cells were each grown in four FluoroDishes, to achieve the three differentiation stages (and one spare). WMRS was performed on cells from each dish to determine the ability of Raman spectroscopy to discriminate between the three differentiation states. In an effort to reduce the background fluorescence cells were grown in a serum free medium (replaced with SR2 supplement) and without any phenol red indicator dye. The growth medium was replaced with PBS during Raman measurements.

5.5.3 Characterisation of SH-SY5Y differentiation states by WMRS

WMRS spectra were obtained from approximately 80 cells from each of the three differentiation states. Raman spectra were analysed in the region of $600-1800\,\mathrm{cm}^{-1}$. The mean WMRS spectrum for each differentiation state can be seen in figure 5.9. A point of concern is that the baseline of the WMRS spectra is not zeroed, which is an artefact of the high fluorescence background. Although WMRS is a useful tool for suppressing background fluorescence, it is not completely effective in the presence of a strong fluorescence background. In this case the Raman bands no longer correspond to the zero crossing points and the presence of fluorescence may affect the discrimination ability. The data was thus further analysed in two different manners: by reducing the spectral range for analysis and by employing a third party background subtraction algorithm.

As a first step spectral analysis was confined to the region of $1000-1800\,\mathrm{cm}^{-1}$, which contains the major Raman peaks whilst having a relatively flat baseline. Data were then further analysed by PCA and LOOCV. The first three PCs were used to form scatter plots as seen in figure 5.10 B-E. The first 10 PCs were used to estimate the discrimination efficiency and pairwise sensitivities and specificities were calculated, as summarised in table 5.2.

This method of analysis is still quite limited; by reducing the spectral range there is an accompanying loss of Raman information, which may make discrimination more challenging. Additionally, the baseline is still not centred about the zero line,

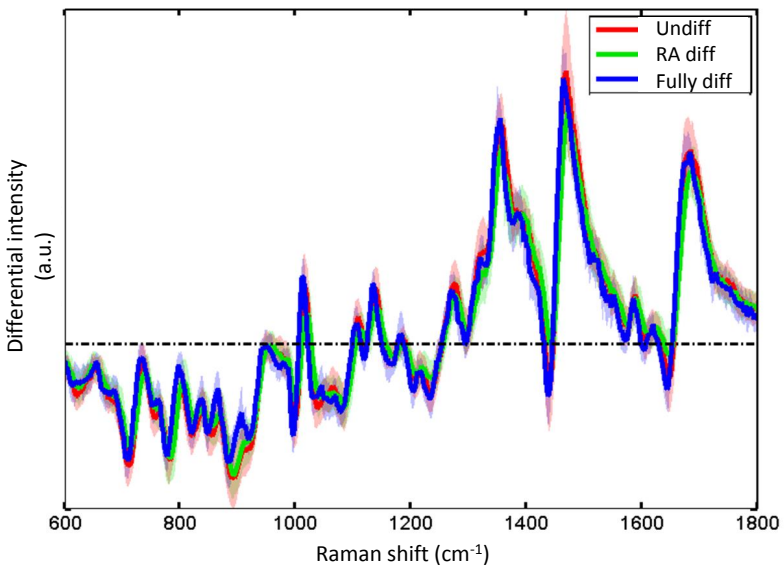

FIGURE 5.9: WMRS spectra for three differentiation states of SH-SY5Y cells; undifferentiated, RA differentiated and fully differentiated. The solid line represents the mean spectrum and shadowed regions represent the standard deviation. The differential spectra are not centred about the zero line which can be attributed to the high fluorescence background.

making Raman band assignments challenging. A better method of analysis may be to utilise a third party background subtraction algorithm.

A background subtraction algorithm [58] (discussed previously in section 4.4.3) was applied to each spectrum after normalisation. An asymmetric truncated quadratic polynomial of order 7 gave a good fit to the fluorescence background. That is to say upon subtraction of the polynomial fit the Raman spectra had a flat baseline (see figure 5.11 A-B). The background corrected spectra were then used to produce a zero-centred WMRS differential spectrum. Figure 5.11 C illustrates the mean background corrected WMRS spectra for each differentiation state. Subsequent treatment by PCA and LOOCV gave a quantitative estimation of the discrimination ability. PC scatter plots were produced using the first 3 PCs (figure 5.11 D-G). It was observed that RA differentiated and undifferentiated cells formed well separated clusters, indicating they may be successfully identified. Interestingly, it was more challenging to discriminate between the fully differentiated and undifferentiated cell populations. Sensitivities and specificities were calculated and are summarised in table 5.2.

Regardless of the method of analysis RA differentiated cells formed the most distinct cluster and some overlap was observed between the clusters representing

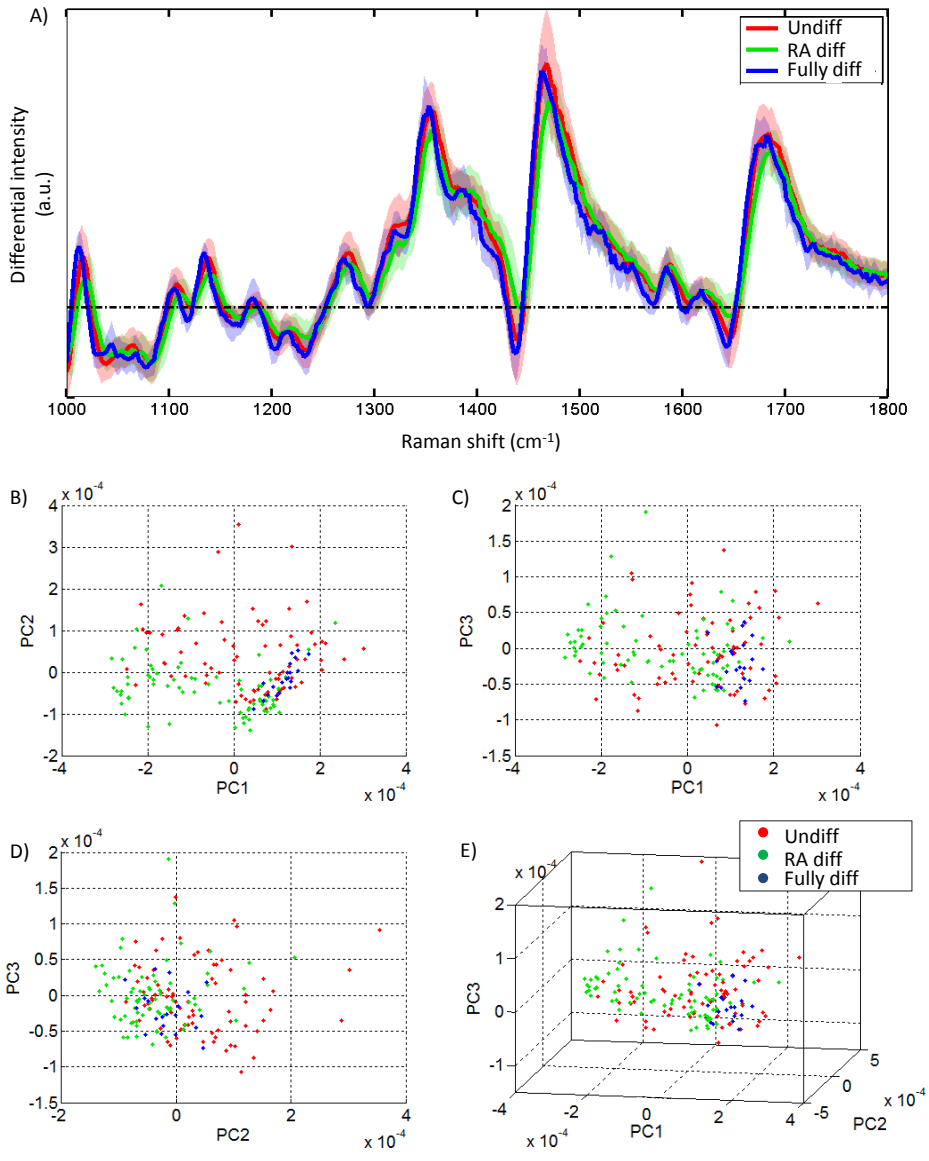

FIGURE 5.10: WMRS spectra are analysed in the region of $1000 - 1800\,\mathrm{cm}^{-1}$ which naturally has a flatter baseline, thereby minimising contributions from fluorescence. A) Mean spectra for each differentiation state, B-E) scatter plots using the first 3 PCs. RA differentiated and undifferentiated cells produce the most distinct clustering, with some overlap between fully differentiated and undifferentiated populations.

undifferentiated and fully differentiated cell populations. This may be attributed to the function of RA in a cell, which acts to strip proteins from DNA dictating which genes to switch on or off, hence controlling the switch between proliferation and differentiation [306]. Molecular modifications such as chromatin and DNA methylation state also accompany RA exposure [307] and may contribute to producing a more distinct Raman signature.

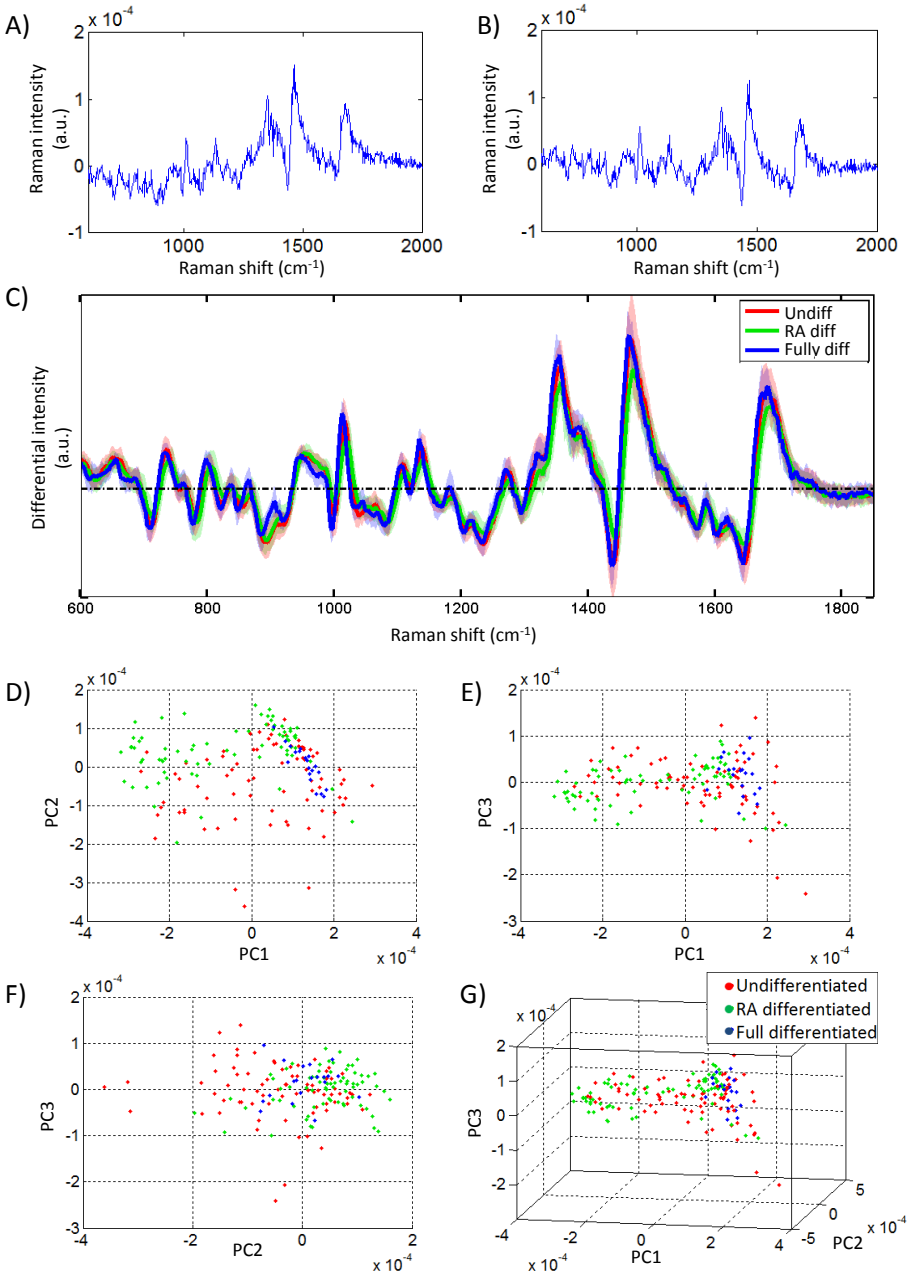

FIGURE 5.11: A background subtraction algorithm was applied to further suppress background fluorescence. A) Single Raman spectrum before and B) after background subtraction. The flat baseline indicates a good polynomial fit. C) Mean background subtracted WMRS spectra for each differentiation state. The zero-centred baseline confirms fluorescence suppression. Solid lines represent the mean spectrum and shadowed regions represent the standard deviation. D-G) scatter plots produced using the first 3 PCs. Clusters representing undifferentiated and RA differentiated cells are well separated. Some overlap exists between fully differentiated undifferentiated populations.

Raman peaks can be assigned based on the zero crossing points of the background corrected WMRS spectra and may be attributed to C-C skeletal modes ($930\,\mathrm{cm}^{-1}$), symmetric ring breathing modes of phenylalanine ($1003\,\mathrm{cm}^{-1}$), PO_2

	No background correction		Reduced range		Background Corrected	
	sens %	spec %	sens %	spec %	sens %	spec %
Undiff V RA diff	86.1	85.1	84.8	76.8	74.7	80.6
Undiff V Fully diff	96.9	78.9	93.3	75.0	88.9	46.7
RA diff V Fully diff	95.0	71.4	93.0	54.6	89.3	63.6

TABLE 5.2: Sensitivity and specificity values achieved for the discrimination of undifferentiated, RA differentiated, and fully differentiated SH-SY5Y cells.

symmetric stretching from DNA backbone ($1095\,\mathrm{cm}^{-1}$), C-C stretch in proteins ($1125\,\mathrm{cm}^{-1}$), Amide III ($1253\,\mathrm{cm}^{-1}$), CH_2 twisting from lipids, proteins, DNA and RNA (Guanine and adenine) (1305 and $1340\,\mathrm{cm}^{-1}$), CH_2 bending ($1450\,\mathrm{cm}^{-1}$), ring stretching from DNA, RNA (adenine and guanine) and cytochrome c ($1578\,\mathrm{cm}^{-1}$), and C=O and amide I ($1656\,\mathrm{cm}^{-1}$) [297].

The large fluorescence can predominantly be attributed to FluoroDishes. The greatest discrimination efficiency was achieved for the raw data, in which no background correction was applied (see table 5.2). This implies that the dish to dish variance introduced by the fluorescence background was sufficient to contribute to the discrimination ability. Ideally discrimination would be based entirely on the biochemical composition of the cells, making background subtraction algorithms necessary. Furthermore the purity of the samples presents a limitation to the discrimination ability as undifferentiated cells can naturally differentiate.

5.6 Mitochondrial response to irradiation

It was observed during experiments that a white intracellular organelle would sometimes move into focus during laser irradiation. These components possess a distinct and strong Raman signal with two major peaks at $1440\,\mathrm{cm}^{-1}$ and $1659\,\mathrm{cm}^{-1}$. An example of this intracellular component under white light microscopy and its respective WMRS spectrum is illustrated in figure 5.12.

Mitochondria are dynamic intracellular organelles which play a key role of producing energy for cells, consequently influencing metabolism, cell growth, and survival. Although they are not inherently motile, they make use of microtubule motors such as kinesins and dyneins to move along cytoskeletal elements [308].

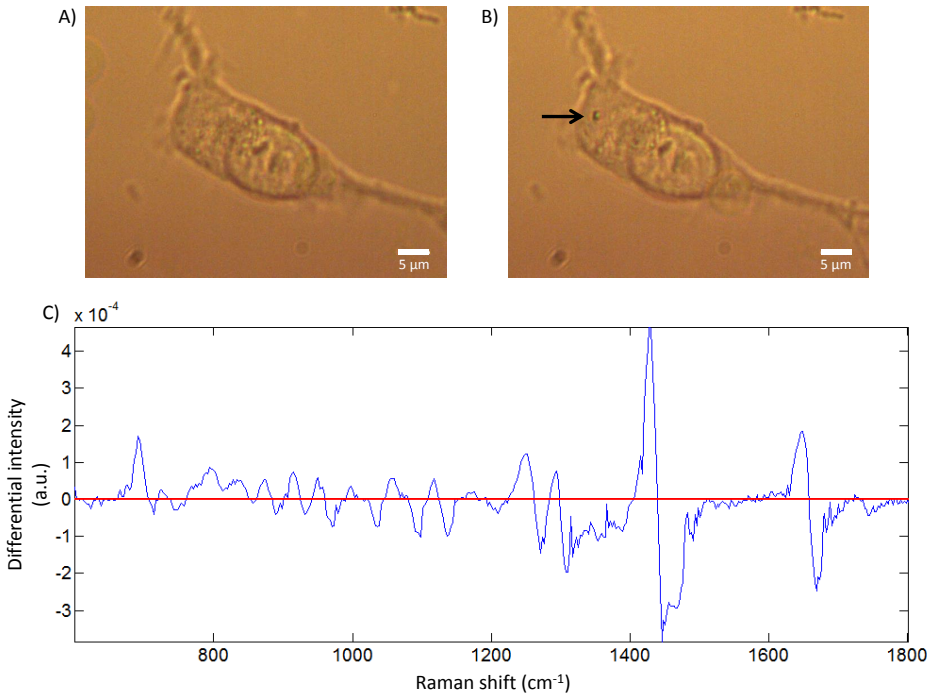

FIGURE 5.12: White light images of SH-SY5Y cell A) before and B) after irradiation. The white intracellular component that came into focus at the location of laser irradiation is highlighted by a black arrow. C) WMRS spectrum of the intracellular organelle; two intense peaks can be observed at $1440\,\mathrm{cm}^{-1}$ and $1659\,\mathrm{cm}^{-1}$. Scale bar represents $5\,\mu\mathrm{m}$

MTT is a yellow tetrazolium salt which is often used as a colorimetric assay. It is reduced in the mitochondria of metabolically active cells to yield a water insoluble purple formazin crystal [309]. As a first step to understanding this behaviour, MTT was added to the cells. After waiting 10-15 minutes for the MTT to be absorbed and undergo oxidation, it was observed to have been adsorbed by the white organelles, changing their colour to a dark purple. Raman spectra were obtained from the white components before addition of MTT, from MTT in the cytoplasm, and from the resulting purple organelles. Raman spectra acquired from the purple organelle contained peaks characteristic of both MTT and the white organelles thus confirming MTT absorption and intimating the organelles to be mitochondria.

It is instructive to compare the movement observed due to irradiation against the natural movements of mitochondria. The distance between MTT dyed mitochondria were measured before and after laser irradiation. Measurements were made in several positions across the cell; only one spot was irradiated allowing the other locations to act as a control. For example, two cells are shown in figure 5.13, where the

location of laser irradiation is highlighted by a red arrow and the other positions are indicated by green arrows. The distance between the mitochondria were measured using image J and converted into speed (nm/s). Measurements are summarised in table 5.3. Mitochondria at the site of irradiation appear to travel an order of magnitude faster when compared to other locations in the cell.

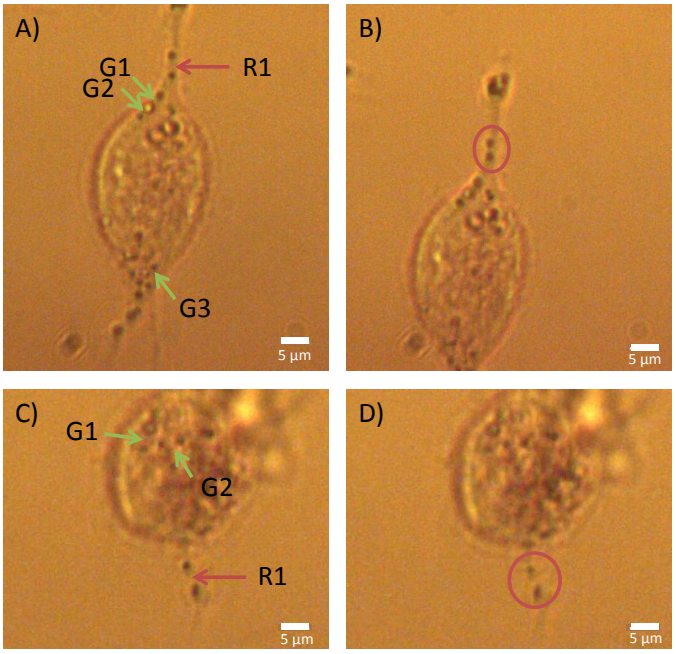

FIGURE 5.13: White light microscopy images show SH-SY5Y cells with mitochondria labelled with MTT. Mitochondria positions are compared before and after laser irradiation for two cells in A-B and C-D respectively. Distances were measured between mitochondria at various locations across the cells. Red arrows show the position of laser irradiation and green arrows show regions of natural mitochondrial movement. Red circles in B and D highlight the region where mitochondria have moved towards the point of laser irradiation.

Cell 1		Cell 2	
Position	Speed nm/s	Position	Speed nm/s
R1	20.0	R1	21.0
G1	6.9	G1	2.9
G2	2.0	G2	3.9
G3	2.9		

TABLE 5.3: Speed of mitochondrial movement at various positions across two SH-SY5Y cells. The position of laser irradiation is indicated by 'R1' and other control locations are indicated by 'G#'. Mitochondria at the position of laser irradiation move approximately an order of magnitude faster.

This is an interesting preliminary study indicating that mitochondria respond to

laser irradiation in differentiated SH-SY5Y cells. The effect was most commonly observed in fully differentiated cells suggesting there may be a relationship between mitochondrial response and cell survival ability, or the presence of more cytoskeleton. Further studies on this effect are necessary to better understand the relationship. It would also be interesting to investigate the relationship between mitochondrial movement and varying laser intensities, wavelengths, and irradiation times. As MTT forms heavy crystals upon reduction, which may limit mitochondrial movement, a suggested improvement for future studies would be to employ a much smaller mitochondria label, such as MITO red.

There are several reports on motor proteins transporting mitochondria along microtubules for long range movements and the actin cytoskeleton anchoring mitochondria for short range movements [308, 310, 311], however the motility of mitochondria under different light conditions is still relatively unexplored. Islam et al have conducted a study on the movement of mitochondria in leaf mesophyll cells under different light conditions, reporting a discernible redistribution of mitochondria under red, green, or blue light illumination [312]. Light is known to be an important environmental stimuli for plant cells, although the effect of light on mitochondrial dynamics in mammalian cells remains an open question.

Mitochondrial distribution is recognised to play an essential role for the viability of neuronal cells as well as the growth of neuronal axons. It has been observed that when an axon is actively elongating, mitochondria move preferentially away from the nucleus (anterograde) and accumulate in the region of the active growth cone. Mitochondria have attracted the attention of the scientific community due to their unique metabolic functions and patterns of motility, making their transport and distributions essential for the structure and function of the neuron [308, 311].

Perhaps more importantly, mitochondria may have possible involvement with Alzheimers disease, Huntington's disease, and PD [310]. It has also been reported that defects in mitochondrial dynamics can lead to neurodegenerative diseases such as Charcot-Marie-Tooth disease and autosomal dominant optic atrophy [313].

NIR lasers are commonly used with biological samples due to their low absorption. A variety of studies have demonstrated NIR light interacting with neuronal

cells to promote axonal growth and nerve regeneration [314–316], which could potentially aid the formation of neural circuits *in-vitro*, as well as nerve regeneration *in-vivo*. *In-vitro* studies have also indicated that exposure to NIR may defend against excitotoxicity, oxidative stress, and oxygen-glucose deprivation, conditions similar to those experienced by neuronal cells during a stroke or neurodegeneration [317–319]. The underlying molecular and cellular mechanisms of these neuroprotective interactions however remain poorly understood.

The relationship between mitochondrial dynamics and disease is particularly intriguing. The potential ability to control mitochondrial movement with NIR light could play a role in modelling these conditions to better understand the relationship, and perhaps provide an insight into when and where during development organisms are sensitive to mitochondrial distribution.

5.7 Conclusion

In this chapter three differentiation states of SH-SY5Y cells were obtained; undifferentiated, RA differentiated, and fully differentiated. The successful differentiation to a dopaminergic neuronal cell type was demonstrated by ICC detection of TH.

It was shown that WMRS was capable of quantitatively measuring dopamine concentration, down to $7\,\mathrm{mM}$. This is not sensitive enough for physiologically relevant concentrations, which are as low as nanomolar in PD patients. The use of dopamine targeted AuNPs could provide a SERS enhancement to improve detection sensitivity. An interesting future study would be to investigate if SERS could enable intracellular dopamine detection. The major challenge to overcome, with respect to the use of functionalised NPs as intracellular probes, is to bypass, or escape, the endosomes during cellular uptake of the NPs.

The ability of WMRS to discriminate between the closely related differentiation states of SH-SY5Y cells in a label-free manner was assessed. As a first step, a comparison was made between various growth substrates on which to grow cells and obtain Raman spectra. Quartz slides are non permissive and prevented cells from adhering and putting out processes. Extracellular matrices coating a quartz slide

did permit cell growth but generated a fluorescence signal and was time consuming. FluoroDishes were found to be the optimum substrate for SH-SY5Y growth and subsequent Raman analysis. However, due to the large fluorescence background, WMRS processing alone was not sufficient to suppress the fluorescence and a third party background subtraction algorithm was also employed.

RA differentiated cells gave the most distinct Raman signature which may be due to chemical and morphological modifications attributed to RA exposure. As a result RA differentiated cells generated the most well defined cluster in the PC scatter plot, achieving a sensitivity and specificity of 74.7% and 80.6% respectively when compared to undifferentiated cells, and 89.3% and 63.6% respectively when compared to fully differentiated cells. Fully differentiated cells and undifferentiated cells were more difficult to discriminate between, achieving a sensitivity value of 88.9% and a specificity of only 46.7%.

An interesting future study may be to discriminate between the SH-SY5Y differentiation states using a multimodal approach, such as the combined Raman and DHM microscope. The morphological differences between undifferentiated and differentiated populations may improve the discrimination ability without the need for exogenous probes. This may prove useful in establishing the purity of cell cultures or sorting neuronal from non-neuronal cells in a label-free manner.

Finally, an experimental observation showed interesting preliminary results that mitochondria may respond to laser irradiation. By tracking mitochondrial movement, speeds an order of magnitude greater were recorded at the site of irradiation. Further studies on this effect are required to better understand the relationship.

Contributions

Lisa Strother provided guidance for all biological techniques and acquired the ICC fluorescence images. I cultured the cells, conducted the western blot, and prepared cells for ICC. I acquired and analysed the Raman data, assigned Raman bands, and analysed mitochondria images. Gayle Doherty shared her insight in many helpful discussions.

6 Applications for Raman and fluorescence spectroscopy in the food and drinks industry

6.1 Introduction

The use of optical spectroscopic methods for the analysis of food and drinks has been garnering respect and recognition in the industry due to their non-invasive nature and ability to rapidly characterise a wide range of chemical compounds.

The use of Raman spectroscopy for the food and drinks industry has been previously discussed in section 2.4. Raman spectroscopy offers the advantage of being insensitive to water content making it ideal for analysing liquid samples. Additionally there is no need for any specific sample preparation or the addition of chemicals making it compatible with in-line testing procedures. Raman spectroscopy can offer detailed chemical information with a rapid acquisition time in comparison to other commonly used techniques such as GC-MS or HPLC.

Fluorescence spectroscopy is also a useful tool for providing information regarding a samples chemical make-up and its environment. Fluorescence spectroscopy has previously been used to characterise red wines; successfully identifying wines according to grape type and region of origin [15]. Fluorescence spectroscopy has also shown potential for monitoring beer during storage [14] and frying oil deterioration [320]. The disadvantage is that fluorescence spectroscopy is limited to samples which possess fluorescence.

Standard Raman spectroscopy is capable of recording both Raman and fluorescence information. Although background fluorescence is often considered a nuisance in Raman spectroscopy, in the case of characterising food or drink samples it may actually provide useful information and give a more complete description of the sample. This could be used as a means for quality checking, monitoring storage conditions, or detecting adulteration or counterfeiting of food and beverage substances.

This chapter will deal with standard Raman spectroscopy, containing both Raman and fluorescence information, for the classification of whisky and extra-virgin olive oil samples. The detection of adulterants or counterfeited samples is important for both the market and food safety. To investigate the compatibility of this technology with in-field testing the performance of a compact Raman device will be compared to that of a microfluidic chip or free space system for whisky and olive oil analysis respectively.

6.2 Compact Raman spectroscopy device

In an effort to make Raman spectroscopy more accessible there is a drive towards compact, portable Raman spectrometers. The IDRaman mini 2.0 (Ocean Optics) is a powerful, compact, easy-to-use Raman system. A model was provided by MSquared Lasers Ltd for use within these studies. Figure 6.1 shows a photograph of the device, which has dimensions $91\,\mathrm{mm}$ x $71\,\mathrm{mm}$ x $38\,\mathrm{mm}$.

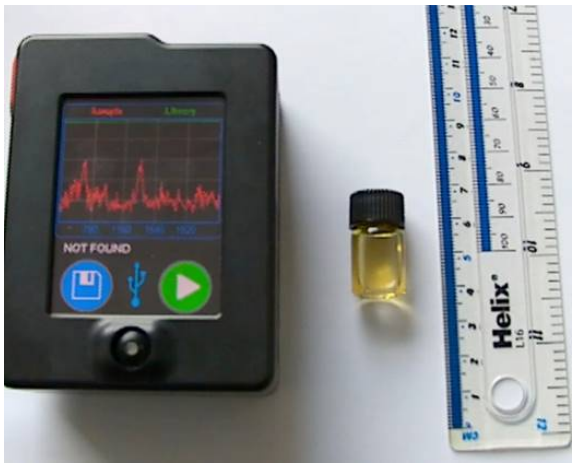

FIGURE 6.1: Photograph of the IDRaman mini (Ocean Optics) with a sample vial.

A sample vial holding up to $2\,\mathrm{ml}$ of liquid may be inserted and a spectrum rapidly obtained (minimum acquisition time of $10\,\mathrm{ms}$). The system employs a diode laser of wavelength $785\,\mathrm{nm}$ with a line width of $2\,\mathrm{cm}^{-1}$ and stability $< 0.1\mathrm{cm}^{-1}$. The output power of the laser is $100\,\mathrm{mW}$, providing $50\,\mathrm{mW}$ to the sample. The collection optics have a NA of 0.5 and a working distance of $8\,\mathrm{mm}$. The laser rasters in an orbital fashion which has the advantage of a larger effective scanning area, providing

more efficient collection of Raman signal from an inhomogeneous sample and minimising any potential photodamage. A back-illuminated, deep depletion CCD array is used to detect the collected photons. Raman scattered light may be analysed in the region of $400\,\mathrm{cm}^{-1}$ - $2300\,\mathrm{cm}^{-1}$ and are obtained with a resolution of approx 18 - $20\,\mathrm{cm}^{-1}$.

6.3 Optical methods for the identification of whisky

6.3.1 Introduction to whisky authentication

Scottish whisky is one of the most important exports for the U.K. with sales contributing around £4 billion a year to the economy [321]. The popularity and price for genuine scotch whisky has however attracted global counterfeiting, costing the industry close to £500 million a year. In addition to the cost to the economy, fake whisky poses a serious health threat. Incorrectly managed distillation processes can produce high concentrations of methanol. Methanol and other toxic substances such as ethylene glycol (antifreeze) and isopropyl alcohol are also known to be added as fortification to some counterfeit alcoholic products [322, 323].

A variety of methods have been explored to assist in the detection of whisky counterfeits such as mass spectroscopy [324, 325] or infrared spectroscopy [326]. To move away from laboratory based methods and improve the accessibility for in-field testing there have been attempts to implement portable analytical devices. One group reported the use of a handheld device employing UV/visible absorption spectroscopy for the authentication of whisky [327]. Previously developed in Dholakia's group was an optofluidic chip which successfully identified scotch whisky based on a Raman and fluorescence signature [53]. The optofluidic chip offers the advantage of requiring small sample volumes ($20\,\mu\mathrm{l}$) and short acquisition times of just $2\,\mathrm{s}$. However the sample must be carefully loaded to avoid the introduction of bubbles and the chip itself can take several days to manufacture and must be cleaned between samples.

The compact Raman device (IDRaman mini, Ocean Optics) would be an ideal candidate for in-field analysis due to its ease of use and portability. The aim of this section is to compare the performance of the compact Raman device to that of

the optofluidic chip for classification of various whiskies. Further to this, American whiskeys such as bourbon, Tenessee, and rye, which are also vulnerable to counterfeiting [328], will be analysed using the compact Raman device.

6.3.2 Methods

Microfluidic chip

The microfluidic chip is fabricated in PDMS with channels defined by soft-lithography [53, 329]. Two multimode optical fibres with core sizes of $200\,\mu\mathrm{m}$ are embedded in the chip, acting as the excitation and collection path for Raman signals. They are positioned at a $90°$ angle to each other to maximise the overlap of excitation and collection areas whilst minimising the collection of Rayleigh scattered photons. A further two channels act as the microfluidic pathway for the sample. $20\,\mu\mathrm{l}$ of sample is placed over the sample inlet using a pipette. A syringe is attached to the sample outlet which acts to pull the sample through into the detection region. It is important to ensure that there are no bubbles present in the system before acquiring any Raman measurements. The optofluidic chip is shown in figure 6.2.

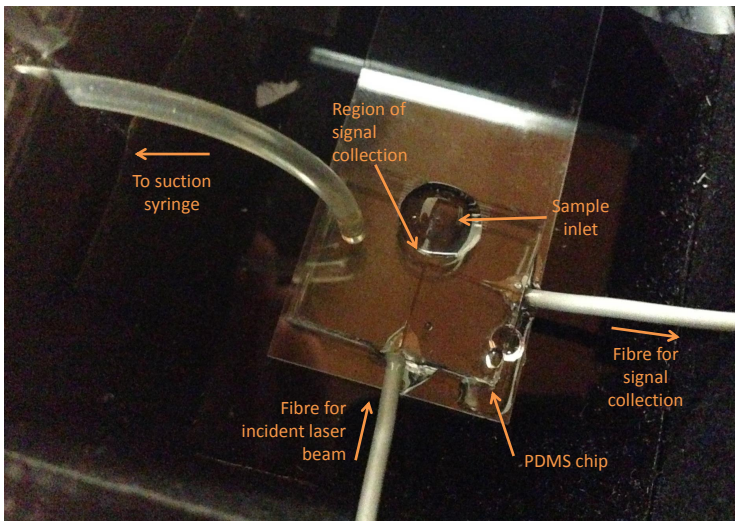

FIGURE 6.2: Photograph of optofluidic chip for whisky analysis. $20\,\mu\mathrm{l}$ of sample is placed on the sample inlet and drawn into the detection region by a syringe. Two optical fibres placed at $90°$ act as the excitation and collection channel for Raman signal.

The sample was excited using a diode laser (Laser2000 (UK) Ltd. with maximum power $450\,\mathrm{mW}$ and wavelength $785\,\mathrm{nm}$) providing $200\,\mathrm{mW}$ power to the sample

plane. Raman photons were collected by a second fibre and delivered to a spectrometer (Shamrock SR-303i, Andor Technology) employing a 400 lines/mm grating and was blazed at $850\,\mathrm{nm}$. Raman photons were detected on a deep-depletion, back-illuminated and thermoelectrically cooled CCD camera (Newton, Andor Technology). Spectra were recorded with an acquisition time of $2\,\mathrm{s}$ and 25 spectra were recorded per sample. A microfluidic pump was employed to pull through small volumes of sample between measurements.

The microfluidic chip was cleaned between different whisky samples by passing $40\,\mu\mathrm{l}$ of deionised water through the chip. This rinsing was sufficient to avoid cross contamination.

Compact Raman device

The compact Raman device is described in detail in section 6.2. $50\,\mathrm{mW}$ power was provided to the sample plane. $2\,\mathrm{ml}$ of sample was loaded into a glass vial designed to fit the device. 25 spectra were recorded for each sample, using the same acquisition time as the microfluidic chip of $2\,\mathrm{s}$. The sample vial was removed between measurements and reinserted at a random orientation to avoid biasing due to the shape of sample vial. The vial was thoroughly cleaned and dried before reuse with a new sample.

Sample preparation

Seven commercially available Scotch whisky brands and their variants were used for comparing the performance of the microfluidic chip and the compact Raman device. These were used in three studies comparing

- five 12 year old single malts (Bowmore, Glenfiddich, The Balvenie, Highland Park and Laphroig)
- different casks of the same brand (MaCallan Gold and Macallan fine oak) and
- various ages of the same brand (Tomintoul 10 years, 16 years, and 33 years).

To further assess the ability of the compact Raman device to classify whiskies, 25 commercially available single malt scotch whisky brands were bought and analysed.

30 spectra were acquired for each sample with an acquisition time of 2 s. The name and age of each whisky is detailed in appendix J.

For the classification of American whiskeys 6 commercially available whiskeys were analysed; 4 of which were bourbons (Buffalo Trace, Evan Wiliams 2003 single barrel, Elijah Craig, and Heaven hill), one Tennessee (Jack Daniels) and one rye (High west).

Data processing

A detailed description of statistical analysis methods used is given in section 2.8. Specific details of this study will be outlined in this section. Background subtraction was applied to all spectra; for the microfluidic chip a background spectrum was recorded from a water filled channel, which was subtracted from all subsequent data. For the compact device 25 spectra were recorded from an empty vial at random orientations, the average of these spectra was used as the background spectrum and was subtracted from all subsequent data.

All spectra were then normalised, according to the area under the curve, to account for any power fluctuations in the laser. No base-lining or smoothing algorithms were applied to avoid the introduction of any artefacts.

PCA was applied to reduce the dimensionality and scatter plots were produced using the first 2 PCs. Whisky classification was determined by LOOCV and nearest neighbour algorithms using the first 3 PCs, which accounted for the majority of the total variance. Confusion matrices recorded the number of correct and incorrect classifications allowing pairwise sensitivity and specificity values to be calculated providing an estimation of the discrimination efficiency.

6.3.3 Results

Classification of whisky samples

The major peaks observed in the Raman spectra correspond to ethanol, in addition to this there may be contributions from higher order alcohols, esters, and aldehydes. The wood of the cask, where whisky is matured, is responsible for extractives such as tannin and acids. These minor components are known as congeners and are

responsible for the distinct flavour and colour of a particular whisky. Additionally caramel may be added to whisky to adapt its colour. The colouring of a whisky will have an associated fluorescence signature which plays an important role for the discrimination between brands. As standard Raman spectra are acquired, both a Raman and fluorescence signature is obtained, where each provides useful information for the discrimination between various whiskies.

As a first step five 12 year old single malt whiskies were analysed using both the microfluidic chip and the compact Raman device. Scatter plots were produced using the first 2 PCs as shown in figure 6.3. Distinct clusters formed for each brand indicating an ability to successfully discriminate between the five whisky brands. The microfluidic chip and the compact Raman device each provided a sensitivity and specificity of 100% for all pairwise comparisons.

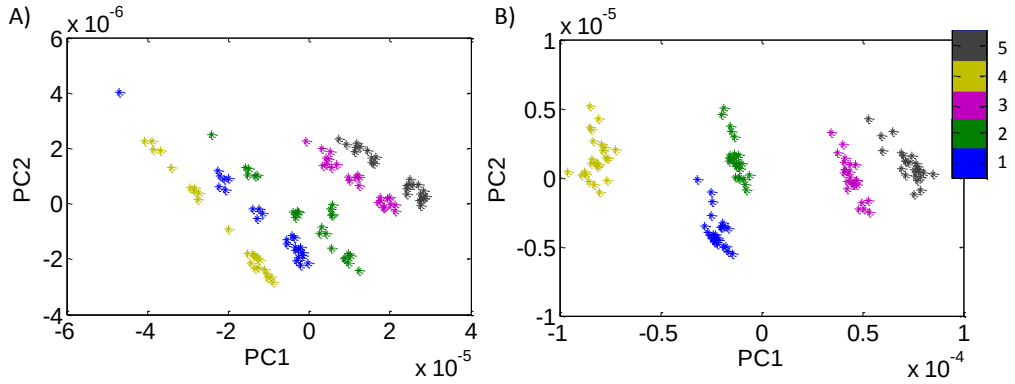

FIGURE 6.3: Scatter plots illustrating the discrimination between five 12 year old single malt Scotch whiskies using A) the microfluidic chip and B) the compact Raman device. Each provide distinct clustering indicating successful discrimination. Whiskies 1-5 are Bowmore, Glenfiddich, The Balvenie, Highland Park and Laphroaig.

The ability to classify the same brand of whisky according to different casks was also investigated. Two types of Macallan, 'Gold' and 'Fine oak', were analysed, which mature in a sherry cask and American oak bourbon seasoned cask respectively. The difference in the cask alters the congener profile of the whisky and result in differences between their respective colours, consequently providing different fluorescence signatures. The two whiskies produce distinct clusters in the PC scatter plot as shown in figure 6.4. The microfluidic chip and the compact Raman device each provided a sensitivity and specificity of 100%.

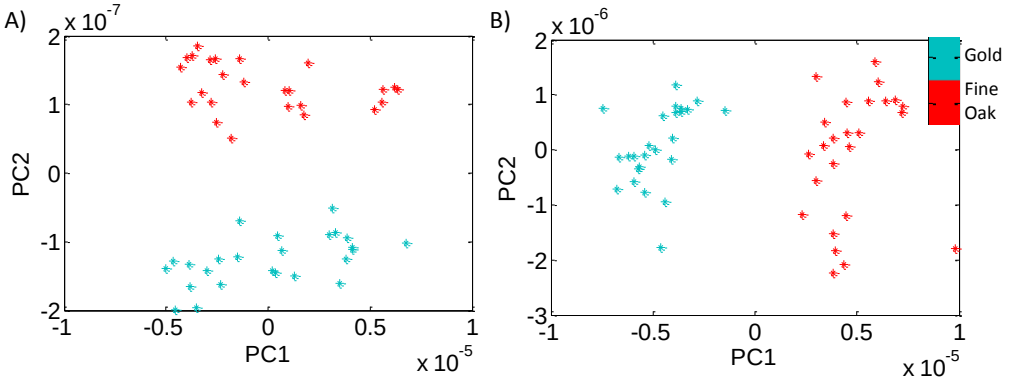

FIGURE 6.4: Scatter plots illustrating the discrimination between the same brand of whisky (MaCallan) matured in two different casks for data obtained on A) the microfluidic chip and B) the compact Raman device; each provide distinct clustering indicating successful discrimination.

A further important factor for whisky classification is its age. The maturation process can alter the congener profile of a whisky and often produces darker coloured whiskies. This is due to the length of time spent in a wooden barrel; more time gives the alcohol longer to leach pigments from the wood although this can also depend on the age of the barrel. Three samples of the same whisky brand with different ages (Tomintoul: 10, 16, and 33 years) were analysed. In this case the microfluidic chip provided a better discrimination achieving sensitivities and specificities of 100% for each pairwise comparison. This is illustrated by the three distinct clusters in the PC scatter plot (figure 6.5 A). The compact Raman device was successful at identifying the 10 year old whisky with sensitivity and specificity values of 100% and 100% respectively against the 16 year old whisky, and 96.2% and 100% respectively against the 33 year old whisky. However it was not able to successfully discriminate between the 16 and 33 year old whiskies achieving sensitivity and specificity values of only 53.8% and 52.2% respectively. This is illustrated by the distinct cluster representing the 10 year old samples and overlap between clusters representing the 16 and 33 year old whiskies in the PC scatter plot (figure 6.5 B).

25 single malt scotch whiskies (detailed in appendix J) were analysed in order to expand the library of whiskies which may be classified by the compact Raman device. Figure 6.6 illustrates the scatter plot produced using the first 2PCs. Distinct clusters were formed for each brand of whisky, illustrating each generates a

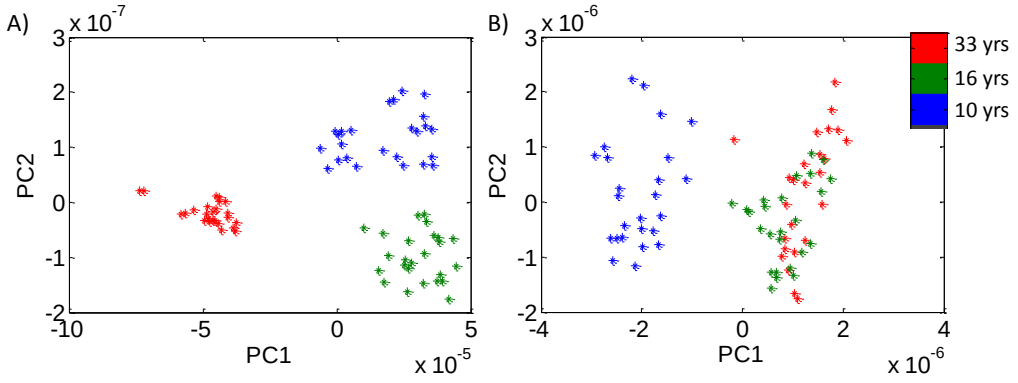

FIGURE 6.5: Scatter plots illustrating the discrimination between the same brand of whisky (Tomintoul) with three different ages for data obtained on A) the microfluidic chip and B) the compact Raman device. The microfluidic chip provides distinct clustering indicating successful discrimination, whereas there is some confusion between the 16 and 33 year old whiskies when analysed by the compact device.

distinct fluorescence and Raman signature and may be successfully identified. Pairwise comparisons gave an average sensitivity and specificity of 95.9% and 95.9% respectively.

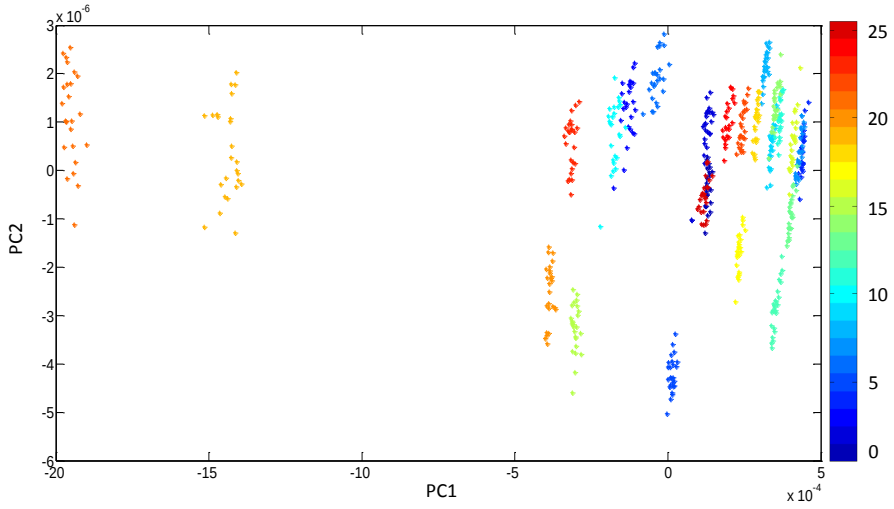

FIGURE 6.6: Scatter plot illustrating the ability of the compact Raman device to discriminate between 25 different brands of single malt scotch whisky. The formation of distinct clusters indicates successful discrimination.

American whiskey is an important contributor to the U.S. economy and as such is also vulnerable to counterfeiting. To assess the applicability of this technology for American whiskeys, data were acquired on the compact Raman device for 6 different brands of American whiskey including 4 bourbons, 1 Tenessee whiskey and 1 rye.

The differences between these types of whiskey essentially comes from the grain mash used and the ageing process. Scotch whisky must be made from malted barley, aged in an oak cask for a minimum of three years, and must come from Scotland. Bourbon on the other hand is made from a grain mixture of at least 51% corn and has no minimum ageing period. Tennessee whiskey is essentially a bourbon but must be matured for at least two years and come from the state of Tennessee. American rye whiskey must be made from a grain mixture of at least 51% rye and has no minimum ageing requirements. Jack Daniels is the Tenessee whiskey used here, it should be noted that Jack Daniels use a unique charcoal filtering process which will also influence the spectral signature.

Data were collected and a PC scatter plot was produced (figure 6.7). Separation of clusters along PC1 shows some correlation to the age of the whiskey; Heaven hill is a bourbon aged for 4 years and has the smallest PC1 value. Jack Daniels, a Tennessee whiskey, is also aged for 4 years but has a higher PC1 value, which may be due to the charcoal filtering process producing a darker colour (often associated with ageing). Continuing to higher PC1 values is Buffalo Trace, a bourbon aged between 7 and 9 years. Evan Williams and Elijah Craig are both bourbons aged for 10 and 12 years respectively and have the highest PC1 values. High West is a rye whiskey which is also aged for 12 years, possessing a high PC1 value but separated along PC2.

A high discrimination efficiency was achieved; Elijah Craig and Evan Williams were the most challenging to discriminate between, achieving 100% sensitivity and 90% specificity. This confusion is also observed by some overlap between their respective clusters in the PC scatter plot. This may be expected as they are quite closely related, both are produced in the Heaven Hill distillery and have similar ages. All other pairwise comparisons achieved 100% sensitivity and specificity.

Analysis of whisky flavour profile

Variations in the fluorescence spectra of different whiskies may be due to variations in their respective congener profiles. As it is the congener components that contribute most to the distinct flavour of a whisky, two clusters formed close to each

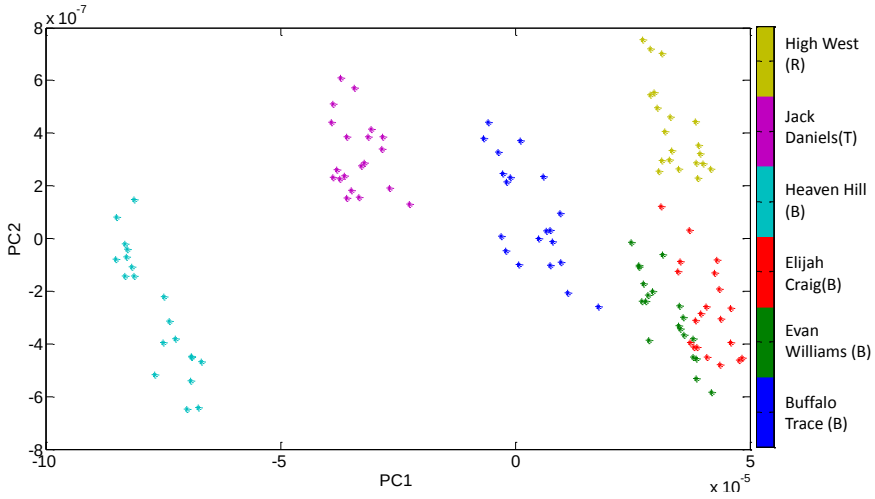

FIGURE 6.7: Scatter plot illustrating the discrimination between six brands of American whiskey. R, T, and B indicate rye, Tennessee, and bourbon whiskeys respectively. Data were acquired on the compact Raman device and distinct clusters for each brand indicate successful discrimination.

other may share similar aromatic features. It is then conceivable that scatter plots may be able to predict the taste of a whisky.

Whisky is commonly categorised according to two key sets of variables and may be plotted on a grid. One variable (often plotted on the horizontal) ranges from light to rich, and the other (often plotted on the vertical) ranges from delicate to smoky. The horizontal axis differentiates floral or soft fruits flavours (lighter) from woody or nutty flavours (richer). The vertical axis is a measure of the whisky's degree of 'peatiness'. When peat is used to heat and dry the malt, smoke can infuse into the barley; whether peat is used and for how long gives the whisky varying degrees of smokiness.

The relationship between the PCs on a scatter plot and a flavour map, where axes correspond to taste variables, was investigated. A scatter plot of PC1 against PC3 was qualitatively compared to a flavour map created by David Broom. As a preliminary study six whiskies, which were also on the flavour map, were analysed and are labelled as A-F (details in appendix J). Results show that the delicate-smoky axis correlates with PC3, where smokier whiskies have a larger PC3 value, as seen in figure 6.8 A-B. Additionally the light-rich tastes appear to correlate with PC1, where lighter whiskies tend to cluster at higher PC1 values, as seen in figure 6.8 C-D.

This observed correlation indicates that clustering may be achieved according to

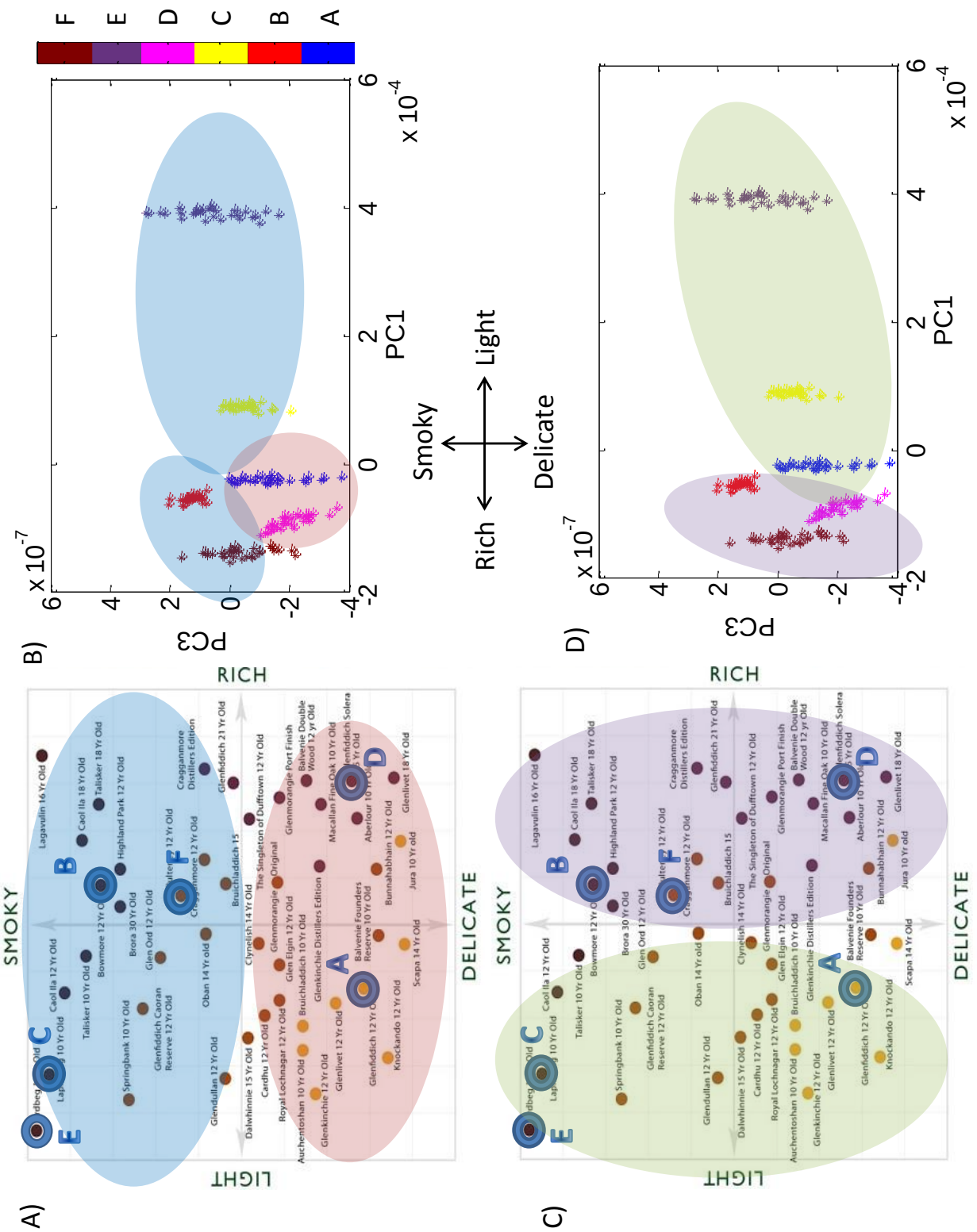

FIGURE 6.8: Correlation of PC scatter plot with a whisky flavour map. The main taste variables can be categorised along two axis A) illustrates the smoky- delicate axis which shows a correlation to PC3 (B) where smoky whiskies have a higher PC3 value. C) Illustrates the light-rich axis which shows a correlation to PC1 (D) where lighter whiskies have a higher PC1 value.

the whisky's flavour. There is therefore potential that the PC scatter plots can be a guide to the whisky's flavour. It would be interesting to follow up this study with a larger sample population.

6.4 Optical methods for the identification of extra-virgin olive oil

6.4.1 Introduction to olive oil authentication

There are other substances which would also benefit from a rapid and portable technology for authentication, one such example is olive oil. Olive oil is an important part of the Mediterranean diet and is becoming increasingly more popular due its known associated health benefits. It is produced from the fruit of the *Olea* tree using cold press manufacturing methods that do not introduce chemicals or high temperatures which may degrade the oil. Extra-virgin olive oil (EVOO) is the highest quality of olive oil and must meet very specific standards to be classified as such. EVOO is thus more expensive than other common edible oils such as vegetable oil. A consequence of this is that EVOOs are often adulterated [330]. It was reported in 2013 that 70% of EVOOs sold are adulterated, i.e. combined with cheaper inferior oils and sold as genuine EVOO [331]. In some Asian countries this is of significant importance as it poses a real food-safety concern, particularly with regards to the use of 'gutter oil' which is produced from waste oil obtained from restaurants, sewers, and even slaughterhouses [332, 333].

An additional concern for the olive oil industry is quality control; ambient conditions such as temperature, light, and exposure to oxygen play an important role in the oxidation of olive oil. Oxidation is the key contributor to rancidity and chemical degradation of EVOO. The international olive council (IOC) have established chemistry standards for the assessment of olive oil quality. Test methods include the analysis of the free fatty acid (FFA) content, peroxide value, UV absorption at bands K232 and K268, and testing by a sensory panel [334]. A study in 2011 at the UC Davis Olive Center revealed that of the five top-selling imported olive oil brands sold in California, 73% did not meet the IOC standards for EVOO [335]. Storage conditions,

production, and transportation methods all play an important role in maintaining the quality of EVOO. It is often during these process that EVOO degrades, even to the extent that it would no longer qualify as EVOO by the time of purchase. Oxidation is a self-catalytic process which makes the monitoring of changes in the oxidation state of EVOO particularly important. Current methods for analysis require skilled personnel and laboratory resources that are both costly and time consuming. Moving towards an inexpensive portable device for analysis could offer the benefit of rapid, in-field, and affordable testing without the need for extensive laboratory training.

EVOO has become a major area of interest in the food technology industry, with research ranging from its health benefits [336–338] to determining geographical origin [339], as well investigations into adulteration [340] and quality control [335, 341–343]. Raman spectroscopy has previously been employed for studies regarding olive oil quality, providing information on the FFA content [49], oxidation [342], and adulteration of oils [340, 344].

A further important consideration would be to identify different brands of EVOO based on its Raman spectrum. This may aid the identification of counterfeit oils, which is particularly important given the price differential between brands in this market and the potential health risks of some contaminants. It is instructive to explore whether Raman spectroscopy or another photonics based approach, such as fluorescence spectroscopy, can lead to successful discrimination between EVOO brands.

This section will deal with the identification of five commercially available EVOO brands using three key approaches:

1. Standard Raman spectroscopy (giving both Raman and fluorescence information)
2. WMRS (a solely Raman signature) and
3. Fluorescence spectroscopy alone.

Measurements are taken on both a free space Raman system and the compact Raman device to investigate the compatibility of Raman spectroscopy with in-field testing.

6.4.2 Methods

Standard Raman spectroscopy

Details of the instrumentation used for the Raman spectrometer are provided in section 2.7.3. $145\,\mathrm{mW}$ power was provided to the sample plane and spectra were acquired over $3\,\mathrm{s}$. Data were analysed in the wavenumber region 800-1800 cm^{-1}.

The compact Raman device was described previously in section 6.2. $50\,\mathrm{mW}$ power was provided to the sample plane. Spectra were recorded with an acquisition time of $500\,\mathrm{ms}$ in the wavenumber region 400-2300 cm^{-1}. No baselining of the data was performed to minimise artefacts that may otherwise be introduced.

Wavelength modulated Raman spectroscopy

The same free space system was used for WMRS measurements. The wavelength was tuned over a total range of $\Delta\lambda = 1\,\mathrm{nm}$. Five spectra were acquired at equidistant wavelengths; each single spectrum was acquired for $3\,\mathrm{s}$ giving a total acquisition time of $15\,\mathrm{s}$ per WMRS spectrum.

Fluorescence spectroscopy

A simple and relatively portable fluorescence spectrometer was set-up according to figure 6.9. A blue LED of wavelength $473\,\mathrm{nm}$ was focussed into the centre of a quartz cuvette and a collection lens was positioned at 90° to the illumination arm. The collected signal was coupled into an optical fibre and detected by a USB mini spectrometer (Ocean Optics). An acquisition time of $500\,\mathrm{ms}$ was used.

Sample preparation

Five brands of commercially available certified EVOO were purchased from the supermarket; Tesco's own brand, Napolina, Felippo Berio, Olea Maxima, and Peña de Martos. All bottles were opened at the same time, resealed, and stored in a dark space at room temperature (298K).

A sample chamber was prepared for the free space system using two quartz slides (SPi supplies). A well was constructed by placing a vinyl spacer of thickness $80\,\mu\mathrm{m}$ onto one quartz slide. $18\,\mu\mathrm{l}$ of EVOO was loaded into the well and the

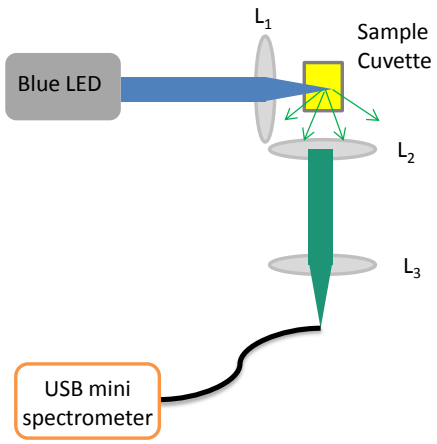

FIGURE 6.9: Schematic of the fluorescence spectrometer (not to scale). A blue LED is coupled into the sample cuvette using L_1: coupling lens. Emitted light is collected at $90°$ by L_2: collection lens, and coupled into a fibre using L_3: fibre coupling lens, before being detected by a mini USB spectrometer.

second quartz slide was used to seal the chamber. The sample was placed on the microscope stage with the thin quartz slide (0.15-$0.18\,\mathrm{mm}$ thick) nearest the microscope objective. A total of 25 spectra were recorded for each sample, moving the slide between each measurement.

The compact Raman device is designed to hold a glass vial with illumination from underneath. $2\,\mathrm{ml}$ of EVOO was loaded into the vial and sealed with a plastic screw cap. Five different vials were used for each EVOO sample, five spectra were taken per vial, providing a total of 25 spectra per EVOO sample. The vials were removed and reinserted to a new position between each measurement. This process aimed to prevent bias due to the sample vial.

The quartz cuvette used for fluorescence spectroscopy measurements was loaded with $3\,\mathrm{ml}$ of EVOO and sealed with a plastic cap. The cuvette was removed and inserted to a new position between measurements. The cuvette was thoroughly washed and dried before a new sample was tested.

Samples were tested for any photobleaching by irradiating continuously for 10 minutes. No signs of signal degradation or burning were observed in the Raman spectra or fluorescence peak intensity.

Data processing

A detailed description of the statistical analysis methods used is given in section 2.8 and the method of processing WMRS data to obtain a single differential spectrum is detailed in section 2.5. Specific details of this study will be outlined in this section. All spectra were normalised, according to the area under the curve, to account for any power fluctuations in the laser. A parametric student's t-test was used with a significance level of $p < 10^{-10}$, to highlight regions of significant difference between the mean spectra of any two EVOO brands.

PCA was applied to the full data set to reduce the dimensionality. The number of PCs used varies according to the system, in order to optimise the amount of variability accounted for, whilst minimising the number of PCs for faster processing. Data taken on the free space system were analysed using the first 4 PCs; for standard Raman spectroscopy this accounted for 99.7% of the variance, and for WMRS data this accounted for 94.1% of the variance. Data acquired on the compact device were analysed using the first 3 PCs which accounted for 97.9% of the variance, and solely fluorescence data were analysed using the first 4 PCs, which accounted for 77.3% of the total variance. Figure 6.10 summarises the amount of variance accounted for in the first 5 PCs for each system.

Scatter plots were produced using the first 3 PCs to visualise trends in the data. The discrimination efficiency was assessed by means of LOOCV and nearest neighbour algorithm. This was repeated for each spectrum and correct and incorrect EVOO brand classifications were summarised in a confusion matrix. Sensitivities and specificities were then calculated in a pairwise manner for each EVOO brand.

Fatty acids and methyl ester analysis

The lipids from each EVOO were analysed using fatty acids and methyl ester (FAME) analysis by gas chromatography-mass spectroscopy (GC-MS). Lipids were extracted and FAME analysed for the five brands of EVOO at a two week interval to understand the underlying reason for changes in Raman spectra on different days.

Total lipids were extracted by the method of Bligh and Dyer [345]. Briefly, $100\,\mu$l of EVOO was added to $100\,\mu$l of PBS in a glass tube. $750\,\mu$l of 1:2 (v/v) chloroform:

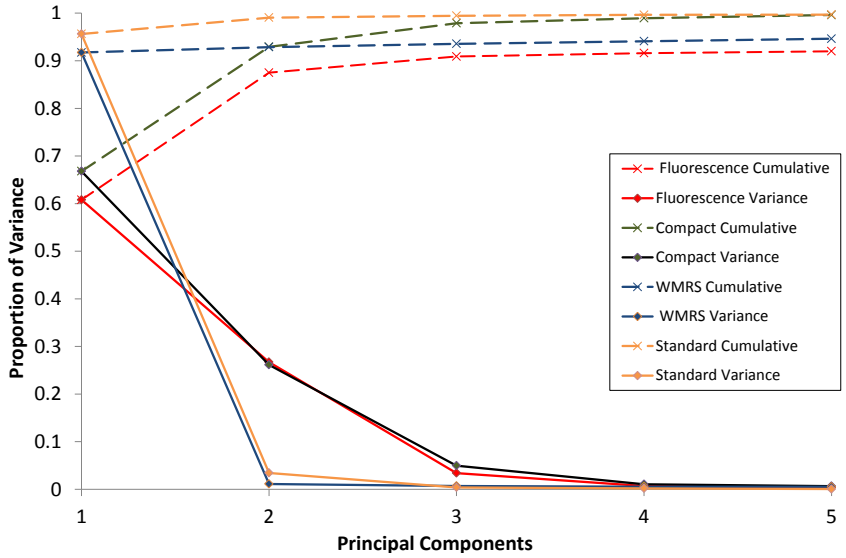

FIGURE 6.10: Scree plot illustrating the proportional variance accounted for the in the first 5 PCs, for the four systems used for discrimination between EVOO brands: fluorescence only, compact Raman device, WMRS and standard Raman spectroscopy on the free space system. Dashed lines represent the cumulative variance and the solid line represents the individual contributions from each PC.

methanol ($CHCl_3$:MeOH) was added and vortexed. The sample was further agitated for 10-15 minutes. The sample was made biphasic with the addition of $250\,\mu$l of $CHCl_3$. This was vortexed and $250\,\mu$l of water was added before vortexing again. Finally, the sample was centrifuged at $1000\,$g at room temperature for 5 minutes. The lower organic phase was transferred to a new glass vial and dried under nitrogen until testing.

Both the organic and inorganic parts underwent Raman analysis to confirm the changes in Raman peaks were due to changes in the lipids.

Full characterisation and quantification of the fatty acids were conducted by conversion to the corresponding FAME followed by GC-MS analysis. Briefly, the samples were spiked with an internal standard fatty acid 17:0 ($20\,\mu$l of $1\,$mM) and dried under nitrogen. The fatty acids from the lipids (neutral and phospholipid) were released by base hydrolysis and converted to methyl esters by adding an ethereal solution of diazomethane [346].

The FAME products were dissolved in 10-20 μl dichloromethane and 1-2 μl was analysed by GC-MS on an Agilent Technologies GC-6890N, MS detector -5973 (Agilent Technologies) with a ZB-five column ($30\,$m x $25\,$mm x $25\,$mm, Phenomex), with a

temperature programme of 70° C for 10 minutes, followed by a gradient to 220° C at 5° C/minute and held at 220° C for a further 15 minutes. Mass spectra were acquired from 50-$500\,\mathrm{amu}$. The identity of FAMEs was determined by comparison of the retention time and fragmentation pattern with a bacterial FAME standard (Supelco).

6.4.3 Results

Comparison of standard Raman spectroscopy and WMRS for the identification of EVOO brands

Raman spectra were acquired from five commercially available EVOO brands on the free space Raman system. Measurements were taken with both standard Raman spectroscopy (no fluorescence suppression) and WMRS (with fluorescence suppression). The Raman peaks observed may be assigned to the following vibrational modes: ν (C-C) ($870\,\mathrm{cm}^{-1}$ and $1080\,\mathrm{cm}^{-1}$), in-plane δ(=C-H) deformation in the unconjugated *cis* double bond ($1266\,\mathrm{cm}^{-1}$), in-phase methylene twisting motion ($1301\,\mathrm{cm}^{-1}$), $\delta(CH_2)$ ($1441\,\mathrm{cm}^{-1}$), ν(c=c) *cis* ($1646\,\mathrm{cm}^{-1}$), and ν(C=O) ($1747\,\mathrm{cm}^{-1}$). These peaks are used to identify unsaturated fatty acids [347], where the major one in EVOO is oleic acid. These peaks correspond well with those observed by Dong et al in previous studies regarding olive oil [340].

Standard Raman spectra acquired from the five brands of EVOO are demonstrated in figure 6.11 A, where the mean spectrum of each brand is shown. A student's t-test was employed to calculate regions of significant difference between two EVOO brands at a significance level of $p<10^{-10}$. It can be observed that these regions of significant difference are due to both Raman peaks and regions of fluorescence background. The loadings of the first two PCs are visualised spectrally in figure 6.11 B, illustrating the most important contributions towards the variance between the data sets. It can be observed that Raman peaks around $1266\,\mathrm{cm}^{-1}$, $1301\,\mathrm{cm}^{-1}$, $1441\,\mathrm{cm}^{-1}$, and $1646\,\mathrm{cm}^{-1}$ are key contributors to the first PC, whereas the second PC also has some fluorescence contribution in the low wavenumber region 800-$1100\,\mathrm{cm}^{-1}$. Scatter plots were produced using the first three PCs and well defined clusters were formed for each EVOO brand (figure 6.11 C-F), indicating they may be successfully identified using standard Raman spectroscopy. LOOCV and nearest

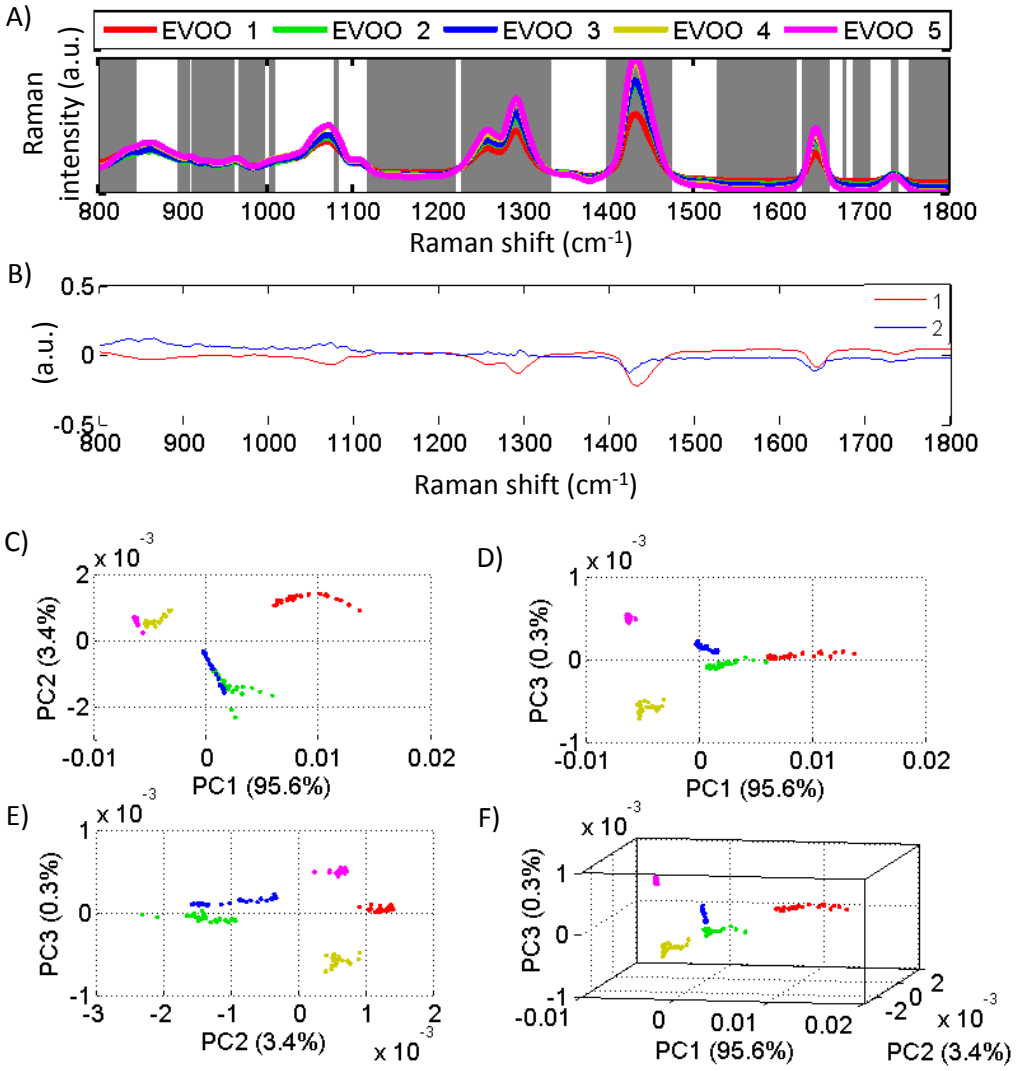

FIGURE 6.11: A) Standard Raman spectra for five brands of EVOO where solid lines represent the mean spectrum of each sample and shadowed regions represent the standard deviation. Grey vertical bars highlight regions of significant different between EVOO 1 and 2 at a significance level of $p<10^{-10}$. B) Loadings for PC1 (red) and PC2 (blue) indicating the Raman peaks that contribute most to the variance. C-F) Scatter plots produced from the first 3 PCs. Each EVOO brand forms a well defined cluster indicating they may be successfully identified.

neighbour algorithms were employed to estimate the discrimination efficiency. A confusion matrix summarising correct and incorrect classifications can be found in table 6.1. Sensitivity and specificity values of 100% and 100% were achieved for each pairwise comparison of the five EVOO brands.

WMRS spectra were acquired and the resulting mean differential Raman spectrum for each EVOO brand can be seen in figure 6.12 A. With the fluorescence background suppressed the student's t-test revealed only Raman peaks as regions

of significant difference between EVOO brands. This can also be observed in the PC loadings, represented in figure 6.12 B, which have a flat baseline, indicating there are no fluorescence contributions to the variance in the first two PCs. The fewer regions of difference between EVOO brands consequently makes discrimination more challenging. This is reflected in the clustering of data points in the scatter plots (figure 6.12 C-F) which produce less tightly bound clusters with respect to the standard Raman spectroscopy data. The discrimination ability of WMRS to identify EVOO brands was calculated by LOOCV, where correct and incorrect classifications are summarised by the confusion matrix in table 6.1. The average pairwise sensitivity and specificity achieved was 97.1% and 99.5% respectively.

Compact Raman device for EVOO identification

Standard Raman spectroscopy measurements were taken on a compact device to investigate the compatibility of this technique with in-field testing. The mean spectrum acquired for each of the five EVOO brands are illustrated in figure 6.13 A. The Raman peaks corresponding to oleic acid can be observed with a broad fluorescence background. The first three PC loadings are represented spectrally in figure 6.13 B, where the most important contributions to variance can be visualised. PC1 contains information regarding the full Raman spectrum as well as some fluorescence contribution in the region 500-$800\,\mathrm{cm}^{-1}$. PC2 contains mostly fluorescence information with some small contributions from the key Raman peaks. PC3 contains very little useful information and indeed only accounts for 5% of the total variance across the whole data set.

Scatter plots were produced using the first three PCs and well defined clusters can be observed for each EVOO brand (figure 6.13 C-E), which indicates the compact Raman device is capable of successfully identifying various EVOO brands. A confusion matrix summarising correct and incorrect classifications, as determined by LOOCV and nearest neighbour algorithms, can be found in table 6.1. An average pairwise sensitivity and specificity value of 98.4% and 99.6% respectively was achieved.

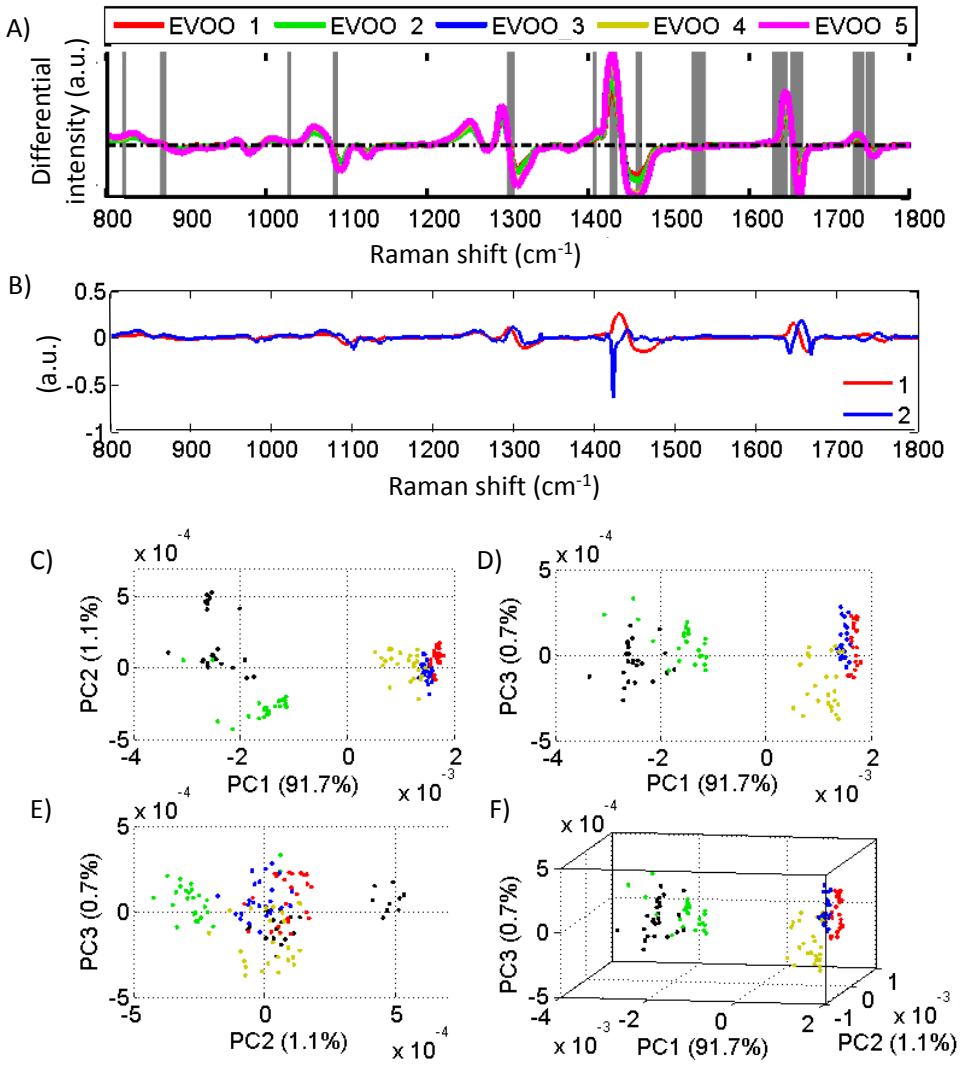

FIGURE 6.12: A) Differential WMRS spectra for five brands of EVOO where zero crossing points represent Raman peaks. Solid lines represent the mean spectrum of each sample and shadowed regions represent the standard deviation. Grey vertical bars highlight regions of significant different between EVOO 1 and 2 at a significance level of $p<10^{-10}$. B) Loadings for PC1 (red) and PC2 (blue) indicating the Raman peaks which contribute to the variance. C-F) Scatter plots representing the first 3 PCs. Each EVOO brand forms a cluster indicating they may be successfully identified. The clusters are not as well defined as with standard Raman spectroscopy.

Fluorescence spectroscopy

The improved discrimination ability for standard Raman spectroscopy over WMRS suggests that the fluorescence background, although commonly thought of as detrimental, actually provides useful information for the identification of various brands of EVOO. Purely fluorescence spectroscopy measurements were taken to determine the ability of fluorescence alone to discriminate between EVOO brands. Figure 6.14

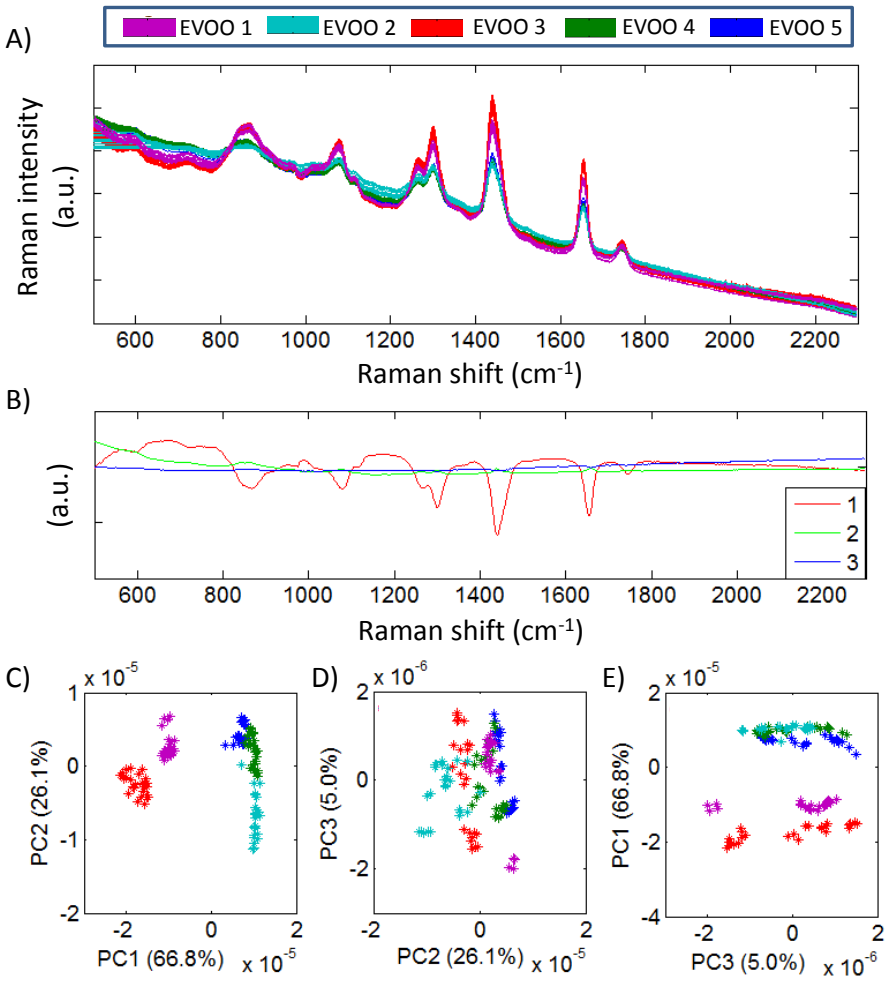

FIGURE 6.13: A) Standard Raman spectra for five brands of EVOO as measured on the compact Raman device. B) Loadings for the first 3 PCs indicating the contributions to the variance between EVOO brands. C-E) Scatter plots representing the first 3 PCs. Each EVOO brand forms a well defined cluster indicating the ability of the compact device to successfully discriminate between various brands of EVOO.

demonstrates the mean fluorescence spectrum acquired for each EVOO and the scatter plots produced using the first three PCs. Each brand of EVOO forms a well defined cluster, indicating successful identification of various EVOO brands is possible using a solely fluorescence signal. Pairwise sensitivities and specificities were calculated to be 100% and 100% for each pairwise comparison of EVOO brands.

Discrimination based on fluorescence alone may be due to a range of factors including the fruit itself, environmental factors, and production methods. The colour of the olive oil can be attributed to various pigments relating to the ripeness of the

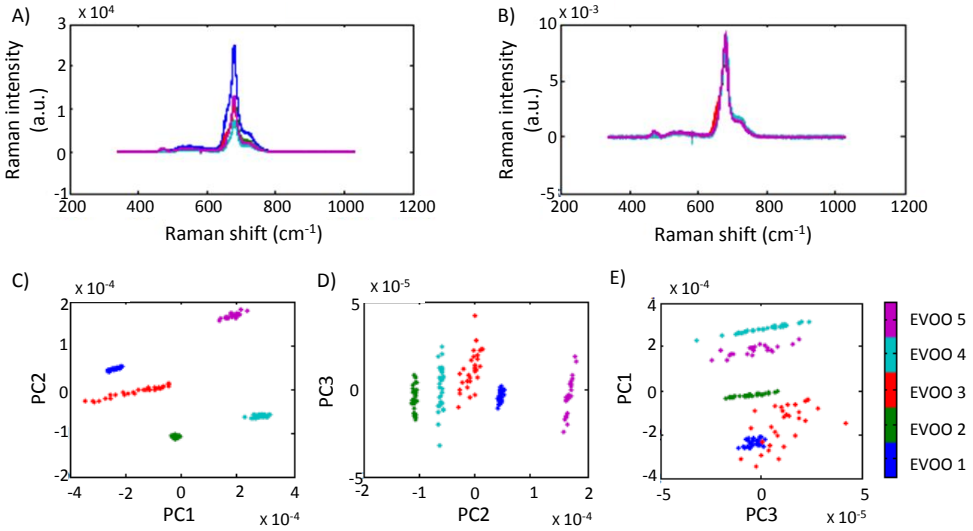

FIGURE 6.14: A) Raw data for fluorescence spectra obtained from five brands of EVOO. B) Normalised data before analysis with PCA. C-E) Scatter plots representing the first 3 PCs. Each EVOO brand forms a well defined cluster indicating they may be successfully identified by fluorescence spectroscopy alone.

fruit, the soil, and climate conditions, as well as the extraction and processing procedures used. Ripe olives, for example, have a higher carotenoid content which produce a yellow oil, whereas green olives have a high chlorophyll content which produce a green oil. Chlorophyll and pheophytin promote the production of oxygen radicals in the presence of light, where oxidation is associated with a yellowing of the oil. Vivid greens may be associated with the addition of twigs or leaves during the grinding process [348]. Chlorophyll is also known to be responsible for strong fluorescence signals at long wavelengths.

6.4.4 Discrimination of EVOO on different days

Discrimination between five EVOO brands was successful across all four platforms. To have a robust technology suitable for use in the olive oil industry it is crucial that measurements are robust over time. However, subtle shifts in Raman peak intensities were observed on different days. Figure 6.15 illustrates the drift observed over nine days. The same trend was noted for all EVOO brands although only three are shown here for simplicity. This poses a challenge as regular retraining would be necessary for an effective analysis over time, severely limiting the technology's applicability. To overcome this, it is vital to understand the reason for the drift.

	Predicted/ Actual EVOO	1	2	3	4	5
Standard Raman Spectroscopy	1	25	0	0	0	0
	2	0	25	0	0	0
	3	0	0	25	0	0
	4	0	0	0	25	0
	5	0	0	0	0	25
WMRS	1	25	0	0	0	0
	2	2	23	0	0	0
	3	0	0	24	0	1
	4	0	0	3	22	0
	5	0	0	2	0	23
Compact device	1	24	1	0	0	0
	2	2	23	0	0	0
	3	0	0	25	0	0
	4	0	2	0	23	0
	5	0	0	0	0	25
Fluorescence	1	25	0	0	0	0
	2	0	25	0	0	0
	3	0	0	25	0	0
	4	0	0	0	25	0
	5	0	0	0	0	25

TABLE 6.1: Confusion matrices summarising the ability of four methods (standard Raman spectroscopy on a free space system, WMRS on a free space system, standard Raman spectroscopy on a compact device, and fluorescence spectroscopy) to identify five brands of EVOO. Each method shows a good discrimination ability where values on the diagonal represent correct classifications. Standard Raman spectroscopy and fluorescence spectroscopy achieved the maximum discrimination efficiency with no incorrect classifications.

Measurements were acquired every 30 minutes over an 8 hour period for 10 days whilst simultaneously recording the ambient conditions (room temperature, humidity, and pressure). No correlations were found between fluctuations in the ambient conditions and drift in the Raman peaks. All spectra were normalised to account for power fluctuations of the laser and the same trend was observed on both the free space system and the compact Raman device. This indicates that the origin of the Raman drift is likely due to a chemical change occurring in the EVOO samples, such as oxidation.

GC-MS is regarded as the gold standard for measuring such chemical changes. To better understand the cause of changes occurring in the Raman spectra, lipids

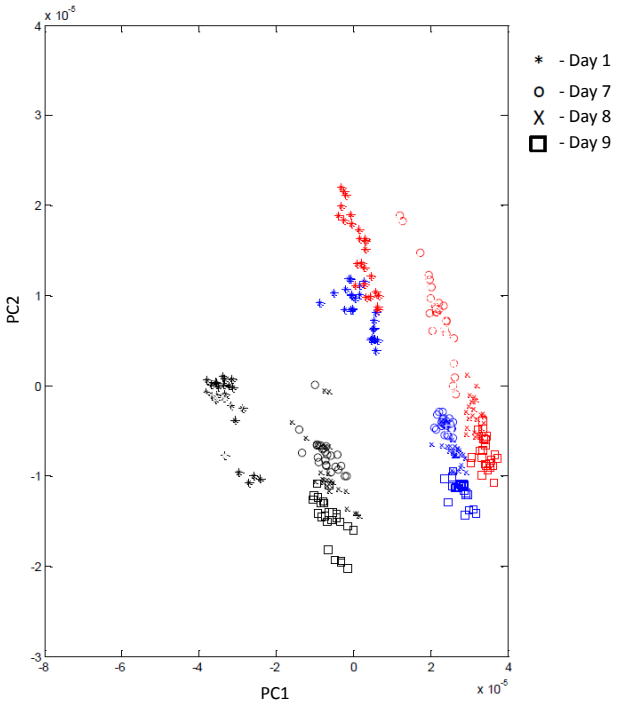

FIGURE 6.15: Raman data of three EVOO brands (indicated by colours) acquired on different days (indicated by markers). Subtle changes in Raman peak intensities result in a continuous drift of data points on a PC scatter plot.

were extracted from each EVOO, on week 3 and week 5 after opening the bottles, using the method of Bligh and Dyer [345]. A two week time period was chosen to ensure any changes in EVOO due to oxidation would be observable by GC-MS. The lipids underwent both Raman spectroscopy on the free space system and GC-MS FAME analysis.

Raman spectra were acquired from both the organic and non-organic products to confirm the drift was due to chemical changes in the lipids. The non-organic part did not show any observable changes in Raman spectra and so are not shown here. The Raman spectra obtained from lipids on week 3 and week 5 may be seen in figure 6.16 A. Changes in the Raman peak intensities are detailed in table 6.2. The most notable change was an increase the Raman peak at $1219\,\mathrm{cm}^{-1}$, corresponding to C-O-C asymmetric stretching, and a decrease in the Raman peak at $1654\,\mathrm{cm}^{-1}$, corresponding to C=C double bond, in week 5 compared to week 3. This implies the possible formation of an epoxide across a double bond (chemical structure shown in figure 6.18).

Figure 6.16 B-C illustrate the scatter plots using the first three PCs; a similar drift

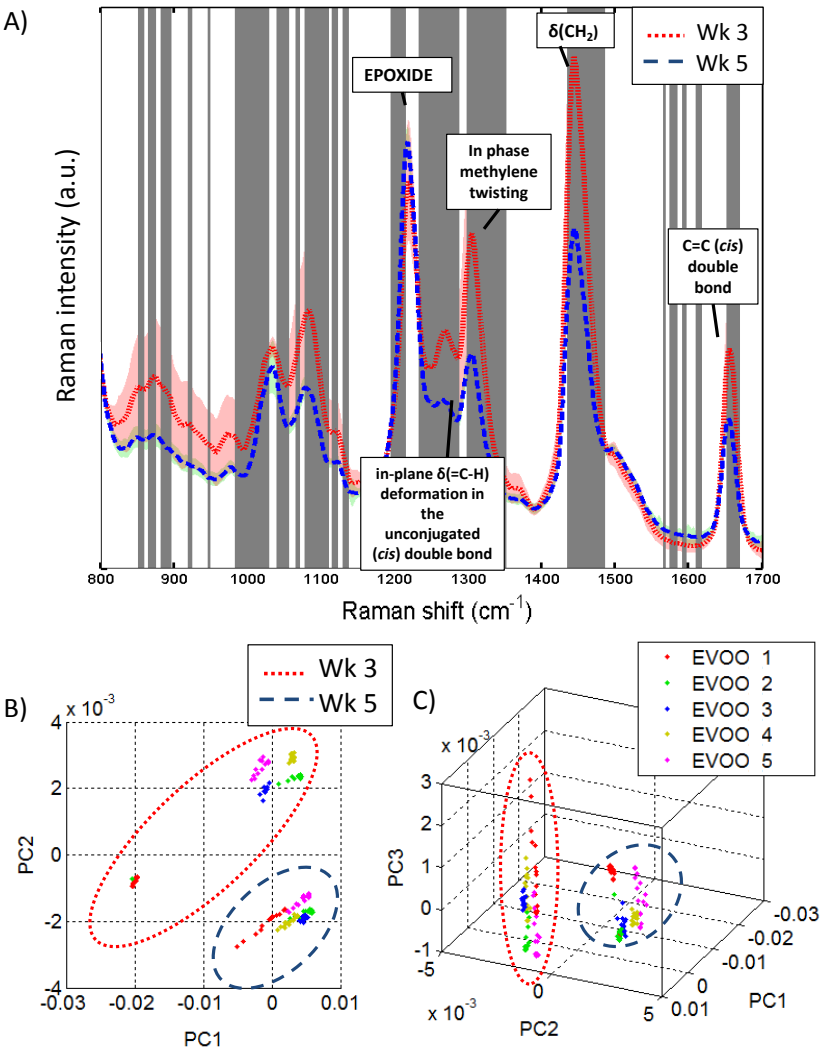

FIGURE 6.16: A) Standard Raman spectra obtained from lipids extracted on weeks 3 and 5. Dashed lines show the average recorded spectrum from all five EVOO brands and shadowed regions indicate the standard deviation. Grey vertical bars highlight regions of significant difference as calculated by the student's t-test at a significance level of $p<10^{-13}$. Most notably week 3 shows a more intense Raman band corresponding to C=C and week 5 shows an increase in the Raman band corresponding to epoxide. B-C) Scatter plots using the first three PCs indicating a distinct drift between data obtained on week 3 and week 5.

to that noted previously (see figure 6.15) can be observed, indicating the shift is indeed due to chemical changes in the lipids.

These results correlate with those of the GC-MS FAME analysis. The total ion traces showing relative abundances of FAMES from one EVOO brand on week 3 and week 5 can be seen in figure 6.17. Note that CX:Y(a,b) represents X total number of carbons in the fatty acid and Y unsaturated bonds at a position along the chain represented by a and b. The peak at 39.55 minutes, corresponding to C18:2(9,12)

Raman shift (cm^{-1})	Change observed	Vibrational bond
670	Increased	νC-C (aliphatic)
760	Increased	νC-C (aliphatic)
1219	Increased	C-O-C asymmetric stretching
1740	Increased	νC=C
1085	Decreased	νC-C
1305	Decreased	In-phase methylene twisting
1280	Decreased	δ=C-H deformation in *cis* double bond
1441	Decreased	δCH
1684	Decreased	c=c *cis* double bond

TABLE 6.2: Summary of the intensity changes in Raman peaks of lipids extracted on week 3 to week 5.

(linoleic acid), decreases by 4.1% relative abundance in week 5 compared to week 3. The peak at 43.85 minutes however, increases by 4.2% relative abundance, which corresponds to C18:1 epoxide species. A complete summary of relative percentage changes can be seen in table 6.3. Although the ion trace is only shown for one EVOO brand similar ion traces were recorded for all five EVOOs.

Relative %	Week 3	Week 5
C14:0	0.1	0.1
C16:0	17.1	17.3
C16:1	0.5	0.3
Branched C18:0	5.8	5.7
C18:1 (9)	47.4	47.9
C18:1 (12)	2.6	2.5
C18:2	6.3	1.2
C20:0	0.4	0.3
C20:1 (11)	14.5	14.7
C20:1 (14)	0.1	0.1
C20:2	0.6	0.5
C18:1 (Epoxide)	0.1	4.3

TABLE 6.3: Relative abundances of total fatty acids on week 3 and week 5, as determined by GC-MS FAME analysis.

One of two epoxides can be formed from linoleic acid when the double bond is attacked by a lipid peroxide radical. The chemical structure for this reaction is illustrated in figure 6.18. Linoleic acid is present in EVOO in much smaller quantities

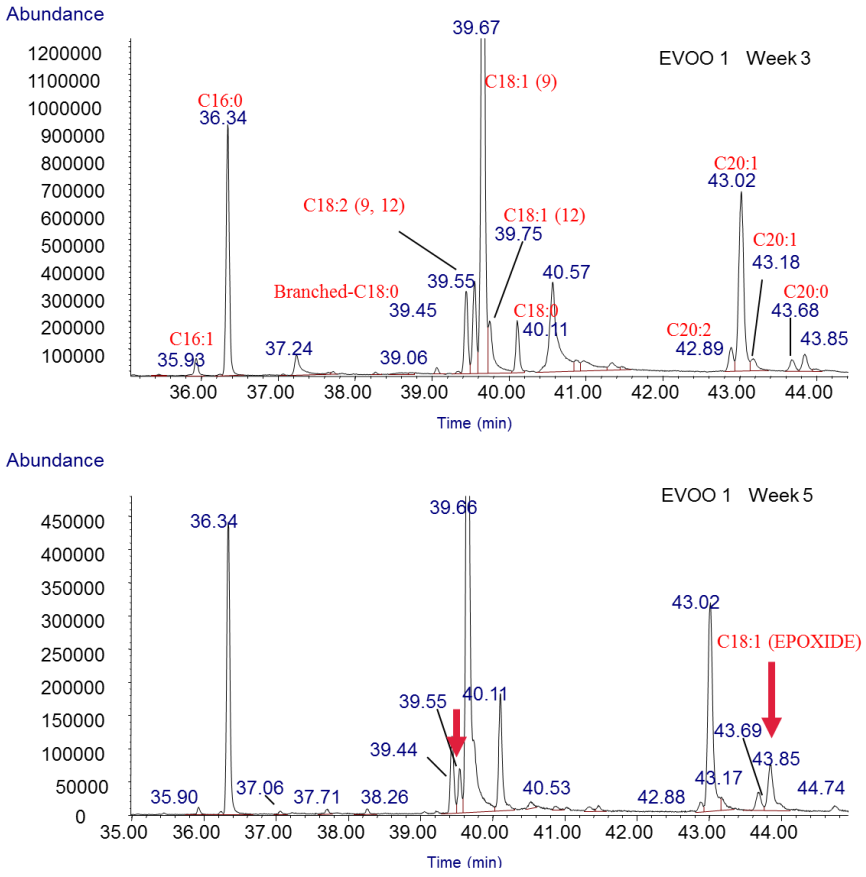

FIGURE 6.17: GC-MS total ion traces showing the relative abundances of FAMES in EVOO 1 on week 3 (top) and week 5 (bottom). All FAMES were identified by retention time and fragmentation pattern. Of significance is the reduction in C18:2 (9,12) at 39.55 minutes and the increase in C18:1 (epoxide) at 43.85 minutes from week 3 to week 5.

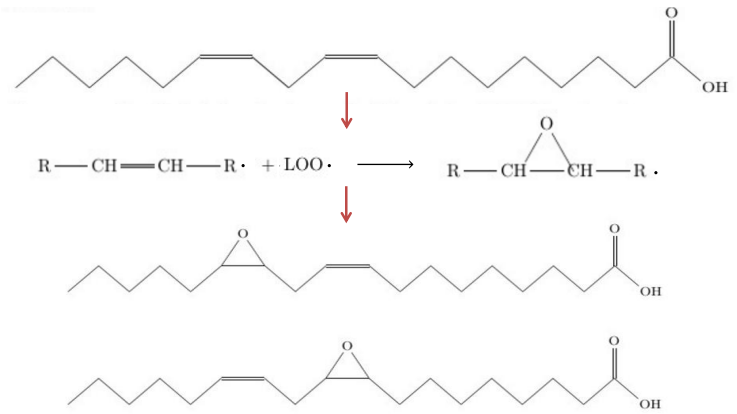

FIGURE 6.18: Chemical structure describing the oxidation of linoleic acid to form an epoxide. (From top to bottom) Linoleic acid, C18:2 (9,12) can form one of two epoxides: 12,13-epoxy-9-octadecenoic acid or 9,10-epoxy-12-octadecenoic acid, via the attack of a double bond by a lipid peroxide radical.

than oleic acid but oxidises an order of magnitude faster, owing to its additional double bond.

To overcome the effects that ageing has on the discrimination efficiency, and to ensure a more robust identification technology, the PCs used for discrimination were further investigated. The changes due to oxidation on different days were notable and contributed to the first PC. The remaining PCs however account for very little variation in the data set. The total number of PCs used for analysis was thus increased to include PCs 2-7 (containing 6.2% of the total variance); this provided the optimal discrimination efficiency.

The total data set, including Raman spectra obtained on both week 3 and week 5, for all five EVOO brands was analysed using PCs 1-7 (including oxidation information) and PCs 2-7 (with oxidation effects suppressed). The resulting confusion matrices can be found in table 6.4. The average pairwise sensitivity and specificity values achieved were 99.7% and 98.7% respectively when using PCs 1-7, and 99.7% and 99.7% respectively when using PCs 2-7.

The shift in Raman spectra caused by oxidation of the EVOO was enough to cause some confusion between data taken on different days. By careful selection of PCs used for analysis it was possible to minimise the effects of ageing and improve the discrimination ability.

	Predicted/ Actual EVOO	1	2	3	4	5
PCs 1-7	1	29	1	0	0	0
	2	1	26	1	2	0
	3	0	0	30	0	0
	4	0	0	0	30	0
	5	0	0	0	0	30
PCs 2-7	1	29	1	0	0	0
	2	1	29	0	0	0
	3	0	0	30	0	0
	4	0	0	0	30	0
	5	0	0	0	0	30

TABLE 6.4: Confusion matrices indicating the ability of Raman spectroscopy to identify five EVOO brands when data are acquired on different days. Analysis is conducted using PCs 1-7 and with PCs 2-7. PC1 contains information regarding oxidation of EVOO over time which can cause some confusion in their identification. A better discrimination efficiency was achieved by discarding the first PC and using PCs 2-7 for analysis.

6.4.5 Identification of EVOO using paper devices

Paper devices [349] offer various advantages as a diagnostic platform, such as portability, ease of use, low production cost, and compatibility with various optical techniques. Paper devices are discussed in greater detail in section 7.4.

Paper is naturally suitable for wicking liquid samples by capillary action and could therefore offer a convenient method for analysing small volumes of EVOO in the field. In this study filter paper (Whatman No.1) is used to hold small volumes of EVOO which are then analysed using the compact Raman device.

The filter paper is cut into circles with a diameter of $1\,\mathrm{cm}$ and pressed flat at the bottom of the glass vial. Five background spectra were recorded from the paper, before any EVOO was added, with an acquisition time of $5\,\mathrm{s}$ per spectrum. The vial was removed and reinserted to a different position between measurements. $7\,\mu\mathrm{l}$ of EVOO was pipetted onto the paper and left to sit for $3\,\mathrm{minutes}$. Twenty spectra were recorded, each with an acquisition time of $5\,\mathrm{s}$, changing the vial position between each measurement. Three paper devices were used per EVOO brand. This was repeated for three different EVOO brands.

The paper itself contains Raman peaks corresponding to cellulose. The position of the vial can affect the Raman spectrum due to the random orientation of overlapping fibres in the paper. The raster of the laser in the compact device can help to average out the Raman signal. Nevertheless five background measurements were made per device to provide an average background spectrum, as seen in figure 6.19 A. This was subtracted from each raw Raman spectrum (figure 6.19 B) to provide a standard Raman spectrum for subsequent EVOO analysis (figure 6.19 C). The background subtracted spectra were then used to form a training data set on which PCA was applied. Scatter plots were produced using the first 3PCs (figure 6.19 D-F). EVOOs were classified according to LOOCV and nearest neighbour algorithms, correct and incorrect classifications were summarised in a confusion matrix (table 6.5). An average sensitivity and specificity of 86.9% and 92.3% was achieved.

There was still some confusion between EVOO brands, indicated by the overlap of clusters in the PC scatter plot and the incorrect classifications recorded in the confusion matrix. This could potentially be improved with some consideration to

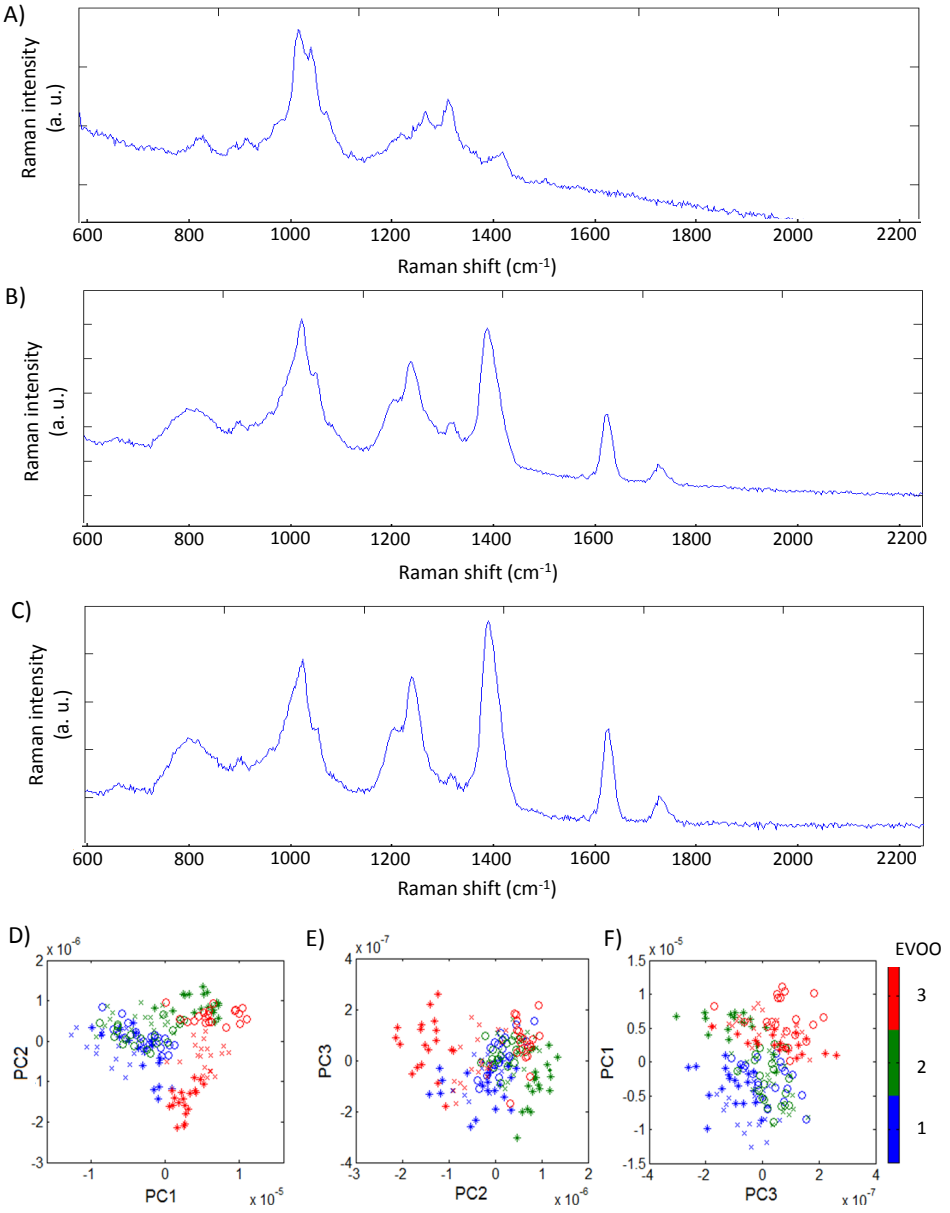

FIGURE 6.19: Raman spectra were acquired of EVOO on a paper substrate by the compact Raman device. A) Typical Raman spectrum of paper alone, B) raw Raman spectrum of EVOO on paper, and C) background subtracted spectrum of EVOO. D-F) Scatter plots using the first three PCs for three EVOO brands on paper, three devices were used for each EVOO represented by different markers 'o', 'x' and '∗'.

	Predicted EVOO		
Actual EVOO	1	2	3
1	48	10	2
2	19	41	0
3	0	5	55

TABLE 6.5: Confusion matrix summarising correct and incorrect classifications of three EVOO brands using paper devices.

the experimental design. For example, the laser in the IDRaman mini has a working distance of $8\,\mathrm{mm}$. Finding the optimum height at which to place the paper device may improve the Raman efficiency and consequently improve the discrimination ability.

Data points correlating to a specific paper device are indicated by different markers in the PC scatter plot. It can be observed that the individual paper devices can form distinct clusters, this can be seen most clearly in figure 6.19 D for EVOO brand 3, where the markers are separated along PC2. This suggests that each paper device generates a unique Raman signature. The variations introduced by the paper devices are not more significant than the variations between EVOO brands, as separation occurs within the cluster for a particular brand. This is likely due to the varying degrees of curling caused by wetting the paper, and could be prevented through an improved experimental design. An ideal solution would be to have a device that can hold the paper flat, for example sandwiching the paper device between two glass slides or 3D printing a clamp designed to fit in the chamber of the IDRaman mini.

6.5 Conclusion

It has been demonstrated in this chapter that classification of both Scottish and American whiskies is possible based on their Raman and fluorescence signatures. Discrimination was based on the ethanol content (Raman peak intensity) and the colour of the whisky (fluorescence signal). The physical origins of these differences arise from variations in the grain mixture used, the malting process, the cask used for maturation, and the age of the whisky.

A high discrimination efficiency was achieved with both the optofluidic chip and the compact Raman device using small sample volumes ($20\,\mu\mathrm{l}$ and $2\,ml$ respectively) and a relatively low acquisition time ($2\,\mathrm{s}$). These results indicate that there a real potential to integrate this technology to in-field sensing, which may aid the combating of counterfeit whiskies.

By comparison of the PCs to two key flavour variables on a 'flavour map', there appear to be some correlations between PC values and the whisky's flavour. That

is to say PC1 correlates to light-rich tastes and PC3 corresponds to delicate-smoky flavours. It would be interesting to expand this study to a larger sample size to further explore the relationship.

It has also been demonstrated that it is possible to use either Raman spectroscopy alone or fluorescence spectroscopy alone for the discrimination of five commercially available EVOO brands. Each providing discrimination based on different physical properties of the oil; Raman spectroscopy probes the chemical composition of the oil and has key peaks corresponding to oleic acid, and fluorescence spectroscopy discriminates between EVOOs based on variations in their colour. Standard Raman spectroscopy combines both Raman and fluorescence information giving a more complete description of the samples. Indeed it was observed that standard Raman spectroscopy provided an improved discrimination efficiency over WMRS.

Standard Raman spectroscopy therefore shows potential for combating the counterfeiting and adulteration of EVOO. An interesting next step would be to intentionally adulterate samples of EVOO to test the lowest limit of detection. It would be of significant interest to employ spatially offset Raman spectroscopy (SORS) [126] which would obviate the need for opening bottles, creating a truly useful technology for in-field analysis.

The key challenge to overcome when implementing this technology is that the effect of ageing can cause confusion for classification by PCA and would necessitate frequent retraining, thus limiting its applicability. It has been demonstrated that the effect of oxidation can be minimised by careful selection of the PCs used for analysis. This is a promising approach although future studies would be required on a larger data set, including same brand EVOOs from different years, to account for variations in weather and soil conditions. Additionally it would be useful to intentionally strongly oxidise samples, either through exposure to oxygen, light, or high temperatures and thus test the limits of the ability to suppress the effects of oxidation on EVOO classification.

It is surprising that Raman spectroscopy is sensitive to oxidation over such short time periods. The highly sensitive nature of Raman spectroscopy may therefore be useful for monitoring changes in the oxidation state of EVOO during production, transportation, and storage to ensure high quality EVOO at the point of sale. The

compact Raman device gave a high discrimination efficiency achieving an average sensitivity and specificity of 98.4% and 99.6% respectively. This indicates a real potential to bring this technology to in-field sensing and avoids the need for centralised laboratories that require highly trained personnel. Furthermore, as neither Raman spectroscopy nor fluorescence spectroscopy require the use of any additional chemicals it would be an ideal technology to integrate into in-line quality testing procedures in the future.

The use of paper devices appears to be a promising candidate for a cheap, disposable, and easy to use analytical substrate compatible with in-field testing and the compact Raman device. However, further optimisations to the design of the sample holder are required to improve the discrimination efficiency.

Relevant Publications

- **N. McReynolds**, J. M. A. Garcia, Z. Guengerich, T. K. Smith, K. Dholakia, "Optical spectroscopic analysis for the discrimination of extra-virgin olive oil", (2016) Appl. Spectrosc. 70(11), 1872-1882.

Contributions

J.M.A.G., Z.G. and I acquired data for EVOO studies. I was also responsible for acquisition of whisky data, data analysis, Raman band assignments, and lipid extraction for FAME analysis. T.K.S conducted the FAME analysis by GC-MS.

7 Towards SERS and optical manipulation with ultrasmooth gold nanoparticles

7.1 Introduction

Previous chapters have discussed that a key challenge concerning high throughput measurements, is the long acquisition time required for collecting Raman data (25s per WMRS spectrum). Chapter 4 explores the use of multimodal analysis to overcome this limitation, however an alternative technique would be enhance the Raman signal itself, thus permitting shorter acquisition times. The method of SERS can offer signal enhancement, as discussed in section 2.6. SERS is currently an area of significant interest as it is an attractive tool for sensing and detecting trace amounts of molecules with high specificity and sensitivity. SERS may therefore also benefit studies on detection of adulterants in food and drinks substances. However, it has not yet been established as a routine analytical method, which is most likely due to low substrate uniformity and poor reproducibility of SERS signal [350]. Recognising that there are problems with regards to the reproducibility of SERS spectra is the main motivation for studies presented in this chapter.

The main concern is the reproducibility of the intensity, as opposed to position, of the Raman bands, as the stokes Raman shift is typically constant [350]. As gold nanoparticles (AuNPs) are commonly used as SERS substrates, one important consideration is that the electromagnetic (EM) field enhancement has a strong dependence on the size and shape of the NP [99, 351, 352]. To obtain more uniform and reproducible EFs it is crucial that NPs are synthesised in a controlled manner, such that the particle size and shape is uniform and reproducible to a high degree. A method to synthesise ultrasmooth gold nanoparticles (USAuNPs) with improved monodispersity has recently been demonstrated [353], which may be able to provide more reproducible SERS scattering.

It is important to note that surface roughness can provide stronger surface-electron-photon-coupling, leading to an improved EF [93, 101]. Therefore, although USAuNPs may offer a more reproducible SERS signal, it will be at the cost of signal

enhancement. Indeed in some situations it may be more desirable to have minimal signal variation with a less enhanced SERS signal.

USAuNPs may also find use in applications such as optical trapping, which will be discussed further in section 7.5. The shape of a NP has direct relevance to its trapping characteristics [354–356]. Monodisperse USAuNPs could therefore provide a means for more reproducible studies, and a better comparison between theory and experimental observations for spherical NPs.

In this chapter USAuNPs are synthesised and characterised according to size distribution and circularity. Following this two potential applications are explored; SERS and optical trapping.

7.2 Nanoparticle synthesis

USAuNPs were synthesised according to a method based on a cyclic growth and chemical etching process, as established by Lee et al [353]. In the growth phase, mono-crystalline polyhedral shapes are formed with corners, which are isotropically removed by the slow chemical etching processes creating smooth, spherical AuNPs. The fabrication protocol for USAuNPs is described in full in Appendix K. Briefly, $20\,\mathrm{ml}$ ethylene glycol (Sigma-Aldrich), $0.4\,\mathrm{ml}$ pDADMAC (poly(diallyldimethylamonium chloride) 20% wt in H_20, Sigma-Aldrich) and $0.8\,\mathrm{ml}$ of $1\,\mathrm{M}$ phosphoric acid (Sigma-Aldrich) were added in a round-bottom flask and stirred for 2 minutes at room temperature. $0.02\,\mathrm{ml}$ of $0.5\,\mathrm{M}$ Chloroauric acid ($HAuCl_4$, Sigma-Aldrich) aqueous solution was added and this was stirred for 15 minutes at room temperature. The flask temperature was then controlled at $195°\mathrm{C}$ and continuously stirred for 30 minutes. The reaction was allowed to cool until the flask was at room temperature and a further $0.005\,\mathrm{ml}$ of $HAuCl_4$ was added. The solution was left stirring at room temperature for 20 hours. The NPs obtained were then purified by centrifugation and redispersion cycles. The NP solution was centrifuged at $11000\,\mathrm{rpm}$ at $5°\mathrm{C}$ for 20 minutes. The colourless supernatant solution was then carefully discharged to avoid collecting the precipitated NPs. The solid obtained was suspended in fresh ethanol and sonicated for 15 minutes. The entire purification process was repeated two further times.

7.3 Characterisation of nanoparticles

Two batches of USAuNPs were synthesised to be around $50\,\mathrm{nm}$ and $100\,\mathrm{nm}$ in diameter. Roughly 200 NPs were randomly selected from each batch and imaged using a scanning electron microscope (SEM) (Hitachi S-4800, $30\,\mathrm{kV}$), which were used for subsequent characterisation using MATLAB. NPs of the corresponding size were purchased from BBI solutions (BBI), which were also imaged and underwent the same analysis. Fig. 7.1 shows a collection of SEM images comparing USAuNPs to the commercially available BBI NPs, for particle sizes of $50\,\mathrm{nm}$ (A and C) and $100\,\mathrm{nm}$ (B and D). The NPs were characterised in terms of their size distribution and circularity. All the images were batch processed and analysed using MATLAB to compute the major and minor axis lengths, area, eccentricity, and perimeter of each NP. The same analysis was carried out using ImageJ for validation, which yielded the same results.

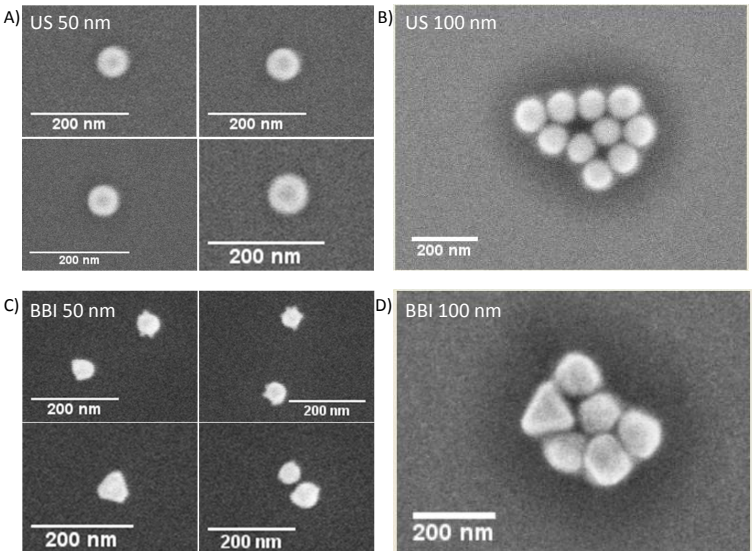

FIGURE 7.1: SEM images illustrating USAuNPs of A) $50\,\mathrm{nm}$ and B) $100\,\mathrm{nm}$, and BBI AuNPs of C) $50\,\mathrm{nm}$ and D) $100\,\mathrm{nm}$. USAuNPs appear more spherical with smoother surfaces than BBI NPs. Scale bar shows $200\,\mathrm{nm}$.

7.3.1 Size distribution

Particle size was measured as the major-axis length. The measured length of USAuNPs gave an average diameter of $62.5\,\mathrm{nm}\pm5.4\,\mathrm{nm}\,(2\sigma)$ and $103.6\,\mathrm{nm}\pm8.6\,\mathrm{nm}\,(2\sigma)$, where σ denotes a standard deviation. BBI NPs were characterised in the same

manner and yielded an average diameter of $60.1\,\mathrm{nm} \pm 6.6\,\mathrm{nm}\,(2\sigma)$ and $129.7\,\mathrm{nm} \pm 13.1\,\mathrm{nm}\,(2\sigma)$, respectively. The size distribution was comparable between USAuNPs and BBI NPs, with $\sigma \leq 10\%$. Table 7.1 and figure 7.2 summarise these results.

7.3.2 Circularity

Feret's diameter, also known as the caliper length, measures the distance between any two parallel boundaries of an object. Circularity, C is defined as the ratio between the area expected from the maximum Feret's Diameter, F_d of the object and the actual measured area, A of the object. These parameters were measured by Matlab and subsequently used to determine circularity, according to equation 7.1

$$C = \frac{4A}{\pi\, F_d^2}. \tag{7.1}$$

Thus circularity can have a value between one and zero, where one represents a perfect circle and zero represents a line segment.

Circularity was found to be greater for USAuNPs with $0.94 \pm 0.03\,(2\sigma)$ for $50\,\mathrm{nm}$ and $0.97 \pm 0.01\,(2\sigma)$ for $100\,\mathrm{nm}$, compared to $0.86 \pm 0.08\,(2\sigma)$ and $0.90 \pm 0.12\,(2\sigma)$ for the corresponding size of BBI NPs. This implies that BBI NPs deviate from perfect circularity ($\mathrm{C} = 1$) more than twice that of USAuNPs, which is comparable to that found by Lee et al [353]. Importantly, the monodispersity of circularity, measured as σ, is much improved for USAuNPs, which have almost three times narrower circularity distribution than that of BBI NPs for $50\,\mathrm{nm}$, and twelve times narrower for $100\,\mathrm{nm}$ NPs respectively. These results are summarised in table 7.1 and figure 7.2.

	US	BBI	US	BBI
	($50\,\mathrm{nm}$)		($100\,\mathrm{nm}$)	
Ave diameter (nm)	62.5	60.1	103.6	129.7
σ (nm)	5.4	6.6	8.6	13.1
Circularity	$0.94 \gg$	0.86	$0.97 \gg$	0.90
σ	$0.03 \ll$	0.08	$0.01 \ll$	0.12

TABLE 7.1: Physical properties of AuNPs: particle size and circularity of US-AuNPs and BBI NPs.

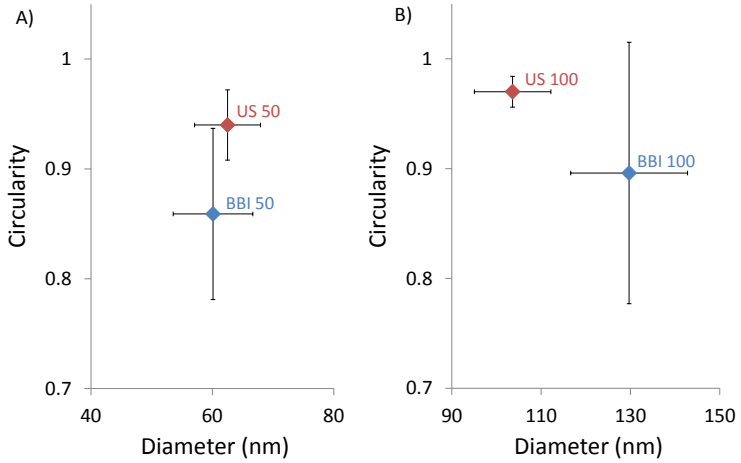

FIGURE 7.2: Physical properties of AuNPs. Comparison between US and BBI NPs of sizes A) $50\,\mathrm{nm}$ and B) $100\,\mathrm{nm}$. Data points represent the average value from approximately 200 NPs and error bars represent 2σ. USAuNPs have a greater circularity with a narrower σ compared to BBI NPs. US and BBI NPs have a similar σ in particle diameter.

7.4 Paper based SERS substrates

This section will address the use of AuNP treated paper as a substrate for SERS studies.

Paper analytical devices are a modern diagnostic platform offering advantages such as portability, ease of use and fabrication, fast response time, low cost, and compatibility with various optical techniques. They offer a potential solution to the ever increasing demand for inexpensive and easy to use point-of-care analytical devices; such technology could aid early disease diagnosis, and find use in monitoring chronic diseases, environmental monitoring, and food quality control.

Introduced by Whitesides et al in 2007 [349] paper devices are in their early developmental stages and offer many exciting possibilities. Patterning the paper with wax printing can produce hydrophilic channels and define detection zones [357]. The use of different detection reagents in multiple test-beds allows simultaneous analysis of various analytes, such as simultaneous detection of glucose, lactic acid, and uric acid [358] or measuring protein and glucose levels [349, 359]. Colorimetric assays enable qualitative detection where the unaided eye serves as a detector, as well as quantitative analysis by light transmission, where point-of-care devices, such as hand-held colorimeters [360], scanners [361], or mobile phones [362] can serve as

the detector.

Although these devices show promise to truly realise lab-on-a-chip (as opposed to chip in a lab) there are a number of limitations, such as poor accuracy and sensitivity [363, 364]. To overcome these challenges, paper based devices have been integrated with other optical techniques such as fluorescence, providing a more specific analysis for enzyme biomarkers [365], WMRS, with which quantitative detection of pharamaceuticals at nanomolar concentrations have been reported [366], and SERS [367–371]. Paper based devices treated with AuNPs have enabled SERS detection of trace amounts of narcotics, such as heroin and cocaine, with detection limits as low as $9\mathrm{ng}$ and $15\mathrm{ng}$ respectively [367], where the flexible nature of paper allowed it to act as a swab. AuNP treated paper may also be functionalised for antibody-antigen detection for biomedical applications [369]. Furthermore, only small sample volumes are required, as demonstrated by detection of Rhodamine 6G dye for samples as low as 10 femtomoles of analyte in $1\,\mu\mathrm{l}$ sample volume [368].

The performance of AuNP paper as a SERS substrate was assessed by Ngo et al [370] in comparison to other substrates such as a silcon wafer and hydrophobised paper. It was reported that after dipping filter paper in a AuNP solution for 24 hours most of the AuNPs where retained in the bulk of the paper. The surface and z-distribution of AuNPs essentially produced a 3-dimensional multilayer structure, which proved crucial for amplifying the SERS signal through inter and intralayer plasmon coupling, effectively creating more "hot spots" and providing an amplified SERS signal in comparison to the other substrates. A second method of loading the AuNPs was used to better understand NP distribution on the various substrates; a $1\,\mu\mathrm{l}$ droplet of AuNP solution was dropped on paper and silicon. Due to the wicking nature of paper allowing diffusion and rapid drying of water, and the intertwined structure of cellulose fibres "freezing" the adsorption state of the AuNPs, a uniform distribution of AuNPs was observed. In comparison, the nonporous and smooth nature of silicon wafer caused slower evapouration of water, allowing the AuNP suspension to concentrate around the edge of the droplet, essentially forming a "coffee ring" distribution. Similar to the silicon, hydrophobised paper took a longer time to dry and formed a smaller ring, as well as higher levels of NP aggregation. It was therefore concluded that the AuNPs adsorbed more uniformly on paper giving an

improved reproducibility of the SERS signal. It is for these reasons that paper was chosen as the substrate to explore the SERS performance of USAuNPs.

7.4.1 Methods

Paper device production

Whatman no 1 chromatography paper was chosen as it has a well defined, homogeneous structure and is pure (98% α-cellulose), thereby minimising the interference from process components such as polymers or coatings. It is also relatively inexpensive, costing less than 1p per device.

Paper devices were designed in Microsoft PowerPoint and bulk printed onto the filter paper using a solid wax printer (Xerox ColourQube 8570 DN). Upon heating at $150°$C on a hot plate for 2 minutes, the wax dispersed through the paper creating a hydrophobic barrier around a circular test-bed of 5mm diameter. The devices were cut such that a single spot was on each device, with a small border that could be used for taping to a microscope coverslip. The devices were allowed to cool prior to use. The process is outlined in figure 7.3.

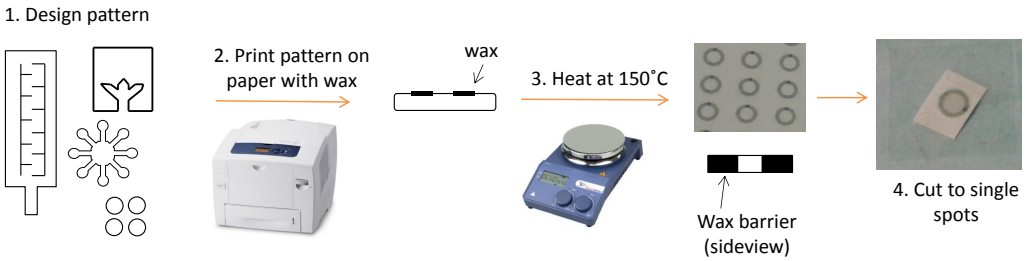

FIGURE 7.3: Devices can be designed using Microscoft PowerPoint, in this case small circles. The devices were then printed on an A4 sheet of Whatman no.1 filter paper using a solid wax printer. The paper was heated to $150°$C for 2 minutes to distribute the wax through the paper, creating a wax barrier. The devices were then cut to single spots for further use.

Procedure to load NPs on paper

AuNPs were loaded onto the paper in three manners: (1) by soaking the paper in AuNP solution for 24 hours, (2) pipetting a 1μl drop of AuNP solution on the paper, or (3) pipetting five 1μl drops of AuNP solution on the paper (allowing the paper to

dry between droplets). The devices were allowed to completely dry before further use. A comparison of drying in the oven at $46°C$ for 2 hours or in vaccuum for 2 hours showed no difference to the SERS performance. Devices were therefore dried in the oven for convenience. SEM images were acquired from paper devices, prepared in each of the three manners, to assess the dependence of the NP distribution on the surface of the paper to the loading procedure.

Sample preparation

4-Mercaptobenzoic acid (MBA) was chosen as a test analyte due to its ability to adsorb on the surface of AuNPs [372]. MBA solutions were made in $100\,\mathrm{nM}$ and $10\,\mathrm{nM}$ concentrations. A $1\mu\mathrm{l}$ drop of MBA solution was added to the AuNP treated paper and left to dry for 20 minutes at room temperature. For use with a microscope stage the paper edges were taped to a microscope coverslide. This had the added advantage of reducing any curling of the paper that can happen when wet.

Raman spectroscopy set-up

The Raman system has been described previously in section 2.7 and the specifications to this study are detailed here. The paper structure consists of intertwining fibres that can cause the background signal to vary from spot to spot. A low NA objective was therefore used (20X Nikon, 0.5 NA) as a larger field of view can provide an averaging effect, minimising such variations. The laser power at the sample plane was reduced to $40\,\mathrm{mW}$ to prevent burning of the paper. As SERS signal is frequency dependent, standard Raman spectra (as opposed to WMRS) were acquired. An acquisition time of 4 seconds per spectrum was used. An air objective was used and the microscope slide was positioned such that the paper device was towards the objective, so as to avoid unnecessary reflections from the glass surface.

Three standard Raman spectra were acquired from each of three different locations on 5 paper devices per MBA concentration.

7.4.2 Results

NP distribution

SEM images were acquired from AuNP paper devices following the three loading procedures. It was observed that soaking the paper in AuNP solution for 24 hours does not provide a uniform distribution; the NPs were focused around air pockets in the paper and were more likely to form aggregates. One 1μl drop of AuNP solution did not contain enough NPs and therefore resulted in a sparse distribution, however with five 1μl drops there was a much more uniform distribution. SEM images for methods (1) and (3) can be seen in figure 7.4. These results indicate that the process of rapidly drying the water (as with small volume drops) helps to provide a more even coverage and prevents the NPs from clustering in air pockets (as with method (1)). This is comparable to the observations made by Ngo et al [370].

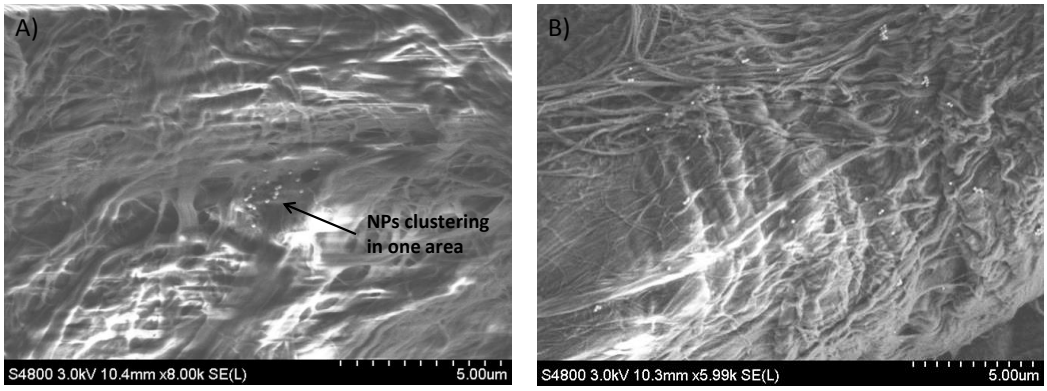

FIGURE 7.4: SEM images of NP distribution on paper following the loading procedure of A) soaking in AuNP solution for 24 hours or B) adding five 1μl drops of AuNP solution. The method of applying droplets provides a more uniform distribution of NPs.

SERS detection of MBA

Standard Raman spectra were acquired from MBA in the solid state, revealing key peaks at $814\,\mathrm{cm}^{-1}$, $1103\,\mathrm{cm}^{-1}$, $1191\,\mathrm{cm}^{-1}$, $1297\,\mathrm{cm}^{-1}$, and $1599\,\mathrm{cm}^{-1}$, which can be seen in figure 7.5 A. The cellulose fibres in paper also have characteristic standard Raman peaks at $1105\,\mathrm{cm}^{-1}$, $1343\,\mathrm{cm}^{-1}$, and $1386\,\mathrm{cm}^{-1}$ (as shown in figure 7.5 B). A $1\,\mu$l drop of $100\,\mathrm{nM}$ MBA was added to USAuNP treated paper, where devices had been prepared in each of the three different loading methods. Methods (1) and (2)

did not reveal any MBA SERS signal, as illustrated in figure 7.5 C-D, where only cellulose Raman peaks were recorded. The final method (3) was successful, and two intense SERS peaks were observed at $1084\,\mathrm{cm}^{-1}$ and $1591\,\mathrm{cm}^{-1}$ (figure 7.5 E), which correspond with the literature [372–374]. The peaks may be assigned as CH in-plane bending and CC stretching respectively.

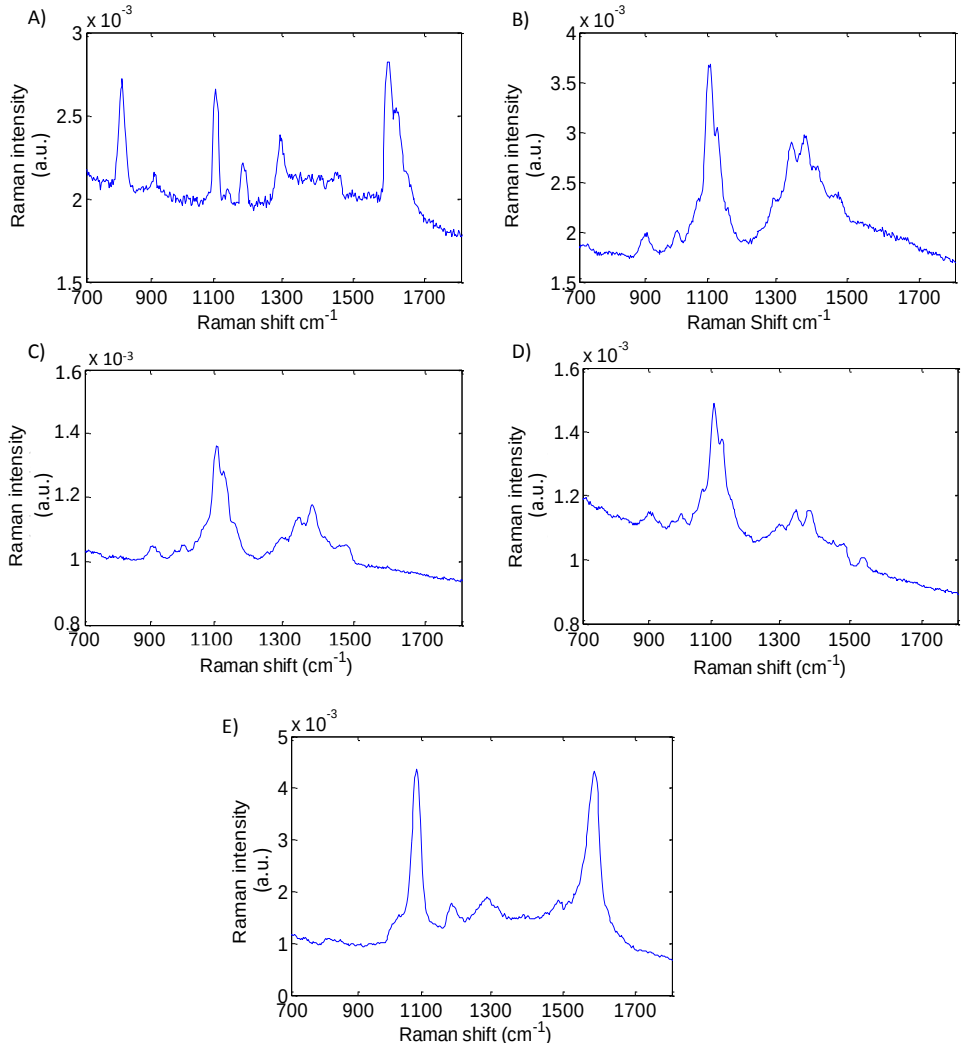

FIGURE 7.5: A) Standard Raman spectra of MBA in the solid state and of B) cellulose fibres in paper. $100\,\mathrm{nM}$ MBA was loaded onto AuNP treated paper prepared in three manners where C-E) show typical spectra obtained from devices prepared in manners (1) - (3) respectively. C-D)(1) - (2) were not successful and show only Raman scattering from cellulose. E) Illustrates SERS signal from MBA, with two key peaks at $1084\,\mathrm{cm}^{-1}$ and $1591\,\mathrm{cm}^{-1}$.

In comparison to the AuNP distribution, as observed in figure 7.4, it can be expected SERS active regions are sparse across devices prepared by methods (1) and (2). The more uniform distribution of AuNPs following five $1\,\mu\mathrm{l}$ drops of AuNP

solution, effectively provided more SERS hotspots, enabling a SERS signal to be recorded from MBA.

Reproducibility of SERS signal

Three spectra were acquired from three different locations on each of five devices for two different concentrations of MBA solution, $100\,\mathrm{nM}$ and $10\,\mathrm{nM}$. The average SERS spectrum and standard deviation for each concentration is illustrated in figure 7.6. The signal from one specific location was constant and repeatable over time, however spot to spot variations were significant, even on a single device. This resulted in a large standard deviation, represented by the shadowed region, around the mean spectrum.

Observations of the paper devices under white light show dark regions, often at the crossing point of cellulose fibres, that correspond to SERS active regions. It is reasonable then to conclude that these are areas of AuNP clusters. It was observed that stronger SERS signal intensities were recorded at darker regions of the paper. To demonstrate this point figure 7.6 B-C illustrate two spectra obtained from two locations on the same device, loaded with $10\,\mathrm{nM}$ MBA. When the darker region was probed (C), a greater SERS signal was recorded. This can be interpreted as varying numbers of NPs in a region, or the spacing between them, results in a varying SERS signal.

Spot to spot variations highlight the need for a more uniform distribution and controlled spacing between NPs. Only once this is addressed can the influence of NP shape and size variation be assessed. An obvious first step would be to optimise the NP loading process by using a solution with greater NP concentration or by loading more AuNP solution droplets on the paper. It would be expected that more droplets could provide a better coverage and an averaging effect.

Another important consideration is in controlling the spacing between NP aggregates, which can strongly influence the EM field distribution, and consequently the SERS intensity. Several chemistry solutions to this problem are being developed, such as planet-satellite assemblies, which can precisely control interparticle gaps [375], or the use of linker molecules to function as precise rigid spacers [376–378].

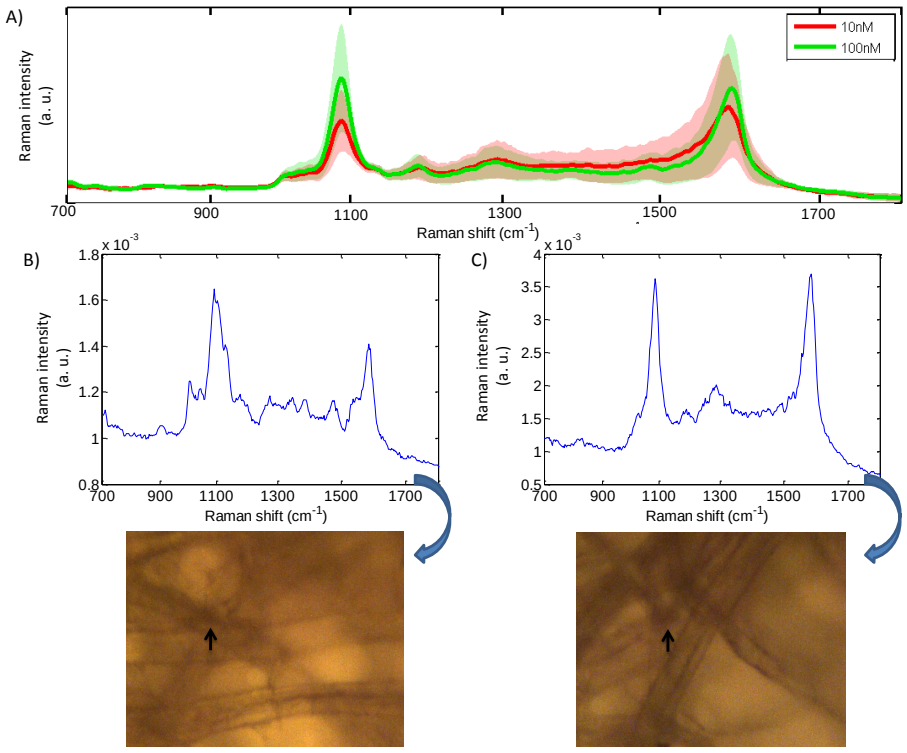

FIGURE 7.6: A) Solid lines represent mean spectra of 10 nM and 100 nM MBA across locations of five different paper devices. The standard deviation is illustrated by the shaded region. It can be seen that spot to spot intensity variations are more significant than intensity difference of MBA concentration. B-C) Spectra of 10 nM MBA were acquired from two different positions on the same AuNP treated paper device. Areas of more densely packed NPs appear darker under white light microscopy and provide a larger SERS enhancement. Consequently there are spot to spot variations illustrated by B) less NPs and C) more NPs.

After optimisation of the loading procedure, achieving a more uniform particle distribution and spacing, it would then be interesting to assess the reproducibility of SERS signals when utilising USAuNPs compared to commercially available AuNPs. However, there are some additional considerations when comparing USAuNPs to BBI NPs. For example, they are synthesised in a different manner and consequently each have different coatings; BBI are citrate coated, while the USAuNPs have a polymer coating. This will affect how the test analyte adsorbs to the NP surface, not to forget the minimum possible gap size between NP aggregates [379]. Furthermore, BBI NPs are negatively charged whereas the USAuNPs are positively charged, which may affect how they are distributed about the negatively charged paper.

It should be noted that there are other factors at play that can affect the reproducibility of a SERS signal. As SERS is a near-field effect the EM field distribution

plays an important role on the SERS intensity reproducibility. Only several regions of large enhancement (hot-spots) exist around a NP cluster [380]. The position that the molecule is attached on the metal surface, in relation to the EM field distribution, can therefore influence the reproducibility of SERS signal, or whether it can produce a SERS signal at all [381]. Furthermore, the number of molecules adsorbed on the metallic surface in the detection region, or its orientation to the metallic surface, can also make it challenging to achieve high uniformity and reproducibility [350, 382].

7.5 Introduction to optical trapping

Lasers are also useful tools for optical manipulation of mesoscopic particles. One particular type of optical manipulation is known as optical tweezers for optical trapping. Optical trapping was first realised by A. Ashkin in the early 1970s when he demonstrated that the forces of radiation pressure from a focussed laser beam could displace and levitate small transparent micrometer sized particles [383]. He later developed a stable 3-dimensional trap based on counter-propagating laser beams [384], followed by a single-beam gradient force optical trap [385, 386].

Optical trapping has found a range of applications in both physics and biology, such as trapping and cooling of atoms [387], manipulation of DNA or live bacteria [388], the application and measurement of picoNewton level forces, and measurement of displacements in the nanometer range [389]. Beads are commonly used as handles to probe molecular motors [390] and the elasticity of cells or DNA [391, 392]. Optical tweezers may also be combined with other techniques such as Raman spectroscopy [393] or cell sorting [394].

The principal of optical trapping is based on radiation pressure forces in a tightly focussed laser beam. As light rays are refracted through a transparent particle there is a resulting change in momentum of the light. Consequently, to conserve the momentum of the whole system (according to Newton's third law), the momentum of the particle must also change. Traditionally the resulting optical force is considered in two components: a scattering force, in the direction of the incident light beam, and a gradient force, in the direction of the intensity gradient of the beam.

In the case of trapping a small sphere (with radius much smaller than the wavelength of the trapping laser) the optical forces can be calculated by treating the particle as a point dipole [30]. In this approximation the scattering and gradient forces can be considered separately. The scattering force is due to absorption and reradiation of the light and may be calculated according to equation 7.2

$$F_{\text{scat}} = \frac{I_0 \sigma n_2}{c} \tag{7.2}$$

where I_o is the intensity of the incident light, σ is the scattering cross-section of the sphere, n_2 is the index of refraction of the medium, and c is the speed of light in vacuum. Upon substitution of the scattering cross-section [30, 395] we get

$$F_{\text{scat}} = \frac{I_0 n_2}{c} \frac{128\pi^5 r^6}{3\lambda^4} \left(\frac{m^2 - 1}{m^2 - 2} \right)^2 \tag{7.3}$$

where m is the ratio of the index of refraction of the particle to the index of refraction of the medium (n_1/n_2).

When $r \ll \lambda$ the external field induces positive and negative charges on the opposite poles of the sphere. This induces a polarisation of the sphere and a resulting gradient force, as described in equation 7.4

$$F_{\text{grad}} = \frac{2\pi\alpha}{c n_m^2} \Delta I_o \tag{7.4}$$

where α is the polarisability of the sphere given by

$$\alpha = n_m^2 r^3 \frac{m^2 - 1}{m^2 + 2} \tag{7.5}$$

The gradient force is proportional to the optical intensity gradient at the focus as well as the polarisability of the sphere.

An equilibrium point exists, from which any displacement of the particle results in a restoring force towards that point. The optical trap essentially acts as a Hookean spring, with a characteristic trap stiffness dependant on the light intensity. These forces can be used to form a stable 3-dimensional optical trap, as illustrated in figure 7.7.

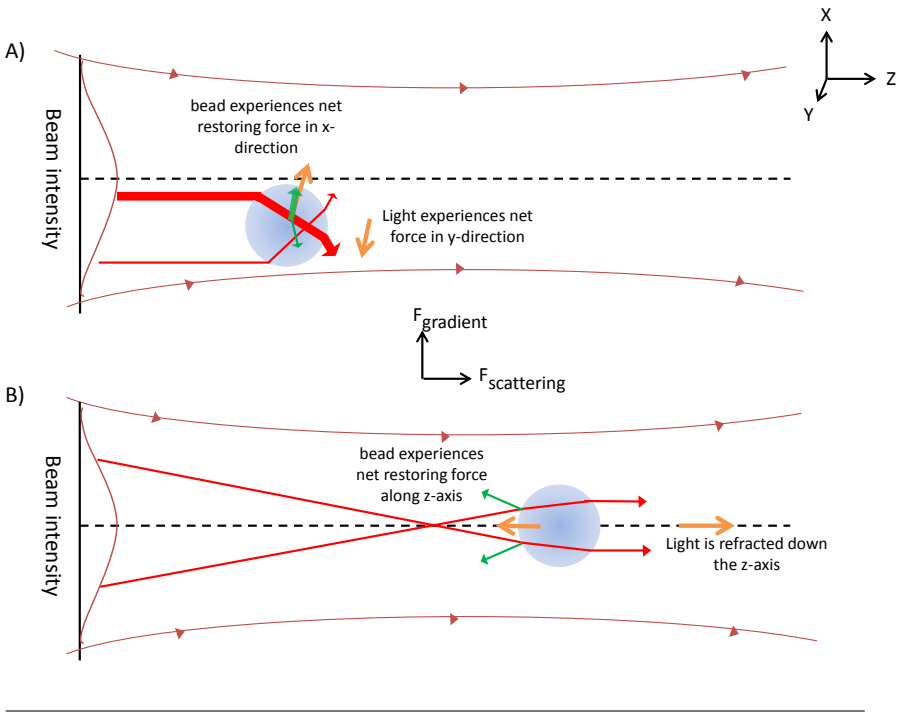

FIGURE 7.7: Ray description of the A) gradient forces and B) scattering forces experienced in an optical trap. Intensity of light rays is represented by line thickness, refracted ray lines are shown in red, forces on the particle in green, and net forces in orange. A) When light rays are refracted by the particle, the photons experience a change in momentum. This is balanced by an equal but opposite force on the bead, the net force is in the direction of the intensity gradient and slightly down the z-axis. B) A stable trap requires focused light, producing a 3-dimensional intensity gradient. In this case refraction results in a net force on the particle towards the focus. Any displacement of the particle away from the focus causes an imbalance of optical forces, returning it to the equilibrium position.

Polystyrene or silica beads are used in the majority of optical trapping studies as they are highly refractile and may therefore be strongly trapped [396]. As a stable 3-dimensional trap necessitates that the gradient force must overcome the scattering and absorption forces, metallic objects have generally been considered a poor candidate due to the relatively large associated scattering and absorption forces. Dielectric NPs, however, are generally more challenging to trap (in comparison to larger particles) as the scattering force scales with r^6 and the gradient force scales with the particle volume ($F_{\text{grad}} \propto r^3$) (equations 7.3 - 7.5). Consequently, optical trapping of NPs becomes governed by the gradient forces in the system, which must be sufficient to overcome Brownian motion.

The gradient force can be enhanced by choosing a material with a large polarisability (equation 7.4), which occurs at certain frequencies for metallic spheres. The

polarisability of metallic NPs is strongly wavelength-dependent due to the property of surface plasmon resonance (the collective oscillations of free electrons excited with light). As a result optical forces can be significantly enhanced for metallic NPs at certain wavelengths and enable the, otherwise impossible, trapping of small NPs [355, 397–399]. It should also be noted that the absorption is also enhanced, which can come at the price of heating and partially cancel out the effects of an enhanced gradient force. Svoboda and Block first demonstrated that AuNPs in the Rayleigh regime ($r \ll \lambda$) may be stably trapped. Due to the much greater polarisability of gold, trapping forces achieved were 7 times greater for AuNPs when compared to latex particles of a similar size [400]. The use of smaller sized particles is important for the study of biological systems, in order to minimise any interference with natural dynamics and functions.

Gold possesses several physical and chemical properties which make it an attractive material for biological applications, for example the inert nature of gold makes it non-toxic to cells, and AuNPs may be easily functionalised by anchoring thiol linkers in their monolayers. AuNPs may therefore be utilised in both therapeutic and diagnostic applications and have their surface chemically modified to enable cellular uptake [296, 401]. Other studies include making use of the high absorption coefficient to use AuNPs as a local heat source [402, 403]. Additionally, a range of studies exploring fundamental physics have been conducted such as optical binding [404], trapping in air or vacuum [405], and ultrafast spinning using circularly polarised light [406].

The morphology of AuNPs is an important consideration. Surface plasmon resonances are sensitive to the particle's shape and can therefore tune its optical properties [407, 408]. It has also been demonstrated that the shape of a NP has direct relevance to its trapping characteristics and particle orientation [354–356]. Experimental trapping and theory have experienced some divergence for large NPs when sphericity is assumed; theoretical calculations predict that AuNPs with $d > 170\,\mathrm{nm}$ should not be able to be trapped, although experimental observations demonstrate trapping of NPs with diameters up to $254\,\mathrm{nm}$ [354, 355, 409, 410]. Non-spherical AuNPs add another element of complexity as they tend to orient with respect to the

trapping beam propagation and polarisation. Brzobohaty et al propose a coupled-dipole model which begins to explain the complex behaviour and orientation [354].

Commercially available NPs are virtually always used in trapping studies although they inherently have subtle non-uniformity in shape. More homogeneous NPs, such as the USAuNPs, may provide a means for more reproducible studies, and provide a better comparison between theoretical models and experimental trapping observations for spherical NPs. The use of these USAuNPs in optical trapping studies is therefore of significant interest and has led to this preliminary study, where the optical trapping properties of USAuNPs are explored in liquid. Data are also recorded for the commercially available BBI NPs for comparison.

7.6 Optical trapping of ultrasmooth gold nanoparticles

7.6.1 Experimental set-up

An optical trapping set-up was implemented around an inverted microscope (Nikon, TE2000) with a high NA microscope objective (Nikon E Plan $100\times$, NA=1.25 in oil). A linearly polarised beam of $1070\,\mathrm{nm}$ (IPG Laser GmbH, YLM-5-1070-LP, CW, $5\,\mathrm{W}$ maximum power) was expanded to overfill the BA of the objective, to obtain a diffraction limited focal spot at the trapping plane. To avoid significant laser-induced heating of AuNPs, the optical power used for trapping is maintained as low as $21.8\,\mathrm{mW}$ at the trap, where a modest surface temperature increase of $5.8^{\circ}\mathrm{C}$ was estimated [403]. The power in the trapping plane can be difficult to directly measure, and was therefore approximated according to the power measured at the BA ($58.8\,\mathrm{mW}$), the transmission of the objective at $1070\,\mathrm{nm}$ (58%), and the truncation of the beam at the BA ($\approx 64\%$).

AuNP samples were prepared in heavy water (deuterium oxide, D_2O) to minimise laser-induced heating of the surrounding medium by the absorption of the trapping laser at $1070\,\mathrm{nm}$. $20\,\mu\mathrm{l}$ of the colloidal suspension was placed in a chamber, created using a circular vinyl sticker spacer of $10\,\mathrm{mm}$ diameter and $100\,\mu\mathrm{m}$ thickness, and enclosed with type-1 glass coverslips. AuNPs were trapped at an axial distance of $4-5\,\mu\mathrm{m}$ above the glass substrate to avoid any proximity effects. Care was taken to ensure no second particle was trapped whilst taking measurements.

A fast framing CMOS camera (Mikrotron MC1362) was used to acquire images of back-scattered light from a trapped AuNP at a frame rate of $1100\,\mathrm{fps}$ for $2.7\,\mathrm{s}$, recording 3000 frames in total. Approximately 75 measurements were carried out for each batch of AuNPs, which were subsequently used to analyse the trap stiffness based on the equipartition theorem.

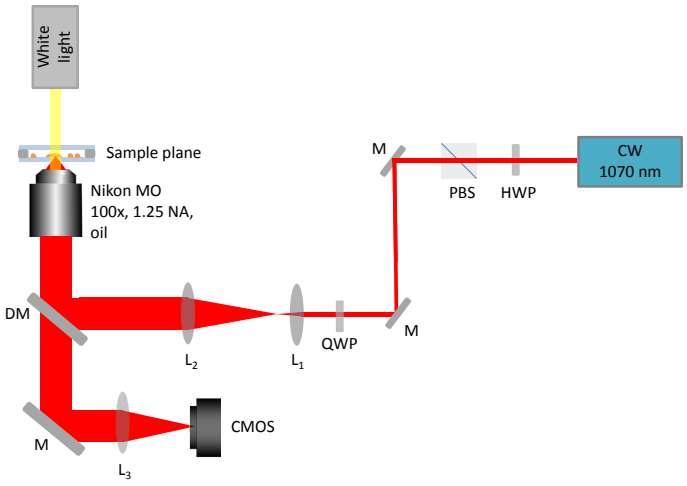

FIGURE 7.8: Schematic of optical trapping system (not to scale). HWP- half-wave plate, PBS- polarising beam splitter, M-mirror, QWP- quarter wave plate, DM- dichroic mirror, MO- microscope objective, L- lens. Note that white light was only used for beam correction and was turned off during recordings.

7.6.2 Video-based position sensing

The position measurement for the trapped AuNPs was determined along the x and y axes for each frame using a centre-of-mass (COM) tracking algorithm. The key steps are depicted in figure 7.9. The first step was to subtract the background; videos were recorded when no NP was trapped as a measure of the background. These were recorded frequently to account for any laser drift or change in stage height. For each background video an average frame was calculated, which was then subtracted from each individual frame of subsequent trapping videos (figure 7.9 B). To further reduce the noise a Gaussian filter was applied. The Fourier transform was taken (figure 7.9 C) and a Gaussian fit, G was modelled as G$= e^{(-\frac{x^2+y^2}{\sigma})}$, where σ is related to the peak width. The σ value was chosen such that the central frequencies were kept and the noisy region was rejected (figure 7.9 D). The product of the Fourier transform and the Gaussian fit was then inverse Fourier transformed, to produce smoother scattering

rings with reduced background noise (figure 7.9 E). To check the Gaussian fit was optimised, the Fourier transform was multiplied by (1-G), this enabled visualisation of the rejected components (figure 7.9 F). Ideally this would not contain any useful information (from scattering rings) and only display random noise. The optimum Gaussian filter was found when $\sigma = 500$. The COM was then calculated along x and y, and displayed as a marker over the original image to monitor the NP position in each frame (figure 7.9 G).

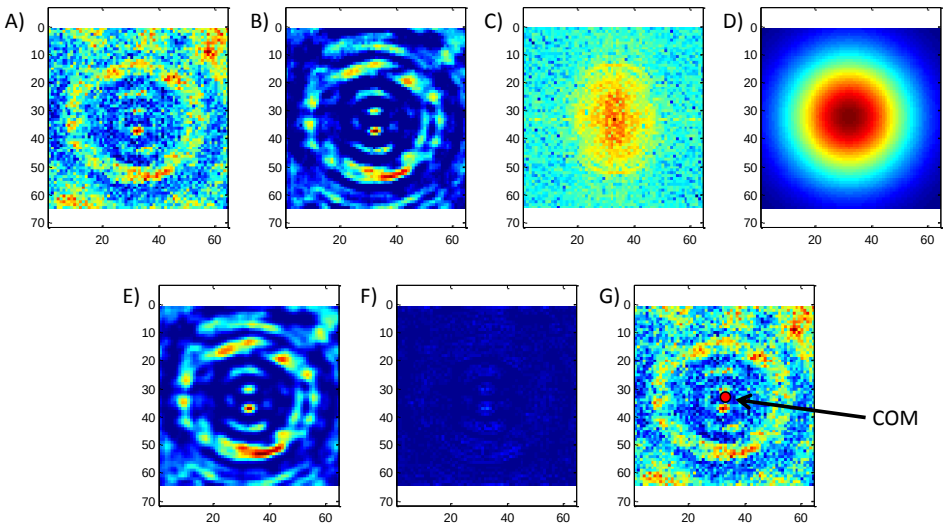

FIGURE 7.9: A) Raw frame of trapping video where rings represent light scattering, B) background subtracted frame. C) Fourier transform of B, and D) Gaussian filter. E) Product of Fourier transform and Gaussian filter was inverse Fourier transformed to produce smoother rings. F) Visualise rejected components to ensure Gaussian filter has not rejected important frequencies. G) COM is calculated along X and Y of the processed frame (E) and visualised by a marker on the original frame, to monitor COM position.

7.6.3 Trap stiffness calculation by equipartition theorem

A position distribution histogram of the 3000 COM data points was built for each video, which was then used to evaluate the position variance. Equipartition theorem was then applied to determine the trap stiffness according to equation 7.6

$$\kappa = k_B T / \sigma^2_{\text{com}} \tag{7.6}$$

where κ is the trap stiffness, k_B is the Boltzmann constant, T the temperature and σ^2_{com} denotes the variance of the particle position distribution [411].

25 AuNPs were trapped for each of USAuNPs and BBI NPs, for NP sizes of $50\,\mathrm{nm}$ and $100\,\mathrm{nm}$. Three videos were recorded for each trapped NP, giving a total of 75 trap stiffness measurements for each sample. The laser was blocked for $45\,\mathrm{s}$ between trapping instances, which was sufficient to allow the NP to leave the trap due to diffusion. Total intensity was monitored to ensure a second particle did not enter the trap during measurements.

7.6.4 Results

Fig. 7.10 shows the trap stiffness along the x and y axes, κ_x and κ_y respectively, of USAuNPs and BBI NPs for particle sizes of $50\,\mathrm{nm}$ and $100\,\mathrm{nm}$.

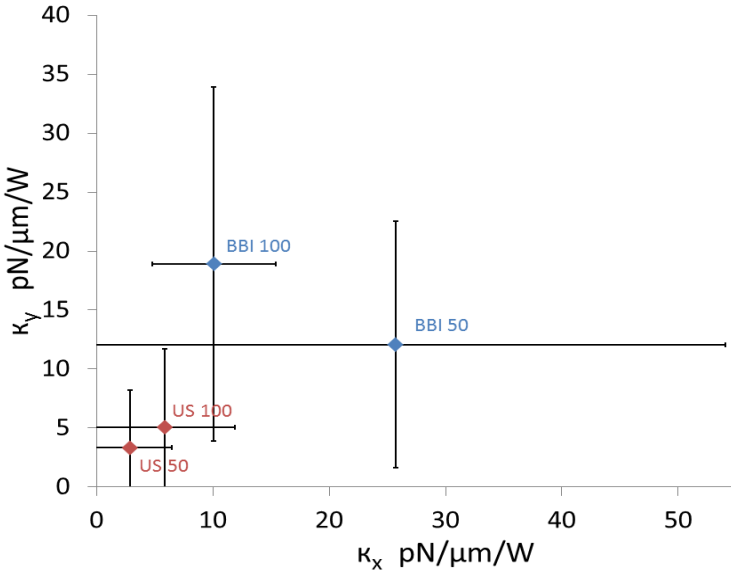

FIGURE 7.10: Comparison of trap stiffness measurements between US and BBI NPs, where κ_x and κ_y represent the trap stiffness along the x and y axes respectively. The more spherical USAuNPs exhibit a weaker trap stiffness than BBI NPs. Data points represent the average trap stiffness and error bars show 2σ.

Despite the differences in the experimental conditions, the average stiffness values obtained for BBI NPs are comparable (within one order of magnitude) to those reported in the literature [354, 355].

Notably trap stiffness was found to be much weaker for USAuNPs compared to BBI NPs. For USAuNPs of $50\,\mathrm{nm}$, for example, $\kappa_\mathrm{x} = 2.9 \pm 3.6\,\mathrm{pN}/\mu\mathrm{m}/\mathrm{W}\ (2\sigma)$, compared to $\kappa_\mathrm{x} = 25.7 \pm 28.3\,\mathrm{pN}/\mu\mathrm{m}/\mathrm{W}\ (2\sigma)$ for BBI. This can imply that the morphology of an AuNP strongly affects the trapping forces [354]. Importantly, the variation of κ measured as its standard deviation, σ is three to eight times smaller for USAuNPs

compared to that of BBI NPs of the corresponding size (see figure 7.10 and table 7.2 for summary).

	US	BBI	US	BBI
	($50\,\mathrm{nm}$)		($100\,\mathrm{nm}$)	
κ_x (pN/μm/W)	2.9	$\ll$ 25.7	5.9	$<$ 10.1
σ	3.6	$\ll$ 28.3	6.0	$\approx$ 5.3
κ_y (pN/μm/W)	3.3	$\ll$ 12.1	5.1	$\ll$ 18.9
σ	4.9	$<$ 10.5	6.7	$<$ 15.0

TABLE 7.2: Trap stiffness of USAuNPs and BBI nanoparticles of $50\,\mathrm{nm}$ and $100\,\mathrm{nm}$ in diameter.

Although a limited particle size range and number of AuNPs were considered, a qualitative agreement was observed with the experimental observations by Hansen et al and Brzobohatý et al, that stiffness is dependent on the particle size and is weaker for smaller AuNPs [354, 355]. However, non-spherical AuNPs can exhibit complex trapping behaviour because they typically orient with respect to the direction of the trapping beam propagation and polarisation, which can cause additional stiffness to the trap. Indeed for a large non-spherical AuNP ($d > 170\,\mathrm{nm}$) the coupled-dipole theory confirms the longitudinal trapping, which in contrast does not occur for spherical AuNPs. Our observation that USAuNPs exhibit much weaker trap stiffness compared to that of commercial AuNPs further validates the theory (see table 7.2). Supporting this there have been demonstrations [410] that the excitation of plasmonic resonances can enhance the optical trapping force experienced by non-spherical NPs, even enabling 3-dimensional trapping of plasmonic NPs with a low NA microscope objective [356, 407, 408].

Importantly, the variation of stiffness, σ is typically smaller for USAuNPs due to the monodispersity in circularity compared to BBI NPs (see table 7.1). This may enable more reproducible force measurements, and a reliable means to compare theoretical predictions and experimental observations for trapping of spherical NPs.

Further, for a spherical AuNP the lateral stiffness and its variation, σ along the x and y axes are expected to be comparable, as there is no preferential particle orientation, which is indeed the case for USAuNPs. On the other hand, BBI NPs exhibit a much higher trap stiffness with a larger σ on one axis compared to the other. This

further suggests that non-spherical AuNPs tend to align with the direction of polarisation of light and hence experience a different trapping force along that axis [354]. It should be noted that the lateral stiffness along these axes is also dependent on the trapping light field, which is often asymmetric due to a high NA microscope objective.

As discussed by Seol et al, laser-induced heating of trapped AuNPs can affect the trap stiffness measurement, as the equipartition theorem does not account for temperature increase with an accompanying decrease in viscosity of the surrounding water. To avoid such a problem a relatively low trapping power of $21.8\,\mathrm{mW}$ was used at the sample plane, causing a modest temperature increase of $5.8^{\circ}\mathrm{C}$ [403]. Thus the hydrodynamic effect on trap stiffness due to non-uniform viscosity around the trapped particle is minimised at this temperature. However, it would be intriguing to investigate how an USAuNP changes its light absorption, and consequently its hydrodynamic behaviour, compared to non-spherical AuNPs [412, 413]. To ensure measurements are robust to heating, it would be of benefit to check for agreement between trap stiffness values obtained by equipartition and power spectrum methods.

7.7 Conclusions

USAuNPs of $50\,\mathrm{nm}$ and $100\,\mathrm{nm}$ diameter were synthesised and characterised. They demonstrated a much improved circularity of $0.97 \pm 0.01\,(2\sigma)$, in comparison to $0.90 \pm 0.12\,(2\sigma)$ for conventional AuNPs.

A preliminary study of loading the NPs on paper devices demonstrated that it was possible to obtain a SERS signal for MBA. However, spot to spot variations were caused by a non-uniform distribution of NPs across the paper. The next steps would be to optimise the NP loading procedure, so as to obtain a more even NP distribution, and to control the spacing between NP aggregates. Generating a more reproducible SERS substrate is crucial for the integration of this powerful technique to a wide range of applications. The uniform USAuNPs may offer the ability to minimise SERS signal variations caused by inhomogeneities in NP size and shape.

Further to this, the first optical manipulation of USAuNPs was demonstrated, yielding a lower trap stiffness with a smaller standard deviation than that of conventional AuNPs. This observation supports the theoretical predictions and highlights the sensitivity of the optical trapping parameters of AuNPs to their morphology. The use of USAuNPs should allow a better comparison between theory and experiment where future studies would include investigating the effects of heating by comparison to power spectrum methods, trapping in air or vacuum, or rotation with circularly polarised light.

Contributions

Nicolas Marro trained me in the synthesis of USAuNPs, Blair Kirkpatrick and Alexandros Liles trained me in the use of the SEM. I conducted the characterisation of NPs and the SERS study. Yoshi Arita and Georgiy Tkachenko trained me in optical trapping and maintained the trapping system. I obtained the trapping data, wrote the Matlab code, and conducted the analysis, where Y.A and G.T. were always available for discussions regarding the analysis.

8 Conclusion and future outlook

8.1 Summary of the thesis

The work presented in this thesis focuses on Raman spectroscopy for applications in biomedicine and the food and drinks industry. The high chemical specificity of this technique alongside its non-invasive, label-free nature makes it an ideal candidate for use in these fields. The main limitation of Raman spectroscopy is its inherently weak Raman scattering, which either limits the SNR or necessitates long acquisition times. Various techniques to overcome this limitation were explored such as WMRS, SERS, or combination with a complementary optical technique for multimodal analysis, such as Raman spectroscopy with DHM or fluorescence spectroscopy.

Chapter 2 introduces the basics of Raman spectroscopy and its relevance in the fields of biomedicine and the food and drinks industry. A discussion is provided on methods for fluorescence suppression, with particular focus on the method of WMRS. The basic principle of SERS is discussed, followed by a detailed description of the construction of a free space Raman spectrometer. Finally, an overview of the post processing methods used throughout the thesis is provided.

Chapter 3 explored the use of WMRS to discriminate between key immune cell subsets. Monitoring the numbers of immune cell populations can indicate the presence of infection or inflammation, and monitor the body's response to drugs or therapy. It was demonstrated that WMRS may be used to discriminate between the closely related immune cell types CD8+ T cells, CD4+ T cells, NK cells, B cells, monocytes, and dendritic cell subsets mDC and pDC, with a high discrimination efficiency. Importantly, no inter-donor variability was observed, which is a step towards a label-free haemograph which would find use in both a clinical and research environment.

The main limitation for such a technology is the relatively long acquisition time required. Chapter 4 therefore deals with the combination of Raman spectroscopy with DHM, a fast imaging modality. Construction of the multimodal system was outlined, and simultaneous acquisition of Raman spectra and DHM phase images

was demonstrated; obtaining both chemical and morphological information on immune cell subsets: B cells, CD4+ T cells, and monocytes. Each modality was considered individually and in combination, where each was capable of providing a high discrimination ability. The two modalities may therefore be used as a means of validation against each other and to provide complementary information regarding a sample. Importantly, the rapid acquisition rates of DHM offers potential for high throughput screening, making the technology more clinically applicable.

Following this, chapter 5 expanded to demonstrate the applicability of label-free methods in neuroscience. Obtaining pure cultures of dopaminergic primary neuronal cells, in a label-free manner, would be a significant advance for modelling PD. WMRS was successfully able to quantitatively detect dopamine, however the limit of detection was not sensitive enough for physiologically relevant concentrations. SH-SY5Y cells may be differentiated into dopaminergic neuronal cells and are commonly used to study PD. The feasibility of using WMRS to discriminate between various differentiation states of SH-SY5Y cells was assessed. It was observed that RA differentiated cells had a distinct signature, although specificity was poor between undifferentiated and fully differentiated cells.

The food and drinks industry also benefits from the development of label-free technology, particularly when considering in-field analysis. One of the key challenges facing the whisky and the olive oil industry is the counterfeiting or adulteration of samples. Although background fluorescence is usually detrimental to Raman spectroscopy, studies presented in chapter 6 demonstrate that it also contains useful information regarding a sample. The combined Raman and fluorescence signal was successfully employed to identify various whisky and EVOO brands. The performance of a compact Raman device was compared to that of a free space system, and also demonstrated a high discrimination ability, indicating its potential for use in the field. A key challenge addressed was that oxidation of EVOO can cause confusion for classification by PCA. It was demonstrated that effects of ageing can be minimised by careful selection of the PCs used for analysis. Furthermore, it was demonstrated that paper offers potential as a cheap, disposable substrate for sample analysis and is compatible with the compact Raman device.

SERS is a promising enhancement technique with potential for trace analysis,

however it is limited in applicability due to its poor reproducibility. Size and shape of NPs have a large influence on their plasmonic properties; it is considered in chapter 7 that more uniform NPs may provide a more reproducible enhancement factor. Monodisperse, ultrasmooth AuNPs were synthesised and characterised, revealing high circularity with a comparable size distribution to commercially available AuNPs. USAuNPs were loaded on paper devices for use as a SERS substrate. Significant spot to spot variations were observed in the SERS signal, which is likely due to varying number of NPs in different detection regions across the device. Another potential application for USAuNPs, optical trapping, was considered. USAuNPs demonstrated a lower trap stiffness, and a smaller variation in trap stiffness, in comparison to conventional AuNPs. These results correlate well with the theoretical predictions, and demonstrates the sensitive relationship between optical trapping parameters and particle morphology.

8.2 Future outlook

The following sections will discuss new directions each of these works can take in the future.

8.2.1 Label-free haemograph

Chapter 3 demonstrated the use of WMRS to discriminate between closely related immune cell subsets. Current methods to indentify WBCs to a high degree of specificity requires the use of fluorescence tags functionalised for specific cell surface markers. Such labels pose the risk of changing the cell behaviour, making label-free technologies more attractive. The next step in the development of this technology would be to include further cell subsets, for example CD4+ T cells can further differentiate into TH17 cells, which play a role in inflammatory diseases. The potential to identify cells in an activated or naïve state was highlighted in chapter 3 by discrimination between activated and naïve B cells. However a follow up study using other B cell activators would be beneficial to confirm the results. It would be interesting to take this study further and include other cell populations in activated

and naïve states, which would find use in the study of cell-cell interactions and the body's response to drugs.

8.2.2 Multimodal system for cell classification

Chapter 4 demonstrated the combination of Raman spectroscopy and DHM to obtain both chemical and morphological information, which can be used for the discrimination of immune cell subsets. To make this technique clinically applicable it is necessary to achieve high throughput rates. The next step would therefore be to use the multimodal system such that DHM can provide a fast initial screening, allowing Raman spectroscopy to probe cells of interest. A first step may be to make use of the large field of view of DHM with real-time analysis. A further possibility would be to integrate this technology with a microfluidics based system for cell sorting. Furthermore, the additional morphological information could aid the discrimination between cells in an activated or naïve state, as they typically differ morphologically.

It was demonstrated in chapter 5 that discrimination between undifferentiated and fully differentiated SH-SY5Y cells was challenging, as they are chemically very similar, however, they appear different in their morphology. RA differentiated cells demonstrated a distinct Raman signature, although were morphologically indistinguishable from fully differentiated cells. This indicates that a multimodal analysis may aid the discrimination ability between all three cell types, which would be a step towards a label-free method to obtain pure neuronal cell cultures.

8.2.3 Intracellular dopamine detection

Detecting intracellular dopamine concentrations would be a significant step forward in understanding PD and the body's response to treatment. The work presented in chapter 5 demonstrated that WMRS was able to quantitatively measure dopamine down to millimolar concentrations. However, the detection of physiologically relevant concentrations would require signal enhancement of approximately 10^3 for a healthy person, or 10^6 for a PD patient. A future goal would therefore be to utilise dopamine-targeted AuNPs as intracellular probes, for SERS detection of intracellular dopamine levels.

8.2.4 Whisky flavour profile

Whiskies are currently classified according to their flavour by a small panel of experts, with no scientific validation. It was demonstrated in chapter 6 that Raman and fluorescence spectroscopy, accompanied by PCA analysis, has potential for classifying the flavour profile from a sample of whisky. This proof of principle experiment would benefit from further studies using a larger sample size.

8.2.5 EVOO classification

It was demonstrated in chapter 6 that Raman and fluorescence spectroscopy can successfully identify various brands of EVOO. An interesting next step for this technology would be to employ SORS, which would obviate the need to open bottles, thus becoming truly applicable to in-field analysis and counterfeit detection. It was also demonstrated that by careful selection of the PCs the effect of oxidation can be minimised. It would be useful to expand this study to include strongly oxidised samples, by exposure to heat, light, or oxygen. Additionally it would be useful to investigate the robustness of the technology to identify EVOOs of the same brand from different years.

8.2.6 Improving accessibility of Raman spectroscopy

The use of paper devices, demonstrated in chapter 6 and 7, offer potential as a portable, cheap, and easy to use substrate. Chapter 6 demonstrated the use of paper devices in the compact Raman device for the identification of EVOOs. Future steps would be to optimise the sample holder, which may improve the signal collection and solve the reproducibility issues, which are likely due curling of the paper. For example, a custom sample holder to keep the devices flat and at the focal plane of the incident laser. There is a wide range of potential applications for such devices in the food and drinks industry and also for biomedicine. By treating paper devices with AuNPs, as seen in chapter 7, the Raman signal can be enhanced; offering potential for trace analysis. Furthermore the AuNPs may be easily functionalised for the detection of specific biochemical markers.

Paper devices could also be used as colorimetric indicators. A prototype of a portable and inexpensive detection device "lab-in-a-pipe" was produced using 3-D printed components, a wifi enabled camera, and a diode laser, as demonstrated in figure 8.1. With the addition of appropriate filters, such a device can easily be modified to be compatible with fluorescence detection. Lab in a pipe could be used in potential future applications with paper microfluidic devices, and would be ideal for in-field analysis.

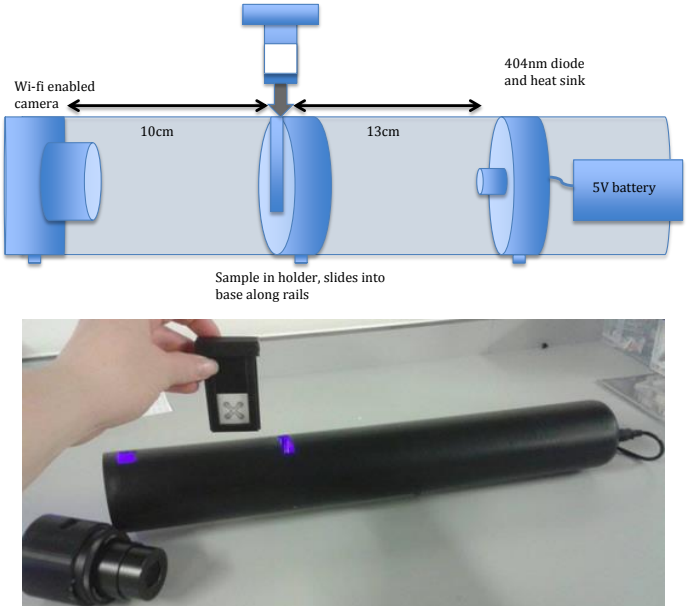

FIGURE 8.1: A prototype "lab-in-a-pipe" apparatus for portable analysis of paper devices.

8.2.7 Ultrasmooth gold nanoparticles

SERS detection typically suffers from poor reproducibility, which may be due to the sensitive relationship between plasmonic behaviour and particle size and shape. Chapter 7 demonstrated the synthesis of monodisperse, ultrasmooth AuNPs and investigated their potential to provide a more reproducible SERS signal. However, other important contributing factors such as the gap size between NP clusters, and the number of NPs in a region, can affect the SERS signal. This preliminary study would benefit from loading more NPs on the paper to provide a more uniform NP distribution. It would also be of great interest to employ USAuNP assemblies to provide controlled NP spacing.

USAuNPs may provide a better comparison between theory and experimental observation concerning the optical trapping of spherical AuNPs. A preliminary study in chapter 7 explored their optical trapping properties in liquid. It would be interesting to further expand this study to include analysis by power spectrum method, to account for any heating effects, and to probe their optical trapping properties in air and vacuum, or with circularly polarised light.

8.3 Conclusion

The applications presented in this thesis highlight the potential for Raman spectroscopy in the field of biomedicine. The importance of a multimodal approach, to overcome limitations imposed by a single modality is also demonstrated. Importantly, the studies demonstrated here pave the way for the development of a label-free haemograph, a powerful tool for both researchers and clinicians. The broader applicability of label-free methods was demonstrated with studies in the fields of neuroscience and the food and drinks industry. The potential for Raman and fluorescence spectroscopy to identify different brands of whisky or EVOO may aid the detection of counterfeiting or adulteration. Furthermore, the integration of Raman spectroscopy to in-field analysis was addressed through the use of a compact Raman device or by utilising paper devices as a cheap and easy-to-use substrate.

A Ethics Statement

University of St Andrews
from first to foremost

600 YEARS
1413 – 2013

Project Title	**Investigation of immune cell behaviour**
Researchers Name(s)	**Dr Simon Powis, Miss Fiona Cooke, Professor Malte Gather, Dr Marcel Schubert, Dr Andrew Morton, Dagmara Wiatrek, Professor Garry Taylor, Dr Helen Connaris, Professor Kishan Dholakia**
Supervisor(s)	**Dr Simon Powis**
Department/Unit	**School of Medicine**
Ethical Approval Code (Approval allocated to Original Application)	**MD10814**
Original Application Approval Date	**14th February 2014**
Amendment Application Approval	**24th September 2015**

Ethical Amendment 3 Approval

Thank you for submitting your amendment application which was considered by the School of Medicine Ethics Convener on the 24th September 2015. The following documents were reviewed:

1. Ethical Amendment Application Form YES

The University Teaching and Research Ethics Committee (UTREC) approves this study from an ethical point of view. Please note that where approval is given by a School Ethics Committee that committee is part of UTREC and is delegated to act for UTREC.

Approval is given for ten years from the original application only. Ethical Amendments do not extend this period but give permission to an amendment to the original approval research proposal only. If you are unable to complete your research within the original 10 year validation period, you will be required to write to your School Ethics Committee and to UTREC (where approval was given by UTREC) to request an extension or you will need to re-apply. You must inform your School Ethics Committee when the research has been completed.

Any serious adverse events or significant change which occurs in connection with this study and/or which may alter its ethical consideration, must be reported immediately to the School Ethics Committee, and an Ethical Amendment Form submitted where appropriate.

Approval is given on the understanding that the 'Guidelines for Ethical Research Practice' (http://www.st-andrews.ac.uk/media/UTRECguidelines%20Feb%2008.pdf) are adhered to.

Yours sincerely

Morven Shearer

Dr Morven Shearer
Convenor of the School Ethics Committee

UTREC Convenor, Mansefield, 3 St Mary's Place, St Andrews, KY16 9UY
Email: utrec@st-andrews.ac.uk Tel: 01334 462866
The University of St Andrews is a charity registered in Scotland: No SC013532

FIGURE A.1: Ethics approval to work with immune cells under the supervision of Dr Simon Powis and Prof Kishan Dholakia

B Immune cell purification and characterisation methods

All samples were acquired after obtaining written and informed consent. The study was approved by the School of Medicine Ethics Committee, University of St. Andrews: Project MD6324 - Investigation of immune cell behaviour. Participant consent forms and information sheets were also approved by the School Ethics Committee.

B.1 Cell purifications for CD4+ and CD8+ T cells, NK cells, plasmacytoid and myeloid dendritic cells, B cells, and monocytes

10-30 ml blood was collected into heparin Vacutainer tubes from healthy donors. Peripheral blood mononuclear cells (PBMC) were separated on Histopaque (Sigma, Poole UK) and washed in PBS/0.1% bovine serum albumin (BSA) (Sigma) or PBS/0.5% fetal calf serum (FCS) (Life Technologies, Paisley, UK). Cells were isolated using Dynabeads (Life Technologies) untouched human CD4 T cell kit (depleting antibodies comprising anti-CD8, CD14, CD16a, CD16b, CD19, CD36, CD123, and CD235a), Dynabeads untouched human CD8 T cell kit (depleting antibodies CD4, CD14, CD16a, CD16b, CD19, CD36, CD123, and CD235a) and Dynabeads untouched human NK cell kit (depleting antibodies CD3, CD14, CD36, HLA class II CD123, and CD235a). Dendritic cells were isolated using Meltenyi Biotec (Bisley, UK) MACS plasmacytoid dendritic cell isolation kit II, and MAC myeloid dendritic cell isolation kit (depleting antibodies not specified in DC isolation kits). B cells were isolated using Dynabeads untouched human B cell kit (depleting antibodies comprising anti-CD2, CD14, CD16, CD36, CD43, and CD235a), and monocytes using Dynabeads untouched human monocytes isolation kits (depleting antibodies comprising anti-CD3, CD7, CD16, CD19, CD56, CDw123, and CD235a). The method by which the dynabeads isolation kit works is depicted in figure B.1.

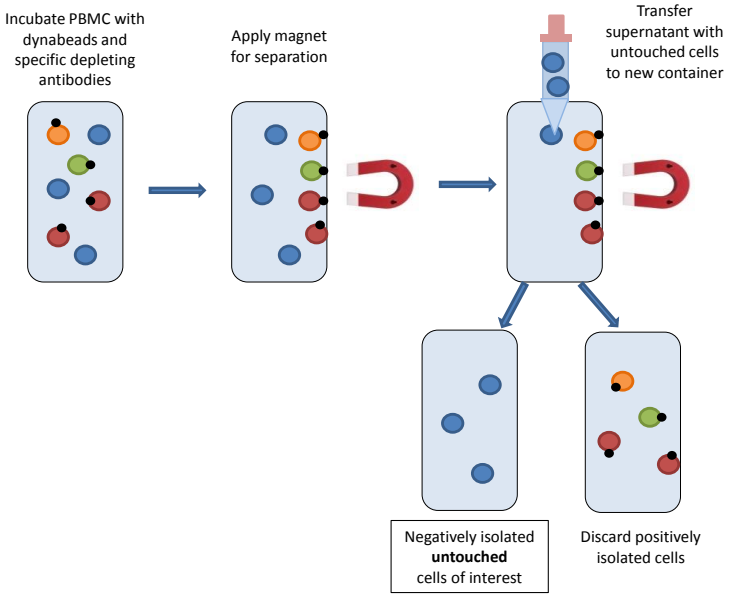

FIGURE B.1: Graphical depiction showing method of cell purification using negatively depleting Dynabeads isolation kits for an untouched isolated cell population.

B.2 Characterisation by flow cytometry and functional assays

B.2.1 Flow cytometry methods

Cells were blocked in 50% PFN buffer (PBS and 2% FCS) and 50% human plasma, then stained with PE-anti human CD4, PE-anti human CD8, PE-anti human CD56, APC-anti human CD303 and APC-anti human CD1c. B cells and monocytes were blocked in PFN buffer with 20% human serum. B cells were stained with FITC-CD3 or FITC CD19, and monocytes with FITC-CD3 or FITC-CD14 (ebiosciences, Hatfield, UK). Flow cytometry was performed using a Guava 8HT (Millipore, UK) running Guavasoft 2.5.

B.2.2 Functional assays

IL-2 Assay: 80,000 CD4+ T cells were incubated with or without $0.5\,\mu$l Human T-Activator CD3/CD28 Dynabeads (Life Technologies) and left at 37 °C in a 5% CO_2 incubator overnight. The supernatant was then assayed using a Human IL-2 ELISA Kit (Life technologies).

IFN-γ ELISPOT Assay: IFN-γ was assayed using Human IFN-γ alkaline phosphatase conjugated ELISPOT kit (MABTECH, Nacka Strand, Sweden). 200,000 PBMC and untouched CD8+ T cells were incubated with $10\,\mu\mathrm{g/ml}$ of the HLA-A11 restricted Epstein-Barr virus (EBV) peptide AVFDRKSDAK at 37 °C in a 5% CO_2 incubator for 48 hours.

CD107a Degranulation Assay: 100,000 NK cells were incubated with or without 10,000 major histocompatibility complex (MHC) class I deficient 721.221 cells for 6 hours at 37 °C in a 5% CO_2 incubator. After the first hour $2\,\mu\mathrm{l}$ of FITC conjugated CD107a (ebioscience) was added to samples. Samples were blocked, washed and analysed by flow cytometry as above.

B.2.3 Characterisation of CD4+ and CD8+ T cells, NK cells, and dendritic cell subsets pDC and mDC

The isolated cells were analysed for purity by flow cytometry and tested for biological activity corresponding with their phenotype. CD4+ T lymphocytes were obtained at a purity level typically up to 96% (figureB.2 A), and secreted high levels of the cytokine IL-2 in response to incubation with beads coupled with anti-CD3 and -CD28 antibodies (figureB.2 B). CD8+ T lymphocytes were obtained at a purity level typically up to 76% (figureB.2 C). When stimulated with the EBV peptide AVFDRKSDAK using cells from an individual known to express HLA-A11, which binds this peptide, IFN-γ secretion was induced from PBMC and in increased amounts from purified CD8+ cells (figureB.2 D). CD56+ NK cells were obtained at a purity level typically up to 88.7% , and displayed a typical CD56 low phenotype (figureB.2 E). NK cells are sensitive to the lack of MHC class I molecules on target cells, and upon incubation with the HLA class I deficient. 221 cell line, an increased expression of CD107a from 1% to 17% was observed, indicating redistribution of CD107a to the cell surface during degranulation leading to target cell lysis (figureB.2 F). CD303+ plasmacytoid (also known as lymphoid) DC were obtained at purity levels up to 92.1% (figureB.2 G) and CD1c+ myeloid DC were obtained at purity levels up to 77.8% (figureB.2 H). Light microscopy images representative of the purified cell populations are also shown, revealing the CD4+ and CD8+ T lymphocytes to be small

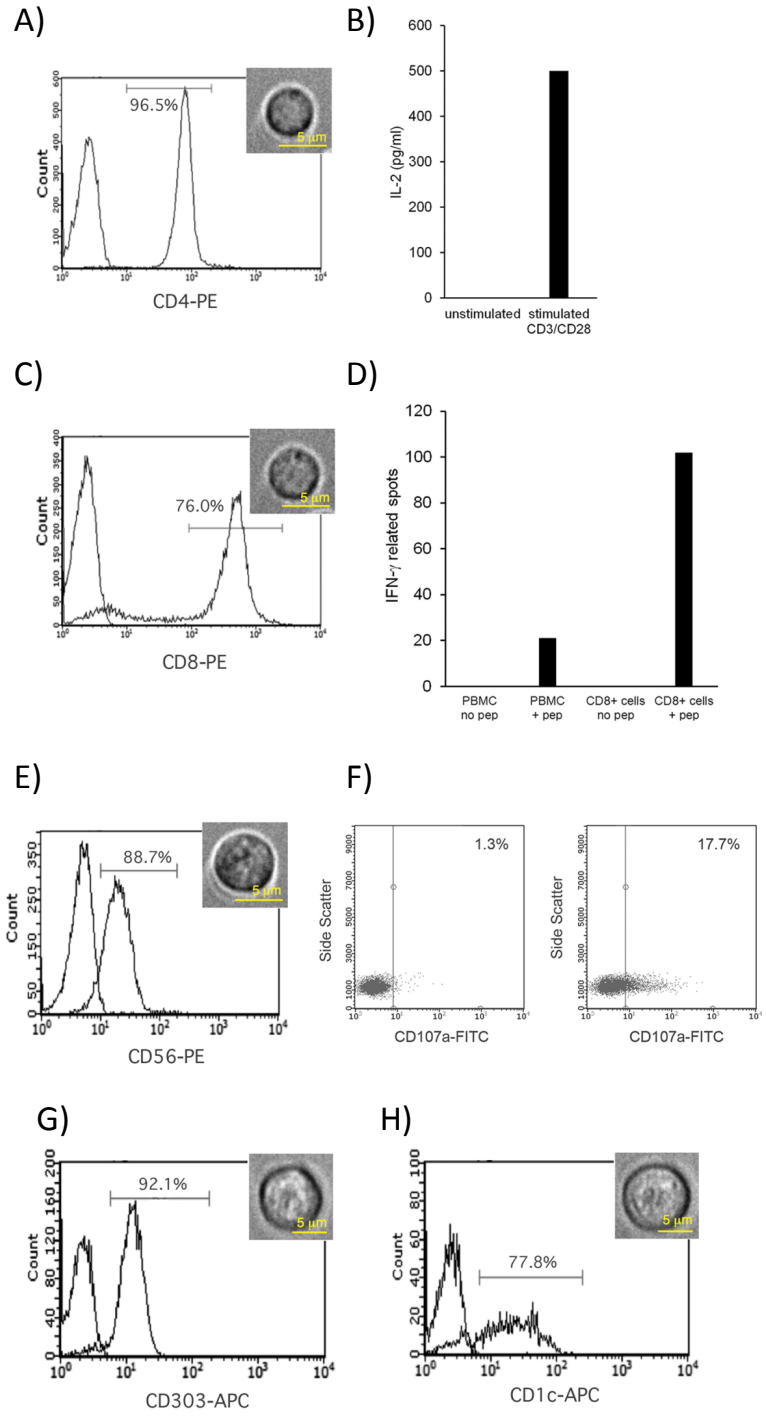

FIGURE B.2: Flow cytometric and functional characterisation of purified cell subsets. A) CD4 staining of isolated CD4+ T cells. B) IL-2 ELISA of CD4+ T cells stimulated with or without anti-CD3/CD28 beads. C) CD8 staining of isolated CD8+ T cells. D) IFNγ ELISPOT assay of PBMC and purified CD8+ T cells incubated with and without EBV derived peptide AVFDRKSDAK. E) CD56 staining of isolated NK cells. F) NK cell degranulation assay—CD107a staining of NK cells incubated without (left panel) or with (right panel) MHC class I deficient. 221 cells at a 10:1 effector to target ratio. G) CD303 staining of isolated pDC. H) CD1c staining of isolated mDC. The x-axis in each flow cytometry plot indicates fluorescent intensity. The left hand peak in each flow cytometry plot indicates control staining with an irrelevant antibody. Representative white light microscopy images of each of the purified cell populations used in Raman spectroscopy experiments are also shown.

lymphocytes around $7\,\mu m$ in size (figureB.2 A and C), the NK cells to be larger at around $9\,\mu m$ (figureB.2 E), typical of their historical classification as large granular lymphocytes. pDC and mDC are also shown to be around $9\,\mu m$ in size (figureB.2 G and H).

B.2.4 Characterisation of CD4+ and CD8+ T cells, B cells, and monocytes

The isolated cells were analysed for purity by fluorescence activated cell sorting (FACS) assay. Cells were obtained from two donors and the following purity levels were achieved: 89% and 91% for CD4+ T lymphocytes (figureB.3 A), 80% and 91% for CD8+ T lymphocytes (figureB.3 B), 100% and 100% for B cells (figureB.3 C), and 96% and 99% for monocytes (figureB.3 D). Data is shown for one donor only, although both gave essentially identical curves.

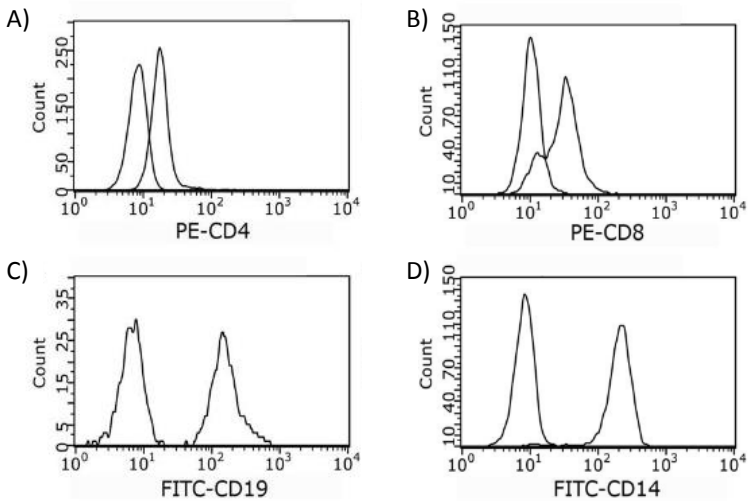

FIGURE B.3: Facs analysis of A) CD4 + T cells, B) CD8 + T cells, C) B cells, and D) monocytes from two donors revealing purity levels of 89% and 91% for CD4+ T cells, 80% and 91% for CD8+ T cells, 100% and 100% for B cells, and 96% and 99% for monocytes. The x-axis in each FACS plot indicates fluorescent intensity. The left hand peak in each FACS plot indicates the negative control (staining with an irrelevant antibody) and the right hand peak is the staining of the relevant antibody.

C Raman band assignments for immune cell populations

WMRS peak position (cm^{-1})	DNA/ RNA	Proteins	Lipids
621		C-C twist in phenylalanine	
645		C-C twist in tyrosine	
671		C-S stretching in cysteine	
725	adenine ring breathing		
800	O-P-O symmetric stretching		
938		C-C skeletal modes	
1007		symmetric ring breathing mode of phenylalanine	
1097	O-P-O symmetric stretching nucleic acids		
1129			C-C stretch
1209		phenylalanine, tyrosine, C-N stretching	
1259		Amide III	
1304	adenine, cytosine	adenine/amide III	
1345	polynucleotide chain		
1378	thymine, adenine, guanine		
1455		CH_2, CH_3 stretching	CH_2 deformation
1585	adenine, guanine		
1665		amide I α-helix, β-turn	C=C stretching

TABLE C.1: Assignment of bands in Raman spectra of immune cell populations discussed in chapter 3.

D WMRS spectra for immune cell subsets: a pairwise comparison

D.1 Pairwise comparisons of WMRS spectra for CD4+ T cells against CD8+ T cells, B cells, and monocytes

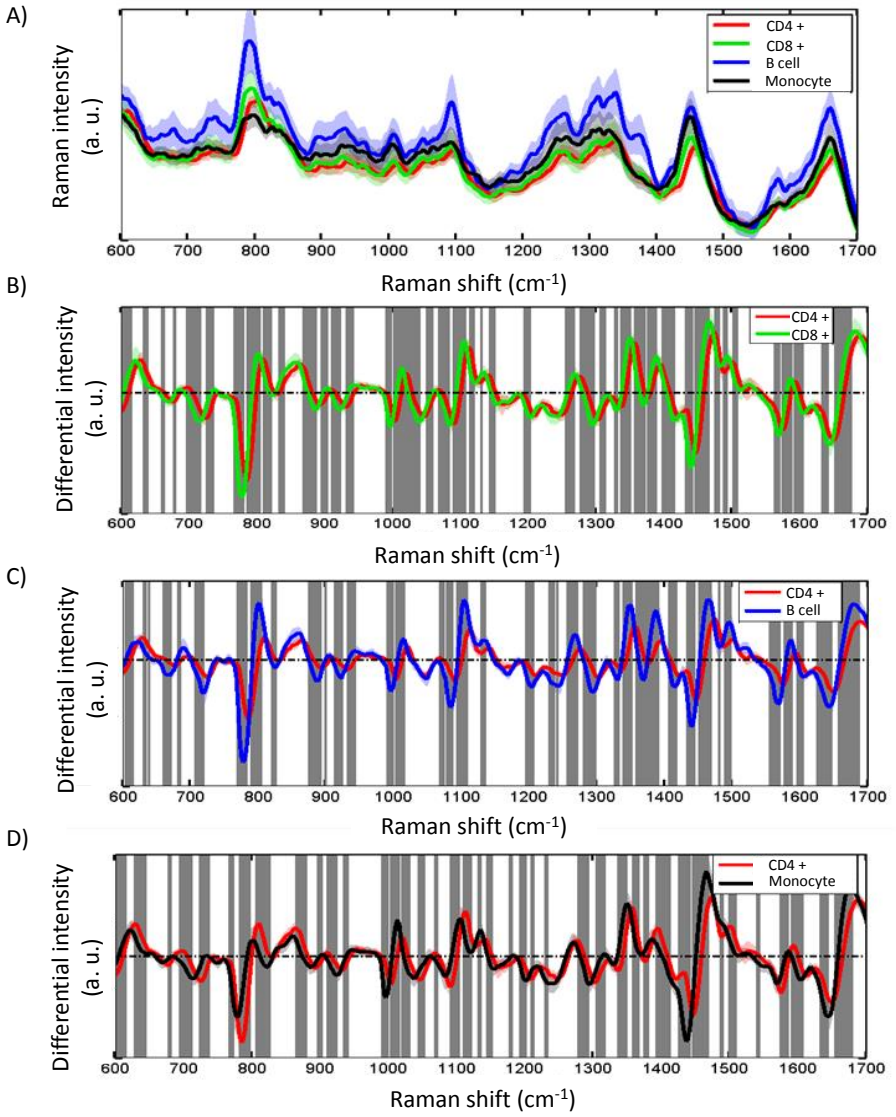

FIGURE D.1: WMRS spectra of purified immune cell subsets CD4+ T cells, CD8+ T cells , B cells, and monocytes. A) Mean standard Raman spectra of CD4+, CD8+, B cells and monocytes. Mean WMRS spectra of B) CD4+ and CD8+ T cells, C) CD4+ T cells and B cells, and D) CD4+ T cells and monocytes. Solid lines show the average spectrum of each cell population and shaded regions show the standard deviation. Grey vertical bars indicate regions of significant difference between two cell subsets, as estimated by student's t-test at a significance level of $p < 10^{-15}$.

D.2 Pairwise comparisons of WMRS spectra for CD8+ T cells against CD4+ T cells, B cells, and monocytes

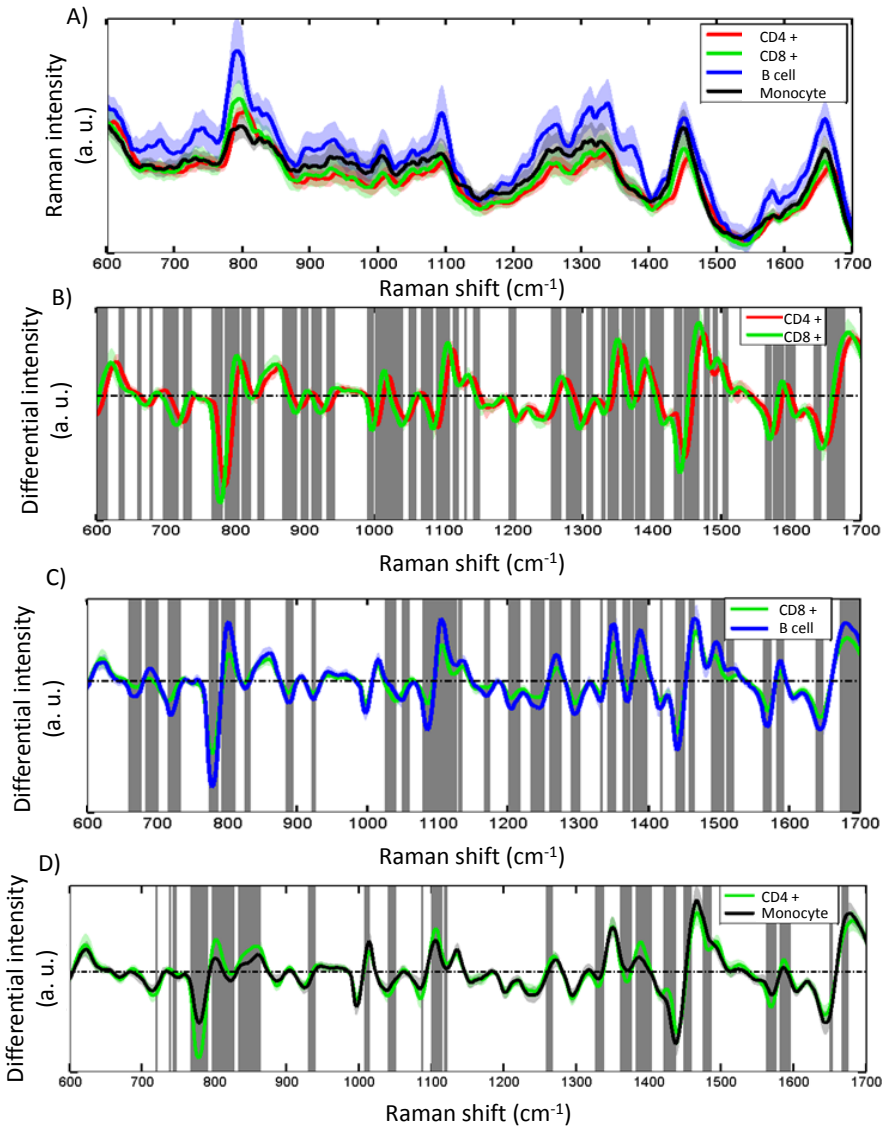

FIGURE D.2: WMRS spectra of purified immune cell subsets CD4+ T cells, CD8+ T cells , B cells, and monocytes. A) Mean standard Raman spectra of CD4+, CD8+, B cells and monocytes. Mean WMRS spectra of B) CD4+ and CD8+ T cells, C) CD8+ T cells and B cells, and D) CD8+ T cells and monocytes. Solid lines show the average spectrum of each cell population and shaded regions show the standard deviation. Grey vertical bars indicate regions of significant difference between two cell subsets, as estimated by student's t-test at a significance level of $p < 10^{-15}$.

E Matlab code for DHM analysis

E.1 Proccess raw DHM image to produce a phase map

```
%Analyze fringe patterns using FFT method.

file = '  '; \% insert path address to DHM image

fg = imread(file,'bmp');
frg = fg(:,:,1);
snap = frg;
snap = double(frg);

%%
fsnap=fftshift(fft2(snap));
figure(67);
subplot(231);imagesc(snap);axis image; title('orignal fringe
    pattern');
if ~exist('newmask')
newmask=false;
subplot(232);imagesc(log(abs(fsnap)));title('zeroth order')
h=imellipse(gca)
position0 = wait(h);
ma0=createMask(h);
subplot(232);imagesc(log(abs(fsnap)));title('first order')
h=imellipse(gca)
position1 = wait(h);
ma1=createMask(h);
else
subplot(232);imagesc(log(abs(fsnap)));title('fft2')
h=impoly(gca,position0);
```

```
h=impoly(gca,position1);
end
m0=ma0.*abs(fsnap);
[va p0t]=max(m0(:));
[y0 x0]=ind2sub(size(m0),p0t);
m1=ma1.*abs(fsnap);
[va p1t]=max(m1(:));
[y1 x1]=ind2sub(size(m1),p1t);

%% centre the first order
%  to remove the carrier phase before IFFT

matrix = ma1.*fsnap;
centrey=ceil(length(matrix(:,1))/2);
centrex=ceil(length(matrix(1,:))/2);
while y1~= centrey
    matrix=circshift(matrix,[1,0]);
    [va p1t]=max(matrix(:));
    [y1 x1]=ind2sub(size(matrix),p1t);
end
while x1~= centrex
    matrix=circshift(matrix,[0,1]);
    [va p1t]=max(matrix(:));
    [y1 x1]=ind2sub(size(matrix),p1t);
end
%% do ifft on frequency shifted first order
fmfsnap1=ifft2(ifftshift(matrix));
%plot amplitude and phase components
asnap=abs(fmfsnap1);
asnap=asnap/max(asnap(:));
```

```
57 subplot(233);imagesc(abs(fmfsnap1));axis image; title('
       amplitude');
58 subplot(234);imagesc(angle(fmfsnap1));axis image; title('
       phase');
59 subplot(235);imagesc(unwrap(angle(fmfsnap1)));axis image;
       title('unwraping phase');
60 %%
61 IM = fmfsnap1;
62 IM_mask=ones(size(IM));          %Mask (if applicable)
63 IM_mag=abs(IM);                  %Magnitude image
64 IM_phase=angle(IM);
65 max_box_radius=4;
66
67 residue_charge=PhaseResidues(IM_phase, IM_mask);
                                    %Calculate phase residues
68 branch_cuts=BranchCuts(residue_charge, max_box_radius,
       IM_mask);                %Place branch cuts
69 [IM_unwrapped, rowref, colref]=FloodFill(IM_phase,
       branch_cuts, IM_mask);   %Flood fill phase unwrapping
70 tempmin=min(min(IM_unwrapped));          %This bit is just
       done to create a pleasing display when a mask is used
71 temp=(IM_unwrapped==0);
72 temp_IM=IM_unwrapped;
73 temp_IM(temp)=tempmin;
74 %%
75 %temp_IM is unwrapped phase.
76 %need to fit quadratic to background and subtract
77
78 figure(68);
79 imagesc(temp_IM)
80
```

```
%first find centre to approximate x0 and y0
h=imrect(gca) %use rectangle to allow cropping
position5 = wait(h);
ma5=createMask(h);

t_IMcrop=imcrop(temp_IM,position5);
[minVal, POSIT]=min2(abs(t_IMcrop));
fitX0=position5(1)+POSIT(1);
fitY0=position5(2)+POSIT(2);

%define x, y, and z using meshgrid,
%use polyfitn to find quadratic fit a, x^2, b, y^2
[xx, yy]=meshgrid([1:size(temp_IM,2)]-fitX0,[1:size(temp_IM
    ,1)]-fitY0);

z=temp_IM(:,:,1);

%%
%use polyfitn
p=polyfitn([xx(:),yy(:)],z(:),2);
eqn=polyn2sym(p);
zz=polyvaln(p,[xx(:),yy(:)]);
zz=reshape(zz,size(xx));
figure(69),imagesc(temp_IM-zz)
finalIM= temp_IM-zz;
%%
%crop image around cell
%want same image size for all cells to use in PCA
imshow(finalIM);
h = imrect(gca, [50 50 220 220]); % create rectangle on the
    image
```

```
message = sprintf('Drag, set position of the rectangle
    cropping box and double click on the rectangle box');
uiwait(msgbox(message));
    position = wait(h); % get position
    I_crop = imcrop(finalIM,position); % crop image
    %message = sprintf('Image has been cropped');
    %msgbox(message);
figure(60); imagesc(I_crop);
```

E.2 Histogram or TA on phase map

```
%%PCA for DHM phase images from .fig files
%Naomi McReynolds 19/05/16


clear all
dirname='  '; % insert path to folder
d=dir(dirname);

nd=length(d)-2; cell=[]; data0=[];
offsets = [0 1; -1 1;-1 0;-1 -1];
for t=1:nd
    filename=d(t+2).name;
    imgpath=strcat(dirname,filename);
    open(imgpath);
    A=get(gca);
    B=get(A.Children);
    img=B.CData;
    close(gcf);
    %glcm=graycomatrix(img,'offset',offsets);   %use for TA
        in different directions
    glcm=graycomatrix(img);
```

```
21      stats=graycoprops(glcm);  %for TA
22
23     %histogram for pixel values
24      area=nnz(img); %all non-zero elements within ellipse
            count as 1
25      TotOPD=sum(img(:));
26      maxOPD=max(img(:));
27      xlo=0;
28      xhigh=6.5;
29      X=xlo:(xhigh-xlo)/64:xhigh; %set x axis between 0 and
            6.5(max OPD for macro)
30      h=hist(img(:),X);
31      %select parameters to analyse on 1: all, 2: TA, 3:
            histogram
32
33      %params=horzcat(stats.Contrast,stats.Correlation,stats.
            Energy,stats.Homogeneity,area,TotOPD, maxOPD,h);
34      %params=horzcat(h,stats.Contrast,stats.Correlation,stats.
            Energy,stats.Homogeneity);
35      params=horzcat(area,TotOPD, maxOPD,h);
36      data0(:,t)=params;
37
38  end
39  %%
40  % PCA using selected parameters
41  %83 Bcell; 46 CD4; 66 Macro;   (total 195)
42
43  cell1=repmat(1,1,83); %bcell
44  cell3=repmat(3,1,66); %macro
45  cell2=repmat(2,1,46); %cd4
46  cells=horzcat(cell1, cell2, cell3);
```

```
47
48 data=data0';
49 nd=size(data,2);
50 %%
51 col=colormap(lines(3));
52
53 mdat=mean(data,2);
54 vdat=data-repmat(mdat,1,nd);
55
56 mat=vdat'*vdat;
57 [vec, val]=eigs(mat,nd);
58 %pr=vdat'*vdat*vec;
59 %%
60 figure()
61 pc1=vdat*vec(:,1);
62 pc2=vdat*vec(:,2);
63 pc3=vdat*vec(:,3);
64 subplot(141);plot(1:size(vdat,1),vdat*vec(:,1),'r',1:size(
       vdat,1),vdat*vec(:,2),'g',1:size(vdat,1),vdat*vec(:,3),'b'
       );
65 colormap(col)
66 labels = {'PC1','PC2','PC3'};
67 lcolorbar(labels,'fontweight','bold');
68 %subplot(231); imagesc(pc1); title 'first principal component
       '
69 %subplot(232); imagesc(pc2); title '2nd principal component'
70 %subplot(233); imagesc(pc3); title '3rd principal component'
71
72 %%
73
74 for t=1:length(cells)
```

```
75      subplot(1,4,2);plot(pc1(t,1),pc2(t,1),'*','color',col(
            cells(t),:));hold on
76      %title '1st and 2nd PCs';
77      xlabel('PC1','fontsize',14); ylabel('PC2','fontsize',14);
78      subplot(1,4,3);plot(pc1(t,1),pc3(t,1),'*','color',col(
            cells(t),:));hold on
79      xlabel('PC1','fontsize',14); ylabel('PC3','fontsize',14);
80      %title '1st and 3rd PCs';
81      subplot(1,4,4);plot(pc2(t,1),pc3(t,1),'*','color',col(
            cells(t),:));hold on
82      xlabel('PC2','fontsize',14); ylabel('PC3','fontsize',14);
83      %title '2nd and 3rd PCs';
84  end
85  colormap(col)
86  labels = {'Bcell','CD4','Monocyte'};
87  lcolorbar(labels,'fontweight','bold');
88  %%
89   cc=zeros(length(cells),3);
90   for i=1:length(cells)
91       if cells(i)==1
92           cc(i,1)= 1;
93       elseif cells(i)==2
94           cc(i,2)=1;
95       elseif cells(i)==3
96           cc(i,3)=1;
97       end
98       i=i+1;
99   end
100
101 %% specificity and sensitivity
102 spec0=data';
```

```
103
104 cb = 0;
105 for m = 1:3  %3 is how many cell types we have
106     cb = cb+cc(:,m)*2^(m-1);
107 end
108 cases=union(cb,cb);
109 ncases=length(cases);
110 xval=[];
111 cm=zeros(ncases,ncases);
112 [vv,dd]=eig(mat);
113 dd = diag(rot90(dd,2));
114 dd(dd<0)=0;
115 %%
116 nd=3;
117 perc = sum((dd(1:nd)/sum(dd)));
118 disp(['First ' num2str(nd) ' PCs used corresponds to '
    num2str(perc*100,3) '%']);
119 %%
120
121 for jj=1:size(spec0,2)
122     spec=spec0;
123     unknown=spec(:,jj);
124     spec(:,jj)=[];
125     m=0*mean(spec'); %%%% mean of the imput spectra
126     y=spec'-ones(size(spec',1),1)*m;   % normalise by
        subtracting mean
127     yun=unknown'-ones(size(unknown',1),1)*m;   % normalise by
         subtracting mean
128     co=cov(y); % find covariance matrix
129     [vc,dc]=eigs(co,nd); % find eigenvectors (v) and
        eigenvalues (d) of covariance matrix
```

```
130     pc=y*vc; % normalised data projected onto eigenspace
131     pcun=yun*vc;
132     ch=dsearchn(pc,pcun);
133     fs=cb(jj);        %really
134     fsch=cb(ch);      %diagnostic
135     cm(find(cases==fs),find(cases==fsch))=cm(find(cases==fs),
            find(cases==fsch))+1;
136     [fs fsch];
137 end
138 Sensitivity=(cm(2,2)/(cm(2,2)+cm(3,2)));
139 Specificity=(cm(3,3)/(cm(2,3)+cm(3,3)));
140 disp(['Sensitivity: ' num2str(Sensitivity)]);
141 disp(['Specificity: ' num2str(Specificity)]);
142 %
143 % cm : confusion matrix;
144 cm
```

F Protocol to split and count SH-SY5Y cells

F.1 Passage cells

This section will detail the technique to split SH-SY5Y cells which is done twice a week.

1. Check under a microscope that the cells are confluent ($\approx 80\%$ coverage)
2. Pour off the culture medium
3. Add $2 - 5\,\mathrm{ml}$ PBS (warmed to $37°$ in a water bath) to wash off remaining medium
4. Gently swirl PBS on bottom of flask and pour off the PBS
5. Add $0.5\,\mathrm{ml}$ trypsin
6. Place the flask back in the incubator for 5 minutes
7. Check that the cells have become free-floating (may need to tap flask to encourage cells to detach)
8. Add $4.5\,\mathrm{ml}$ of warmed medium to give a total volume of $5\,\mathrm{ml}$. Gently pass up and down the pipette to mix solution.
9. Take off $3\,\mathrm{ml}$
10. Replace with $3\,\mathrm{ml}$ medium and gently mix
11. Return the flask to the incubator

F.2 Cell counting

Before plating cells an aliquot is used to count the number of cells per ml. The ideal concentration for plating is 1×10^5 cells/ml.

1. After cells have been trypsonised take a $10\,\mu\mathrm{l}$ aliquot and transfer to an eppendorf tube

2. Add $10\,\mu$l of trypan blue and leave for a couple of minutes. Trypan blue will selectively colour the membrane of dead cells.
3. Clean glass hemocytometer and coverslip with ethanol. Moisten the coverslip and affix it to the hemocytometer.
4. Using a pipette gently fill the chamber of the hemocytometer with the $20\,\mu$l solution
5. Place the hemocytometer on a microscope with a 10X objective
6. The hemocytometer has four grids of 4×4 squares. Consider each individually. Count and record the number of live cells in one 16 square grid.
7. Move the hemocytometer to the next 16 square grid and repeat until all corners have been counted.
8. Find the average cell count over the four corners
9. Multiply by 2 to correct for the 2 times dilution by trypan blue.
10. Multiply by 10^4
11. The final value is the number of cells/ml in the original cell suspension

G Method to differentiate SH-SY5Y cells

Three differentiation stages of SH-SY5Y cells were analysed: undifferentiated, mixed differentiation population, and fully differentiated. This appendix will detail the method followed to grow the cells into each differentiation stage.
The incubator is kept at $37\,^{\circ}$, 5% CO_2.

G.1 Grow undifferentiated SH-SY5Y cells

1. Dilute the cells at a density of 1×10^5 cells/ml in 10% fetal calf serum (FCS) medium.
2. Plate $2\,\mathrm{ml}$ in each plate or dish
3. Return the plated cells to the incubator
4. After 48 hours undifferentiated SH-SY5Y cells should have reached confluence and are ready for analysis.
5. If they have not reached confluence do not start experiments early. Half of the medium may be replaced with fresh 10% FCS medium. (Using a pipette to carefully remove $1\,\mathrm{ml}$ medium, without touching the dish.)

G.2 Differentiation with retinoic acid

1. Grow the cells as above, until 70% confluence.
2. Carefully remove the culture medium
3. Replace the medium with $2\,\mathrm{ml}$ 1% FCS medium containing $10\,\mu\mathrm{M}$ retinoic acid (RA) (pre-warmed in a water bath)
4. Return the plates to the incubator
5. Replace half of the medium with fresh 1% FCS medium containing $10\,\mu\mathrm{M}$ RA every 48 hours
6. After 5 days a culture of RA differentiated SH-SY5Y cells will be established.

G.3 Differentiation with retinoic acid and mitotic inhibitor

1. Grow the cells as above until RA differentiated
2. Remove the culture medium
3. Replace the medium with $2\,\mathrm{ml}$ 1% FCS medium containing $80\,\mu\mathrm{M}$ 5-fdu, a mitotic inhibitor.
4. Leave the cells in the incubator for 1 week, replacing the medium twice.
5. A culture of fully differentiated cells will be established.

H Immunocytochemistry protocol

1. Fix the cells in neurtral buffered formalin for 15-20 minutes
2. Wash three times with PBS for 5 minutes each
3. Incubate in 10% horse serum block (HSB) for 30 minutes
4. Add the primary antibody diluted in HSB
5. Leave at 4° overnight
6. Wash three times in PBS with TWEEN for 5 minutes each
7. Add flourescin congjugated (FITC) secondary antibody (goat-antimouse) in HSB (1:200)
8. Leave at room temperature in the dark (cover in tin foil) for 2 hours
   (The plate is now always kept in the dark)
9. Wash three times in PBS for 5 minutes each
10. Add DAPI at 1:10000 in PBS and leave for 15 minutes
11. Wash three times in PBS for 5 minutes each
12. Mount the cover-slip onto a microscope slide using antifade mountant and seal with nail varnish

I Western blot and preparation techniques

I.1 Protein extraction

1. Take plate from incubator and carefully remove all medium. Take care not to touch the bottom of the plate with the pipette tip
2. Add $500\,\mu$l of TBS-T (tris-buffered saline and 1% Triton X-100) and $5\,\mu$l protease inhibitor. TBS is a salt solution that soluble proteins dissolve in, Triton X-100 is a detergent that will lyse cell and organelle walls.
3. Use a cell scraper to dislodge all cells from the dish
4. Use pipette to rinse solution over the bottom of dish to collect all cells
5. Transfer cells to an eppendorf. Run sample up and down pipette until no obvious solids remain
6. Centrifuge sample for 10 minutes at 13000 rpm
7. Separate the supernatent from the pellet and put into a labelled tube. Soluble protein will be in the supernatant.
8. Keep an aliquot of the supernatant separate to perform Bradford assay
9. Freeze the pellet and the supernatant

I.2 Bradford Assay

1. Place $10\,\mu$l of protein sample and $10\,\mu$l NaOH in a fresh tube
2. Add $500\,\mu$l Bradford reagent (Brilliant Blue G)
3. Leave for 5 minutes
4. Read absorbance at $590\,\mathrm{nm}$

Standard solutions are made for calculating absolute concentration:

1. Prepare stock solution of $100\,\mu\mathrm{g}/\mu\mathrm{l}$ BSA
2. Dilute 1:10 to give a range of concentrations ($100\,\mu\mathrm{g}/\mu\mathrm{l}$, $10\,\mu\mathrm{g}/\mu\mathrm{l}$, $1\,\mu\mathrm{g}/\mu\mathrm{l}$, $0.1\,\mu\mathrm{g}/\mu\mathrm{l}$, $0.01\,\mu\mathrm{g}/\mu\mathrm{l}$)

3. Carry out the Bradford assay for each concentration
4. Produce a standard curve
5. From the graph determine the protein concentration of each SH-SY5Y sample.

I.3 Western blot

Prepare gel

1. Boil sample for 10 minutes on a heated water stirrer to denature proteins
2. Gels are kept at 4°. Remove gel from the packet and wash with dH_2O. (Use squeezy bottle to pour water over the wells and tap to get rid of any bubbles)
3. Assemble gels into gel rig such that the wells face inwards.
4. Fill the inner chamber with running buffer and $1/3$ outside chamber with running buffer
5. Load the first well with the protein ladder (marker)
6. Load the other wells with $30\,\mu\mathrm{g}/\mu\mathrm{l}$ of protein. A maximum of $24\,\mu\mathrm{l}$ can be loaded.
   Use a separate tip for each well to avoid cross contamination. Tip is held just above the well and sample slowly sinks in. Care is to be taken not to load too quickly as the sample may then flow into other wells.

Run gel

1. Put lid on gel tank (Cleaver Scientific Ltd) and set voltage to $150\,\mathrm{V}$ for 40 minutes
2. Check the gel is running. Lighter proteins get pulled further through the gel. (40 minutes as ideal as if not left long enough bands are not well separated, if left too long small proteins are missed)
3. The blue marker should be near the foot of the gel at the end. After 40 minutes switch off the power pack.

Set up blot

1. Soak 5 sponges (machine can run two Western blots) in 10% Tris glycine buffer and methanol. Only need three sponges to run one gel
2. Cut four rectangles of blotting (chromatography) paper per gel, make as long as proteins and as wide as the ladder
3. Soak with the sponges
4. Cut one nitrocellulose membrane per gel and soak with sponges and blotting paper
5. Take two plates of the blotting chamber and lay flat side down
6. Place two sponges in the blotting chamber and roll them flat to remove any bubbles. (Bubbles can prevent transfer of proteins to the membrane)
7. Layer two sheets of blotting paper and roll flat
8. Add nitrocellulose membrane and roll flat
9. Cut the gel open and soak in the buffer for a few seconds
10. Lay the gel on the transfer membrane with the ladder on the left hand side and proteins on the bottom
11. Layer with two more blotting papers and roll flat
12. Add a sponge and roll flat
13. Fill the inner chamber with the transfer buffer and 1/2 of the outer chamber
14. Close plates together

Run blot

1. Set voltage to $30\,\mathrm{V}$ and current to $200\,\mathrm{mA}$
2. Run for 90 minutes

Check protein transfer

1. Disassemble the blot and take the two membranes
2. Place the membrane in a square dish
3. Pour on Ponceau S, a stain to reveal if protein ran through. Rock the dish gently until red protein bands are visible on the membrane. Check all the wells worked.

4. Pour off the Ponceau S
5. Wash the membrane quickly in TBS three times
6. Wash the membrane in TBS on the rocker for 5 minutes and repeat until the red has completely washed out.
7. If transfer didn't work no need to continue

Block

1. Make up blocking solution: $1\,\mathrm{g}$ powdered milk per $20\,\mathrm{ml}$ TBST (need $20\,\mathrm{ml}$ per gel or $10\,\mathrm{ml}$ for dot blot). Stir with magnetic stirrer
2. Pour TBS off the membrane
3. Pour milk over the membrane
4. Leave on rocker for 15 minutes at room temperature

Primary antibody

1. The primary antibody α-tubulin is diluted 1:2000 in $20\,\mathrm{ml}$ milk blocking solution
2. Pour off the blocking solution from the membrane
3. Add primary antibody solution and leave on a rocker overnight in a cold room (4°)

Secondary antibody

1. Wash the membrane three times in TBS-T for 5 minutes each, on the rocker
2. Add the secondary antibody solution, HRP conjugated at 1:10000 in TBS-T
3. Leave on a rocker for 2 hours at room temperature

Detection of bands

1. Wash the membrane three times in TBS-T for 5 minutes each, on the rocker
2. Dab off any excess liquid
3. Mix together $150\,\mu\mathrm{l}$ each of HRP chemiluminescence substrate reagent kit
4. Pour onto the membrane and swirl to cover the whole area. Ensure there are no bubbles as these will appear as a bright spot

5. Take membrane to ChemiDoc-It for imaging
6. image with Vision Works software

I.4 Dot blot

1. Cut nitrocellulose membrane in small squares
2. Denature the protein sample by placing in boiling water for 10 minutes
3. Put $2.5\,\mu\mathrm{l}$ of sample in the centre of the paper
4. Let dry for 30-60 minutes, until completely dry
5. Cover membrane in milk blocking solution for 30 minutes on rocker to block any non-specific binding
6. Pour off the milk
7. Add $1\,\mathrm{ml}$ of the primary antibody at various concentrations (1:500, 1:1000, 1:2000, 1:5000, 1:10000) in milk blocking solution
8. Leave overnight on a rocker in a cold room (4°)
9. Pour off the primary antibody
10. Wash three times in TBS-T for 5 mins each on the rocker
11. Add 1:10000 secondary antibody conjugated with HRP, diluted in TBS-T
12. Leave at room temperature on the rocker for 2 hours
13. Pour off the secondary antibody
14. Wash the membrane three times in TBS-T for 5 minutes each, on the rocker
15. Transfer papers to a plastic sleeve and dab off any excess liquid
16. cover papers in HRP chemiluminescent substrate reagent mixture. Ensure there are no bubbles
17. Membrane is ready to image in ChemiDoc-It with Vision Works software

J Scotch whisky details- name and age

J.0.1 25 Scotch whiskies (as seen in figure 6.6)

Number	Whisky	Number	Whisky
1	Glenfiddich- 12 year old	14	Bowmore- 12 year old
2	Glenlivet- 12 year old	15	Highland Park- 12 year old
3	Glenmorangie original- 10 year old	16	Auchentoshan- 10 year old
4	Aberlour- 10 year old	17	Glenfiddich Solera- 15 year old
5	Bunnahabhain- 12 year old	18	Old Pulteney- 12 year old
6	Dalwhinnie- 15 year old	19	Ardbeg- 10 year old
7	Jura- 10 year old	20	Macallan Fine Oak- 10 year old
8	Talisker- 10 year old	21	Springbank- 10 year old
9	Glenlivet- 18 year old	22	Cragganmore- 12 year old
10	Glenkinchie- 12 year old	23	Caol Ila- 12 year old
11	The singleton of Dufftown- 12 year old	24	Oban- 14 year old
12	Laphroag- 12 year old	25	Clynelish- 14 year old
13	Balvenie Double Wood- 12 year old		

TABLE J.1: Name and age of the 25 whiskies used for classification by Raman and fluorescence spectroscopy.

J.0.2 Scotch whiskies used to build a flavour map (section 6.3.3)

Key	Whisky
A	Glenfiddich- 12 year old
B	Bowmore- 12 year old
C	Laphroig- 10 year old
D	Glenfiddich Solera- 15 year old
E	Ardbeg- 10 year old
F	Old Pulteney- 12 year old

TABLE J.2: Name and age of the whiskies used to build a Raman based flavour map.

K Protocol for synthesis of ultrasmooth gold nanoparticles

1. Prepare 1M Phosphoric acid by adding $0.137\,\mathrm{ml}$ Conc acid (85% wt) and $1.863\,\mathrm{ml}$ H_2O
2. Add
   - $20\,\mathrm{ml}$ ethylene glycol*
   - $0.04\,\mathrm{ml}$ pDADMAC (poly(diallyldimethylamonium chloride), average M_w400,000-500,000, 20% wt in H_2O
   - $0.8\,\mathrm{ml}$ 1M Phosphoric acid

   to a clean $50\,\mathrm{ml}$ single-neck round bottom flask with a stirrer bar.
3. Stir at room temperature for approximately 2 minutes
4. Add $0.02\,\mathrm{ml}$ of 0.5M Chlorauric acid solution ($9.29\,\mathrm{mg}$ $HAuCl_4 \bullet 3H_2O$ and $0.047\,\mathrm{ml}$ H_2O) via pipette
5. Stir at room temperature for 15 minutes
6. Fit a condenser to the flask and place on a heating block. Heat to $195°$C and maintain at that temperature for 30 minutes. The reaction will undergo the following transitions:
   - yellow to colourless after approximately 1 minute heating
   - colourless to purple after a further 5 minutes heating
   - purple to orange after a further 10 minutes heating

   as shown in figure K.1.
7. Allow reaction mixture to cool to room temperature and add a further $0.005\,\mathrm{ml}$ Chlorauric acid solution
8. Leave stirring at room temperature for 20 hours
9. Pour reaction mixture into a $50\,\mathrm{ml}$ falcon tube and centrifuge at $10,000\,\mathrm{rpm}$ at $4°$C for 30 minutes

10. Remove supernatant and re-suspend NPs in approximately $20\,\mathrm{ml}$ ethanol
11. Repeat the purification process a further two times with centrifugation at $4000\,\mathrm{rpm}$.

*The size of particles produced can vary depending on the viscosity of the solution. The ethylene glycol may be wet, in which case distillation can be employed to vaporise some of the water content, providing a more viscous solution to achieve larger nanoparticles.

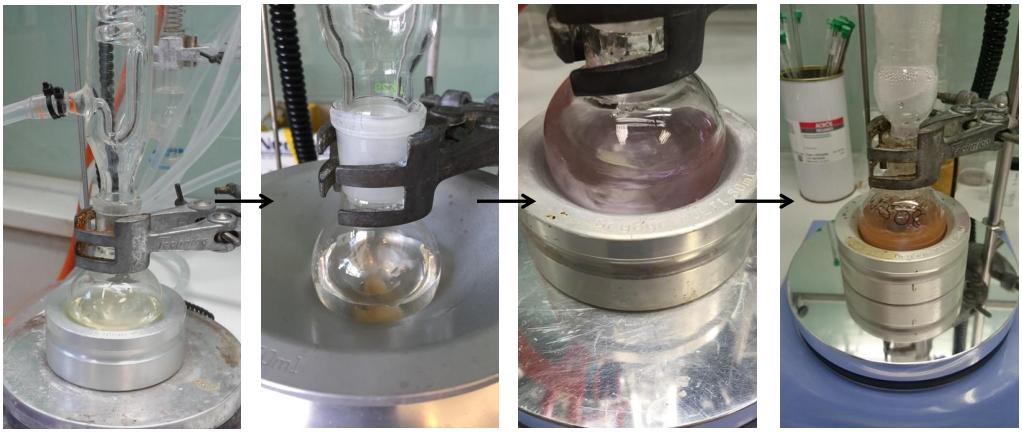

FIGURE K.1: Colour change transitions observed during heating; from yellow to colourless (after 1 minute), to purple (a further 5 minutes), and finally to orange (a further 10 minutes).

Bibliography

[1] E. C. Jenson. "Use of fluorescent probes: Their effect on cell biology and limitations." In: *Anat. Rec.* 295 (2012), pp. 2031–2036.

[2] A. Simeonov and M. I. Davis. "Interference with fluorescence and absorbance." In: *Assay Guidance Manual [Internet]* (2015). URL: https://www.ncbi.nlm.nih.gov/books/NBK343429/.

[3] G. Crivat and J. W. Tarasaka. "Imaging proteins inside cells with fluorescent tags." In: *Trends Biotechnol.* 30.1 (2012), pp. 8–16.

[4] A. M. Ansari et al. "Cellular GFP toxicity and immunogenicity: Potential confounders in in vivo cell tracking experiments." In: *Stem cell Rev. and Rep.* 12 (2016), pp. 553–559.

[5] R. Stripecke et al. "Immune response to green fluorescent protein: implications for gene therapy." In: *Gene Therapy.* 6.7 (1999), pp. 1305–1312.

[6] K. Kong et al. "Raman spectroscopy for medical diagnostics — From in-vitro biofluid assays to in-vivo cancer detection." In: *Adv. Drug Deliv. Rev.* 89 (2015), pp. 121–134.

[7] H. J. Butler et al. "Using Raman spectroscopy to characterize biological materials." In: *Nat. Protoc.* 11.4 (2016), pp. 664–687.

[8] K. J. I. Ember et al. "Raman spectroscopy and regenerative medicine: a review." In: *NPJ Regen. Med.* 2.12 (2017).

[9] D. Yang and Y. Ying. "Applications of Raman spectroscopy in agricultural products and food analysis: A review". In: *Appl. Spectrosc. Rev.* 46.7 (2011), pp. 539–560.

[10] D. I. Ellis et al. "Point-and-shoot: rapid quantitative detection methods for on-site food fraud analysis- moving out of the laboratory and into the food supply chain." In: *Anal. Methods* 7 (2015), pp. 9401–9414. DOI: 10.1039/C5AY02048D.

[11] N. Yoshioka and K. Ichihashia. "Determination of 40 synthetic food colors in drinksand candies by high-performance liquid chromatography using a short column with photodiodearray detection." In: *Talanta* 74.5 (2008), pp. 1408–1413.

[12] W. Wardencki et al. "Application of gas chromatography, mass spectrometry and olfactometry for quality assessment of selected food products." In: *Ecol. Chem. Eng. S.* 16.3 (2009), pp. 288–300.

[13] B. M. T. Jimaré, C. B. Ojeda, and F.S. Rojas. "Process analytical chemistry: Applications of near infrared spectrometry in environmental and food analysis: An Overview." In: *Appl. Spectros. Rev.* 43 (2006), pp. 452–484.

[14] E. Sikorska et al. "Monitoring beer during storage by fluorescence spectroscopy." In: *Food Chem.* 96 (2006), pp. 632–639.

[15] D. Airado-Rodríguez et al. "Usefulness of fluorescence excitation-emission matrices in combination with PARAFAC, as fingerprints of red wines." In: *J. Agric. Food Chem.* 57 (2009), pp. 1711–1720.

[16] Y-S. Li and J. S. Church. "Raman spectroscopy in the analysis of food and pharmaceutical nanomaterials." In: *J. Food Drug Anal.* 22.1 (2014), pp. 29–48.

[17] D. I. Ellis et al. "Illuminating disease and enlightening biomedicine: Raman spectroscopy as a diagnostic tool." In: *Analyst* 138 (2013), pp. 3871–3884.

[18] A. Smekal. "On the quantum theory of dispersion". In: *Die Naturwissenschaften* 11 (1923), pp. 873–875.

[19] C. V. Raman and K. S. Krishnan. "A new type of secondary radiation." In: *Nature* 121.3048 (1928), p. 501.

[20] R. S. Krishnan and R. K. Shankar. "Raman effect: history of the discovery". In: *J. Raman. Spectrosc.* 10 (1981), pp. 1–8.

[21] G. Dent and E. Smith. *Modern Raman spectroscopy: a practical approach*. Chichester, England: John Wiley and Sons, Ltd, 2005.

[22] B&W Tek. *Theory of Raman spectroscopy*. accessed on 24/02/2017. URL: http://bwtek.com/raman-theory-of-raman-scattering/.

[23] Prasad. N. Prasad. *Introduction to Biophotonics*. New Jersey: John Wiley and Sons, Inc, 2003. Chap. 4.

[24] D. W. Hahn. *Raman scattering theory*. 2007. URL: http://plaza.ufl.edu/dwhahn/Raman%20Scattering%20Theory.pdf.

[25] *Standard spectra*. accessed on 02/08/2017. URL: https://www.chem.ualberta.ca/~mccreery/ramanmaterials.html.

[26] G. E. Walrafen, Y. C. Chu, and M. S. Hokmabadi. "Interaction-induced Raman scattering from fused silica". In: *J. Phys. Chem* 94 (1990), pp. 5658–5661.

[27] M. Dračínský, L. Benda, and P. Bouř. "Ab initio modeling of fused silica, crystal quartz, and water Raman spectra". In: *Chem. Phys. Lett.* 512.1 (2011), pp. 54–59. DOI: http://dx.doi.org/10.1016/j.cplett.2011.06.077.

[28] P. J. Larkin et al. "Polymorph characterization of active pharmaceutical ingredients (APIs) Using low-frequency Raman spectroscopy." In: *Appl. Spectrosc.* 68.7 (2014), pp. 758–776.

[29] Bavishna Balagopal. "Advanced methods for enhanced sensing in biomedical Raman spectroscopy." PhD thesis. The university of St. Andrews, 2014.

[30] K. C. Neuman and S. M. Block. "Optical trapping." In: *Rev. Sci. Instrum.* 75.9 (2006), pp. 2787–2809.

[31] M. R. Hamblin. *Mechanisms of low level light therapy*. accessed on 08/03/2017. URL: http://photobiology.info/Hamblin.html.

[32] E. Canetta et al. "Modulated Raman spectroscopy for enhanced identification of bladder tumor cells in urine samples." In: *J. Biomed. Optic.* 16.3 (2011), p. 037002.

[33] A. C. De Luca, K. Dholakia, and M. Mazilu. "Modulated Raman spectroscopy for enhanced cancer diagnosis at the cellular level." In: *Sensors* 15 (2015), pp. 13680–13704. DOI: 10.3390/s150613680.

[34] G. Clemens et al. "Vibrational spectroscopic methods for cytology and cellular research." In: *Analyst* 139 (2014), pp. 4411–4444.

[35] A. Downes and A. Elfick. "Raman spectroscopy and related techniques in biomedicine." In: *Sensors* 10 (2010), pp. 1871–1889.

[36] C. Krafft and J. Popp. "The many facets of Raman spectroscopy for biomedical analysis." In: *Anal. Bioanal. Chem.* 407 (2015), pp. 699–717.

[37] M. Li et al. "Single cell Raman spectroscopy for cell sorting and imaging." In: *Curr. Opin. Biotechnol.* 23.1 (2012), pp. 56–63.

[38] P. Matousek et al. "Subsurface probing in diffusely scattering media using spatially offset Raman spectroscopy." In: *Appl. Spectrosc.* 59.4 (2005), pp. 393–400.

[39] J. Zheng and L. He. "Surface-enhanced Raman spectroscopy for the chemical analysis of food." In: *Compr. Rev. Food Sci. Food Saf.* 13.3 (2014), pp. 317–328. DOI: 10.1111/1541-4337.12062.

[40] J. Moros, S. Garrigues, and M. De La Guardia. "Evaluation of nutritional parameters in infant formulas and powdered milk by Raman spectroscopy." In: *Anal. Chim. Acta.* 593 (2007), pp. 30–38.

[41] A. Fehrmann et al. "Dairy product analysis: identification of microorganisms by mid-infrared spectroscopy and determination of constituents by Raman spectroscopy". In: *J. AOAC Int.* 78 (1995), pp. 1537–1542.

[42] C. M. McGoverin et al. "Raman spectroscopic quantification of milk powder constituents." In: *Anal. Chim. Acta.* 673 (2010), pp. 26–32.

[43] H. Yang and J. Irudayaraj. "Rapid detection of foodborne microorganisms on food surface using Fourier transform Raman spectroscopy." In: *J. Mol. Struct.* 646 (2003), pp. 35–43.

[44] P. X. Zhang et al. "Raman spectra from pesticides on the surface of fruits". In: *J. Phys.* 28 (2006), pp. 7–11.

[45] B. Liu et al. "Detection of pesticides in fruits by surface-enhanced Raman spectroscopy coupled with gold nanostructures." In: *Food Bioprocess Tech.* 6.3 (2013), pp. 710–718.

[46] S. W. Ellepola et al. "Raman spectroscopic study of rice globulin." In: *J. Cereal. Sci.* 43 (2006), pp. 85–93.

[47] C. Siu-Mei and M. Ching-Yung. "Structural characterization of globulin from common buckwheat (Fagopyrum esculentum Moench) using circular dichroism and Raman spectroscopy." In: *Food Chem.* 102 (2007), pp. 150–160.

[48] N. K. Afseth and V. Larat. *Fat acids characterization for food quality using Raman spectroscopy. (Application note: Food Beverage RA51.)* URL: http://www.horiba.com/fileadmin/uploads/Scientific/Documents/Raman/RA51.pdf.

[49] R. M. El-Abassy, P. Donfack, and A. Materny. "Rapid determination of free fatty acid in extra virgin olive oil by Raman spectroscopy and multivariate analysis". In: *J. Am. Oil Chem. Soc.* 86.6 (2009), pp. 507–511.

[50] B. Muik et al. "Direct, reagent-free determination of free fatty acid content in olive oil and olives by Fourier transform Raman spectrometry." In: *Anal. Chim. Acta.* 487 (2003), pp. 211–220.

[51] M. Lopez-Sanchez, M. Joseayora-Cañada, and A. Molína Diaz. "Olive fruit growth and ripening as seen by vibrational spectroscopy." In: *J. Agr. Food Chem.* 58 (2010), pp. 82–87.

[52] C. Frausto-Reyesa et al. "Qualitative study of ethanol content in tequilas by Raman spectroscopy and principal component analysis." In: *Spectrochim. Acta. A* 61 (2005), pp. 2657–2662.

[53] P. C. Ashok, B. B. Praveen, and K. Dholakia. "Near infrared spectroscopic analysis of single malt Scotch whisky on an optofluidic chip". In: *Opt. Express* 19 (2011), pp. 212982–22992.

[54] L. Silveira Jr et al. "Determination of sucrose concentration in lemon-type soft drinks by dispersive Raman spectroscopy." In: *Spectroscopy* 23 (2009), pp. 217–226.

[55] S. Mazurek and R. Szostak. "Quantification of aspartame in commercial sweeteners by FT-Raman spectroscopy." In: *Food Chem.* 125 (2011), pp. 1051–1057.

[56] A. Nawrocka and J. Lamorska. *Advances in Agrophysical Research.* InTech, 2013. Chap. 14. DOI: 10.5772/52722. URL: http://cdn.intechopen.com/pdfs-wm/39943.pdf.

[57] Y. Cheng et al. "Screening melamine adulterant in milk powder with laser Raman spectrometry." In: *J. Food Compos. Anal.* 23 (2010), pp. 199–202.

[58] V. Mazet et al. "Background removal from spectra by designing and minimising a non-quadratic cost function". In: *Chemom. Intell. Lab. Syst.* 76.2 (2005), pp. 121–133.

[59] J. Zhao et al. "Automated autofluorescence background subtraction algorithm for biomedical Raman spectroscopy." In: *Appl. Spectrosc.* 61.11 (2007), pp. 1225–1232.

[60] D. Wei, S. Chen, and Q. Liu. "Review of fluorescence suppression techniques in Raman spectroscopy." In: *Appl. Spec. Rev.* 50.5 (2015), pp. 387–406.

[61] C-H. Liu et al. "Raman, fluorescence, and time-resolved light scattering as optical diagnostic techniques to separate diseased and normal biomedical media." In: *J. Photochem. Photobiol. B* 16.2 (1992), pp. 187–209.

[62] P. Matousek et al. "Efficient rejection of fluorescence from Raman spectra using picosecond Kerr grating." In: *Appl. Spectrosc.* 53.12 (1999), pp. 1485–1489.

[63] T. Rojalin et al. "Fluorescence-suppressed time-resolved Raman spectroscopy of pharmaceuticals using complimentary metal-oxide semiconductor (CMOS) single- photon avalanche diode (SPAD) detector." In: *Anal. Bioanal. Chem.* 408 (2016), pp. 761–774.

[64] A. Laubereau, D. Von der Linde, and W. Kaiser. "Direct measurement of the vibrational lifetimes of molecules in liquids." In: *Phys. Rev. Lett.* 28.18 (1972), pp. 1162–1165.

[65] J. R. Lakowicz. *Introduction to fluorescence. In: Principles of fluorescence spectroscopy 3rd ed*. New York: Springer Science + Business Media, 2006, pp. 1–26.

[66] N. Everall et al. "Picosecond time-resolved Raman spectroscopy of solids: capabilities and limitations for fluorescence rejection and the influence of diffuse reflectance." In: *Appl. Spectrosc.* 55.12 (2001), pp. 1701–1708.

[67] R. L. McCreery. *Raman spectroscopy for chemical analysis.* Hoboken, NJ, U.S.A: Wiley-Interscience, 2000. DOI: 10.1002/0471721646.

[68] C. A. Arguello, G. F. Mendes, and R. C. C. Leite. "Simple technique to suppress spurious luminescence in Raman spectroscopy". In: *Appl. Opt.* 13.8 (1974), pp. 1731–1732.

[69] S. M. Angel et al. "Computer-controlled instrument for the recovery of a resonance Raman-spectrum in the presence of strong luminescence." In: *Anal. Chem.* 56.14 (1984), pp. 3000–3001.

[70] M. Kasha. "Characterization of electronic transitions in complex molecules". In: *Discuss. Faraday Soc.* 9 (1950), pp. 14–19.

[71] J. Funfschilling and D. F. Williams. "CW laser wavelength modulation in Raman and site selection fluorescence spectroscopy." In: *Appl. Spectrosc.* 30.4 (1976), pp. 443–446.

[72] K. H. Leven and C. L. Tang. "Wavelength-modulation Raman spectroscopy." In: *Appl. Phys. Lett* 33.9 (1978), pp. 817–819.

[73] A. P. Shreve, N. J. Cherepy, and R. A. Mathies. "Effective rejection of fluorescence interference in Raman-spectroscopy using a shifted excitation difference technique." In: *Appl. Spectrosc.* 46.4 (1992), pp. 707–711.

[74] S. E. J. Bell, E. S. O. Bourguignon, and A. Dennis. "Analysis of luminescent samples using subtracted shifted Raman spectroscopy." In: *Analyst* 123.8 (1998), pp. 1729–1734.

[75] A. C. De Luca et al. "Online fluorescence suppression in modulated spectroscopy". In: *Anal. Chem.* 82.2 (2012), pp. 738–745. DOI: 10.1021/nl303035p.

[76] M. Mazilu et al. "Optimal algorithm for fluorescence suppression of modulated Raman spectroscopy." In: *Opt. Express* 18 (2010), pp. 11382–11395.

[77] S. Dochow et al. "Classification of Raman spectra of single cells with autofluorescence suppression by wavelength modulated excitation." In: *Anal. Methods* 5.18 (2013), pp. 4608–4614.

[78] B. B. Praveen et al. "Optimisation of wavelength modulated Raman spectroscopy: Towards high throughput cell screening." In: *PLoS One* 8.6 (2013), e67211.

[79] E. J. Blackie, E. C. Le Ru, and P. G. Etchegoin. "Single-molecule surface-enhanced Raman spectroscopy of nonresonant molecules." In: *J. Am. Chem. Soc.* 131 (2009), pp. 14466–14472.

[80] L. Kastrup and S. W. Hell. "Absolute optical cross section of individual fluorescent molecules." In: *Angew. Chem. Inst. Ed.* 43 (2004), pp. 2–5.

[81] C. L. Haynes and R. P. Van Duyne. "Plasmon-sampled surface-enhanced Raman excitation spectroscopy." In: *J. Phys. Chem. B* 107 (2003), pp. 7426–7433.

[82] S. Nie and S. R. Emory. "Probing single molecules and single nanoparticles by surface-enhanced Raman scattering." In: *Science* 275.5303 (1997), pp. 1102–1106.

[83] M. Culha et al. "Surface-enhanced Raman scattering as an emerging characterization and detection technique." In: *J. Nanotechnol.* 2012 (2012). DOI: 10.1155/2012/971380.

[84] E. C. Le Ru et al. "Surface enhanced Raman scattering enhancement factors: A comprehensive study". In: *J. Phys. Chem. C* 111 (2007), pp. 13794–13803.

[85] K. Kneipp et al. "Single molecule detection using surface-enhanced Raman scattering (SERS)." In: *Phys. Rev. Lett.* 78.9 (1997), pp. 1667–1670.

[86] K. Kneipp et al. "Ultrasensitive chemical analysis by Raman spectroscopy." In: *Chem. Rev.* 99 (1999), pp. 2957–2975.

[87] A. Otto. "What is observed in single molecule SERS, and why?" In: *J. Raman Spectrosc.* 33 (2002), pp. 593–398.

[88] M. Fleischmann, P. J. Hendra, and A. J. McQuillan. "Raman spectra of pyridine adsorbed at a silver electrode." In: *Chem. Phys. Lett.* 26.2 (1974), pp. 163–166.

[89] J. R. Lombardi and R. L. Birke. "A unified approach to surface-enhanced Raman spectroscopy." In: *J. Chem. Phys. C* 112 (2008), pp. 5605–5617.

[90] W. Zhu. "Plasmonics for surface-enhanced Raman scattering: from classical to quantum." PhD thesis. Harvard University, 2014. URL: https://dash.harvard.edu/handle/1/12269877.

[91] S. K. Saikin et al. "On the chemical bonding effects in the Raman response: Benzenethiol adsorbed on silver clusters." In: *Phys. Chem. Chem. Phys.* 41.11 (2009), pp. 9401–9411. DOI: 10.1039/B906885F.

[92] J. R. Lombardi et al. "Charge-transfer theory of surface enhanced Raman spectroscopy: Herzberg-Teller contributions." In: *J. Chem. Phys.* 84.8 (1986), pp. 4174–4180.

[93] A. Otto et al. "Surface-enhanced Raman scattering." In: *J. Phys. Condens. Matter* 4 (1992), pp. 1143–1212.

[94] P. G. Etchegoin and E. C. Le Ru. *Surface enhanced Raman spectroscopy: Analytical, biophysical and life science applications*. Wiley-VCH Verlag GmbH and Co. KGaA, 2010. Chap. 1: Basic Electromagnetic theory of SERS. Pp. 1–37. ISBN: 978-3-527-32567-2.

[95] G. C. Schatz and R. P. Van Duyne. *Handbook of vibrational spectroscopy*. John Wiley and Sons Ltd, 2002. Chap. Electromagnetic mechanism of surface-enhanced spectroscopy.

[96] P. L. Stiles et al. "Surface-enhanced Raman spectroscopy". In: *Annu. Rev. Anal. Chem.* 1 (2008), pp. 601–626.

[97] E. C. Le Ru and P. G. Etchegoin. "Rigorous justification of the $|E|^4$ enhancement factor in surface enhanced Raman spectroscopy". In: *Chem. Phys. Lett* 423.1-3 (2006), pp. 63–66.

[98] A. Kinkhabwala et al. "Large single-molecule fluorescence enhancements produced by a bowtie nanoantenna." In: *Nat. Photon.* 3 (2009), pp. 654–657. DOI: 10.1038/nphoton.2009.187.

[99] K. L. Kelly et al. "The optical properties of metal nanoparticles: The influence of size, shape, and dielectric environment." In: *J. Phys. Chem. B* 107.3 (2003), pp. 668–677. DOI: 10.1021/jp026731y.

[100] A. X. Wang and X. Kong. "Review of recent progress of plasmonic materials and nano-structures for surface-enhanced Raman scattering." In: *Materials* 8 (2015), pp. 3024–3052. DOI: 10.3390/ma8063024.

[101] M. Moskovitz. "Surface roughness and the enhanced intensity of Raman scattering by molecules adsorbed on metals." In: *J. Chem. Phys.* 69 (1978), pp. 4159–4161.

[102] S. L. Kleinman et al. "Creating, characterizing, and controlling chemistry with SERS hot spots." In: *Phys. Chem. Chem. Phys.* 15 (2013), pp. 21–36.

[103] A. A. Lazarides and G. C. Schatz. "DNA-linked metal nanosphere materials: structural basis for the optical properties." In: *J. Phys. Chem.* 104 (2000), pp. 460–467.

[104] E. Bailo and V. Deckert. "Tip-enhanced Raman scattering." In: *Chem. Soc. Rev.* 37 (2008), pp. 921–930.

[105] B. Sharma et al. "SERS: Materials, applications, and the future". In: *Mater. Today* 15.1-2 (2012), pp. 16–25.

[106] F. La Plant. *Emerging Raman applications and techniques in biomedical and pharmaceutical fields*. Berlin, Heidelberg: Springer, 2010. Chap. 1:Lasers, Spectrographs, and Detectors, pp. 1–24. DOI: 10.1007/978-3-642-02649-2_1.

[107] Spectra-Physics. *213A, Rev.C, Model 3900S: User's Manual*. California, 2002. URL: http://www.who.int/environmental_health_emergencies/poisoning/methanol_information.pdf.

[108] S. M. Kobtsev and N. A. Sventsitskaya. "Application of birefringent filters in continuous-wave tunable lasers: a review". In: *Opt. Spektrosk.* 73 (1992), pp. 196–212.

[109] J. Hutchings et al. "The potential for histological screening using a combination of rapid Raman mapping and principal component analysis." In: *J. Biophotonics.* 2 (2009), pp. 91–103.

[110] T. G. Spiro. "Resonance Raman spectroscopy: a new structure probe for biological chromophores." In: *Acc. Chem. Res.* 7 (1974), pp. 339–334.

[111] I. K. Hu S. Z.and Morris, K. M. Singh J. P.and Smith, and T. G Spiro. "Complete assignment of cytochrome-C resonance Raman-Spectra via enzymatic reconstitution with isotopically labeled hemes." In: *J. Am. Chem. Soc.* 115 (1993), pp. 12446–12458.

[112] S. T. Mayne et al. "Resonance Raman spectroscopic evaluation of skin carotenoids as a biomarker of carotenoid status for human studies." In: *Arch. Biochem. Biophys.* 539.2 (2013), pp. 163–170. DOI: http://dx.doi.org/10.1016/j.abb.2013.06.007.

[113] L.E. Jamieson et al. "Simultaneous intracellular redox potential and pH measurements in live cells using SERS nanosensors." In: *Analyst* 140 (2015), pp. 2330–2335.

[114] C. Shi et al. "Intracellular surface-enhanced Raman scattering probes based on TAT peptide-conjugated Au nanostars for distinguishing the differentiation of lung resident mesenchymal stem cells". In: *Biomaterials* 58 (2015), pp. 10–25.

[115] J. D. Driskell et al. "Surface-enhanced Raman scattering immunoassays using a rotated capture substrate." In: *Anal. Chem.* 79 (2007), pp. 4141–4148.

[116] H. Tu and S. A. Boppart. "Coherent anti-Stokes Raman scattering microscopy: overcoming technical barriers for clinical translation." In: *J. Biophotonics* 7 (2014), pp. 9–22.

[117] C. H. Champ et al. "High-speed coherent Raman fingerprint imaging of biological tissues." In: *Nat. Photonics* 8 (2014), pp. 627–634.

[118] C.L. Evans et al. "Chemical imaging of tissue in vivo with video-rate coherent anti-Stokes Raman scattering microscopy." In: *Proc. Natl. Acad. Sci. U. S. A.* 102 (2005), pp. 16807–16812.

[119] O. Uckermann et al. "Label-free delineation of brain tumors by coherent anti-Stokes Raman scattering microscopy in an orthotopic mouse model and human glioblastoma." In: *PLoS ONE* 9.e107115 (2014).

[120] B. G. Saar et al. "Video-rate molecular imaging in vivo with stimulated Raman scattering." In: *Science* 330 (2010), pp. 1368–1370.

[121] W. J. Tipping et al. "Stimulated Raman scattering microscopy: an emerging tool for drug discovery." In: *Chem. Soc. Rev.* 45 (2016), pp. 2075–2089.

[122] C. Zhang et al. "Stimulated Raman scattering flow cytometry for label-free single particle analysis." In: *Optica* 4.1 (2017), pp. 2334–2536.

[123] C. W. Freudiger et al. "Stimulated Raman scattering microscopy with a robust fibre laser source." In: *Nat. Photon.* 8 (2014), pp. 153–158.

[124] C. W. Freudiger et al. "Label-free biomedical imaging with high sensitivity by stimulated Raman scattering microscopy." In: *Science* 322 (2008), pp. 1857–1860.

[125] D. W. Kukura P. McCamant and R. A. Mathies. "Femtosecond stimulated Raman spectroscopy". In: *Annu. Rev. Phys. Chem.* 58 (2007), pp. 461–488.

[126] P. W. Loeffen et al. "Spatially offset Raman spectroscopy (SORS) for liquid screening." In: *Proc. of SPIE Optics and Photonics for Counterterrorism and Crime Fighting VII; Optical Materials in Defence Systems Technology VIII; and Quantum-Physics-based Information Security*. Vol. 8189. SPIE, 2011. DOI: 10.1117/12.898109.

[127] H.-n. Xie et al. "Tracking bisphosphonates through a 20 mm thick porcine tissue by using surface-enhanced spatially offset Raman spectroscopy". In: *Angew. Chem. Int. Ed.* 51.34 (2012), pp. 8509–8511. DOI: 10.1002/anie.201203728.

[128] I. Latka et al. "Fibre optic probes for linear and nonlinear Raman applications-Current trends and future development." In: *Laser Photon. Rev.* 7.5 (2013), pp. 698–731.

[129] M. D. Keller et al. "Development of a spatially offset Raman spectroscopy probe for breast tumor surgical margin evaluation." In: *J. Biomed. Opt.* 16 (2011), p. 077006.

[130] P. Matousek and N. Stone. "Recent advances in the development of Raman spectroscopy for deep non-invasive medical diagnosis." In: *J. Biophotonics* 6 (2013), pp. 7–19.

[131] J. C. C. Day and N. Stone. "A subcutaneous Raman needle probe." In: *Appl. Phys. Lett.* 67 (2013), pp. 349–354.

[132] M. G. Shim et al. "Study of fiber-optic probes for in vivo medical Raman spectroscopy." In: *Appl. Spectrosc.* 53 (1999), pp. 619–627.

[133] A. S. Haka et al. "In vivo margin assessment during partial mastectomy breast surgery using Raman spectroscopy". In: *Cancer Res.* 66.6 (2006), pp. 3317–22.

[134] *Diffraction Grating Handbook*. Thermo RGL, 2002. Chap. 2: The physics of diffraction gratings. URL: http://www.ino.it/home/lucamerca/Reticolo%20Diffrazione.pdf.

[135] Spectral Instruments Inc. *What is a CCD?* accessed on 28/02/2017. URL: http://www.specinst.com/What_Is_A_CCD.html.

[136] S. Li and L. Dai. "An improved algorithm to remove cosmic spikes in Raman spectra for online monitoring." In: *Appl. Spectrosc.* 65.11 (2011), pp. 1300–1306.

[137] H. Shinzawa et al. "Multivariate data analysis for Raman spectroscopic imaging." In: *J. Raman Spectrosc.* 40.12 (2009), pp. 1720–1725.

[138] J. Jauregui. *Principal component analysis with linear algebra*. 2012. URL: http://www.math.union.edu/~jaureguj/PCA.pdf.

[139] I. T. Jolliffe. *Principal component analysis*. New York: Springer-Verlag, 2002.

[140] M. Stone. "Cross-validatory choice and assessment of statistical predictions". In: *J. R. Stat. Soc. B. Stat. Methodol* 36.2 (1974), pp. 111–147.

[141] S. Geisser. "The predictive sample reuse method with applications." In: *J. Amer. Statist. Assoc.* 70 (1975), pp. 320–328.

[142] A. B. Barber, D. P. Dobkin, and H. Huhdanpaa. "The quickhull algorithm for convex hulls." In: *ACM Trans. Math. Softw.* 22.4 (1996), pp. 469–483.

[143] T. K. Kim. "T test as a parametric statistic." In: *Korean J. Anesthesiol.* 68.6 (2015), pp. 540–546.

[144] J. J. Filliben and A. Heckert. *Handbook of statistical methods*. accessed on 06/03/2017. URL: http://www.itl.nist.gov/div898/handbook/eda/section3/eda353.htm.

[145] PubMed Health. *Leukocytes (White Blood Cells)*. accessed on 12/05/2017. URL: https://www.ncbi.nlm.nih.gov/pubmedhealth/PMHT0022046/.

[146] J. W. Chan. "Recent advances in laser tweezers Raman spectroscopy (LTRS) for label-free analysis of single cells." In: *J. Biophotonics* 6 (2013), pp. 36–48.

[147] R. J. Swain and M. M. Stevens. "Raman microspectroscopy for non-invasive biochemical analysis of single cells." In: *Biochem. Soc. Trans.* 35.3 (2007), pp. 544–549.

[148] A. B. Zoladek et al. "Label-free molecular imaging of immunological synapses between dendritic and T cells by Raman micro-spectroscopy." In: *Analyst* 135.12 (2010), pp. 3205–3212.

[149] A. Ramoji et al. "Toward a spectroscopic hemogram: Raman spectroscopic differentiation of the two most abundant leukocytes from peripheral blood." In: *Anal. Chem.* 84.12 (2012), pp. 5335–5342.

[150] P. C. Ashok et al. "Label-free haemogram using wavelength modulated Raman spectroscopy for identifying immune-cell subset." In: *Biomedical Vibrational Spectroscopy Vi: Advances in Research and Industry*. Vol. 8939. SPIE, 2014.

[151] W. Ellmeier, S. Sawada, and D. R. Littman. "The regulation of CD4 and CD8 coreceptor gene expression during T cell development". In: *Annu. Rev. Immunol.* 17 (1999), pp. 523–554.

[152] J. Zhu, H. Yamane, and W. E. Paul. "Differentiation of effector CD4 T cell populations." In: *Annu. Rev. Immunol* 28 (2010), pp. 445–489.

[153] P. Wong and E. G. Pamer. "CD8 T cell responses to infectious pathogens." In: *Annu. Rev. Immunol.* 21 (2003), pp. 29–70.

[154] T. W. Le Bien and T. F. Tedder. "B lymphocytes: how they develop and function". In: *Blood* 112 (2008), pp. 1570–1580.

[155] S. G. Tangye et al. "Intrinsic differences in the proliferation of naive and memory human B cells as a mechanism for enhanced secondary immune responses." In: *J. Immunol.* 170.2 (2003), pp. 686–694.

[156] B. Alberts et al. *Molecular Biology of the Cell. 4th edition.* New York: Garland Science, 2002. Chap. 24. URL: https://www.ncbi.nlm.nih.gov/books/NBK26884/.

[157] M. B. Lodoen and L. L. Lanier. "Viral modulation of NK cell immunity". In: *Nat. Rev. Microbiol.* 3 (2005), pp. 59–69.

[158] G. J. Randolph, J. Ochando, and S. Partida-Sanchez. "Migration of dendritic cell subsets and their precursors". In: *Annu. Rev. Immunol.* 26 (2008), pp. 293–316.

[159] J. Banchereau and R. M. Steinman. "Dendritic cells and the control of immunity." In: *Nature* 392 (1998), pp. 245–252.

[160] H. Ueno et al. "Dendritic cell subsets in health and disease". In: *Immunol. Rev.* 219.1 (2007), pp. 118–142.

[161] F. Sallusto and A. Lanzavecchia. "The instructive role of dendritic cells on T-cell responses." In: *Arthritis Res.* 4 (2002), s127–s132.

[162] K. McKenna, A.-S. Beignon, and N. Bhardwaj. "Plasmacytoid dendritic cells: linking innate and adaptive immunity". In: *J. Virol.* 79.1 (2005), pp. 17–27.

[163] C. Shi and E. G. Pamer. "Monocyte recruitment during infection and inflammation." In: *Nat. Rev. Immunol.* 11 (2011), pp. 762–774. DOI: 10.1038/nri3070.

[164] A. J. Hoboro et al. "Raman spectroscopy as a tool for label-free lymphocyte cell line discrimination". In: *Analyst* 141 (2016), pp. 3756–3764.

[165] P. R. Jess et al. "Early detection of cervical neoplasia by Raman spectroscopy." In: *Int. J. Cancer* 121.12 (2007), pp. 2723–2728.

[166] V. V. Pully, A. T. M. Lenferink, and C. Otto. "Time-lapse Raman imaging of single live lymphocytes." In: *J. Raman Spectrosc.* 42.2 (2011), pp. 167–173.

[167] N. Uzunbajakava et al. "Nonresonant Raman imaging of protein distribution in single human cells". In: *Biopolymers* 72 (2003), pp. 1–9.

[168] N. Onai et al. "A clonogenic progenitor with prominent plasmacytoid dendritic cell developmental potential." In: *Immunity* 38.5 (2013), pp. 943–957.

[169] C. Bourgeois, B. Rocha, and C. Tanchot. "A role for CD40 expression on CD8+ T cells in the generation of CD8+ T cell memory". In: *Science* 297.5589 (2002), pp. 2060–2063.

[170] C. Tanchot and B. Rocha. "CD8 and B cells memory: same strategy, same signals". In: *Nature. Immunol.* 4.5 (2003), pp. 431–432.

[171] A. Coutinho et al. "Mechanism of thymus-independent immunocyte triggering mitogenic activation of B cells results in specific immune responses." In: *J. Exp. Med.* 139 (1974), pp. 74–92.

[172] R. Dziarski. "Preferential induction of autoantibody secretion in polyclonal activation by peptidoglycan and lipopolysaccharide. II. In vivo studies". In: *J. Immunol.* 128.3 (1982), pp. 1026–1030.

[173] S. Minguet et al. "Enhanced B-cell activation mediated by TLR4 and BCR crosstalk". In: *Eur. J. Immunol.* 38.9 (2008), pp. 2475–2487. DOI: 10.1002/eji.200738094. URL: http://dx.doi.org/10.1002/eji.200738094.

[174] K. Hoshino et al. "Cutting edge: Toll-like receptor 4 (TLR4)-deficient mice are hyporesponsive to lipopolysaccharide: evidence for TLR4 as the Lps gene product." In: *J. Immunol.* 162.7 (1999), pp. 3749–3752.

[175] C. Kalis et al. "Toll-like receptor 4 expression levels determine the degree of LPS-susceptibility in mice". In: *Eur. J. Immunol.* 33.3 (2003), pp. 798–805. ISSN: 1521-4141. DOI: 10.1002/eji.200323431. URL: http://dx.doi.org/10.1002/eji.200323431.

[176] C. Vaure and Y. Liu. "A comparative review of toll-like receptor 4 expression and functionality in different animal species." In: *Front. Immunol.* 5 (2014), p. 316.

[177] S. Romagnani. "Regulation of the T cell response." In: *Clin. Exp. Allergy* 36 (2006), pp. 1357–1366.

[178] P. Mouchacca, A. M. Schmitt-Verhulst, and C. Boyer. "Visualization of cytolytic T cell differentiation and granule exocytosis with T cells from mice expressing active fluorescent granzyme B." In: *PLos One* 8 (2013), e67239.

[179] L. A. Tesmer et al. "TH17 cells in human disease." In: *Immunol. Rev* 223 (2008), pp. 87–113.

[180] N. Eastaff-Leung et al. "Foxp3+ regulatory T cells, Th17 effector cells, and cytokine environment in inflammatory bowel disease." In: *J. Clin. Immunol.* 30 (2010), pp. 80–89.

[181] D. Peng et al. “A high frequency of circulating th22 and th17 cells in patients with new onset graves’ disease.” In: *PLos One* 8 (2013), e68446.

[182] M. I. Vargas-Rojas et al. “Increase of Th17 cells in peripheral blood of patients with chronic obstructive pulmonary disease.” In: *Respir. Med* 105.11 (2011), pp. 1648–1654.

[183] A. Kelso et al. “Single-cell analysis by RT-PCR reveals differential expression of multiple type 1 and 2 cytokine genes among cells within polarized CD4+ T cell populations.” In: *Int. Immunol.* 11 (1999), pp. 617–621.

[184] S. Zhao et al. “Comparison of RNA-Seq and microarray in transcriptome profiling of activated T cells.” In: *PLoS One* (2014), e78644.

[185] H. Yamakoshi et al. “Imaging of EdU, an alkyne-tagged cell proliferation probe, by Raman microscopy”. In: *J. Am. Chem. Soc.* 133.16 (2011), pp. 6102–6105.

[186] X. Xu et al. “Near-field enhanced plasmonic-magnetic bifunctional nanotubes for single cell bioanalysis.” In: *Adv. Funct. Mater.* 23.35 (2013), pp. 4332–4338.

[187] N. Pavillon, F. Katsumasa, and N. I. Smith. “Multimodal label-free microscopy.” In: *J. Innov Opt Health Sci* 7.5 (2014), p. 1330009.

[188] P. Marquet et al. “Red blood cell structure and dynamics explored with digital holographic microscopy.” In: *Imaging, Manipulation, and Analysis of Biomolecules, Cells, and Tissues VII*. Vol. 7182. San Jose CA: SPIE, 2009.

[189] T. Colomb and J. Kuhn. *Digital holographic microscopy*. Berlin Heidelberg: Springer, 2011.

[190] C. A. Patil et al. “Combined Raman spectroscopy and optical coherence tomography device for tissue characterization.” In: *Opt. Lett.* 33.10 (2008), pp. 1135–1137.

[191] C. A. Patil et al. “A Clinical Instrument for Combined Raman Spectroscopy Optical Coherence Tomography of Skin Cancers”. In: *Lasers Surg Med* 43.2 (2011), pp. 143–151.

[192] P. C. Ashok et al. "Multi-modal approach using Raman spectroscopy and optical coherence tomography for the discrimination of colonic adenocarcinoma from normal colon". In: *Biomed. Opt. Express* 4.10 (2013), pp. 2179–2186.

[193] E. Cuche, F. Bevilacqua, and C. Depeursinge. "Digital holography for quantitative phase-contrast imaging." In: *Opt. Lett.* 24.5 (2014), pp. 291–293.

[194] Z. Monemhaghdoust et al. "Off-axis digital holographic camera for quantitative phase microscopy". In: *Biomed. Opt. Express* 5.6 (2014), pp. 1721–1730.

[195] M. Mihailescu et al. "Automated imaging, identification, and counting of similar cells from digital hologram reconstructions." In: *Appl. Opt.* 50.20 (2011), pp. 3589–3597.

[196] A. Mölder et al. "Non-invasive, label-free cell counting and quantitative analysis of adherent cells using digital holography". In: *J. Microsc.* 232.2 (2008), pp. 240–247.

[197] S. Murata and N. Yasuda. "Potential of digital holography in particle measurement". In: *Opt. Laser Technol.* 32 (2000), pp. 567–574.

[198] B. Mir, K. Tangella, and G Popescu. "Blood testing at the single cell level using quantitative phase and amplitude microscopy". In: *Biomed. Opt. Express* 2.12 (2011), pp. 3259–3266.

[199] N. Pavillon and N.I. Smith. "Implementation of simultaneous quantitative phase with Raman imaging". In: *EPJ Tech Instrum* 2.5 (2015).

[200] N. Pavillon, A. J. Hobro, and N. I. Smith. "Cell optical density and molecular composition revealed by simultaneous multimodal label-free imaging". In: *Biophys. J.* 105 (2013), pp. 1123–1132.

[201] J. W. Kang et al. "Combined confocal Raman and quantitative phase microscopy system for biomedical diagnosis." In: *Biomed Opt Express* 2.9 (2011), pp. 2482–2492.

[202] B. Rappaz et al. "Measurement of the integral refractive index and dynamic cell morphometry of living cells with digital holographic microscopy". In: *Opt. Express* 13.23 (2005), pp. 9361–9373.

[203] N. K. Das et al. “Raman Plus X: Biomedical Applications of Multimodal Raman Spectroscopy”. In: *Sensor. Rev.* 17 (2017), p. 1592.

[204] O.and Henderson M.H.and Kim S.and Rinehart M.T.and Kashuba A.D.M.and Wax A.and Katz D.F Maher J.R.and Chuchuen. “Co-localized confocal Raman spectroscopy and optical coherence tomography (CRS-OCT) for depth-resolved analyte detection in tissue.” In: *Biomed. Opt. Express* 6 (2015), pp. 2022–2035.

[205] A.M.and Setlow P.and Li Y.Q Wang S.W.and Shen. “Characterization of the dynamic germination of individual clostridium difficile spores using Raman spectroscopy and differential interference contrast microscopy.” In: *J. Bacteriol.* 197 (2015), pp. 2361–2373.

[206] A. D. Hitchins and R. A Kahn A. J.and Slepecky. “Interference contrast and phase contrast microscopy of sporulation and germination of bacillus megaterium.” In: *J. Bacteriol.* 96 (1968), pp. 1811–1817.

[207] N. Pavillon and N.I. Smith. “Maximizing throughput in label-free microspectroscopy with hybrid Raman imaging.” In: *J. Biomed. Opt.* 20.1 (), p. 016007.

[208] N.and Mitchell M.F.and Malpica A.and Thomsen S.and Richardskortum R Mahadevan A.and Ramanujam. “Optical techniques for the diagnosis of cervical precancers: A comparison of Raman and fluorescence spectroscopies.” In: *Adv. Fluoresc. Sens. Technol. II* 2388 (1995), pp. 110–120.

[209] C.J.and Varma S.and Perkins W.and Leach I.H.and Koloydenko A.A.and Williams H.C.and Notingher I. Kong K.and Rowlands. “Diagnosis of tumors during tissue-conserving surgery with integrated autofluorescence and Raman scattering microscopy”. In: *Proc. Natl. Acad. Sci. USA* 110 (2013), pp. 15189–15194.

[210] K.and Varma S.and Leach I.and Williams H.C.and Notingher I. Takamori S.and Kong. “Optimization of multimodal spectral imaging for assessment of resection margins during mohs micrographic surgery for basal cell carcinoma.” In: *Biomed. Opt. Express* 6 (2015), pp. 98–111.

[211] K.and Gibson G.and Varma S.and Williams H.and Padgett M.and Notingher I. Sinjab F.and Kong. "Tissue diagnosis using power-sharing multifocal Raman micro-spectroscopy and auto-fluorescence imaging." In: *Biomed. Opt. Express.* 7 (2016), pp. 2993–3006.

[212] H. J. van Manen et al. "Single-cell Raman and fluorescence microscopy reveal the association of lipid bodies with phagosomes in leukocytes." In: *Proc. Natl. Acad. Sci. U. S. A.* 102.29 (2005), pp. 10159–64.

[213] B. Kang et al. "Exploiting the nanoparticle plasmon effect: observing drug delivery dynamics in single cells via Raman/fluorescence imaging spectroscopy." In: *ACS Nano* 7.8 (2013), pp. 7420–7427.

[214] J.and Lankers M.and Trunk M.and Hartmann I.and Urlaub E.and Musick J. Kiefer W.and Popp. "Raman-mie scattering from single laser trapped microdroplets." In: *J. Mol. Struct.* 408 (1997), pp. 113–120.

[215] J.and Trunk M.and Kiefer W Musick J.and Popp. "Investigations of radical polymerization and copolymerization reactions in optically levitated microdroplets by simultaneous Raman spectroscopy, mie scattering, and radiation pressure measurements." In: *Appl. Spectrosc.* 52 (1998), pp. 692–701.

[216] Z.J. Smith and A. J. Berger. "Validation of an integrated Raman- and angular-scattering microscopy system on heterogeneous bead mixtures and single human immune cells." In: *Appl. Opt.* 48.10 (2009), pp. 109–120.

[217] Z.J. Smith and A. J. Berger. "Integrated Raman- and angular-scattering microscopy." In: *Appl. Opt.* 33.7 (2008), pp. 714–716.

[218] Z.J. Smith and A. J. Berger. "Construction of an integrated Raman- and angular-scattering microscope." In: *Rev. Sci. Instrum.* 80 (2009), p. 044302.

[219] S.and Foster T.H.and Berger A.J. Shipp D.W.and Mitra. "Effect of photodynamic therapy on single cancer cells studied by integrated Raman and angular scattering microscopy." In: *Proceedings of Biomedical Vibrational Spectroscopy V: Advances in Research and Industry* (2012), p. 82190G.

[220] Y.C. Meher A.K.and Chen. "Combination of Raman spectroscopy and mass spectrometry for online chemical analysis." In: *Anal. Chem.* 88 (2016), pp. 9151–9157.

[221] A.C.and Matthaus C.and Tarcea N.and von Eggeling F.and Schmitt M.and Schubert U.S.and Popp J Bocklitz T.W.and Creceius. "Deeper understanding of biological tissue: Quantitative correlation of MALDI-TOF and Raman imaging." In: *Anal. Chem.* 85 (2013), pp. 10829–10834.

[222] D. Gabor. "Holography, 1948-1971". In: *Science* 177.4046 (1972), p. 299.

[223] G. K. Ackermann and J. Eichler. *Holography: A practical approach.* Weinheim, Germany: Wiley-VCH Verlag GmbH & Co. KGaA, 2007.

[224] F. Yi, I. Moon, and Y. H. Lee. "Three-dimensional counting of morphologically normal human red blood cells via digital holographic microscopy." In: *J. Biomed. Opt.* 20.1 (2015).

[225] E. Cuche, P. Marquet, and C. Depeursinge. "Simultaneous amplitude-contrast and quantitative phase-contrast microscopy by numerical reconstruction of Fresnel off-axis holograms." In: *Appl. Opt.* 38.34 (1999), pp. 6994–7001.

[226] G. Coppola et al. "A digital holographic microscope for complete characterization of microelectromechanical systems." In: *Meas. Sci. Technol.* 15.3 (2004), pp. 529–539.

[227] P. Marquet et al. "Digital holographic microscopy: a noninvasive contrast imaging technique allowing quantitative visualization of living cells with subwavelength axial accuracy." In: *Opt. Lett.* 30.5 (2005), pp. 468–470.

[228] B. Kemper and G. V. Bally. "Digital holographic microscopy for live cell applications and technical inspection." In: *Appl. Opt.* 47.4 (2007), A52–A61.

[229] M. Antkowiak et al. "Quantitative phase study of the dynamic cellular response in femtosecond laser photoporation." In: *Biomed. Opt. Express* 1.2 (2010), pp. 414–424.

[230] V. Micó, J. García, and Z. Zalevsky. "Quantitative phase imaging by common-path interferometric microscopy: application to super-resolved imaging and nanophotonics." In: *J. Nanophotonics* 3 (2009), p. 031780.

[231] G. Popescu et al. "Diffraction phase microscopy for quantifying cell structure and dynamics." In: *Opt. Lett.* 31.6 (2006), pp. 775–777.

[232] P. Girshovitz and N. T. Shaked. "Compact and portable low-coherence interferometer with off-axis geometry for quantitative phase microscopy and nanoscopy." In: *Opt. Express* 21.5 (2013), pp. 5701–5714.

[233] B. Bhaduri et al. "Diffraction phase microscopy with white light". In: *Opt. Lett.* 37.6 (2012), pp. 1094–1096.

[234] E. N. Leith and J. Upatneiks. "Reconstructed wavefronts and communication theory." In: *J. Opt. Soc. Amer.* 52 (1962), pp. 1123–1130.

[235] E. N. Leith and J. Upatneiks. "Wavefront reconstruction with continuous-tone objects". In: *J. Opt. Soc. Amer.* 53 (1963), pp. 1377–1381.

[236] E. N. Leith and J. Upatneiks. "Wavefront reconstruction with diffused illumination and three-dimensional objects." In: *J. Opt. Soc. Amer.* 54 (1964), pp. 1295–1301.

[237] M. K. Kim. "Applications of digital holography in biomedical microscopy." In: *J. Opt. Soc. Korea* 14.2 (2010), pp. 77–89.

[238] G. R. Toker. *Holographic interferometry: A Mach-Zehnder approach*. CRC Press, 2016. Chap. 2.

[239] K. Itoh. "Analysis of the phase unwrapping algorithm." In: *Appl. Opt.* 21.14 (1982), pp. 2470–2470.

[240] L. Ying. "Phase unwrapping". In: *Wiley Encyclopaedia of Biomedical Engineering* (2006). DOI: 10.1002/9780471740360.ebs1356.

[241] S. Heshmat, S. Tomioka, and S. Nishiyama. "Phase extraction and unwrapping using rotational and direct compensators for digital hologram." In: *Opt. Eng.* 52.10 (2013), pp. 101910–1–8.

[242] X. Su and W. Chen. "Reliability-guided phase unwrapping algorithm: a review." In: *Opt. Lasers Eng.* 42.3 (2004), pp. 245–261.

[243] D. C. Ghiglia and M. D. Pritt. *Two-dimensional phase unwrapping: theory, algorithms and software.* New York: Wiley-Interscience, 1998.

[244] S. Van der Jeught and J. J. J. Dirckx. "Real-time structured light profilometry: A review." In: *Opt. Lasers Eng.* (2016), pp. 2723–2728. DOI: 10.1016/j.optlaseng.2016.01.011.

[245] K. W. Gossage et al. "Texture analysis of optical coherence tomography images: feasibility for tissue classification". In: *J. Biomed. Opt* 8.3 (2003), pp. 570–575.

[246] M. Bhattacharjee et al. "Binary tissue classification studies on resected human breast tissues using optical coherence tomography images". In: *J. Innov. Opt. Health Sci* 4.1 (2011).

[247] R. M. Haralick, K. Shanmugam, and I. Dinstein. "Textural features for image classification." In: *IEEE Trans. Sys. Man. Cybern.* SMC-3.6 (1973), pp. 610–621.

[248] B. Rappaz et al. "Simultaneous cell morphometry and refractive index measurement with dual-wavelength digital holographic microscopy and dye-enhanced dispersion of perfusion medium." In: *Opt. Lett.* 33.7 (2008), pp. 744–746.

[249] Z. Monemhaghdoust et al. "Dual wavelength full field imaging in low coherence digital holographic microscopy". In: *Opt. Lett.* 19.24 (2011), pp. 24005–24022.

[250] Y. Sung et al. "Optical diffraction tomography for high resolution live cell imaging". In: *Opt. Express* 17.1 (2009), pp. 266–277.

[251] J. Yoon et al. "Label-free characterization of white blood cells by measuring 3D refractive index maps." In: *Biomed. Opt. Express* 6.10 (2015), pp. 3865–3875.

[252] T. Tahara et al. "Parallel phase-shifting digital holographic microscopy." In: *Biomed. Opt. Express* 1.2 (2010), pp. 610–616.

[253] J. W. Parker et al. "Morphologic and cytochemical comparison of human lymphoblastoid T-cell and B-cell lines: light and electron microscopy." In: *J. Natl. Cancer. Inst.* 60.1 (1978), pp. 59–68.

[254] D. I. Strokotov et al. "Is there a difference between T- and B- lymphocyte morphology?" In: *J. Biomed. Opt.* 14.6 (2009), p. 064036.

[255] *Use of intracellular flow cytometry*. accessed on 14/03/2017. URL: https://www.cellsignal.com/contents/resources-applications/uses-of-intracellular-flow-cytometry/apps-uses-intracellular-flow-cytometry/.

[256] S. Kosmeier et al. "Reduction of parasitic interferences in digital holographic microscopy by numerically decreased coherence length." In: *Appl. Phys. B.* 106.1 (2012), pp. 107–115.

[257] B. Bhaduri, K. Tangella, and G. Popescu. "Fourier phase microscopy with white light". In: *Biomed. Opt. Express* 4.8 (2013), pp. 1434–1441.

[258] B. Kemper et al. "Characterisation of light emitting diodes (LEDs) for application in digital holographic microscopy of micro and nanostructured surfaces." In: *Opt. Laser. Eng.* 46.7 (2008), pp. 499–507.

[259] L. M. L. de Lau and M. M. B. Breteler. "Epidemiology of Parkinson's disease." In: *Neurol.* 5.6 (2006), pp. 525–535.

[260] E. R. Dorsey et al. "Projected number of people with Parkinson disease in the most populous nations, 2005 through 2030." In: *Neurol.* 68.5 (2007), pp. 384–386.

[261] C. A. Davie. "A review of Parkinson's disease." In: *Br. Med. Bull* 86 (2008), pp. 109–127.

[262] A. H. V. Schapira. "Dopamine agonists and neuroprotection in Parkinson's disease." In: *Eur. J. Neurol.* 9.s3 (2002), pp. 7–14.

[263] G. H. Doherty. "Homocysteine and Parkinson's disease: A complex relationship." In: *J. Neurol. Disord.* 1.1 (2013), p. 1000107.

[264] F. Gavin, P. Marin, and S. Claeysen. "Primary culture of mouse dopaminergic neurons." In: *J. Vis. Exp.* 91 (2014), e51751.

[265] W.-T. Chiu et al. "Real-time electrochemical recording of dopamine release under optogenetic stimulation." In: *PLoS One* 9.2 (2014), e89293.

[266] J. A. Korecka et al. "Phenotypic characterization of retinoic acid differentiated SH-SY5Y cells by transciptional profiling." In: *PLoS ONE* 8.5 (2013), e63862.

[267] H. Shinohara, F. Wang, and S. M. Z. Hossain. "A convenient, high-throughput method for enzyme-luminescence detection of dopamine released from PC12 cells." In: *Nat. Protoc.* 3 (2008), pp. 1639–1644. DOI: doi:10.1038/nprot.2008.158.

[268] M.-V. Clement et al. "The cytotoxicity of dopamine may be an artefact of cell culture". In: *J. Neurochem.* 81.3 (2002), pp. 414–421. DOI: 10.1046/j.1471-4159.2002.00802.x.

[269] J. J. Chen. "The role of levodopa in the treatment of Parkinson's disease." In: *Focus on Parkinson's disease* 23.1 (2012), pp. 5–9.

[270] C.B. Levine et al. "57 Diagnosis and treatment of Parkinson's disease: A systematic review of the literature: Summary." In: *AHRQ Evidence Report Summaries.* (2003), pp. 1998–2005.

[271] J. C. M. Schlachetzki, S. W. Saliba, and A. C. P. de Oliveira. "Studying neurodegenerative disease in culture models." In: *Rev. Bras. Psiquiatr.* 35 (2013), s92–s100.

[272] L. Agholme et al. "An in vitro model for neuroscience: Differentiation of SH-SY5Y cells into cells with morphological and biochemical characteristics of mature neurons." In: *J. Alzheimers Dis.* 20.4 (2010), pp. 1069–1082.

[273] H. Xicoy, B. Wieringe, and G. J. M. Martens. "The SH-SY5Y cell line in Parkinson's disease research: a systematic review." In: *Mol. Neurodegener.* 12.10 (2017).

[274] M. P. La Quaglia and K. M. Manchester. "A comparitive analysis of neuroblastic and substrate-adherent human neuroblastoma cell lines." In: *J. Pediatr. Surg.* 31.2 (1996), pp. 315–318.

[275] H. R. Xie, L. S. Hu, and G. Y. Li. "SH-SY5Y human neuroblastoma cell line: in vitro cell model of dopaminergic neurons in Parkinson's disease." In: *Chin. Med. J. (Engl)* 123.8 (2010), pp. 1086–92.

[276] S. Påhlman et al. "Differentiation and survival influences of growth factors in human neuroblastoma." In: *Eur. J. Cancer.* 31.4 (1995), pp. 453–458.

[277] V. Ciccarone et al. "Phenotypic diversification in human neuroblastoma cells: Expression of distinct neural crest lineages." In: *Cancer. Res.* 49 (1989), pp. 219–225.

[278] M. M. Shipley, C. A. Mangold, and M. L. Szpara. "Differentiation of the SH-SY5Y human neuroblastoma cell line." In: *J. Vis. Exp.* 108 (2016), e53193. DOI: 10.3791/53193.

[279] M. Encinas et al. "Sequential treatment of SH-SY5Y Cells with retinoic acid and brain-derived neurotrophic factor gives rise to fully differentiated, neurotrophic factor-dependent, human neuron-like cells." In: *J. Neurochem.* 75.3 (2000), pp. 991–1003. DOI: 10.1046/j.1471-4159.2000.0750991.x. URL: http://dx.doi.org/10.1046/j.1471-4159.2000.0750991.x.

[280] S. P. Presgraves et al. "Terminally differentiated SH-SY5Y cells provide a model system for studying neuroprotective effects of dopamine agonists." In: *Neurotox. Res.* 5.8 (2004), pp. 579–598.

[281] F. M. Lopes et al. "Comparison between proliferative and neuron-like SH-SY5Y cells as an *in-vitro* model for Parkinson disease studies." In: *Brain Res.* 1337 (2010), pp. 85–94.

[282] S. C. Daubner, T. Le, and S. Wang. "Tyrosine hydroxylase and regulation of dopamine synthesis." In: *Arch. Biochem. Biophys.* 508.1 (2011), pp. 1–12.

[283] I. B. Buchwalow, E. A. Minin, and W. Boecker. "A multicolor fluorescence immunostaining technique for simultaneous antigen targeting." In: *Acta. Histochemica* 107.2 (2005), pp. 143–148.

[284] A. E. Kalyuzhny. *Immunocytochemistry: Essential elements and beyond. Techniques in life science and biomedicine for the non-expert*. New York: Springer, 2016.

[285] H. Towbin, T. Staehelin, and J. Gordon. "Electrophoretic transfer of proteins from polyacrylamide gels to nitrocellulose sheets: procedure and some applications." In: *Proc. Natl. Acad. Sci. U S A* 76.9 (1979), pp. 4350–4354.

[286] R. B. Corley. *A guide to methods in the biomedical sciences.* New york, USA: Springer science and business media, Inc, 2004. Chap. 1: Detection and analysis of proteins.

[287] T. Mahmood and P-C. Yang. "Western blot: Technique, theory, and trouble shooting." In: *North Am. J. Med. Sci.* 4.9 (2012), pp. 429–434.

[288] G-Biosciences. *7 common problems with Western blotting solved.* accessed on 16/05/2017. URL: https://info.gbiosciences.com/blog/bid/130848/7-common-problems-with-western-blotting-solved.

[289] I. U. Rehman, Z. Movasaghi, and S. Rehman. *Vibrational spectroscopy for tissue analysis, series in medical physics and biomedical engineering.* Florida, U.S.A: Taylor and Francis, 2012, pp. 215–271.

[290] S. Gunasekaran, R. T. Kumar, and S. Ponnusamy. "Vibrational spectra and normal coordinate analysis of adrenaline and dopamine." In: *Indian J. Pure Appl. Phys.* 45 (2007), pp. 884–892.

[291] B. J. Venton and R. M. Wightman. "Psychoanalytical electrochemistry: Dopamine and behaviour." In: *Anal. Chem.* 75 (2003), 414A–421A.

[292] A. R. Ali et al. "A nonoxidative sensor based on a self-doped polyaniline/-carbon nanotube composite for sensitive and selective detection of the neurotransmitter dopamine." In: *Anal. Chem.* 79 (2007), pp. 2583–2587.

[293] J.-H. An et al. "Surface-enhanced Raman scattering of dopamine on self-assembled gold nanoparticles." In: *J. Nanosci. Nanotechnol.* 11 (2011), pp. 4424–4429.

[294] A. Huefner et al. "Intracellular SERS nanoprobes for distinction of different neuronal cell types." In: *Nano Lett.* 13 (2013), pp. 2463–2470.

[295] S. Schlücker et al. "Immuno-Raman microspectroscopy: In *situ* detection of antigens in tissue specimens by surface-enhanced Raman scattering." In: *J. Raman Spectrosc.* 37 (2006), pp. 719–721.

[296] R. Lévy et al. "Gold nanoparticles delivery in mammalian live cells: a critical review." In: *Nano Rev.* 1.4889 (2010). DOI: 10.3402/nano.v1i0.4889.

[297] S. Caponi et al. "Raman micro-spectroscopy study of living SH-SY5Y cells adhering on different substrates." In: *Biophys. Chem.* 208 (2016), pp. 48–53.

[298] E. K. Purcell, A. Singh, and D. R. Kipke. "Alginate composition effects on a neural stem cell-seeded scaffold." In: *Tissue Eng. Part C Methods* 15.4 (2009), pp. 541–550.

[299] H. Ge et al. "Poly-L-ornithine promotes preferred differentiation of neural stem/progenitor cells via ERK signalling pathway." In: *Sci. Rep.* 5 (2015), p. 15535.

[300] T. Hazel and T. Müller. "Culture of neuroepithelial stem cells." In: *Curr. Protoc. Neurosci.* (2001). DOI: 10.1002/0471142301.ns0301s00.

[301] S. Rghavan and K. N. Bitar. "The influence of extracellular matrix composition on the differentiation of neuronal subtypes in tissue engineered innervated intestinal smooth muscle sheets." In: *Biomaterials* 35.26 (2014), pp. 7429–7440.

[302] L. A. Flanagan et al. "Regulation of human neural precursor cells by laminin and integrins." In: *J. Neurosci. Res.* 83.5 (2006), pp. 845–856.

[303] L. M. Y. Yu, N. D. Leipzig, and M. S. Shoichet. "Promoting neuron adhesion and growth." In: *Mater. Today* 11.5 (2008), pp. 36–43.

[304] Sigma-Aldrich. *ECL Cell Attachment Matrix*. accessed on 21/04/2017. URL: http://www.sigmaaldrich.com/catalog/product/mm/08110?lang=en&region=GB.

[305] J. Chad and H. V. Wheal. *Cellular neurobiology: A practical approach. Vol 78 of practical approach series.* IRL Press at Oxford University Press, 1991. Chap. 1.

[306] A. Janesick, S. C. Wu, and B. Blumberg. "Retinoic acid signaling and neuronal differentiation." In: *Cell. Mol. Life Sci* 72 (2015), pp. 1559–1576. DOI: 10.1007/s00018-014-1815-9.

[307] T. Angrisino et al. "Chromatin and DNA methylation dynamics during retinoic acid-induced RET gene transcriptional activation in neuroblastoma cells." In: *Nucleic Acids Res.* 39.6 (2011), pp. 1993–2006.

[308] R. A. Frederick and Shaw J. M. "Moving mitochondria: Establishing distribution of an essential organelle." In: *Traffic* 8.12 (2007), pp. 1668–1675.

[309] M. V. Berridge, P. M. Herst, and A. S. Tan. "Tetrazolium dyes as tools in cell biology: New insights into their cellular reduction." In: *Biotechnol. Annu. Rev.* 11 (2005), pp. 127–152.

[310] K. E. Miller and M. P. Sheetz. "Direct evidence for coherent low velocity axonal transport of mitochondria." In: *J. Cell. Biol.* 173.3 (2006), pp. 373–381.

[311] S. R. Chada and P. J. Hollenbeck. "Review mitochondrial movement and positioning in axons: the role of growth factor signaling." In: *J. Exp. Biol.* 206 (2003), pp. 1985–1992.

[312] S. Islam, Y. Niwa, and S. Takagi. "Light dependent intracellular positioning of mitochondria in Arabidopsis thaliana mesophyll cells." In: *Plant Cell Physiol.* 50.6 (2009), pp. 1032–1040.

[313] S. A. Detmer and D. C. Chan. "Functions and dysfunctions of mitochondrial dynamics." In: *Nat. Rev. Mol. Cell Biol.* 8 (2007), pp. 870–879.

[314] J. J. Anders, S. Guena, and S. Rochkind. "Phototherapy promotes regeneration and functional recovery of injured peripheral nerve." In: *Neurol. Res.* 26.2 (2004), pp. 233–239.

[315] K. R. Byrnes et al. "Light promotes regeneration and functional recovery and alters the immune response after spinal cord injury." In: *Lasers Surg. Med.* 36.3 (2005), pp. 171–185. DOI: 10.1002/lsm.20143.

[316] A. Ehrlicher et al. "Guiding neuronal growth with light." In: *Proc. Natl. Acad. Sci. U.S.A.* 99.25 (2002), pp. 16024–16028.

[317] Y.-Y. Huang et al. "Low-level laser therapy (810 nm) protects primary cortical neurons against excitotoxicity in vitro." In: *J. Biophotonics* 7.8 (2014), pp. 656–664. DOI: 10.1002/jbio.201300125.

[318] Y.-Y. Huang et al. "Low-level laser therapy (LLLT) reduces oxidative stress in primary cortical neurons in vitro." In: *J. Biophotonics* 6.10 (2013), pp. 829–838.

[319] Z. Yu et al. "Near infrared radiation rescues mitochondrial dysfunction in cortical neurons after oxygen-glucose deprivation." In: *Metab. Brain. Dis.* 30 (2015), pp. 491–496.

[320] S. B. Engleson. "Explorative spectrometric evaluations of frying oil deterioration." In: *J. Am. Oil Chem. Soc.* 75.12 (1997), pp. 1495–1508.

[321] G. Blackett. "Contribution of the scotch whisky industry to the Scottish economy." In: *BiGGAR Economics* (2012).

[322] World Health Organization. *Information note: Methanol poisoning outbreaks*. 2014. URL: http://www.spectra-physics.com/assets/client_files/files/documents/service/user-manuals/213A,%20Rev.%20C,%20Model%203900S%20User's%20Manual.pdf.

[323] *Fake whisky warning*. accessed on 30/03/2017. URL: http://news.bbc.co.uk/1/hi/health/2831275.stm.

[324] R. I. Aylott et al. "Analytical strategies to confirm scotch whisky authenticity." In: *J. Inst. Brew.* 116.3 (2010), pp. 215–229. ISSN: 2050-0416. DOI: 10.1002/j.2050-0416.2010.tb00424.x. URL: http://dx.doi.org/10.1002/j.2050-0416.2010.tb00424.x.

[325] R. I. Aylott and W. M. MacKenzie. "Analytical strategies to confirm the generic authenticity of scotch whisky." In: *J. Inst. Brew.* 116.3 (2010), pp. 215–229. ISSN: 2050-0416. DOI: 10.1002/j.2050-0416.2010.tb00424.x. URL: http://dx.doi.org/10.1002/j.2050-0416.2010.tb00424.x.

[326] M. Gallignani, S. Garrigues, and M. de la Guardia. "Direct determination of ethanol in all types of alcoholic beverages by near-infrared derivative spectrometry." In: *Analyst* 118 (1993), pp. 1167–1173.

[327] W. M. Mackenzie and R. I. Aylott. "Analytical strategies to confirm Scotch whisky authenticity. Part II: Mobile brand authentication." In: *Analyst* 129 (2004), pp. 607–612.

[328] T. S. Collins, J. Zweigenbaum, and S. E. Ebeler. "Profiling of nonvolatiles in whiskeys using ultra high pressure liquid chromatography quadropole time-of-flight mass spectrometry (UHPLC-QTOF MS)." In: *Food Chem.* 163 (2014), pp. 186–196.

[329] P. C. Ashok et al. "Waveguide confined Raman spectroscopy for microfluidic interrogation." In: *Lab Chip* 11.7 (2011), pp. 1262–1270.

[330] R. M. Maggio et al. "A novel chemometric strategy for the estimation of extra virgin olive oil adulteration with edible oils". In: *Food Control* 21 (2010), pp. 890–895.

[331] T. Mueller. *Extra virginity: The sublime and scandalous world of olive oil.* New York, U.S.A: W. W. Norton & Company, 2013.

[332] A. Ramzy. *China cracks down on "Gutter Oil," a substance even worse than its name*. accessed on 27/03/2017. URL: http://world.time.com/2011/09/13/china-cracks-down-on-gutter-oil-a-substance-even-worse-than-its-name/.

[333] D. Barboza. *Recycled cooking oil found to be latest hazard in China*. accessed on 27/03/2017. URL: http://www.nytimes.com/2010/04/01/world/asia/01shanghai.html?_r=1.

[334] International Olive Council. *European Commission, EEC regulation 2568/91*. 2013.

[335] E. N. Frankel et al. *Evaluation of Extra-Virgin Olive Oil Sold in California.* Tech. rep. Robert Mondavi Institute, Apr. 2011.

[336] M. D. Kontogianni et al. "The impact of olive oil consumption pattern on the risk of acute coronary syndromes: The CARDIO2000 case-control study." In: *Clin. Cardiol.* 30.3 (2007), pp. 125–129.

[337] R. W. Owen et al. "Olives and olive oil in cancer prevention." In: *Eur.J. Cancer Prev.* 13.4 (2004), pp. 319–326.

[338] K. W. Wahle et al. "Olive oil and modulation of cell signaling in disease prevention." In: *Lipids* 39.12 (2004), pp. 1223–1231.

[339] G. Vlahov, P. Del Re, and N. Simone. "Determination of geographical origin of olive oils using 13C nuclear magnetic resonance spectroscopy. I-classificaion of olive oils of the Puglia region with denomination of protected origin". In: *J. Agric. Food. Chem.* 51.19 (2003), pp. 5612–5615.

[340] W. Dong et al. "Quantitative analysis of adulteration of extra virgin olive oil using Raman spectroscopy improved by Bayesian framework least squares support vector machines." In: *Anal. Methods* 4.18 (2012), pp. 2772–2777.

[341] J. C. Cancilla et al. "Linking chemical parameters to sensory panel results through neural networks To distinguish olive oil quality." In: *J. Agric. Food. Chem* 62.44 (2014), pp. 10661–10665.

[342] E. Guzmán et al. "Evaluation of the overall quality of olive oil using fluorescence spectroscopy." In: *Food Chem.* 173 (2015), pp. 927–934.

[343] J. Ayton, R. J. Mailer, and K. Graham. *The effect of storage conditions on extra virgin olive oil quality*. RIRDC, 2012.

[344] M-Q. Zou et al. "Rapid authentication of olive oil adulteration by Raman spectrometry". In: *J. Agric. Food Chem.* 57.14 (2009), pp. 6001–6006.

[345] E. G. Bligh and W. J. Dyer. "A rapid method of total lipid extraction and purification". In: *Can. J. Biochem. Phys.* 37.8 (1959), pp. 911–917.

[346] S. O. Oyola et al. "Functional analysis of Leishmania cyclopropane fatty acid synthetase." In: *PloS one* 7.12 (2012), e51300.

[347] J. De Gelder et al. "Reference database of Raman spectra of biological molecules". In: *J. Raman Spectrosc.* 38.9 (2007), pp. 1133–1147.

[348] The olive oil source. *Chemical characteristics*. accessed on 03/14/2015. URL: http://www.oliveoilsource.com/page/chemical-characteristics.

[349] A. W. Martinez et al. "Patterned paper as a platform for inexpensive, low-volume, portable bioassays." In: *Angew. Chem. Int. Ed.* 46.8 (2007), pp. 1318–1320. DOI: 10.1002/anie.200603817.

[350] M. Xiong and J. Ye. "Reproducibility in surface-enhanced Raman spectroscopy". In: *J. Shanghai Jiaotong Univ. (Sci.)* 19.6 (2014), pp. 681–690. DOI: 10.1007/s12204-014-1566-7.

[351] Y. Xia et al. "Shape-controlled synthesis of metal nanocrystals: Simple chemistry meets complex physics?" In: *Angew. Chem. Int. Ed.* 48.1 (2009), pp. 60–103. DOI: 10.1002/anie.200802248.

[352] J. M. McLellan et al. "The SERS activity of a supported Ag nanocube strongly depends on its orientation relative to laser polarization." In: *Nano Lett.* 7.4 (2007), pp. 1013–1017.

[353] Y.-J. Lee et al. "Ultrasmooth, highly spherical monocrystalline gold particles for precision plasmonics." In: *ACS Nano* 7.12 (2013), pp. 11064–11070. DOI: 10.1021/nn404765w.

[354] O. Brzobohatý et al. "Non-spherical gold nanoparticles trapped in optical tweezers: shape matters". In: *Opt. Express* 23.7 (2015), pp. 8179–8189.

[355] P. M. Hansen et al. "Expanding the optical trapping range of gold nanoparticles." In: *Nano. Lett.* 5.10 (2005), pp. 1937–1942. DOI: 10.1021/nl051289r.

[356] O. Brzobohatý et al. "Three-dimensional optical trapping of a plasmonic nanoparticle using a low numerical aperture optical tweezers." In: *Sci. Rep.* 5 (2015), p. 8106.

[357] E. Carrilho, A. W. Martinez, and G. M. Whitesides. "Understanding wax printing: A simple micropatterning process for paper-based microfluidics." In: *Anal. Chem.* 81 (2009), pp. 7091–7095.

[358] W. Dungchai, O. Chailapakul, and C. S. Henry. "Use of multiple colorimetric indicators for paper-based microfluidic devices." In: *Anal. Chim. Acta.* 674 (2010), pp. 227–233.

[359] D. Sechi et al. "Three-dimensional paper-based microfluidic device for assays of protein and glucose in urine." In: *Anal. Chem.* 85 (2013), pp. 10733–10737.

[360] A. K. Ellerbee et al. "Quantifying colorimetric assays in paper-based microfluidic devices by measuring the transmission of light through paper." In: *Anal. Chem.* 81 (2009), pp. 8447–8452.

[361] G. Zheng, X. Ou, and C. Yang. "0.5 gigapixel microscopy using a flatbed scanner." In: *Biomed. Opt. Exp.* 5.1 (2013), pp. 1–8. DOI: 10.1364/BOE.5.000001.

[362] A. W. Martinez et al. "Simple telemedicine for developing regions: Camera phones and paper-based microfluidic devices for real-time, off-site diagnosis." In: *Anal Chem* 80.10 (2008), pp. 3699–3707. DOI: 10.1021/ac800112r.

[363] J. Hu et al. "Advances in paper-based point-of-care diagnostics." In: *Biosens. Bioelectron.* 54 (2014), pp. 585–597. DOI: 10.1016/j.bios.2013.10.075.

[364] X. Li, D. R. Ballerini, and W. Shen. "A perspective on paper-based microfluidics: Current status and future trends." In: *Biomicrofluidics* 6 (2012), pp. 011301–13. DOI: 10.1063/1.3687398.

[365] N. K. Thom et al. "Quantitative fluorescence assays using a self-powered paper-based microfluidic device and a camera-equipped cellular phone." In: *RSC Adv.* 4.3 (2014), pp. 1334–1340. DOI: 10.1039/C3RA44717K.

[366] D. Craig, M. Mazilu, and K. Dholakia. "Quantitative detection of pharmaceuticals using a combination of paper microfluidics and wavelength modulated Raman spectroscopy." In: *PLoS One* 10.5 (2015), e0123334. DOI: 10.1371/journal.pone.0123334.

[367] W. W. Yu and I. M. White. "Inkjet-printed paper-based SERS dipsticks and swabs for trace chemical detection." In: *Analyst* 138 (2013), pp. 1020–1025.

[368] W. W. Yu and I. M. White. "Inkjet-printed surface enhanced Raman spectroscopy array on cellulose paper." In: *Anal. Chem.* 82.23 (2010), pp. 9626–9630.

[369] Y. H. Ngo et al. "Gold nanoparticles paper as a SERS bio-diagnostic platform." In: *J. Colloid Interface Sci.* 409 (2013), pp. 59–65.

[370] Y. H. Ngo et al. "Gold nanoparticle-paper as a three-dimensional surface enhanced Raman scattering substrate." In: *Langmuir* 28.23 (2012), pp. 8782–8790. DOI: 10.1021/la3012734.

[371] C. H. Lee et al. "Highly sensitive surface enhanced Raman scattering substrates based on filter paper loaded with plasmonic nanostructures." In: *Anal. Chem.* 83 (2011), pp. 8953–8958.

[372] W.-Q. Ma et al. "Adsorption behaviours of 4-mercaptobenzoic acid on silver and gold films." In: *Chin. J. Chem. Phys.* 23.6 (2010), pp. 659–663.

[373] X. Xia et al. "Silica-coated dimers of silver nanospheres as surface-enhanced Raman scattering tags for imaging cancer cells." In: *Interface focus* 3.3 (2013), p. 20120092. DOI: 10.1098/rsfs.2012.0092.

[374] A. Michota and J. Bukowska. "Surface-enhanced Raman scattering (SERS) of 4-mercaptobenzoic acid on silver and gold substrates." In: *J. Raman Spectrosc.* 34 (2003), pp. 21–25.

[375] S. Borsley, S. Flook, and E. R. Kay. "Rapid and simple preparation of remarkably stable binary nanoparticle planet–satellite assemblies." In: *Chem. Commun.* 51 (2015), pp. 7812–7815.

[376] D. O. Sigle et al. "Observing single molecules complexing with cucurbit[7]uril through nanogap surface-enhanced Raman spectroscopy." In: *J. Phys. Chem. Lett.* 7 (2016), pp. 704–710.

[377] S. Mahajan et al. "Raman and SERS spectroscopy of cucurbit[n]urils". In: *Phys. Chem. Chem. Phys.* 12 (2010), pp. 10429–10433.

[378] S. Kasera et al. "Quantitative SERS using the sequestration of small molecules inside precise plasmonic nanoconstructs". In: *Nano Lett.* 12 (2012), pp. 5924–5928.

[379] P. Dey et al. "Self-assembled hyperbranched polymer-gold nanoparticle hybrids: Understanding the effect of polymer coverage on assembly size and SERS performance." In: *Langmuir* 29 (2013), pp. 525–533.

[380] J. Ye et al. "Plasmonic nanoclusters: Near field properties of the Fano resonance interrogated with SERS." In: *Nano. Lett.* 12 (2012), pp. 1660–1667.

[381] R. A. Halvorson and P. J. Vikesland. "Surface-enhanced Raman spectroscopy (SERS) for environmental analyses." In: *Environ. Sci. Technol.* 44.20 (2010), pp. 7749–7755. DOI: 10.1021/es101228z.

[382] B. Pettinger. "Single-molecule surface- and tip-enhanced Raman spectroscopy". In: *Mol. Phys.* 108.16 (2010), pp. 2039–2059. DOI: 10.1080/00268976.2010.506891.

[383] A. Ashkin. "Acceleration and trapping of particles by radiation pressure". In: *Phys. Rev. Lett.* 24.156 (1970).

[384] A. Ashkin and J. M. Dziedzic. "Optical levitation by radiation pressure." In: *Appl. Phys. Lett.* 19.8 (1971), pp. 283–285. DOI: 10.1063/1.1653919.

[385] A. Ashkin et al. "Observation of a single-beam gradient force optical trap for dielectric particles." In: *Opt. Lett.* 11.5 (1986), pp. 288–290.

[386] A. Ashkin. "History of optical trapping and manipulation of small-neutral particle, atoms, and molecules." In: *IEEE J. Sel. Top. Quantum Electron* 6.6 (2000), pp. 841–856.

[387] S. Chu et al. "Experimental observation of optically trapped atoms." In: *Phys. Rev. Lett.* 57 (1986), p. 314.

[388] A. Ashkin, J. M. Dziedzic, and T. Yamane. "Optical trapping and manipulation of single cels using infrared laser beams." In: *Nature* 330.6150 (1987), pp. 769–771.

[389] C. Bustamante, J. C. Macosko, and G. J. L. Wuite. "Grabbing the cat by the tail: manipulating molecules one by one." In: *Nat. Rev. Mol. Cell Biol.* 1 (2000), pp. 130–136. DOI: 10.1038/35040072.

[390] J. A. Spudich et al. "Optical traps to study properties of molecular motors." In: *Cold Spring Harob. Protoc.* 11 (2011), pp. 1305–1318. DOI: 10.1101/pdb.top066662.

[391] M. M. Brandão et al. "Optical tweezers for measuring red blood cell elasticity: application to the study of drug response in sickle cell disease." In: *Eur. J. Haematol.* 70.4 (2003), pp. 207–211.

[392] M. D. Wang et al. "Stretching DNA with optical tweezers." In: *Biophys. J.* 72.3 (1997), pp. 1335–1346.

[393] B. Redding, M. J. Schwab, and Y.-L. Pan. "Raman spectroscopy of optically trapping single biological micro-particles." In: *Sensors* 15 (2015), pp. 199021–19046. DOI: 10.3390/s150819021.

[394] X. Wang et al. "Enhanced cell sorting and manipulation with combined optical tweezer and microfluidic chip technologies." In: *Lab Chip* 7.11 (2011), pp. 3656–3662. DOI: 10.1039/c1lc20653b.

[395] M. Plöscher. "The role of the plasmon resonance for enhanced optical forces." PhD thesis. The university of St. Andrews, 2012. URL: http://hdl.handle.net/10023/3189.

[396] K. Svoboda and S. M. Block. "Biological applications of optical forces." In: *Annu. Rev. Biophys. Biomol. Struct.* 23 (1994), pp. 247–85. DOI: 10.1146/annurev.bb.23.060194.001335.

[397] A. Lehmuskero et al. "Laser trapping of colloidal metal nanoparticles". In: *ACS Nano* 9.4 (2015), pp. 3453–3469.

[398] M. Dienerowitz, M. Mazilu, and K. Dholakia. "Optical manipulation of nanoparticles: A review". In: *J. Nanophoton.* 2 (2008), p. 021875.

[399] S. E. S. Spesyvtseva and K. Dholakia. "Trapping in a material world." In: *ACS Photonics* 3 (2016), pp. 719–736.

[400] K. Svoboda and S. M. Block. "Optical trapping of metallic Rayleigh particles." In: *Opt. Lett.* 19.13 (1994), pp. 930–932.

[401] A. M. Alkilany and C. J. Murphy. "Toxicity and cellular uptake of gold nanoparticles: what we have learned so far?." In: *J. Nanopart. Res.* 12.7 (2010), pp. 2313–2333.

[402] K. Hamad-Schifferli et al. "Remote electronic control of DNA hybridization through inductive coupling to an attached metal nanocrystal antenna." In: *Nature* 415 (2002), pp. 152–155. DOI: 10.1038/415152a.

[403] Y. Seol, A. E. Carpenter, and T. K. Perkins. "Gold nanoparticles: enhanced optical trapping and sensitivity coupled with significant heating." In: *Opt. Lett.* 31.16 (2006), pp. 2419–2431.

[404] V. Demergis and E-L. Florin. "Ultrastrong optical binding of metallic nanoparticles". In: *Nano Lett.* 12 (2012), pp. 5756–5760. DOI: 10.1021/nl303035p.

[405] L. Jauffred et al. "Optical trapping of gold nanoparticles in air." In: *Nano. Lett.* 15 (2015), pp. 4713–4719. DOI: 10.1021/acs.nanolett.5b01562.

[406] A. Lehmuskero et al. "Ultrafast spinning of gold nanoparticles in water using circularly polarized light." In: *Nano. Lett.* 13 (2013), pp. 3129–3134. DOI: 10.1021/nl4010817.

[407] X. Lu et al. "Chemical synthesis of novel plasmonic nanoparticles." In: *Annu. Rev. Phys. Chem.* 60 (2009), pp. 167–192.

[408] B. J. Wiley et al. "Maneuvering the surface plasmon resonance of silver nanostructures through shape-controlled synthesis". In: *J. Phys. Chem. B* 110.32 (2006), pp. 15666–15675.

[409] R. Saija et al. "Optical trapping calculations for metal nanoparticles. Comparison with experimental data for Au and Ag spheres." In: *Opt. Express* 17.12 (2009), pp. 10231–10241.

[410] E. Messina et al. "Plasmon-enhanced optical trapping of gold nanoaggregates with selected optical properties." In: *ACS Nano* 5.2 (2011), pp. 905–913.

[411] M. Sarshar, W. T. Wong, and B. Anvari. "Comparative study of methods to calibrate the stiffness of a single-beam gradient-force optical tweezers over various laser trapping powers". In: *J. Biomed. Opt.* 19.11 (2014), p. 115001. DOI: 10.1117/1.JBO.19.11.115001.

[412] D. Rings et al. "Hot Brownian motion". In: *Phys. Rev. Lett.* 105.9 (2010), p. 090604.

[413] D. Rings, D. Chakraborty, and K. Kroy. "Rotational hot Brownian motion". In: *New J. Phys.* 14 (2012), p. 053012.